Diagnostic rock textures in fault-controlled dolomite bodies: insights from hyperspectral imaging and the integration of petrographical, geochemical, and geomechanical analyses

A thesis submitted to The University of Manchester for the degree of Doctor of Philosophy (Ph.D.) in the Faculty of Science and Engineering

2022

Cole A. McCormick

School of Natural Sciences

Department of Earth and Environmental Sciences

Blank page

TABLE OF CONTENTS

WORD COUNT: 61,266

LIST OF FIGURES

LIST OF TABLES

ABSTRACT

Fault-controlled, often hydrothermal, dolomitization is typically accompanied by a series of "diagnostic" rock textures that are considered to be indicative of elevated pressure (P) and temperature (T) conditions. Zebra textures, for example, comprise alternating, mm- to cm-scale, bands of replacement dolomite (RD) and saddle dolomite (SD) that form symmetrical RD-SD-SD-RD patterns. Such rock textures are closely related to boxwork textures that form similarly banded textures with highly irregular orientations, as well as cement-supported breccias that include floating clasts of RD that are fully surrounded and supported by SD. Recent studies of hydrothermal dolomite (HTD) bodies have focused on the dimensions of their associated geobodies, the timing of dolomitization, and the source of the dolomitizing fluid. Nevertheless, the sedimentological, tectonic, and metasomatic controls on the formation of these diagnostic rock textures have received limited attention.

This Ph.D. thesis presents a multi-proxy approach to determine the genesis of zebra textures, cement-supported breccias, and boxwork textures in HTD bodies. First, shortwave infrared hyperspectral imaging was used to discern the several phases of RD and SD that form these rock textures, as well as to map their spatial distributions in the field (Chapter IV). Next, axisymmetric rock deformation experiments were used to establish an empirical framework by which the stress states that contribute to their formation can be interpreted (Chapter V). Lastly, a conceptual model for the formation of these rock textures is presented, incorporating a range of field, petrographical, and geochemical evidence (Chapter VI). Zebra textures, cement-supported breccias, and boxwork textures are closely associated with faults and carbonate-hosted ore deposits (e.g., magnesite, rare earth element, and Mississippi Valley-type mineralization), thus providing invaluable information regarding the hydrogeological evolution of a sedimentary basin and the metasomatism of carbonate sedimentary rocks under elevated P/T conditions.

DECLARATION

The University of Manchester

Ph.D. by published work Candidate Declaration

Candidate Name: Cole A. McCormick

Title of thesis: Diagnostic rock textures in fault-controlled dolomite bodies: insights from hyperspectral imaging and the integration of petrographical, geochemical, and geomechanical analyses

Faculty of Science and Engineering

School of Natural Sciences

Department of Earth and Environmental Sciences

I declare that no portion of the work referred to in this thesis has been submitted in support of an application for another degree or qualification of this or any other university or other institute of learning.

COPYRIGHT STATEMENT

DEDICATION

The unwavering support of my family throughout the past three years has meant the world to me. Growing up in a small town in Canada, hundreds of kilometers away from a major university, pursuing a Ph.D. is not the "standard" career path, let alone moving 6500 km overseas to do so. This thesis is dedicated to my grandparents, Ron and Hazel McCormick and Gordon and Dorothy Friedrick, who attended hundreds of hockey and football games throughout my childhood and have always supported my education. Even though Ron, Gordon, and Dorothy are not here to see the completion of my Ph.D., I know that they would be incredibly proud of this accomplishment.

ACKNOWLEDGEMENTS

I would like to personally thank my advisors, Cathy Hollis, Hilary Corlett, and Ernest Rutter, for their endless support, guidance, and sharing of knowledge during my three years at The University of Manchester. I am deeply indebted to Cathy, Hilary, and Ernie for their flexibility and unwavering support of my research during the challenges of the coronavirus pandemic. I would also like to acknowledge the President's Doctoral Scholar award at The University of Manchester, without which this Ph.D. thesis would not have been possible. Due to the relatively limited analytical funding for this project, I am greatly appreciative to the various staff and facilities at The University of Manchester, including Ernest Rutter and Julian Mecklenburgh for access to the rock deformation laboratory, Lee Paul and David Oliver for sample preparation, John Waters for conducting the XRD, Lewis Hughes for assistance with the SEM and maintenance of the CL facilities, Jonathan Fellows for conducting the EPMA, and Romain Tartese for conducting the LA ICP-MS. The continued funding and maintenance of these facilities by The University of Manchester was essential to the success of this thesis, and to those that come after me.

External to The University of Manchester, I am greatly appreciative of Benoit Rivard for providing the equipment used for the hyperspectral imaging (University of Alberta), Jenny Omma and Rocktype Ltd. for access to their QEMSCAN facilities, Adrian Boyce and Matthieu Clog for access to their stable and clumped isotope laboratories (Scottish Universities Environmental Research Centre), and of Matthew Steele-MacInnis for access to his fluid inclusion laboratory (University of Alberta). I am also grateful to the British Sedimentological Research Group (Trevor Elliot Memorial Grant), International Association of Sedimentologists, Society for Sedimentary Geology, Geological Society of London, and the American Association of Petroleum Geologists (Classen Family Named Grant), who partially funded this research through various post-graduate research grants.

Blank page

CHAPTER I – INTRODUCTION

1.1. Introduction

Although dolomite has been the subject of extensive research, uncertainty persists regarding how certain rock textures (e.g., zebra textures, cement-supported breccias, boxwork textures) develop during fault-controlled, hydrothermal fluid flow. Models for the formation of hydrothermal dolomite (HTD) are largely based on outcrop, petrographic and geochemical studies (Vandeginste et al. 2005; Davies and Smith Jr., 2006; Gasparrini et al. 2006; Dewit et al. 2012, 2014; Hirani et al. 2018; Kareem et al. 2019; Shelton et al. 2019; Koeshidayatullah et al. 2020a, 2020b) and typically lack a geomechanical characterization. Nevertheless, faults and fractures are widely considered important fluid conduits for diagenesis in sedimentary basins (Sibson et al. 1975; Cox et al. 2001; Sibson, 2001), to the extent that "structural diagenesis" has emerged as a prominent topic of research (Laubach et al. 2010; Anders et al. 2014). The application of structural diagenesis to the study of fault-controlled, hydrothermal dolomite bodies, however, has not yet been considered.

The formation of the rock textures that are typically found in HTD bodies have not been studied in depth and are often amalgamated as a single step in the overall paragenetic sequence of the succession, even though there is little evidence to do so. Zebra textures, for example, consist of alternating, mm- to cm-scale, parallel to sigmoidal, dark host-rock bands (A) and light mineral-filled bands (B) that form symmetrical A-B-B-A patterns (Fig. 1.1). Their presence is considered diagnostic of high pressure, high temperature, fault-controlled fluid flow; particularly in ore- and hydrocarbon-bearing systems (Davies and Smith Jr., 2006; Swennen et al. 2012 Vandeginste et al. 2014; Kareem et al. 2019; Shelton et al. 2019). There are, however, several examples of fault-controlled dolomite bodies that lack zebra textures (Hendry et al. 2015; Hollis et al. 2017). Numerous conceptual models have been postulated to explain the formation of zebra textures, yet there is little consensus and previous studies suggest that they arise either due to dissolution (Krebs and Macqueen,

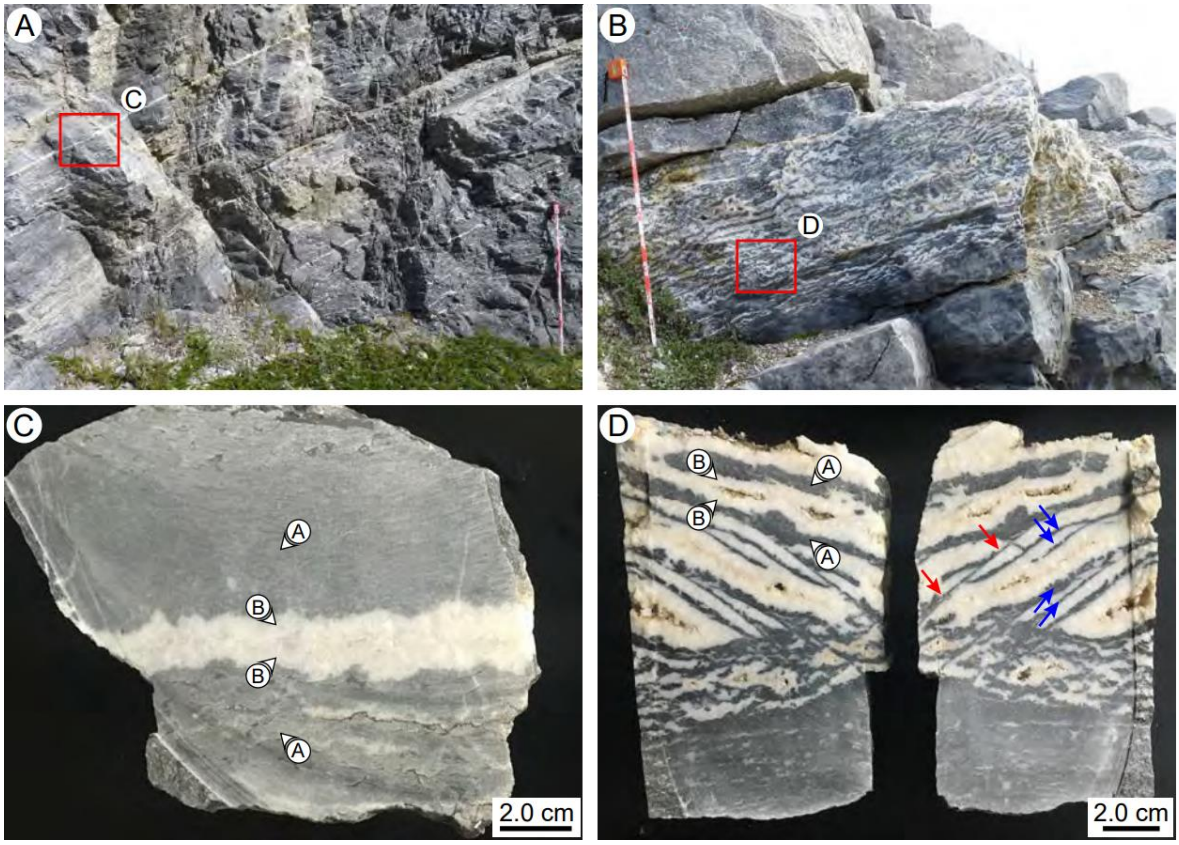

Figure 1.1. (A) Photograph of bedding-parallel zebra textures in the footwall of a transtensional fault at Whirlpool Point (Cathedral Formation, Middle Cambrian, Western Canadian Sedimentary Basin). Scale = 1.0 m. **(B)** Photograph of bedding-inclined zebra textures at Mistaya Canyon (Eldon Formation, Middle Cambrian, Western Canadian Sedimentary Basin. Scale = 1.0 m. **(C)** Hand-sample from Fig. 1.1A showing the alternating dark host-rock bands (A) and light mineral-filled bands (B) that form symmetrical A-B-B-A patterns. **(D)** Hand-sample from Fig. 1.1B showing the alternating A-B-B-A pattern. Note the occurrence of shear fractures (red arrows) and the trails of the dark host-rock bands (blue arrows) that are entrained within the zebra textures.

1984; Fontboté and Gorzawski, 1990; Morrow, 2014), fracturing (Wallace et al. 1994; Nielsen et al. 1998; Boni et al. 2000; Vandeginste et al. 2005; Gasparrini et al. 2006; López-Horgue et al. 2009; Swennen et al. 2012; Wallace and Hood, 2018), or recrystallization/replacement (Lugli et al. 2000; Merino and Canals, 2011; Kelka et al. 2015, 2017). Of the studies that have been conducted, a comprehensive petrographic, geochemical, and geomechanical characterization has yet to be presented and these conceptual models have not been tested by iterative experimental analyses.

This study aims to elucidate the genesis of zebra textures, closely associated with cement-supported breccias and boxwork textures, through the detailed characterization of

exposures of HTD bodies that are hosted in the Middle Cambrian strata in the Western Canadian Sedimentary Basin (WCSB). Shortwave infrared hyperspectral imaging was applied to discern macro-scale diagenetic heterogeneities in these systems, and to guide a rigorous sampling protocol for the ensuing petrographical and geochemical analyses. Such analyses were conducted in parallel with rock deformation experiments that aimed to investigate the conditions that give rise to failure over a wide range of stress states (from true tensile failure to shear failure), and to reproduce zebra textures in the laboratory. Such an approach is original, as it utilizes systematic sampling and analysis of actual zebra textures to inform process-based experimental analysis. The results of this study have wide applications as zebra textures, cement-supported breccias, and boxwork textures are closely associated with faults and carbonate-hosted ore deposits (e.g., Mississippi Valley-type mineralization), which suggests that they provide vital information regarding fluid flux and carbonate diagenesis under high pressure, high temperature conditions.

1.2. Research questions and objectives

Based on the review presented in Chapter II of this thesis, several gaps in the literature have been recognized, and this Ph.D. aims to address the following research questions:

(1) What is the paragenetic sequence of the various dolomite phases that are present in zebra textures (and the associated cement-supported breccias and boxwork textures)?

(2) What is the best method to discern these paragenetic stages, and are there scale limitations to the conventional analyses that are applied to study carbonate diagenesis?

(3) How do rock textures (zebra textures, cement-supported breccias, boxwork textures) in fault-controlled dolomite bodies form? How reliable are the models for their genesis?

(4) Although there is a general consensus that fracturing is involved in their formation, what are the particular stress conditions that give rise to these rock textures?

(5) Can the wide array of rock textures in these systems simply form through dilatational fracturing and cementation, or are there additional processes yet to be recognized?

1.3. Thesis structure

This Ph.D. thesis is presented in a journal-style format that includes an introduction (Chapter I), a literature review (Chapter II), methods (Chapter III), three original research contributions (Chapters IV to VI), and a synthesis of these works that includes the overarching conclusions of the thesis (Chapter VII). The original research contributions are meant to stand alone with their own introductions, methods, results, interpretations, discussions, and conclusions. Accordingly, there will naturally be some repetition between the methods presented in Chapter III and those that are presented in each of the original research contributions. These works include several authors, but the bulk of the data collection, interpretation, and writing was conducted by the first author (C.A. McCormick). Co-authors were primarily responsible for teaching and assisting with analytical methods, ownership of the equipment, supervision, and editorial review. The main conclusions from the three original research contributions (Chapters IV to VI) are summarized as follows:

ORIGINAL CONTRIBUTION #1 (CHAPTER IV)

Shortwave infrared hyperspectral imaging as a novel method to elucidate multi-phase dolomitization, recrystallization, and cementation in carbonate sedimentary rocks

This chapter investigates how the texture and composition of dolomite can be elucidated from its reflectance spectra, thus providing a detailed map of the distribution of each paragenetic stage in a succession. The position of the ~2315 nm absorption-band is commonly used to differentiate dolomite from calcite in hyperspectral imagery, but this study is the first to use this method to infer the Ca to Mg ratio of multiple dolomite phases with varying compositions. The spectral contrast of the reflectance profile, accounting for both the overall reflectance and the depth of the absorption-bands, is also shown here to correlate with dolomite texture (e.g., crystal size, boundary-shape). As a result, the hyperspectral imagery yields mineral distribution maps that provide meter-scale spatial information on the diagenetic history of the strata, which can then be used for sampling.

ORIGINAL CONTRIBUTION #2 (CHAPTER V)

An experimental study of the transition from tensile failure to shear failure in Carrara marble and Solnhofen limestone: Does "hybrid failure" exist?

This chapter investigates the microstructural evolution from true tensile failure to shear failure in Carrara marble and Solnhofen limestone, two carbonate rocks that are widely used in rock mechanical studies. A "hybrid failure" mode is often proposed to describe the orientation of faults between these end-members, but this concept has traditionally been based on a "Griffith-type" failure envelope that was only meant to describe the growth a single crack. This study, however, demonstrates that failure under these transitional conditions involves the formation of several, transgranular tensile cracks, that coalesce into a shear-mode fault, inclined at <10° to the maximum principal stress. Here we propose a continuous parabolic failure envelope, defined by the resolved shear stress and normal stress on the failure surfaces, throughout this transitional region because such a function is rooted in the observation that the lengths, spacing, and apertures of the precursory tensile cracks decrease with increasing differential stress and mean stress.

ORIGINAL CONTRIBUTION #3 (CHAPTER VI)

Basin-scale fluid-flow, dolomitization patterns, and diagnostic rock textures in fault-controlled dolomite bodies: Insights from the Western Canadian Sedimentary Basin

This chapter applies a basin-scale approach to investigate the genesis of zebra textures, cement-supported breccias, and boxwork textures in fault-controlled dolomite bodies. Distal to the source of the dolomitizing fluid, the strata comprise bedding-parallel zebra textures that formed by dilatational fracturing and the precipitation of saddle dolomite as a cement. Proximal to the source of the dolomitizing fluid, however, the strata comprise bedding-inclined zebra textures, cement-supported breccias, and boxwork textures that have been affected by recrystallization. Consequently, the metasomatic evolution of these rock textures reflects the timing, depth, and temperature of

dolomitization, as well as the proximity to the source of the dolomitizing fluid. Such a model resolves the conflicts between existing models for the formation of zebra textures and can be applied to rock textures in fault-controlled dolomite bodies globally.

1.4. CRediT authorship statement for each chapter

Given that this Ph.D. thesis is presented as papers intended for publication, the ensuing section outlines the contributions that were made by each of the co-authors.

ORIGINAL CONTRIBUTION #1 (CHAPTER IV)

Shortwave infrared hyperspectral imaging as a novel method to elucidate multi-phase dolomitization, recrystallization, and cementation in carbonate sedimentary rocks

C.A. McCormick: Methodology, Formal analysis, Investigation, Validation, Writing – original draft, Visualization, Funding acquisition.

H. Corlett: Conceptualization, Supervision, Resources, Writing – review & editing.

J. Stacey: Formal analysis, Data curation.

C. Hollis: Supervision, Resources, Writing – review & editing.

J. Feng: Software, Formal analysis, Data curation.

B. Rivard: Methodology, Supervision, Resources, Writing – review & editing.

J.E. Omma: Software, Formal analysis, Resources, Data curation.

ORIGINAL CONTRIBUTION #2 (CHAPTER V)

An experimental study of the transition from tensile failure to shear failure in Carrara marble and Solnhofen limestone: Does "hybrid failure" exist?

C.A. McCormick: Conceptualization, Methodology, Formal analysis, Investigation, Validation, Writing – original draft.

E.H. Rutter: Conceptualization, Methodology, Software, Formal analysis, Investigation, Supervision, Writing – review & editing.

ORIGINAL CONTRIBUTION #3 (CHAPTER VI)

Basin-scale fluid-flow, dolomitization patterns, and diagnostic rock textures in fault-controlled dolomite bodies: Insights from the Western Canadian Sedimentary Basin

C.A. McCormick: Conceptualization, Methodology, Formal analysis, Investigation, Validation, Writing – original draft, Funding aquisition.

H. Corlett: Conceptualization, Supervision, Writing – review & editing.

M. Clog: Formal analysis, Data curation, Supervision.

A.J. Boyce: Formal analysis, Data curation, Supervision.

R. Tartese: Formal analysis, Data curation, Supervision.

M. Steele-MacInnis: Formal analysis, Supervision.

C. Hollis: Conceptualization, Supervision, Writing – review & editing.

References

Anders, M.H., Laubach, S.E., Scholz, C.H., 2014. Microfractures: A review. Journal of Structural Geology, 69, 377-394.

Boni, M., Iannace, A., Bechstädt, T., Gasparrini, M., 2000. Hydrothermal dolomites in SW Sardinia (Italy) and Cantabria (NW Spain): evidence for late-to post-Variscan widespread fluid-flow events. Journal of Geochemical Exploration, 69, 225-228.

Cox, S.F., Knackstedt, M.A., Braun, J., 2001. Principles of structural control on permeability and fluid flow in hydrothermal systems. In: Richards, J.P., Tosdal, R.M., (Eds.), Structural controls on ore genesis. Society of Economic Geologists, Reviews in Economic Geology, 14, 1-24.

Davies, G.R., Smith Jr., L.B., 2006. Structurally controlled hydrothermal dolomite reservoir facies: an overview. AAPG bulletin, 90, 1641-1690.

Dewit, J., Foubert, A., El Desouky, H.A., Muchez, P., Hunt, D., Vanhaecke, F., Swennen, R., 2014. Characteristics, genesis and parameters controlling the development of a large stratabound HTD body at Matienzo (Ramales Platform, Basque – Cantabrian Basin, northern Spain). Marine and Petroleum Geology, 55, 6-25.

Dewit, J., Huysmans, M., Muchez, P., Hunt, D.W., Thurmond, J.B., Vergés, J., Saura, E., Fernandez, N., Romaire, I., Esestime, P., Swennen, R., 2012. Reservoir characteristics of fault-controlled hydrothermal dolomite bodies: Ramales Platform case study. Geological Society, London, Special Publications, 370(1), 83-109.

Fontboté, L., Gorzawski, H., 1990. Genesis of the Mississippi Valley-type Zn-Pb deposit of San Vicente, central Peru; geologic and isotopic (Sr, O, C, S, Pb) evidence. Economic Geology, 85, 1402-1437.

Gasparrini, M., Bechstädt, T., Boni, M., 2006. Massive hydrothermal dolomites in thesouthwestern Cantabrian Zone (Spain) and their relation to the Late Variscan evolution. Marine and Petroleum Geology, 23, 543-568.

Hendry, J.P., Gregg, J.M., Shelton, K.L., Somerville, I.D., Crowley, S.F., 2015. Origin, characteristics and distribution of fault-related and fracture-related dolomitization: Insights from Mississippian carbonates, Isle of Man. Sedimentology, 62(3), 717-752.

Hirani, J., Bastesen, E., Boyce, A., Corlett, H., Gawthorpe, R., Hollis, C., John, C.M., Robertson, H., Rotevatn, A., Whitaker, F., 2018. Controls on the formation of stratabound dolostone bodies, Hammam Faraun Fault block, Gulf of Suez. Sedimentology, 65(6), 1973-2002.

Hollis, C., Bastesen, E., Boyce, A., Corlett, H., Gawthorpe, R., Hirani, J., Rotevatn, A., Whitaker, F., 2017. Fault-controlled dolomitization in a rift basin. Geology, 45(3), 219-222.

Kareem, K.H., Al-Aasm, I.S., Mansurbeg, H., 2019. Structurally-controlled hydrothermal fluid flow in an extensional tectonic regime: A case study of Cretaceous Qamchuqa Formation, Zagros Basin, Kurdistan Iraq. Sedimentary Geology, 386, 52-78.

Kelka, U., Koehn, D., Beaudoin, N., 2015. Zebra pattern in rocks as a function of grain growth affected by second-phase particles. Frontiers in Physics, 3, 1-14.

Kelka, U., Veveakis, M., Koehn, D., Beaudoin, N., 2017. Zebra rocks: compaction waves create ore deposits. Scientific Reports, 7(1), 1-9.

Koeshidayatullah, A., Corlett, H., Stacey, J., Swart, P.K., Boyce, A., Robertson, H., Whitaker, F., Hollis, C., 2020a. Evaluating new fault-controlled hydrothermal dolomitisation models: Insights from the Cambrian Dolomite, Western Canadian Sedimentary Basin. Sedimentology, 67, 2945-2973.

Koeshidayatullah, A., Corlett, H., Stacey, J., Swart, P.K., Boyce, A., Hollis, C., 2020b. Origin and evolution of fault-controlled hydrothermal dolomitization fronts: A new insight. Earth and Planetary Science Letters, 541, 116291.

Krebs, W., Macqueen, R., 1984. Sequence of diagenetic and mineralization events, Pine Point lead-zinc property, Northwest Territories, Canada. Bulletin of Canadian Petroleum Geology, 32, 434-464.

Laubach, S.E., Eichhubl, P., Hilgers, C., Lander, R.H., 2010. Structural diagenesis. Journal of Structural Geology, 32(12), 1866-1872.

López-Horgue, M.A., Iriarte, E., Schroeder, S., Caline, B., Fernández Mendiola, P.Á., 2009. An example on the tectonic origin of zebra dolomites: the San Martín beach outcrop (Santoña, North Spain). Geogaceta, 47, 85-88.

Lugli, S., Torres-Ruiz, J., Garuti, G., Olmedo, F., 2000. Petrography and geochemistry of the Eugui magnesite deposit (Western Pyrenees, Spain): evidence for the development of a peculiar zebra banding by dolomite replacement. Economic Geology, 95, 1775-1791.

Merino, E., Canals, À., 2011. Self-accelerating dolomite-for-calcite replacement: Self-organized dynamics of burial dolomitization and associated mineralization. American Journal of Science, 311(7), 573-607.

Morrow, D.W., 2014. Zebra and boxwork fabrics in hydrothermal dolomites of northern Canada: Indicators for dilational fracturing, dissolution or in situ replacement? Sedimentology, 61, 915-951.

Nielsen, P., Swennen, R., Muchez, P., Keppens, E., 1998. Origin of Dinantian zebra dolomites south of the Brabant-Wales Massif, Belgium. Sedimentology, 45, 727-743.

Shelton, K.L., Hendry, J.P., Gregg, J.M., Truesdale, J.P., Somerville, I.D., 2019. Fluid Circulation and Fault- and Fracture-related Diagenesis in Mississippian Syn-rift Carbonate Rocks on the Northeast Margin of the Metalliferous Dublin Basin, Ireland. Journal of Sedimentary Research, 89(6), 508-536.

Sibson, R.H., Moore, J.M.M., Rankin, A.H., 1975. Seismic pumping - a hydrothermal fluid transport mechanism. Journal of the Geological Society, 131(6), 653-659.

Sibson, R.H. 2001. Seismogenic framework for hydrothermal transport and ore deposition. In: Richards, J.P., Tosdal, R.M., (Eds.), Structural controls on ore genesis. Society of Economic Geologists, Reviews in Economic Geology, 14, 25-50.

Swennen, R., Dewit, J., Fierens, E., Muchez, P., Shah, M., Nader, F., Hunt, D., 2012. Multiple dolomitization events along the Pozalagua Fault (Pozalagua Quarry, Basque–Cantabrian Basin, Northern Spain). Sedimentology, 59, 1345-1374.

Vandeginste, V., Swennen, R., Gleeson, S.A., Ellam, R.M., Osadetz, K., Roure, F., 2005. Zebra dolomitization as a result of focused fluid flow in the Rocky Mountains Fold and Thrust Belt, Canada. Sedimentology, 52, 1067-1095.

Vandeginste, V., John, C.M., Cosgrove, J.W., Manning, C., 2014. Dimensions, texture distribution, and geochemical heterogeneities of fracture–related dolomite geobodies hosted in Ediacaran limestones, northern Oman. AAPG bulletin, 98, 1789-1809.

Wallace, M.W., Both, R., Morales-Ruano, S., Hach-Ali, P.F., Lees, T., 1994. Zebra textures from carbonate-hosted sulfide deposits: sheet cavity networks produced by fracture and solution enlargement. Economic Geology, 89, 1183-1191.

Wallace, M.W., vS Hood, A., 2018. Zebra textures in carbonate rocks: Fractures produced by the force of crystallization during mineral replacement. Sedimentary Geology, 368, 58-67.

Blank page

2.1. Foundational concepts and dolomitization models

Dolomite, the mineral and the rock, was discovered by Déodat de Dolomieu on a field trip to northeast Italy. In the Journal de Physique, Dolomieu (1791) described a calcareous rock that, unlike limestone, did not effervesce in dilute acid. The following year, the rock was named dolomie (or dolomite, in English) by Nicolas-Théodore de Saussure in the same journal. Ordered dolomite has a chemical formula of $CaMg(CO_3)_2$, with a structure consisting of alternating layers of $Ca^{2+} – CO_3^{2-} – Mg^{2+} – CO_3^{2-}$ that are oriented normal to the crystallographic c-axis. Dolomitization refers to the replacement of $CaCO_3$ by $CaMg(CO_3)_2$ and is most commonly expressed as:

$$2CaCO_3\ (s) + Mg^{2+}\ (aq) \rightleftharpoons CaMg(CO_3)_2\ (s) + Ca^{2+}\ (aq) \quad (2.1)$$

but may also be written as:

$$CaCO_3\ (s) + Mg^{2+}\ (aq) + CO_3^{2-}\ (aq) \rightleftharpoons CaMg(CO_3)_2\ (s) \quad (2.2)$$

Dolomite cementation, which, as a process, is distinct from dolomitization, refers to the precipitation of dolomite directly from an aqueous solution:

$$Ca^{2+}\ (aq) + Mg^{2+}\ (aq) + 2CO_3^{2-}\ (aq) \rightleftharpoons CaMg(CO_3)_2\ (s) \quad (2.3)$$

Reaction 2.1 gives rise to a volume reduction of 6% to 13% (replacement of aragonite and calcite, respectively), whereas reaction 2.2 yields a volume expansion of 75% to 88% (Lippmann, 1973; Morrow, 1982a). The notion of mole-for-mole dolomitization and its relationship to porosity, which was first postulated by De Beaumont (1837), is far too simplistic and these two reactions are typically represented as end-members of possible reaction stoichiometries (Machel, 2004). Morrow (1982a) suggested that volumetric conservation during replacement may be an important constraint and that volume-for-volume dolomitization is expressed as:

$$(2\text{-}x)CaCO_3\ (s) + Mg^{2+}\ (aq) + (x)CO_3^{2-}\ (aq) \rightleftharpoons CaMg(CO_3)_2\ (s) + (1\text{-}x)Ca^{2+}\ (aq) \quad (2.4)$$

Accordingly, dolomitization requires vast amounts of Mg^{2+} and Ca^{2+} to be transported to/from the reaction site. Land (1985) calculated that 650 m^3 of seawater is required to dolomitize 1 m^3 of limestone with 40% porosity. Evapo-concentration reduces the volume required (e.g., 30 m^3 for halite-saturated brine), whereas dilution increases the volume required (e.g., 6500 m^3 for seawater diluted to 10% concentration) (Land, 1985). Although ordered, stoichiometric dolomite has not been experimentally synthesized at near-surface conditions, experimental observations at temperatures >50˚C indicate that dolomitization proceeds by a dissolution-precipitation mechanism via a series of metastable precursors (Zempolich and Baker, 1993; Kaczmarek and Sibley, 2007; Kaczmarek and Thornton, 2017; Morrow, 2020). This dissolution-precipitation mechanism is facilitated by diffusive transport through a porous reaction rim that allows Mg^{2+} ions to be imported to, and Ca^{2+} ions to be exported from, the reaction site (Jonas et al. 2015). The formation of pervasive dolomite bodies requires advection in an open fluid-rock system and dolomitization models are, essentially, hydrogeological models (Budd, 1997; Warren, 2000; Machel 2004; Whitaker et al. 2004; Jones and Xiao, 2005; Whitaker and Xiao, 2010; Morrow, 2020).

2.1.1. Dolomitization models

There are numerous models for the formation of pervasive dolomite bodies (e.g., seepage reflux, sabkha, seawater, burial), each of which provide different hydrogeological mechanisms for the sustained transport of Mg-rich fluids (Warren, 2000; Machel, 2004; Whitaker et al. 2004). Seepage reflux (post-depositional) and sabkha (syn-depositional) dolomitization are similar processes, both hydrogeologically and geochemically. Reflux dolomitization, which was first applied to the Permian Basin of west Texas (Adams and Rhodes, 1960), refers to the downward, density-driven flow of evapo-concentrated seawater in restricted marine settings (Jones et al. 2003; Jones and Xiao, 2005). Sabkha dolomitization, which is exemplified by the Trucial Coast of the Arabian Gulf, refers to the episodic flooding of the supratidal zone and the reflux of evapo-concentrated seawater

(Patterson and Kinsman, 1981, 1982). Seawater dolomitization is a somewhat misleading term that refers to a group of dolomitization models invoking seawater, or modified seawater, as the principle dolomitizing fluid irrespective of the hydrogeological transport mechanism (Machel and Mountjoy, 1986; Whitaker et al. 2004). Seawater dolomitization, which is typified by the well-documented Cenozoic "island dolomite" with extant hydrogeological systems, is characteristic of dolomite that formed at near-surface temperatures on isolated islands that have not been deeply buried (Budd, 1997; Ren and Jones, 2017, 2018; Wang et al. 2018). There are also common examples of dolomitization by near-normal seawater (e.g., Ryan et al. 2020) and/or mesohaline seawater (Newport et al. 2020). In contrast, "modified" seawater has been invoked for dolomitization in a wide array of burial settings with more complex hydrogeological systems (Machel and Anderson, 1989; Gregg et al. 2001; Whitaker and Xiao, 2010; Al-Helal et al. 2012; Isabel Millán et al. 2016; Hollis et al. 2017). Burial dolomitization refers to dolomite that formed in environments where the pore-fluid chemistry is removed from surface processes (Warren, 2000; Whitaker and Xiao, 2010; Benjakul et al. 2020). Evidently, the distinction between burial dolomitization, which is defined by burial depth/hydrogeology, and seawater dolomitization, which is defined by the fluid source, is problematic (Machel, 2004). Consequently, Machel (1999) distinguished these environments by the boundary between "shallow burial" and "intermediate burial", which occurs at ~600 m to ~1000 m.

2.1.2. Hydrogeological transport mechanisms for burial dolomitization

Burial dolomitization involves a wide array of hydrogeological mechanisms that can transport fluids from several different sources during burial (e.g., meteoric water, seawater, formational fluids, basinal fluids). These transport mechanisms, which differ in the nature of the fluid drives and the direction(s) of fluid flow, include (1) compaction/dewatering (Fig. 2.1A), (2) topography-driven flow (Fig. 2.1B), (3) tectonically-driven (i.e., squeegee) flow (Fig. 2.1C), (4) thermal convection (Fig. 2.1D), and (5) seismic pumping (Fig. 2.1E,

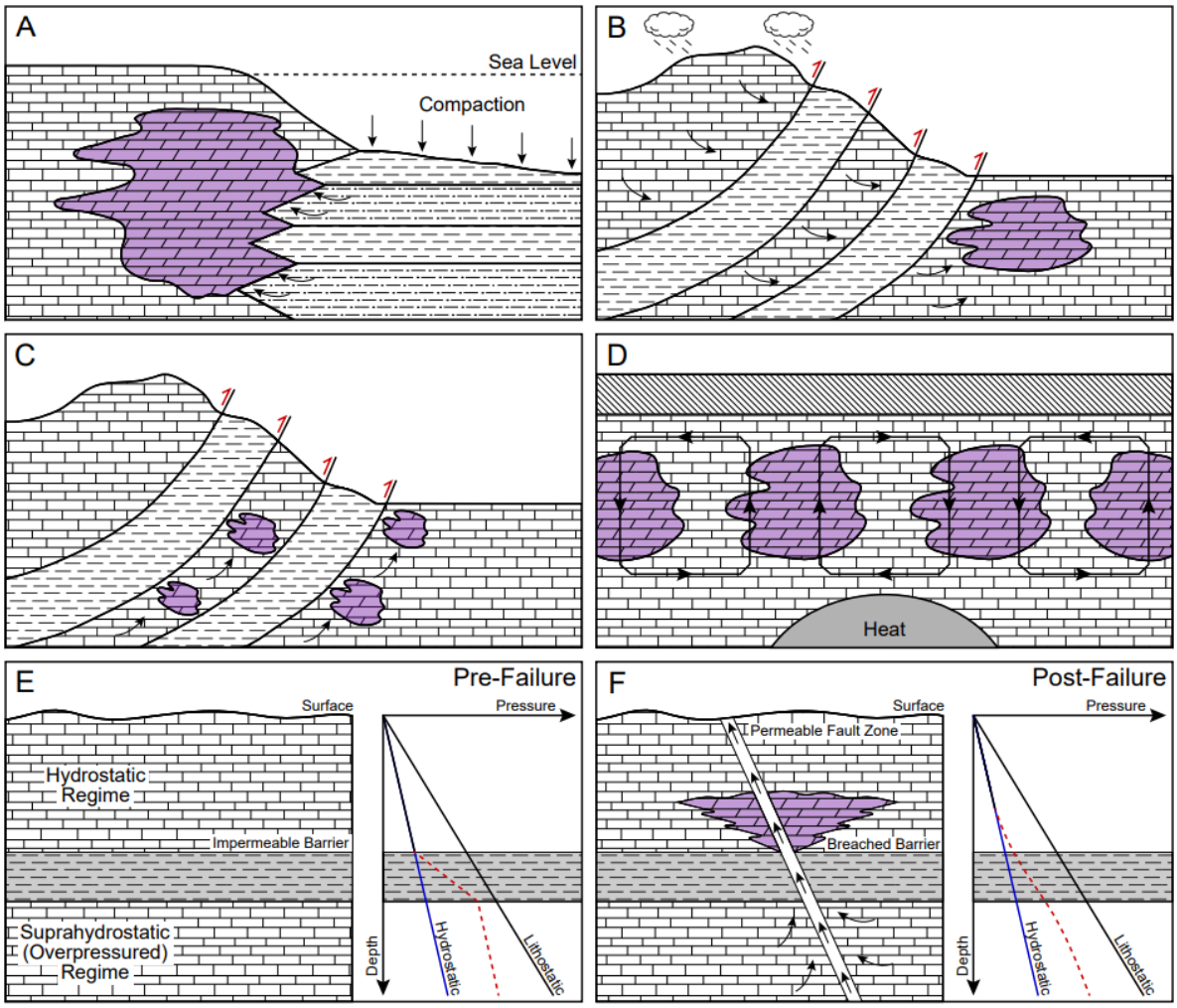

Figure 2.1. Major burial dolomitization models summarized in simplified cross-sections, including the **(A)** compaction/dewatering model, **(B)** topography-driven flow model, **(C)** tectonically-driven flow model, **(D)** thermal convection model, and **(E)** seismic pumping model. Seismic pumping is shown as "pre-failure" and **(F)** "post-failure" to illustrate the change in pore pressure upon faulting. Purple areas show the dolomite bodies. Modified from Sibson (1992) and Gasparrini et al. (2006).

F; Sibson et al. 1975; Morrow, 1999; Warren, 2000; Machel, 2004; Gasparrini et al., 2006). Although the compaction flow model has been demonstrated to be capable of local dolomitization in overpressured basins (e.g., Frazer et al. 2014), the topography-driven and tectonically-driven flow models have been abandoned largely due to low fluid fluxes and mass-balance constraints (Morrow, 1999; Machel, 2004). Fluid flow in each of these geological settings may be the product of several transport mechanisms/fluid sources that act simultaneously or consecutively (Machel, 2004; Whitaker at al., 2004). Accordingly, more recent burial dolomitization models involve a combination of these conventional

models to overcome mass balance constraints and fluid flux requirements (Whitaker and Xiao, 2010; Hollis et al. 2017; Koeshidayatullah et al. 2020a; Benjakul et al. 2020).

2.2. Terminology of zebra textures in carbonate sedimentary rocks

Although the term was not applied, zebra textures were first documented in western Canada by Walcott (1908) in his landmark paper on the Burgess Shale (Stephen Formation, Middle Cambrian, WCSB). While describing the cliff-forming dolomites of the Cathedral Formation (Middle Cambrian), Walcott (1908; p. 239) noted that "At 825 feet [from the base of the section] the massive layers are banded with light and dark grey colors.". The term "zebra rock" was first used by Emmons et al. (1927; p. 33) to describe "white streaks and patches of coarse-grained dolomite" in the Leadville limestone (Mississippian), Colorado, United States. Although the term "zebra rock" was maintained by Engel et al. (1958), numerous terms such as "diagenetic crystallization rhythmites" (Levin and Amstutz, 1976; Fontboté, 1981; Fontboté and Amstutz, 1982, 1983; Fontboté, and Gorzawski, 1990; Arne et al. 1991), "rhythmites" (Sass-Gustkiewicz and Mochnacka, 1994), ribbon structures (Sass-Gustkiewicz et al. 1982), and "banded ores" (Tompkins et al. 1994) were introduced. More recently, the terms "zebra texture" (Beales and Hardy, 1980; Wallace et al. 1994; Kelka et al. 2015, 2017; Wallace and Hood, 2018; Kareem et al. 2019), "zebra dolomite" (Zeeh, 1995; Vandeginste et al. 2005; Iannace et al. 2012; Dewit et al. 2012, 2014; Morrow, 2014; Vandeginste et al. 2014; Kelka et al. 2015, 2017; Hirani et al. 2018; Shelton et al. 2019), "zebra structure" (Boni et al. 1992, 2000; Gasparrini et al. 2006; Iannace et al. 2012; Gabellone et al. 2014), and "zebra fabric" (Sharp et al. 2010; Morrow, 2014; Hirani et al. 2018; Shelton et al. 2019) have been introduced and are the standard nomenclature in the literature; with authors indiscriminately applying the terms interchangeably (Nielsen et al. 1998; López-Horgue et al. 2009; Swennen et al. 2012).

Although dolomite most commonly forms zebra textures, analogous textures were reported in ankerite, siderite, sphalerite, marcasite, barite, fluorite, and magnesite (Fontboté

and Gorzawski, 1990; Arne at al. 1991; Wallace et al. 1994; Tompkins et al. 1994; Sass-Gustkiewicz and Mochnacka, 1994; Zeeh, 1995; Dill et al. 2014). Accordingly, Wallace and Hood (2018) suggested that the term "zebra dolomite" is inadequate. The peculiar, banded sphalerite textures documented by Wallace et al. (1994) and Wallace and Hood (2018; their Fig. 1C), however, include microstalactitic cements and internal sediments that are not typical of zebra textures in HTD bodies. Furthermore, Zeeh (1995) demonstrated that fluorite replaced pre-existing zebra textures in Triassic strata from the Drau Range, Austria, and Shelton et al. (2019) documented silicified zebra textures in Mississippian strata from the Dublin Basin, Ireland. It is, therefore, ambiguous as to whether the zebra textures documented by Wallace and Hood (2018) formed with or without dolomitization as an intermediary step. The term "zebra texture" is used herein because it: (1) has no genetic connotation (i.e., does not imply a depositional, structural, or metamorphic control), (2) can be applied to the texture irrespective of mineralogy, and (3) is the most widely used term in the literature. The zebra textures considered here are distinct from the synsedimentary, marine-cemented, "zebra limestones" that are associated with stromatactis structures and lack evidence of replacement (Bathurst 1980; Bathurst 1982). Zebra textures are unrelated to "zebra rock" (Hobson, 1930) from the East Kimberley region of Western Australia that is a weathered Neoproterozoic claystone (Loughnan and Roberts, 1990).

2.3. Geographic and age distribution of zebra textures

Fault-controlled dolomite and zebra textures are hosted in strata of almost all ages, with examples documented from the Ediacaran (Khufai Formation, Oman Mountains; Vandeginste et al. 2014) to the Miocene (Abu Shaar, Gulf of Suez, Egypt; Clegg et al. 1998). Zebra textures have been reported in compressional (Nielsen et al. 1998; Vandeginste et al. 2005; Gasparinni et al. 2006; Sharp et al. 2010; Iannace et al. 2012; Gabellone et al. 2014; Vandeginste et al. 2014; Kareem et al. 2019), extensional (Boni et al. 2000; Hollis et al. 2017; Hirani et al. 2018; Shelton et al. 2019; Koeshidayatullah et al.

2020a) and transtensional (Davies and Smith Jr., 2006; López-Horgue et al. 2009, 2010; Swennen et al. 2012; Dewit et al. 2014; Breislin, 2018) tectonic settings. Absolute age dating of dolomitization, however, has not yet been applied to these systems and gives rise to considerable error margins when correlating to major tectonic events. Dolomitization of Cambrian strata in the WCSB, for example, was interpreted by Symons et al. (1998) to have occurred during the Laramide Orogeny (Cretaceous to Tertiary), by Vandeginste et al. (2005) to have occurred during the Antler Orogeny (Devonian to Carboniferous), or by Koeshidayatullah et al. (2020a, 2020b) and Stacey et al. (2021) to have occurred during shallow burial under extensional tectonic conditions (middle to late Cambrian).

It is widely recognized that extensional and transtensional tectonics can give rise to HTD (Boni et al. 2000; Davies Smith Jr., 2006; López-Horgue et al. 2009; Hollis et al. 2017; Koeshidayatullah et al. 2020a); however, it is difficult to reconcile cases of hydrothermal dolomitization attributed to compressional tectonics due to the lack of a proximal heat source, mass-balance constraints, and hydrogeological models that fail to circulate large fluid volumes for prolonged periods of time (Machel and Lonnee, 2002; Machel, 2004; Whitaker et al. 2004; Hendry et al. 2015). A compressional tectonic origin is commonly invoked because HTD bodies are often documented in inverted sedimentary basins with known orogenic histories. Fluid inclusion homogenization temperatures, which are typically up to 200°C, have also led numerous authors to interpret a deep burial origin for the formation of zebra textures (Nielsen et al. 1998; Swennen et al. 2003; Vandeginste et al. 2005; Gasparinni et al. 2006; Iannace et al. 2012; Gabellone et al. 2014). In the Middle Cambrian strata in the WCSB, for example, Vandeginste et al. (2005) suggested that the fluid inclusion homogenization temperatures in the zebra textures (150°C to 200°C) are characteristic of a burial depth of 5 km to 7 km. A deep burial origin for the formation of zebra textures elsewhere, however, is not consistent with the observations that (1) HTD bodies typically contain rock-buffered marine rare earth and trace element signatures (Hollis et al. 2017; Breislin, 2018; Hirani et al. 2018; Koeshidayatullah et al.

2020a) and (2) reworked clasts containing Viséan zebra textures were documented in a slightly younger, Viséan debrite in the Dublin Basin, Ireland (Shelton et al. 2019).

It, therefore, may be more effective to consider studies of HTD bodies that have not documented occurrences of zebra textures (e.g., Hendry et al. 2015; Hollis et al. 2017 Rustichelli et al. 2017) or where they are exceptionally poorly developed (e.g., Hirani et al. 2018; Breislin, 2018). Hendry et al. (2015) studied HTD bodies in Viséan limestones on the Isle of Man, which are hosted in porous/permeable platform carbonates, that lacked zebra textures. Zebra textures are rare in the Thebes Formation (Eocene), Gulf of Suez, Egypt that comprises a deepening upward succession with HTD bodies hosted in the more porous/permeable grainstones and rudstones at the base of the succession (Hollis et al. 2017; Hirani et al. 2018). Davies and Smith Jr. (2006) suggested that zebra textures are typically constrained to low permeability precursor limestones, whereas Dewit et al. (2012, 2014) suggested that there is no relation between precursor texture and the resulting dolomite texture. Dewit et al. (2012, 2014) reported that zebra textures were constrained to the central parts of a large HTD body (proximal to the fault source) in Albian strata from the Basque-Cantabrian Basin (northern Spain); which generally consist of low permeability bioclastic wackestones. The occurrence, size, spacing, and geometry of zebra textures may, therefore, be a function of both precursor permeability and paleo-fluid pressure, which can be inferred from fault proximity and dolomitization temperatures.

2.4. Conceptual models for the formation of zebra textures

Numerous conceptual models have been proposed to explain the formation of zebra textures in carbonate sedimentary rocks (Nielsen et al. 1998; Vandeginste et al. 2005; Gasparrini et al. 2006; Morrow, 2014; Wallace and Hood, 2018), each of which typically suggest that the A bands formed by the replacement of the carbonate host rock and that the B bands are elongate mineral-filled cavities (Table 2.1). The prevailing view is that these mineral-filled cavities are cement-filled fractures, however, the timing of fracturing is

Table 2.1. Models for the formation of zebra textures in carbonate sedimentary rocks showing the interpreted genesis of the A bands and the B bands, their timing, and their tectonic setting.

Model	Author	Genesis of Dark (A) Bands	Genesis of Light (B) Bands	Tectonic Setting (Interpreted)	Timing
Fracturing (pre-existing)	Park (1938)	–	Recrystallization and Cementation	–	–
	Wallace et al. (1994)	Replacement of host rock	Cement-filled cavities	–	Late
	Badoux et al. (2001)	Replacement of host rock	Cement-filled cavities	Compressional	Late
	Gasparrini et al. (2006)	Replacement of host rock	Cement-filled cavities	Compressional	Late
	López-Horgue et al. (2009)	Replacement of host rock	Cement-filled cavities	Strike-Slip	Late
	Hiemstra and Goldstein (2015)	Replacement of host rock	Cement-filled cavities	Compressional	Early
	Wallace and Hood (2018)	Replacement of host rock	Dissolution enhanced Cement-filled cavities	–	–
Fracturing (hydraulic over-pressure)	Boni et al. (1992)	Replacement of host rock	Cement-filled cavities	Extensional	Late
	Nielsen et al. (1998)	Replacement of host rock	Cement-filled cavities	Compressional	Late
	Boni et al. (2000)	Replacement of host rock	Cement-filled cavities	Extensional	Late
	Swennen et al. (2003)	Replacement of host rock	Replacement + Cement	Compressional	Late
	Vandeginste et al. (2005)	Replacement of host rock	Replacement + Cement	Compressional	Late
	Davies and Smith Jr. (2006)	Replacement of host rock	Cement-filled cavities	Transtensional	Late
	Dewit et al. (2012)	Replacement of host rock	Cement-filled cavities	Strike-slip	Late
	Iannace et al. (2012)	Replacement of host rock	Cement-filled cavities	Compressional	Late
	Swennen et al. (2012)	Replacement of host rock	Cement-filled cavities	Strike-slip	Late
	Dewit et al. (2014)	Replacement of host rock	Cement-filled cavities	Strike-slip	Late
	Gabellone et al. (2014)	Replacement of host rock	Cement-filled cavities	Compressional	Late
	Vandeginste et al. (2014)	Replacement of host rock	Cement-filled cavities	Compressional	Late
	Kareem et al. (2019)	Replacement of host rock	Cement-filled cavities	Compressional	Late
Dissolution	Beales and Hardy (1980)	Replacement of host rock	Cement-filled cavities	–	–
	Krebs and Macqueen (1984)	Replacement of host rock	Cement-filled cavities	–	Late
	Fontboté and Gorzawski (1990)	–	–	–	–
	Tompkins et al. (1994)	Replacement of host rock	Cement-filled cavities	–	–
	Morrow (2014)	Replacement of host rock	Cement-filled cavities	–	Late

Model	Author	Genesis of Dark (A) Bands	Genesis of Light (B) Bands	Tectonic Setting (Interpreted)	Timing
Recrystallization / Replacement	Fontboté (1981)	–	Recrystallization	–	Early
	Fontboté and Amstutz (1982)	–	Recrystallization	–	Early
	Fischer (1988)	Neomorphism of host rock	Cement-filled cavities	–	–
	Sass-Gustkiewicz and Mochnacka (1994)	Replacement of host rock	Cement-filled cavities	–	–
	Lugli et al. (2000)	Replacement of host rock	Displacive crystallization	–	–
	Dill et al. (2014)	Replacement of host rock	Replacement of evaporites	–	Late
	Merino and Canals (2006)	Replacement of host rock	Displacive crystallization	–	Late
	Merino et al. (2011)	Replacement of host rock	Displacive crystallization	–	Late
	Kelka et al. (2015)	–	Recrystallization	–	Late
	Kelka et al. (2017)	Replacement of host rock	Recrystallization	–	Late
Unspecified Origin	Diehl et al. 2010	Replacement of host rock	Cement-filled cavities	–	Late
	Liu et al. 2014	–	Cement-filled cavities	–	Late

contentious, with numerous studies suggesting that the fractures are pre-existing (Wallace et al. 1994; Gasparrini et al. 2006; López-Horgue et al. 2009; Wallace and Hood, 2018) and numerous studies suggesting that the fractures are induced by elevated pore-fluid pressures during dolomitization (Nielsen et al. 1998; Boni et al. 2000; Vandeginste et al. 2005; Davies and Smith Jr., 2006; Iannace et al. 2012; Swennen et al. 2012). Locally, there is evidence that these fractures may be dissolution-enhanced (Wallace and Hood, 2018), but models suggesting the light bands are exclusively dolomite-cemented dissolution cavities (Beales and Hardy, 1980; Krebs and Macqueen, 1984; Fontboté and Gorzawski, 1990; Tompkins et al. 1994; Morrow, 2014) have received limited support.

There are a few studies that suggest the light mineral-filled (B) bands in zebra textures developed without the formation of a cavity (Merino et al. 2006; Merino and Canals 2011; Kelka et al. 2015, 2017). Merino et al. (2006) and Merino and Canals (2011) suggested that the mineral-filled bands formed by the displacive crystallization of saddle dolomite

veins, whereas Kelka et al. (2015, 2017) suggested that they formed by recrystallization and grain growth affected by impurities (i.e., second-phase particles). These interpretations, however, do not provide a sufficient explanation for the central pore space that is commonly observed between the adjacent B bands in zebra textures (Fig. 1.1). Furthermore, cathodoluminescence (CL) zoning of crystals in the B bands is typical of cement precipitation in an open pore space (Vandeginste et al. 2005; Gasparrini et al. 2006; Wallace and Hood, 2018). Although the A/B band boundary is sharp in plane-polarized light, Merino et al. (2006) argued that crystals crossing this boundary in crossed-polarized light is evidence against a cavity-fill origin for the B bands. Optical continuity in the crystallographic orientation of cement crystals, however, is typical of cements that grow syntaxially on a surface with the same mineralogy (e.g., quartz overgrowths on detrital quartz, calcite cement on echinoderm fragments) and is not evidence against a cavity-filling origin (Bathurst, 1975; Wallace and Hood, 2018). In a study based entirely on hydromechanical modeling, Kelka et al. (2017; their Fig. 3) assumed that 60 MPa to 200 MPa (corresponding to a depth of 2180 m to 7280 m; ρ = 2800 kg/m3) is the "appropriate condition for buried dolomites". Yet, Vandeginste et al. (2005; their Fig. 8) documented stylolites that cross-cut entire zebra textures, and recent studies of HTD bodies in rift basins (Hollis et al. 2017; Hirani et al. 2018; Shelton et al. 2019; Koeshidayatullah et al. 2020a, 2020b) have suggested that dolomitization occurred in a shallow-burial setting.

In a model that differed significantly from prevailing views, Merino et al. (2006) and Merino and Canals (2011) suggested that hydrothermal dolomitization (and the formation of zebra textures) occurs by a self-accelerating, precipitation-dissolution, process in a closed system. This model follows (Maliva and Seiver, 1988a, 1988b) whereby volume-for-volume replacement is facilitated by the "force of crystallization" that requires the growing replacement crystal to cause pressure solution in the mineral being replaced. The force of crystallization mechanism for mineral replacement, which was originally applied by Maliva and Siever (1988a) to the silicification of fossils in limestones, was only

tentatively applied by Maliva and Siever (1988b) to dolomitization and it contradicts modeled and experimental observations that dolomitization proceeds by a dissolution-precipitation mechanism (Zempolich and Baker, 1993; Kaczmarek and Sibley, 2007; Gregg et al. 2015; Jonas et al. 2015; Morrow, 2020). While testing the model presented by Merino and Canals (2011, 2018), Morrow (2018, 2020) demonstrated that there is a progressive decrease in dolomitization potential that is limited by increasing Ca^{2+} concentration in solution and the affinity for calcite to be precipitated over dolomite.

Wallace and Hood (2018) proposed a conceptual model that suggested the "force of crystallization" during mineral replacement provides sufficient stress to fracture the host rock. These fractures are subsequently dissolution-enhanced and cemented to form the light mineral-filled bands in the zebra textures (Wallace and Hood, 2018). Wallace and Hood (2018; p. 64) state that "mechanically, it matters little if the growing crystal is in a pore, or is replacing the rock." and refer to halite crystallization as an analogous process. Mechanically, crystallization in a pore is a fundamentally different process than mineral replacement and Maliva and Seiver (1988a, 1988b) postulated that pressure solution during the replacement process alleviates this induced stress. In nature, there are several examples of fractures caused by the force of crystallization (e.g., halite or gypsum precipitation, calcrete formation), but they are caused by the precipitation of a cement in open pore space and not associated with mineral replacement. The calculations presented by Wiltshcko and Morse (2001), which are cited by Wallace and Hood (2018), explicitly refer to displacive vein growth (e.g., quartz veins, calcite veins) and are not applicable to replacement. Although Wallace and Hood (2018) are clearly referring to mineral replacement in their study, the application of the force of crystallization to fracturing conflates dolomitization with dolomite cementation and implies that the host rock was not replaced. The authors postulate that there is no structural control on the formation of zebra textures, yet their model assumes that the least principal stress is vertical and equal to the lithostatic stress (Wallace and Hood, 2018; their Fig. 4). Extensional fractures are oriented in the plane of

the maximum principal stress and open against the least principal stress (Sibson, 1998; Anders et al. 2014; Perras and Diederichs, 2014), a concept overlooked by Wallace and Hood (2018). Furthermore, the mineral-filled cavities in zebra textures comprise up to 50% of the rock volume and the model proposed by Wallace and Hood (2018) does not provide a mechanism to maintain these open fractures for extended periods of time. Zebra textures are commonly associated with cement-supported breccias that contain floating clasts of the dolomite host rock (Davies and Smith Jr., 2006; Sharp et al. 2010; Iannace et al. 2012; Vandeginste et al. 2014), which suggests that these fractures were not pre-existing.

2.5. Compilation of geochemical data from zebra textures

Although numerous petrographic studies have been conducted on zebra textures, geochemical analyses are much more limited (Fig. 2.2A, B). This section includes a brief compilation of the data available on samples from Dinantian strata, eastern Belgium (Nielsen et al. 1998), Middle Cambrian strata, western Canada (Vandeginste et al. 2005), and Carboniferous strata, northern Spain (Gasparrini et al. 2006). Based on CL characteristics, Nielsen et al. (1998) and Vandeginste et al. (2005) separated the light mineral-filled (B) bands into B1 (dull red/orange luminescent, unzoned) and B2 (bright red/orange luminescent, zoned) saddle dolomite populations. B2 dolomite forms zoned rims on the central parts of the B bands and, therefore, post-dates B1 dolomite. These two dolomite populations, however, were not discriminated for minor and trace element analyses (Fig. 2.2A, Table 2.2). Nielsen et al. (1998) and Vandeginste et al. (2005) found that there was no difference in the concentration of Sr and Na between the A bands and the B bands in the zebra textures (Table 2.2). The B bands typically have higher concentrations of Fe and Mn relative to the A bands (Fig. 2.2A, Table 2.2). Gasparrini et al. (2006) also reported increased concentrations of Fe and Mn in the B bands relative to the A bands in zebra textures hosted in Carboniferous strata from the Cantabrian Zone, northern Spain (Fig. 2.2A, Table 2.2). It is probable that the enrichment of Fe and Mn in the B bands

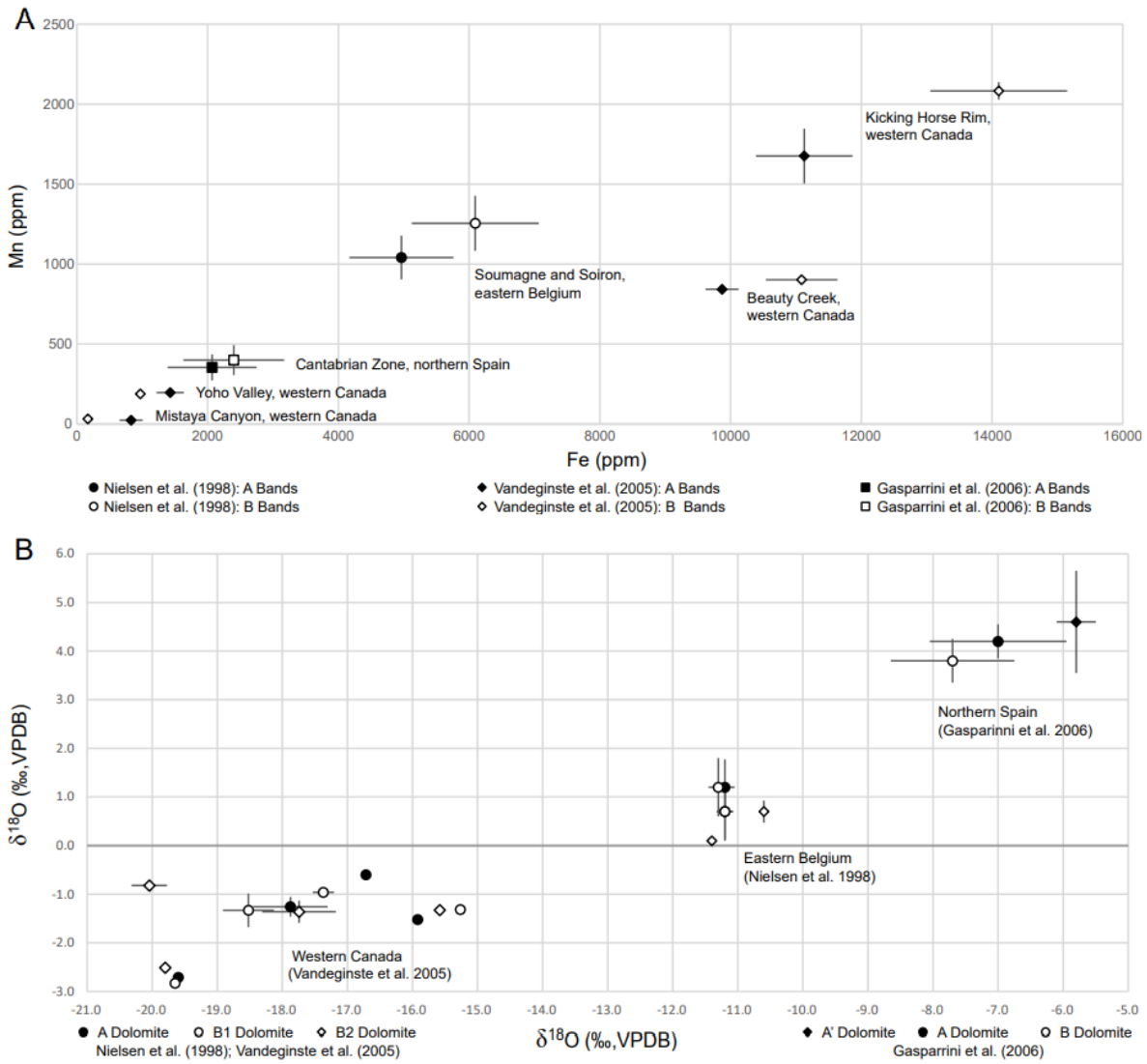

Figure 2.2. (A) Mn vs. Fe plots of the geochemical data compiled from studies that isolated the A (host-rock) bands and the B (mineral-filled) bands in zebra textures. Although multiple dolomite populations were identified in each of the A bands and the B bands, they were not discriminated for minor and trace element analyses. **(B)** $\delta^{13}C$ vs. $\delta^{18}O$ plots of the dolomite populations that were recognized and discriminated for stable isotope analyses. Given that a dentist drill (spatial resolution of ~1.0 mm) was used to collect samples, it is unclear whether Vandeginste et al. (2005) and Gasparrini et al. (2006) reliably isolated each of their respective dolomite populations.

relative to the A bands reported by Nielsen et al. (1998), Vandeginste et al. (2005), and Gasparrini et al. (2006) is largely contributed by the zoned B2 crystals. Vandeginste et al. (2005) reported the opposite trend at Yoho Valley and Mistaya Canyon (western Canada), with enriched Fe and Mn in the A bands relative to the B bands (Fig. 2.2A, Table 2.2). This observation, however, may be due to a decreased relative abundance of B2 dolomite in these samples. Based on their textural and CL characteristics, Gasparrini et al. (2006)

Table 2.2. Minor and trace element data from studies that analyzed the A (host-rock) bands and the B (mineral-filled) bands in zebra textures.

Nielsen et al. (1998)		**A Bands**		**B Bands**	
		Mean (n = 16)	Std. Dev. (σ)	Mean (n = 14)	Std. Dev. (σ)
Soumagne and Soiron boreholes, Dinantian strata, eastern Belgium	K (ppm)	69	15	60	19
	Fe (ppm)	4965	1594	6094	1944
	Mn (ppm)	1041	274	1255	344
	Sr (ppm)	33	6	33	6
	Na (ppm)	336	74	314	75
	F (ppm)	57	11	56	9
Vandeginste et al. (2005)		**A Bands**		**B Bands**	
		Mean (n = 4)	Std. Dev. (σ)	Mean (n = 5)	Std. Dev. (σ)
Kicking Horse Rim, Middle Cambrian strata, western Canada	Fe (ppm)	11127	1479	14102	2066
	Mn (ppm)	1676	343	2083	109
	Sr (ppm)	66	23	49	14
	Na (ppm)	142	13	214	16
		Mean (n = 5)	Std. Dev. (σ)	Mean (n = 6)	Std. Dev. (σ)
Beauty Creek, Middle Cambrian strata, western Canada	Fe (ppm)	9869	505	11087	1068
	Mn (ppm)	843	37	902	24
	Sr (ppm)	47	6	49	6
	Na (ppm)	140	40	140	46
		Mean (n = 5)	Std. Dev. (σ)	Mean (n = 4)	Std. Dev. (σ)
Yoho Valley, Middle Cambrian strata, western Canada	Fe (ppm)	1428	417	972	46
	Mn (ppm)	197	17	189	46
	Sr (ppm)	57	13	51	6
	Na (ppm)	185	16	190	11
		Mean (n = 9)	Std. Dev. (σ)	Mean (n = 19)	Std. Dev. (σ)
Mistaya Canyon, Middle Cambrian strata, western Canada	Fe (ppm)	830	353	168	63
	Mn (ppm)	24	6	32	6
	Sr (ppm)	37	7	36	8
	Na (ppm)	182	22	162	11
Gasparrini et al. (2006)		**A Bands**		**B Bands**	
		Mean (n = 16)	Std. Dev. (σ)	Mean (n = 14)	Std. Dev. (σ)
Cantabrian Zone, Carboniferous strata, northern Spain	Fe (ppm)	2069	1361	2400	1542
	Mn (ppm)	354	163	400	187
	Sr (ppm)	20	7	24	23
	Na (ppm)	356	121	300	130

distinguished two different dolomite populations in the A bands (A and A' dolomite), but only 3 samples from the A' dolomite were analyzed for minor and trace elements.

Alongside dolomite from the A bands, Nielsen et al. (1998) micro-drilled samples (resolution of ~250 μm) from their B1 and B2 populations for $\delta^{13}C$ and $\delta^{18}O$ stable isotope analyses (Fig. 2.2B, Table 2.3). Nielsen et al. (1998) reported that the $\delta^{13}C$ values of the A dolomite and the B1 dolomite have a wide range (–3.6 to 2.1‰ VPDB) but values from the

same sample are nearly identical. In contrast, the $\delta^{13}C$ values of the B2 dolomite have a tight range (0.1 to 1.1‰ VPDB) that differ significantly from the $\delta^{13}C$ values of the A dolomite and the B1 dolomite from the same sample. Nielsen et al. (1998) reported a subtle depletion of $\delta^{18}O$ values from the A dolomite and the B1 dolomite (–11.7 to –10.6‰ VPDB) to the B2 dolomite (–11.4 to –10.5‰ VPDB). Nielsen et al. (1998) also analyzed the $\delta^{18}O$ values of ankerite (–10.9 to –7.5‰ VPDB) that post-dated their B2 dolomite. Gasparrini et al. (2006) powdered samples using a dentist drill (resolution of ~1.0 mm) and reported the opposite trend (Fig. 2.2B, Table 2.3), with enrichment of $\delta^{18}O$ values from their A' dolomite (–10.5 to –3.0‰ VPDB) to their A dolomite (–11.9 to –3.0‰ VPDB) to their B dolomite (–12.0 to –4.2‰ VPDB). Following the petrographic classification of Nielsen et al. (1998), Vandeginste et al. (2005) attempted to sample their A, B1, and B2 dolomite populations using a dentist drill, but reported no observable trend in $\delta^{13}C$ and $\delta^{18}O$ values (Fig. 2.2B, Table 2.3). Based on their results, however, it is not clear if Vandeginste et al. (2005) reliably isolated each of these dolomite populations. Furthermore, the small sample sizes from the Beauty Creek (n = 2), Yoho Valley (n = 1), and Mistaya Canyon (n = 2) areas largely obfuscates the interpretation of these analyses.

Although their tabulated data is not available, Vandeginste et al. (2005; p. 1080) reported no difference in the fluid inclusion homogenization temperatures (T_h) between their A, B1, and B2 dolomite. Vandeginste et al. (2005; their Fig. 11), however, show an increase in T_h with each paragenetic stage, from their A and B1 dolomite to their B2 dolomite. Nielsen et al. (1998) and Gasparrini et al. (2006) also reported no variation for the T_h range between the A bands and the B bands in zebra textures. Nielsen et al. (1998) stated that their B2 dolomite contained no measurable fluid inclusions. Vandeginste et al. (2005) and Gasparinni et al. (2006) reported that there was no variation in stoichiometry or cation ordering between the A bands and the B bands, which are formed of stoichiometric, well-ordered, dolomite. Lastly, Vandeginste et al. (2005) and Gasparinni et al. (2006) reported no difference in the $^{87}Sr/^{86}Sr$ isotope ratios of the A bands and the B bands.

Table 2.3. δ13C and δ18O stable isotope data from studies that analyzed the A (host-rock) bands and the B (mineral-filled) bands in zebra textures.

Nielsen et al. (1998)		**δ13C (‰, VPDB)**		**δ18O (‰, VPDB)**	
	Population	Mean	Std. Dev. (σ)	Mean	Std. Dev. (σ)
Soumagne borehole, Dinantian strata, eastern Belgium	A (n = 9)	0.70	1.20	-11.20	0.25
	B_1 (n = 9)	0.70	1.15	-11.20	0.25
	B_2 (n = 3)	0.70	0.45	-10.60	0.10
	Population	Mean	Std. Dev. (σ)	Mean	Std. Dev. (σ)
Soiron borehole, Dinantian strata, eastern Belgium	A (n = 9)	1.20	1.15	-11.20	0.30
	B_1 (n = 9)	1.20	1.20	-11.30	0.30
	B_2 (n = 1)	0.10	–	-11.40	–
Vandeginste et al. (2005)		**δ13C (‰, VPDB)**		**δ18O (‰, VPDB)**	
	Population	Mean	Std. Dev. (σ)	Mean	Std. Dev. (σ)
Kicking Horse Rim, Middle Cambrian strata, western Canada	A (n = 10)	-1.26	0.41	-17.88	1.14
	B_1 (n = 11)	-1.33	0.69	-18.52	0.79
	B_2 (n = 8)	-1.36	0.45	-17.74	1.13
	Population	Mean	Std. Dev. (σ)	Mean	Std. Dev. (σ)
Beauty Creek, Middle Cambrian strata, western Canada	A (n = 2)	-0.60	0.10	-16.72	0.13
	B_1 (n = 2)	-0.96	0.06	-17.37	0.33
	B_2 (n = 2)	-0.82	0.06	-20.05	0.54
	Population	Mean	Std. Dev. (σ)	Mean	Std. Dev. (σ)
Yoho Valley, Middle Cambrian strata, western Canada	A (n = 1)	-2.71	–	-19.60	–
	B_1 (n = 1)	-2.83	–	-19.65	–
	B_2 (n = 1)	-2.51	–	-19.80	–
	Population	Mean	Std. Dev. (σ)	Mean	Std. Dev. (σ)
Mistaya Canyon, Middle Cambrian strata, western Canada	A (n = 2)	-1.52	0.04	-15.92	0.04
	B_1 (n = 2)	-1.32	0.16	-15.27	0.08
	B_2 (n = 2)	-1.33	0.02	-15.58	0.07
Gasparrini et al. (2006)		**δ13C (‰, VPDB)**		**δ18O (‰, VPDB)**	
	Population	Mean	Std. Dev. (σ)	Mean	Std. Dev. (σ)
Cantabrian Zone, Carboniferous strata, northern Spain	A' (n = 10)	4.60	2.10	-5.80	0.60
	A (n = 37)	4.20	0.70	-7.00	2.10
	B (n = 30)	3.80	0.90	-7.70	1.90

References

Adams, J.E., Rhodes, M.L., 1960. Dolomitization by seepage refluxion. AAPG Bulletin, 44(12), 1912-1920.

Al-Helal, A.B., Whitaker, F.F., Xiao, Y., 2012. Reactive transport modeling of brine reflux: dolomitization, anhydrite precipitation, and porosity evolution. Journal of Sedimentary Research, 82(3), 196-215.

Anders, M.H., Laubach, S.E., Scholz, C.H., 2014. Microfractures: A review. Journal of Structural Geology, 69, 377-394.

Arne, D.C., Curtis, L., Kissin, S., 1991. Internal zonation in a carbonate-hosted Zn-Pb-Agdeposit, Nanisivik, Baffin Island, Canada. Economic Geology, 86, 699-717.

Badoux, V., Moritz, R., Fontbote, L., 2001. The Mississippi Valley-type Zn-Pb deposit of San Vicente, central Peru: an Andean syntectonic deposit. In: Piestrzyñski, A. (Ed.), Mineral Deposits at the Beginning of the 21st Century. Balkema, Amsterdam, 191-195.

Bathurst, R., 1975. Carbonate Sediments and Their Diagenesis. Developments in Sedimentology. vol. 12. Elsevier, New York, 1-658.

Bathurst, R.G., 1980. Stromatactis—Origin related to submarine-cemented crusts in Paleozoic mud mounds. Geology, 8(3), 131-134.

Bathurst, R.G.C., 1982. Genesis of stromatactis cavities between submarine crusts in Palaeozoic carbonate mud buildups. Journal of the Geological Society, 139(2), 165-181.

Beales, F.W., Hardy, J.L., 1980. Criteria for the recognition of diverse dolomite types with an emphasis on studies of host rocks for Mississippi Valley-type ore deposits. In: Zenger, D.H., Dunham, J.B., Ethington, R.L. (Eds.), Concepts and Models of Dolomitization. SEPM Special Publication. 28. Society of Economic Paleontologists and Mineralogists, Tulsa, OK, 197-213.

Benjakul, R., Hollis, C., Robertson, H.A., Sonnenthal, E.L., Whitaker, F.F., 2020. Understanding controls on hydrothermal dolomitisation: insights from 3D Reactive Transport Modelling of geothermal convection. Solid Earth Discussions, 1-35.

Boni, M., Iannace, A., Bechstädt, T., Gasparrini, M., 2000. Hydrothermal dolomites in SW Sardinia (Italy) and Cantabria (NW Spain): evidence for late-to post-Variscan widespread fluid-flow events. Journal of Geochemical Exploration, 69, 225-228.

Boni, M., Iannace, A., Köppel, V., Frueh-Green, G.L., Hansmann, W., 1992. Late to post-Hercynian hydrothermal activity and mineralization in Southwest Sardinia (Italy). Economic Geology, 87(8), 2113-2137.

Breislin, C.J., 2018. Basin-Scale Mineral and Fluid Processes at a Platform Margin, Lower Carboniferous, UK. Unpublished Ph.D. Thesis, The University of Manchester, Manchester, United Kingdom, 236 p.

Budd, D.A., 1997. Cenozoic dolomites of carbonate islands: their attributes and origin. Earth Science Reviews, 42(1-2), 1-47.

Clegg, N., Harwood, G., Kendall, A., 1998. The dolomitization and post-dolomite diagenesis of Miocene platform carbonates: Abu Shaar, Gulf of Suez, Egypt. In: Purser, B.H., Bosence, D.W.J., (Eds.), Sedimentation and Tectonics in Rift Basins, Red Sea – Gulf of Aden. Chapman & Hall, London, 369-387.

Davies, G.R., Smith Jr., L.B., 2006. Structurally controlled hydrothermal dolomite reservoir facies: an overview. AAPG bulletin, 90, 1641-1690.

De Dolomieu, D., 1791. Sur un genre de Pierres calcaires très-peu effervescentes avec les Acides, & phosphorescentes par la collision. Journal de Physique, 39, 3-10.

De Beaumont, E., 1837. Application du calcul a l'hypothese de la formation par epigenic des anhydrites, des gypses et des dolomites: Bulletin de la Société Géologique de France, 8, 174-177.

Dewit, J., Foubert, A., El Desouky, H.A., Muchez, P., Hunt, D., Vanhaecke, F., Swennen, R., 2014. Characteristics, genesis and parameters controlling the development of a large stratabound HTD body at Matienzo (Ramales Platform, Basque – Cantabrian Basin, northern Spain). Marine and Petroleum Geology, 55, 6-25.

Dewit, J., Huysmans, M., Muchez, P., Hunt, D.W., Thurmond, J.B., Vergés, J., Saura, E., Fernandez, N., Romaire, I., Esestime, P., Swennen, R., 2012. Reservoir characteristics of fault-controlled hydrothermal dolomite bodies: Ramales Platform case study. Geological Society, London, Special Publications, 370(1), 83-109.

Diehl, S., Hofstra, A., Koenig, A., Emsbo, P., Christiansen, W., Johnson, C., 2010. Hydrothermal zebra dolomite in the Great Basin, Nevada-attributes and relation to Paleozoic stratigraphy, tectonics, and ore deposits. Geosphere, 6, 663-690.

Dill, H., Nolte, N., Hansen, B., 2014. Lithology, mineralogy and geochemical characterizations of sediment-hosted Sr-F deposits in the eastern Neo-Tethyan region – with special reference to evaporation and halokinesis in Tunisia. Journal of African Earth Science, 92, 76-96.

Emmons, S.F., Irving, J.D., Loughlin, G.F., 1927. Geology and ore deposits of the Leadville mining district, Colorado. U.S. Geological Survey Professional Paper, 148, 368 p.

Engel, A.E.J., Clayton, R.N., Epstein, S., 1958. Variations in isotopic composition of oxygen and carbon in Leadville limestone (Mississippian, Colorado) and in its hydrothermal and metamorphic phases. The Journal of Geology, 66(4), 374-393.

Fischer, H.J., 1988. Dolomite diagenesis in the metaline formation, Northeastern Washington state. In: Shukla, V., Baker, P.A. (Eds.), Sedimentology and geochemistry of dolostones. Society of Economic Paleontologists and Mineralogists Special Publication No 43. Society of Economic Paleontologists and Mineralogists, Tulsa, OK, 209-219.

Fontboté, L., 1981. Stratabound Zn-Pb-F-Ba deposits in carbonate rocks: New aspects of paleogeographic location, facies factors and diagenetic evolution. (With a comparison

of occurrences from the Triassic of southern Spain, the Triassic/Liassic of central Peru and other localities). Unpublished Ph.D. Thesis, University of Heidelberg, Heidelberg, Germany. 1-192.

Fontboté, L., Amstutz, G., 1982. Observations on ore rhythmites of the Trzebionka mine, Upper Silesian-Cracow region, Poland. In: Amstutz, G.C., Frenzel, G., Kluth, C., Moh, G., Wauschkuhn, A., Zimmermann, R.A., (Eds.), Ore Genesis: The State of the Art. Springer-Verlag, 83-91.

Fontboté, L., Amstutz, G.C., 1983. Facies and sequence analysis of diagenetic crystallization rhythmites in strata-bound Pb-Zn-(Ba-F-) deposits in the Triassic of Central and Southern Europe. In: Schneider, H.G., (Ed.), Mineral Deposits of the Alps and of the Alpine Epoch in Europe, Springer, Heidelberg, 347-358.

Fontboté, L., Gorzawski, H., 1990. Genesis of the Mississippi Valley-type Zn-Pb deposit of San Vicente, central Peru; geologic and isotopic (Sr, O, C, S, Pb) evidence. Economic Geology, 85, 1402-1437.

Frazer, M., Whitaker, F., Hollis, C., 2014. Fluid expulsion from overpressured basins: Implications for Pb–Zn mineralisation and dolomitisation of the East Midlands platform, Northern England. Marine and Petroleum Geology, 55, 68-86.

Gabellone, T., Iannace, A., Gasparrini, M., 2014. Multiple dolomitization episodes in deep-water limestones of the Triassic Lagonegro basin (southern Italy): from early reflux to tectonically driven fluid flow. Journal of Sedimentary Research, 84, 435-456.

Gasparrini, M., Bechstädt, T., Boni, M., 2006. Massive hydrothermal dolomites in thesouthwestern Cantabrian Zone (Spain) and their relation to the Late Variscan evolution. Marine and Petroleum Geology, 23, 543-568.

Gregg, J.M., Bish, D.L., Kaczmarek, S.E., Machel, H.G., 2015. Mineralogy, nucleation and growth of dolomite in the laboratory and sedimentary environment: a review. Sedimentology, 62(6), 1749-1769.

Gregg, J.M., Shelton, K.L., Johnson, A.W., Somerville, I.D., Wright, W.R., 2001. Dolomitization of the Waulsortian limestone (lower Carboniferous) in the Irish Midlands. Sedimentology, 48(4), 745-766.

Hendry, J.P., Gregg, J.M., Shelton, K.L., Somerville, I.D., Crowley, S.F., 2015. Origin, characteristics and distribution of fault-related and fracture-related dolomitization: Insights from Mississippian carbonates, Isle of Man. Sedimentology, 62(3), 717-752.

Hiemstra, E.J., Goldstein, R.H., 2015. Repeated injection of hydrothermal fluids into downdip carbonates: a diagenetic and stratigraphic mechanism for localization of

reservoir porosity, Indian Basin Field, New Mexico, USA. Geological Society, London, Special Publications, 406, 141-177.

Hirani, J., Bastesen, E., Boyce, A., Corlett, H., Gawthorpe, R., Hollis, C., John, C.M., Robertson, H., Rotevatn, A., Whitaker, F., 2018. Controls on the formation of stratabound dolostone bodies, Hammam Faraun Fault block, Gulf of Suez. Sedimentology, 65(6), 1973-2002.

Hobson, R.A., 1930. Zebra rock from Kimberley. Journal of the Royal Society of Western Australia, 16, 57-70.

Hollis, C., Bastesen, E., Boyce, A., Corlett, H., Gawthorpe, R., Hirani, J., Rotevatn, A., Whitaker, F., 2017. Fault-controlled dolomitization in a rift basin. Geology, 45(3), 219-222.

Iannace, A., Gasparrini, M., Gabellone, T., Mazzoli, S., 2012. Late Dolomitization in Basinal Limestones of the Southern Apennines Fold and Thrust Belt (Italy). Oil & Gas Science and Technology-Revue d'IFP Energies Nouvelles, 67, 59-75.

Isabel Millán, M., Machel, H., Bernasconi, S.M., 2016. Constraining temperatures of formation and composition of dolomitizing fluids in the Upper Devonian Nisku Formation (Alberta, Canada) with clumped isotopes. Journal of Sedimentary Research, 86(1), 107-112.

Jonas, L., Müller, T., Dohmen, R., Baumgartner, L., Putlitz, B., 2015. Transport-controlled hydrothermal replacement of calcite by Mg-carbonates. Geology, 43(9), 779-782.

Jones, G.D., Smart, P.L., Whitaker, F.F., Rostron, B.J., Machel, H.G., 2003. Numerical modeling of reflux dolomitization in the Grosmont platform complex (Upper Devonian), Western Canada sedimentary basin. AAPG bulletin, 87(8), 1273-1298.

Jones, G.D., Xiao, Y., 2005. Dolomitization, anhydrite cementation, and porosity evolution in a reflux system: Insights from reactive transport models. AAPG bulletin, 89(5), 577-601.

Kaczmarek, S.E., Sibley, D.F., 2007. A comparison of nanometer-scale growth and dissolution features on natural and synthetic dolomite crystals: implications for the origin of dolomite. Journal of Sedimentary Research, 77(5), 424-432.

Kaczmarek, S.E., Thornton, B. P., 2017. The effect of temperature on stoichiometry, cation ordering, and reaction rate in high-temperature dolomitization experiments. Chemical Geology, 468, 32-41.

Kareem, K.H., Al-Aasm, I.S., Mansurbeg, H., 2019. Structurally-controlled hydrothermal fluid flow in an extensional tectonic regime: A case study of Cretaceous Qamchuqa Formation, Zagros Basin, Kurdistan Iraq. Sedimentary Geology, 386, 52-78.

Kelka, U., Koehn, D., Beaudoin, N., 2015. Zebra pattern in rocks as a function of grain growth affected by second-phase particles. Frontiers in Physics, 3, 1-14.

Kelka, U., Veveakis, M., Koehn, D., Beaudoin, N., 2017. Zebra rocks: compaction waves create ore deposits. Scientific Reports, 7(1), 1-9.

Koeshidayatullah, A., Corlett, H., Stacey, J., Swart, P.K., Boyce, A., Robertson, H., Whitaker, F., Hollis, C., 2020a. Evaluating new fault-controlled hydrothermal dolomitisation models: Insights from the Cambrian Dolomite, Western Canadian Sedimentary Basin. Sedimentology, 67, 2945-2973.

Koeshidayatullah, A., Corlett, H., Stacey, J., Swart, P.K., Boyce, A., Hollis, C., 2020b. Origin and evolution of fault-controlled hydrothermal dolomitization fronts: A new insight. Earth and Planetary Science Letters, 541, 116291.

Krebs, W., Macqueen, R., 1984. Sequence of diagenetic and mineralization events, Pine Point lead-zinc property, Northwest Territories, Canada. Bulletin of Canadian Petroleum Geology, 32, 434-464.

Land, L.S., 1985. The origin of massive dolomite. Journal of Geological Education, 33, 112-125.

Levin, P., Amstutz, G.C., 1976. Kristallisation und bewegung in erzrhythmiten am beispiel Triassic-Jurassischer lagerstäten in Ostperu. Münstersche Forschen Geologie und Paläeontologie. Münster, 38/39, 111-128.

Lippmann, F., 1973. *Sedimentary Carbonate Minerals*. New York, Springer Verlag, 228 p.

Liu, S., Huang, W., Jansa, L.F., Wang, G., Song, G., Zhang, C., Sun, W., Ma, W., 2014. Hydrothermal Dolomite in the Upper Sinian (Upper Proterozoic) Dengying Formation, East Sichuan Basin, China. Acta Geologica Sinica, 88, 1466-1487.

López-Horgue, M.A., Iriarte, E., Schroeder, S., Caline, B., Fernández Mendiola, P.Á., 2009. An example on the tectonic origin of zebra dolomites: the San Martín beach outcrop (Santoña, North Spain). Geogaceta, 47, 85-88.

López-Horgue, M.A., Iriarte, E., Schröder, S., Fernández-Mendiola, P.A., Caline, B., Corneyllie, H., Frémont, J., Sudrie, M., Zerti, S., 2010. Structurally controlled hydrothermal dolomites in Albian carbonates of the Asón valley, Basque Cantabrian Basin, Northern Spain. Marine and Petroleum Geology, 27(5), 1069-1092.

Loughnan, F., Roberts, F., 1990. Composition and origin of the ‘zebra rock’ from the East Kimberley region of Western Australia. Australian Journal of Earth Science, 37, 201-205.

Lugli, S., Torres-Ruiz, J., Garuti, G., Olmedo, F., 2000. Petrography and geochemistry of the Eugui magnesite deposit (Western Pyrenees, Spain): evidence for the development

of a peculiar zebra banding by dolomite replacement. Economic Geology, 95, 1775-1791.

Machel, H.G., 1999. Effects of groundwater flow on mineral diagenesis, with emphasis on carbonate aquifers. Hydrogeology Journal, 7, 94-107.

Machel, H.G., 2004. Concepts and models of dolomitization: a critical reappraisal. In: Braithwaite C.J.R., Rizzi, G., Darke, G., (Eds.), The geometry and petrogenesis of dolomite hydrocarbon reservoirs. Geological Society, London, Special Publications, 235(1), 7- 63.

Machel, H. G., Anderson, J. H., 1989. Pervasive subsurface dolomitization of the Nisku Formation in central Alberta. Journal of Sedimentary Research, 59(6), 891-911.

Machel, H.G., Lonnee, J., 2002. Hydrothermal dolomite - A product of poor definition and imagination. Sedimentary Geology, 152(3-4), 163-171.

Machel, H.G., Mountjoy, E.W., 1986. Chemistry and environments of dolomitization – a reappraisal. Earth-Science Reviews, 23(3), 175-222.

Maliva, R.G., Siever, R., 1988a. Mechanism and controls of silicification of fossils in limestones. The Journal of Geology, 96(4), 387-398.

Maliva, R.G., Siever, R., 1988b. Diagenetic replacement controlled by force of crystallization. Geology, 16, 688-691.

Merino, E., Canals, À., 2011. Self-accelerating dolomite-for-calcite replacement: Self-organized dynamics of burial dolomitization and associated mineralization. American Journal of Science, 311(7), 573-607.

Merino, E., Canals, À., 2018. Reply to the Comment by Morrow, D.W., on “Self-accelerating dolomite-for-calcite replacement: Self-organized dynamics of burial dolomitization and associated mineralization”, 311(7), 573-607. American Journal Science, 318(8), 887-892.

Merino, E., Fletcher, R., Canals, À., 2006. Genesis of self-organized zebra textures in burial dolomites: displacive veins, induced stress, and dolomitization. Geologica Acta, 4, 383-393.

Morrow, D.W., 1982a. Diagenesis 1. Dolomite - Part 1: The Chemistry of Dolomitization and Dolomite Precipitation. Geoscience Canada, 9(1), 5-13.

Morrow, D.W., 1999. Regional subsurface dolomitization: models and constraints. Geoscience Canada, 25, 57-70.

Morrow, D.W., 2014. Zebra and boxwork fabrics in hydrothermal dolomites of northern Canada: Indicators for dilational fracturing, dissolution or in situ replacement? Sedimentology, 61, 915-951.

Morrow, D.W., 2018. Comment on “Merino, E., Canals, À. 2011. Self-accelerating dolomite for calcite replacement model: self-organized dynamics of burial dolomitization and associated mineralization”, 311(7), 573-607. American Journal of Science, 318(8), 882-886.

Morrow, D.W., 2020. Self-accelerating volumetric dolomite-for-calcite replacement: A possible mechanism for high-temperature dolomitization? Carbonates and Evaporites, 35(2), 1-13.

Newport, R., Segura, M., Redfern, J., & Hollis, C. (2020). The interaction of tectonics, climate and eustasy in controlling dolomitization: A case study of Cenomanian–Turonian, shallow marine carbonates of the Iberian Basin. Sedimentology, 67(5), 2223-2247.

Nielsen, P., Swennen, R., Muchez, P., Keppens, E., 1998. Origin of Dinantian zebra dolomites south of the Brabant-Wales Massif, Belgium. Sedimentology, 45, 727-743.

Park, C.F., 1938. Dolomite and jasperoid in the Metaline District, northeastern Washington. Economic Geology, 33, 709-729.

Patterson, R.J., Kinsman, D.J.J., 1981. Hydrologic framework of a sabkha along Arabian Gulf. AAPG bulletin, 65(8), 1457-1475.

Patterson, R.J., Kinsman, D.J.J., 1982. Formation of diagenetic dolomite in coastal sabkha along Arabian (Persian) Gulf. AAPG Bulletin, 66(1), 28-43.

Perras, M.A., Diederichs, M.S., 2014. A review of the tensile strength of rock: concepts and testing. Geotechnical and geological engineering, 32(2), 525-546.

Ren, M., Jones, B., 2017. Spatial variations in the stoichiometry and geochemistry of Miocene dolomite from Grand Cayman: Implications for the origin of island dolostone. Sedimentary Geology, 348, 69-93.

Ren, M., Jones, B., 2018. Genesis of island dolostones. Sedimentology, 65(6), 2003-2033.

Rustichelli, A., Iannace, A., Tondi, E., Di Celma, C., Cilona, A., Giorgioni, M., Parente, M., Girundo, M., Invernizzi, C., 2017. Fault-controlled dolomite bodies as palaeotectonic indicators and geofluid reservoirs: New insights from Gargano Promontory outcrops. Sedimentology, 64(7), 1871-1900.

Ryan, B.H., Kaczmarek, S.E., Rivers, J.M., 2020. Early and pervasive dolomitization by near-normal marine fluids: New lessons from an Eocene evaporative setting in Qatar. Sedimentology, 67(6), 2917-2944.

Sass-Gustkiewicz, M., Dżułyński, S., Ridge, J.D., 1982. The emplacement of zinc-lead sulfide ores in the Upper Silesian District; a contribution to the understanding of Mississippi Valley-Type deposits. Economic Geology, 77, 392-412.

Sass-Gustkiewicz, M., Mochnacka, K., 1994. Genesis of sphalerite rhythmites from the Upper Silesian zinc-lead deposits-a discussion. In: Fontbote, L., Boni, M. (Eds.), Sediment Hosted Zn-Pb Ores. Springer-Verlag, Berlin Heidelberg, 219-227.

Sharp, I., Gillespie, P., Morsalnezhad, D., Taberner, C., Karpuz, R., Vergés, J., Horbury, A., Pickard, N., Garland, J., Hunt, D. 2010. Stratigraphic architecture and fracture-controlled dolomitization of the Cretaceous Khami and Bangestan groups: an outcrop case study, Zagros Mountains, Iran. In: Van Buchem, F.S.P., Gerdes, K.D., Esteban, M., (Eds.), Mesozoic and Cenozoic Carbonate Systems of the Mediterranean and the Middle East: Stratigraphic and Diagenetic Reference Models. Geological Society, London, Special Publications, 329(1), 343-396.

Shelton, K.L., Hendry, J.P., Gregg, J.M., Truesdale, J.P., Somerville, I.D., 2019. Fluid Circulation and Fault- and Fracture-related Diagenesis in Mississippian Syn-rift Carbonate Rocks on the Northeast Margin of the Metalliferous Dublin Basin, Ireland. Journal of Sedimentary Research, 89(6), 508-536.

Sibson, R.H., Moore, J.M.M., Rankin, A.H., 1975. Seismic pumping - a hydrothermal fluid transport mechanism. Journal of the Geological Society, 131(6), 653-659.

Sibson, R.H., 1992. Implications of fault-valve behaviour for rupture nucleation and recurrence. Tectonophysics, 211(1-4), 283-293.

Sibson, R.H., 1998. Brittle failure mode plots for compressional and extensional tectonic regimes. Journal of Structural Geology, 20(5), 655-660.

Stacey, J., Corlett, H., Holland, G., Koeshidayatullah, A., Cao, C., Swart, P., Crowley, S., Hollis, C., 2021. Regional fault-controlled shallow dolomitization of the Middle Cambrian Cathedral Formation by hydrothermal fluids fluxed through a basal clastic aquifer. Geological Society of America Bulletin. 133(11-12), 2355-2377.

Swennen, R., Vandeginste, V., Ellam, R., 2003. Genesis of zebra dolomites (Cathedral Formation: Canadian Cordillera Fold and Thrust Belt, British Columbia). Journal of Geochemical Exploration, 78, 571-577.

Swennen, R., Dewit, J., Fierens, E., Muchez, P., Shah, M., Nader, F., Hunt, D., 2012. Multiple dolomitization events along the Pozalagua Fault (Pozalagua Quarry, Basque–Cantabrian Basin, Northern Spain). Sedimentology, 59, 1345-1374.

Symons, D.T.A., Lewchuk, M.T., Sangster, D.F., 1998. Laramide orogenic fluid flow into the Western Canada sedimentary basin; evidence from paleomagnetic dating of the Kicking Horse mississippi valley-type ore deposit. Economic Geology, 93(1), 68-83.

Tompkins, L.A., Rayner, M.J., Groves, D.I., Roche, M.T., 1994. Evaporites; in situ sulfur source for rhythmically banded ore in the Cadjebut mississippi valley-type Zn-Pb deposit, Western Australia. Economic Geology, 89, 467-492.

Vandeginste, V., Swennen, R., Gleeson, S.A., Ellam, R.M., Osadetz, K., Roure, F., 2005. Zebra dolomitization as a result of focused fluid flow in the Rocky Mountains Fold and Thrust Belt, Canada. Sedimentology, 52, 1067-1095.

Vandeginste, V., John, C.M., Cosgrove, J.W., Manning, C., 2014. Dimensions, texture distribution, and geochemical heterogeneities of fracture–related dolomite geobodies hosted in Ediacaran limestones, northern Oman. AAPG bulletin, 98, 1789-1809.

Walcott, C.D., 1908. Mount Stephen rocks and fossils. Canadian Alpine Journal, 1(2), 232-248.

Wallace, M.W., Both, R., Morales-Ruano, S., Hach-Ali, P.F., Lees, T., 1994. Zebra textures from carbonate-hosted sulfide deposits: sheet cavity networks produced by fracture and solution enlargement. Economic Geology, 89, 1183-1191.

Wallace, M.W., vS Hood, A., 2018. Zebra textures in carbonate rocks: Fractures produced by the force of crystallization during mineral replacement. Sedimentary Geology, 368, 58-67.

Wang, R., Yu, K., Jones, B., Wang, Y., Zhao, J., Feng, Y., Bian, L., Xu, S., Fan, T., Jiang, W., Zhang, Y., 2018. Evolution and development of Miocene “island dolostones” on Xisha Islands, South China Sea. Marine Geology, 406, 142-158.

Warren, J., 2000. Dolomite: occurrence, evolution and economically important associations. Earth-Science Reviews, 52(1-3), 1-81.

Whitaker, F.F., Smart, P.L., Jones, G.D., 2004. Dolomitization: from conceptual to numerical models. Geological Society, London, Special Publications, 235(1), 99-139.

Whitaker, F.F., Xiao, Y., 2010. Reactive transport modeling of early burial dolomitization of carbonate platforms by geothermal convection. AAPG bulletin, 94(6), 889-917.

Wiltschko, D.V., Morse, J.W., 2001. Crystallization pressure versus “crack seal” as the mechanism for banded veins. Geology, 29, 79-82.

Zeeh, S., 1995. Complex replacement of saddle dolomite by fluorite within zebra dolomites. Mineralium Deposita, 30(6), 469-475.

Zempolich, W.G., Baker, P.A., 1993. Experimental and natural mimetic dolomitization of aragonite ooids. Journal of Sedimentary Research, 63(4), 596-606.

Blank page

3.1. Shortwave infrared hyperspectral imaging

3.1.1. Collection and processing of the infrared reflectance data

To obtain an overview of the geological succession that is present at Whirlpool Point (Cathedral Formation, WCSB), a set of four SWIR (930 to 2508 nm) spectral images were acquired on June 12, 2018 between 11 am and 2 pm using a Specim SisuROCK hyperspectral scanner (a linescan imager) that is mounted on a rotary stage for wall rock imaging. Note that the acquisition of the hyperspectral imagery in the field occurred prior to the start of this Ph.D. thesis, but the data used in Chapter IV was processed seperately. Integration time varied from 5 to 10 ms depending on the time of acquisition and it required 30 s for the stage to rotate 90°. The scanner contains a 256 spectral by 320 spatial pixels mercury-cadmium-telluride detector array that acquires data at a 6.3 nm sampling interval and a 10 nm spectral bandwidth. Two Spectralon panels of 2% and 99% reflectance were positioned in each scene. Data were acquired under clear sky conditions and the sun directly illuminated the outcrop. For each scene, radiance data was obtained by applying appropriate gain and offset and conversion to reflectance, then an empirical line correction was applied based on the known reflectance of the Spectralon panels relative to their measured radiance spectrum. The latter were obtained as the mean radiance spectrum for a 20 × 20 pixel area over the panel (nominal pixel size of the imagery = 5 cm). The empirical line method has the advantage of correcting for the influence of the atmosphere on the target radiance (Kurz et al. 2011, 2013; Murphy et al. 2015). In contemporaneous studies with the same camera (Lypaczewski and Rivard, 2018; Lypaczewski et al. 2019), the wavelength position of SWIR absorptions of a National Institute of Standards and Technology (NIST) referenced Mylar standard were accurate within 1 nm.

Following calibration of the spectral data to reflectance, bands with the poorest signal to noise (e.g., 930 to 991, 1295 to 1435, 1735 to 1998, and 2461 to 2508 nm) were

removed from the ensuing analysis. The four images were then spatially co-registered using tie points, resulting in a single image for further analysis. Next, an iterative spatial spectral filter was used to compare the spectral similarity of spatially adjacent pixels within a 3 × 3 pixel window (Rogge et al. 2007, 2012; Rogge and Rivard, 2010). When the spectral signatures were within a predefined similarity threshold, an average spectrum was substituted for the original data, thereby reducing the intra-class spectral variability. Lastly, areas in shadow and the calibration panels were masked.

Mineralogical and lithological information in the imagery was obtained by the extraction of endmember spectra and their distributions were mapped. To derive an image endmember set, spatial-spectral endmember extraction (SSEE) was used to divide the image into equal spatial subsets (each subset = 7 × 7 pixels; Rogge et al. 2007, 2012; Rogge and Rivard, 2010). This method is designed to discern spectrally similar endmembers that occupy different portions of the scene. The endmember set derived from SSEE was clustered and labelled to derive final endmember sets for mapping. For clustering, we used a tree cluster that recursively merges a pair of clusters based on a similarity measurement. To start, each endmember was treated as an individual cluster and endmembers that are most similar were successively merged. In this study, the Spectral Angle (SA) between two endmembers was used as the measure of similarity. A minimum SA threshold was defined to stop the merging process that took place when all pairwise clusters had a similarity greater than the threshold. To address the spectral variability of the extracted endmembers, the tree cluster tool was applied twice on the given data. The first time, using all endmembers, a SA threshold of 0.2 radians produced clusters that capture the broad material classes, namely non-geological (e.g., panels, vegetation, weathering) and geological. The next level of clustering focused on the geological class to capture subclasses and define multiple geological endmember clusters. In this case, a smaller SA threshold (0.05 radians) was used because these endmembers are more spectrally similar. Clustered endmembers were then averaged to obtain an individual endmember that

represents the given class, contributing to an endmember set of thirteen geological endmembers. This clustering process was data-driven.

After accounting for the spectral similarity between classes, these thirteen endmembers were condensed into four groups: limestone (Lst), two groups of replacement dolomite (RDa, RDb), and saddle dolomite (SD). Groups were labelled based on spectral interpretations that were supported by field and petrographical observations. Group Lst was defined by all pixels with a carbonate absorption-band position > 2330 nm and was validated in the field using dilute hydrochloric acid. Group RDa includes the spectral endmembers that correspond to light- and medium- grey replacement dolomite. Endmembers that corresponded to clasts, bedding, and bedding-parallel fractures within the RDa intervals were also included. Group RDb includes the endmembers that correspond to light-brown replacement dolomite and the alteration rims along the margins of the saddle dolomite intervals. Group SD includes three subgroups (SDa, SDb, SDc), labelled based on their paragenesis, that correspond to white, coarsely crystalline, saddle dolomite. Their paragenesis was determined by the relative positions of each endmember in macro-pores that were validated by petrographical analyses.

3.1.2. Distribution maps of the spectral endmembers

Mapping of the endmember spectra resulted in two image products. The first examined the distributions of limestone (Lst), replacement dolomite (RDa, RDb), and saddle dolomite (SD) and is suited for a synoptic view of the outcrop. The second, more detailed image product, examined the distribution of the saddle dolomite subgroups (SDa, SDb, SDc). In both instances, mapping the distribution of each endmember was conducted using a spectral angle mapper (SAM) algorithm that treats spectra as multidimensional vectors and computes the angle between spectral pairs (Kruse et al. 1993). For this purpose, the spectrum from each pixel of the image after processing was compared to that of each endmember. Spectra with the smallest SAM angles indicate the greatest similarity.

In the first image product, the SAM results for RDa, RDb, and SD are presented as a red-green-blue composite where a higher color hue corresponds to a higher spectral similarity to the given endmember. If two or more of the endmembers predominate within a given pixel, then a color other than RGB is seen. In the second image product, the SAM results for SDa, SDb and SDc are classified in such a way that the endmember of highest similarity to that of the given pixel is assigned to that pixel. Consequently, only the colors that were assigned to the endmembers are seen in the second image product and when the SAM angle exceeds 5 degrees the pixel is not classified.

3.2. Fieldwork, sample preparation, and petrographical analyses

Fieldwork was conducted over two limited field seasons, during the summers of 2019 (one week, at the start of this Ph.D.) and 2020 (two weeks, during the coronavirus pandemic). Fieldwork focused on describing outcrops of the Cathedral Formation at Whirlpool Point (WP; 52°00′07.5″N, 116°28′13.5″W) and the Kicking Horse Rim (KHR; 51°26′11.5″N, 116°22′48.5″W), and of the Eldon Formation at Mistaya Canyon (MC; 51°55′09.5″N, 116°43′23.5″W) and Num Ti Jah (NTJ; 51°39′13.0″N, 116°29′59.0″W). Photographs were systematically taken in the field to at a range of scales to assess the overall geometry of the HTD bodies, and the characteristic features of the rock textures that are found within them. Where possible, the strata were described according to the Dunham (1962) and Embry and Klovan (1971) classifications. Ninety-two samples were collected from WP (n = 35), MC (n = 30), NTJ (n = 9), and the KHR (n = 18; Appendix 1).

Thirty representative samples of zebra textures, cement-supported breccias, boxwork textures, and the replacement dolomite host rock were prepared for petrographical analyses. Transmitted-light and cathodoluminescence (CL) petrography were established on 10 large-sized (50 x 75 mm) and 20 standard-sized (26 x 47 mm) thin-sections that were prepared from samples impregnated with blue epoxy. These sections were prepared to a thickness of 30 μm and double-polished on their upper surface. To distinguish ferroan and

non-ferroan calcite and dolomite, the sections were half stained with alizarin red S and potassium ferricyanide following the protocol of Dickson (1965, 1966). Dolomite crystal textures are described according to the classification scheme of Sibley and Gregg (1987).

Cathodoluminescence petrography was conducted using a Cambridge Image Technology Limited Mk5 stage, mounted on a Nikon Eclipse LV100N POL microscope, that includes a cold cathode luminescope (beam voltage = 15 to 20 kV, current = 350 to 450 μA). CL microscopy utilizes an electron beam the excites electrons in the crystal lattice to a higher valence position. As these electrons relax and return to their original valence states, photons of characteristic wavelengths are emitted. The CL characteristics of carbonate minerals are largely controlled by Fe^{2+} and Mn^{2+} that act as a quencher and an activator, respectively (Machel and Burton, 1991). Other elements act as activators (e.g., Sm, Tb, Dy, Eu) and quenchers (e.g., Ni, Co), but these will be analysed by inductively coupled mass spectrometry. Backscattered electron (BSE) imaging was conducted with a Thermo Fisher Scientific Quanta 650 FEG scanning electron microscope (SEM), using an accelerating voltage of 15.0 kV. Samples from the rock deformation experiments were also prepared for petrographical analyses, but the analytical methods are described in chapter V.

3.3. XRD, QEMSCAN, and EDX

Powder X-ray diffraction (XRD) was conducted using a Bruker D8 Advance Diffractometer, with Cu Kα1 radiation and silicon as a standard. Samples were scanned at 40 kV and 20 mA, across a range of 2θ values from 5° to 70° with a step size of 0.02° 2θ. Peak identification and qualitative mineralogical analysis were obtained from the EVA software, whereas quantitative mineralogical analysis (i.e., Rietveld refinement) was obtained from Topas 4.2. From the XRD, dolomite stoichiometry was determined by mol%($CaCO_3$) = 333.33d – 911.00 (Lumsden, 1979), where d is the value of 104 reflection peak measured in Å. Stoichiometric dolomite, for example, has a d-spacing of ~2.885 (Lumsden, 1979). Throughout the remainder of this thesis, mol%($CaCO_3$) is converted to a

Ca to Mg ratio (mol%Ca / mol%(Ca + Mg)), typically referred to as %Ca (cf. Jones et al. 2001). Following the method described by Goldsmith and Graf (1958), dolomite cation ordering was determined by the ratio between the d(015) peak and the d(110) peak. Calcite lacks a d(015) peak, whereas well-ordered dolomite has similar intensities of the d(015) and d(110) peaks due to the interlayered Ca and Mg in the crystal lattice (Gregg et al., 2015). As Mg^{2+} ions substitute for Ca^{2+}, ordering increases as the reflection of d(015) peak becomes more commensurate with the reflection of the d(110) peak (Gregg et al., 2015).

Quantitative evaluation of minerals by scanning electron microscopy (QEMSCAN) and energy dispersive X-ray (EDX) spectroscopy were conducted by Rocktype Ltd. using a FEI Aspex eXstreme equipped with Bruker 5030 EDX detectors and an iExplorer software suite. Double-polished mounts, 30 mm in diameter, were specifically made for these analyses. QEMSCAN and EDX spectroscopy involve creating a grid of spot analyses on the SEM. An X-ray spectrum was generated for each point, matched against a standard library, and the maps were constructed by assigning the library mineral to each point. To obtain an overview of the mineralogy of each sample, an initial 10 x 10 mm mineral map was created at a stepping-interval of 50 μm. Based on these low-resolution maps, 4 x 4 mm areas of interest were mapped at a higher resolution using a stepping interval of 4 μm. QEMSCAN mineral maps were generated for both the 50 μm and the 4 μm resolution maps, whereas EDX spectroscopy maps for Ca, Mg, Fe, C, and O were only generated for the 4 μm resolution maps. Other elements of interest (e.g., Mn, Sr, Al, Si) were not detectable in quantities that were significant enough to generate meaningful maps.

3.4. EPMA

Polished sections from WP (n = 2), MC (n = 1), NTJ (n = 1), and the KHR (n = 1), which include each of the identified paragenetic stages, were analysed for their major and trace element compositions by electron probe micro-analysis (EPMA) using a Cameca SX100 at The University of Manchester. To obtain an overview of each sample, an initial 2

x 10 mm map was created at a stepping-interval of 10 μm. The positions of these low-resolution elemental maps were selected to include each of the paragenetic phases that are present in the zebra textures. Based on these low-resolution elemental maps, 1.536 x 1.536 mm areas of interest were mapped at a stepping interval of 3 μm. The positions of these high-resolution elemental maps were selected to discern the detailed geochemical heterogeneities that are present in the final paragenetic stage (i.e., the B2 dolomite of Nielsen et al. 1998, Vandeginster et al. 2005, and Gasparinni et al. 2006). The concentrations of Ca (Kα; PET) and Mg (Kα; TAP) were analysed at 15 kV, 10 nA, and a dwell time of 100 ms using calcite ($CaCO_3$) and magnesite ($MgCO_3$) as standards. The concentrations of Fe (Kα; LLIF) and Mn (Kα; LLIF) were analysed at 15 kV, 200 nA, and a dwell time of 200 ms using fayalite (Fe_2SiO_4) and tephroite (Mn_2SiO_4) as standards.

3.5. LA ICP-MS

Trace and rare earth element concentrations were determined at The University of Manchester using a Teledyne Photon Machines Analyte Excite+ 193 nm ArF Excimer laser ablation (LA) system with a HelEx II active 2-volume ablation cell that is coupled to an Agilent 8900 inductively coupled mass spectrometer (ICP-MS; see Table 3.1 for a summary of the analytical setup and data processing). Ablation of NIST 612 glass was used to tune the instrument, optimize signal intensities, and maintain low levels of oxide formation ($^{232}ThO/^{232}Th < 0.25\%$) and a U/Th ratio that is close to unity. For all carbonate analyses, a spot diameter of 50 μm, a fluence of 3 $J.cm^{-2}$, and a repetition rate of 5 Hz was used. Each analysis lasted 40 s and was preceded by 20 s counting time of the gas blank. The concentrations of ^{24}Mg, ^{27}Al, ^{29}Si, ^{42}Ca, ^{43}Ca, ^{55}Mn, ^{57}Fe, ^{66}Zn, ^{88}Sr, ^{89}Y, ^{137}Ba, ^{139}La, ^{140}Ce, ^{141}Pr, ^{146}Nd, ^{147}Sm, ^{153}Eu, ^{157}Gd, ^{159}Tb, ^{163}Dy, ^{165}Ho, ^{166}Er, ^{169}Tm, ^{172}Yb, ^{175}Lu, ^{208}Pb, ^{232}Th, and ^{238}U were analyzed, with the respective dwell times reported in Table 3.1.

The trace element data reduction scheme from the Iolite4 software (Woodhead et al. 2007; Paton et al. 2011) was applied using known [Ca] of the reference materials (Jochum

Table 3.1: Summary of experimental setup and data processing for LA ICP-MS.

Laboratory and Sample Preparation	
Laboratory name	Department of Earth and Environmental Sciences, The University of Manchester
Sample type/mineral	Dolomite, Western Canadian Sedimentary Basin
Sample preparation	Polished thin sections
Imaging	Back-scattered electron imaging and reflected light microscopy
Laser ablation system	
Make, Model & type	Teledyne Photon Machines Analyte Excite+
Ablation cell & volume	HelEx II active 2-volume ablation cell, 100 mm × 100 mm sample area
Laser wavelength (nm)	193 nm (ArF excimer)
Pulse width (ns)	< 4 ns
Fluence (J.cm^{-2})	3 J.cm^{-2}
Repetition rate (Hz)	5 Hz
Ablation duration (s)	40 s
Ablation pit depth / ablation rate	Not measured
Spot diameter (μm)	50 μm circle
Sampling mode / pattern	Static spot ablation
Carrier gas	100% He in the cell, Ar make-up gas combined using a Y-piece 50% along the sample transport line to the torch; 2.5 to 3.0 ml/min N_2 added to increase sensitivity
Cell carrier gas flow (l/min)	0.8 l/min
ICP-MS Instrument	
Make, Model & type	Agilent 8900 Q-ICP-MS
Sample introduction	Ablation aerosol via smoothing device
RF power (W)	1350W
Make-up gas flow (l/min)	Sourced from Agilent 8900, 0.65 l/min
Detection system	Dual-mode discrete dynode electron multiplier
Masses measured (dwell time in ms)	^{24}Mg (10), ^{27}Al (10), ^{29}Si (5), ^{42}Ca (10), ^{43}Ca (10), ^{55}Mn (10), ^{57}Fe (10), ^{66}Zn (10), ^{88}Sr (10), ^{89}Y (10), ^{137}Ba (10), ^{139}La (25), ^{140}Ce (25), ^{141}Pr (25), ^{146}Nd (25), ^{147}Sm (25), ^{153}Eu (25), ^{157}Gd (25), ^{159}Tb (25), ^{163}Dy (25), ^{165}Ho (25), ^{166}Er (25), ^{169}Tm (25), ^{172}Yb (25), ^{175}Lu (25), ^{208}Pb (10), ^{232}Th (10), ^{238}U (10)
Integration time per output datapoint (s)	0.5274 s
Sensitivity	*ca*. 6700 to 6800 cps/μg.g^{-1} U
Dead time (ns)	39.5 at mass 166
Data Processing	
Gas blank	20 s between each analysis
Calibration strategy	NIST 612 glass used as primary reference material, with known Ca abundances used for internal standardization
Reference Material info	NIST 612 (recommended values from GeoReM as of 05/07/2021)
Data processing package used	Iolite4 v4.6.1 – Trace Element data reduction scheme
Quality control / Validation	Reference carbonate JCp-1 NP treated as unknown and used as quality control (see Table 3.2)

et al., 2011, 2019) and the samples (measured by EPMA) as internal standards. Signal intensities were corrected from background contributions by subtracting the gas blank. Sample analyses were bracketed by analysing the NIST 612 glass and JCp-1 NP nano-powdered pellet reference carbonate (Jochum et al., 2019) after every 10 to 15 analyses. NIST 612 glass was used as the primary reference material, whereas JCp-1 NP was treated as an unknown and used as a quality control secondary reference material. The accuracy of measurements on the secondary standard was typically within ± 20% of the recommended values for JCp1-NP, except for Zn, Ce, and Eu (Table 3.2). Results are reported with their respective 2 standard error and detection limit calculated according to Howell et al. (2013).

3.6. Stable and clumped isotope analyses

The $\delta^{13}C$ and $\delta^{18}O$ stable isotopic compositions of dolomite (n = 101) were analyzed at the Scottish Universities Environmental Research Centre (SUERC) using an Analytical Precision AP2003 mass spectrometer that is equipped with a separate acid injector system. To isolate each paragenetic stage, samples were micro-drilled (using a 50 μm diameter drill-bit) under a binocular microscope. These ~5 mg powders were digested in 105% H_3PO_4 under a helium atmosphere at 70°C. Measured $\delta^{13}C$ and $\delta^{18}O$ values are reported relative to Vienna PeeDee Belemnite (VPDB) using conventional delta (δ) notation. Analytical reproducibility, based on replicates of the internal SUERC standard MAB-2 (Carrara marble), is ± 0.2‰ for both $\delta^{13}C$ and $\delta^{18}O$. The MAB-2 standard was extracted from the same quarry as the IAEA-CO-1 international standard (Carrara marble), each sample having equivalent $\delta^{13}C$ and $\delta^{18}O$ values of –2.5 and 2.4 VPDB, respectively.

Carbonate clumped isotope (Δ_{47}) measurements were performed at SUERC using a manual extraction line and an Thermo Fisher 253 Isotope Ratio Mass Spectrometer (IRMS). Samples (5 to 15 mg for carbonate) were digested in >103% H_3PO_4 at 90°C in a common acid bath. Samples were digested for 30 min because they entirely comprise dolomite (as compared to 13 min for calcite). A glass coil, cooled to –76 °C with a mixture

Table 3.2: Known and measured trace element abundances for the JCp-1 NP reference carbonate (LA ICP-MS).

Session		November 21, 2021					May 22, 2022				
Channel	Known abundance (mg/kg)	Measured abundance (mg/kg)	SD (mg/kg)	Difference (%)	Measured/ Known	±	Measured abundance (mg/kg)	SD (mg/kg)	Difference (%)	Measured/ Known	±
Mg^{24}	855	1230	87	43.9	1.44	0.10	1064	24	24.5	1.24	0.03
Al^{27}	379	386	37	2.0	1.02	0.10	470	19	24.0	1.24	0.05
Mn^{55}	1.13	1.24	0.21	9.9	1.10	0.19	1.09	0.34	–3.3	0.97	0.30
Fe^{57}	67.2	50.6	4.9	–24.7	0.75	0.07	53.5	7.9	–20.4	0.80	0.12
Zn^{66}	2.2	1.1	0.1	–52.0	0.48	0.04	1.0	0.1	–53.9	0.46	0.04
Sr^{88}	6890	8467	175	22.9	1.23	0.03	6965	131	1.1	1.01	0.02
Y^{89}	0.33	0.37	0.05	11.5	1.12	0.15	0.36	0.05	8.2	1.08	0.14
Ba^{137}	9.21	10.89	0.65	18.3	1.18	0.07	10.09	0.37	9.5	1.10	0.04
La^{139}	0.0891	0.0884	0.0057	–0.8	0.99	0.06	0.0857	0.0076	–3.9	0.96	0.09
Ce^{140}	0.1000	0.1307	0.0108	30.7	1.31	0.11	0.1284	0.0134	28.4	1.28	0.13
Pr^{141}	0.0174	0.0175	0.0016	0.8	1.01	0.09	0.0168	0.0014	–3.6	0.96	0.08
Nd^{146}	0.0711	0.0698	0.0068	–1.9	0.98	0.10	0.0671	0.0086	–5.6	0.94	0.12
Sm^{147}	0.0168	0.0141	0.0029	–16.1	0.84	0.17	0.0133	0.0026	–20.8	0.79	0.15
Eu^{153}	0.0055	0.0033	0.0008	–39.9	0.60	0.14	0.0022	0.0004	–59.0	0.41	0.07
Gd^{157}	0.0210	0.0167	0.0038	–20.5	0.80	0.18	0.0179	0.0028	–14.8	0.85	0.13
Tb^{159}	0.0037	0.0028	0.0007	–23.1	0.77	0.20	0.0027	0.0010	–26.9	0.73	0.28
Dy^{163}	0.0189	0.0189	0.0045	0.1	1.00	0.24	0.0228	0.0087	20.5	1.20	0.46
Ho^{165}	0.0051	0.0047	0.0011	–8.1	0.92	0.22	0.0052	0.0025	1.4	1.01	0.48
Er^{166}	0.0155	0.0151	0.0039	–2.3	0.98	0.25	0.0168	0.0075	8.5	1.08	0.49
Tm^{169}	0.0028	0.0024	0.0012	–14.4	0.86	0.45	0.0024	0.0016	–11.3	0.89	0.56
Yb^{172}	0.0158	0.0190	0.0112	20.1	1.20	0.71	0.0180	0.0097	13.9	1.14	0.61
Lu^{175}	0.0035	0.0030	0.0018	–13.7	0.86	0.53	0.0028	0.0014	–20.0	0.80	0.42
Pb^{208}	0.305	0.332	0.019	8.9	1.09	0.06	0.311	0.019	2.1	1.02	0.06
Th^{232}	0.042	0.050	0.012	19.5	1.20	0.28	0.049	0.010	18.6	1.19	0.23
U^{238}	2.640	2.582	0.097	–2.2	0.98	0.04	2.425	0.060	–8.1	0.92	0.02

of propanol and CO_2, was placed immediately after the acid bath to trap the produced water during the acid digestion. The produced CO_2 was condensed continuously during the digestion in a glass coil that was submerged in liquid N_2. In the final 5 min of acid digestion (3 min for calcite), incondensable gases were evacuated using a turbomolecular pump. The produced CO_2 was then transferred to a calibrated volume attached to a strain gauge using liquid N_2. The CO_2 was thawed until it reached room temperature, after which the acid digestion volume yield was measured. The CO_2 was then passed through a 4 m gas chromatography column held at 40°C with a He carrier flow before being diverted to the IRMS. The IRMS measured the CO_2 in a minimum of 7 blocks of 6 dual-inlet measurements (26 s integration time), and recorded intensities of masses 44 to 48. The intensity of mass 48 was used to screen for contamination of the gas and exclude replicates when the Δ_{48} offset was greater than 0.5‰ (Davies and John, 2017). Data reduction was conducted using the Easotope software (John and Bowen, 2016), the IUPAC parameters (Brand et al. 2010, Petersen et al. 2019), and the ^{18}O acid fractionation of Rosenbaum and Sheppard (1986) for dolomite. The values from Bernasconi et al. (2021) for the ETH1 to ETH4 carbonate standards were used to define the empirical transfer function from the measured Δ_{47} to the absolute reference frame. Analytical uncertainties on Δ_{47} were calculated as the larger of the standard error on replicates of each sample or the standard error of the ETH standards (i.e., standard deviation divided by the square root of the number of replicates). The reprojected Δ_{47} values were used to calculate apparent dolomite crystallization temperatures using the calibration of Anderson et al. (2021):

$$\Delta_{47\,(CDES90)} = 0.0391(\pm 0.0004)*10^6/T^2 + 0.154(\pm 0.004)$$

3.7. Fluid inclusion analyses

Following the criteria described by Goldstein and Reynolds (1993), petrographical analysis of all samples was conducted to identify the presence of primary fluid inclusion assemblages in each paragenetic stage. In particular, trails of inclusions that were trapped

along crystallographic growth zones were targeted. Throughout much of the replacement dolomite (RD), however, fluid inclusions were scarce and assemblages were not observed. Therefore, multiple isolated inclusions that were hosted in the same crystal were analyzed to verify that there was consistent microthermometric properties between these inclusions. Fluid inclusion microthermometry was conducted at the University of Alberta using a Linkam THMS600 heating and freezing stage that is mounted on an Olympus BX53 petrographical microscope. The stage temperature was calibrated using synthetic fluid inclusions, according to the triple point of CO_2 (–56.6°C), the triple point of H_2O (0°C), and the critical point of H_2O (373.9°C). Accuracy and precision of the measurements are ± 0.5°C at temperatures above 100°C and ± 0.1°C at temperatures below 0°C. For all inclusions analyzed, the temperature of liquid-vapor homogenization (to the liquid) was recorded. A general heating rate of 6°C/min was used, but the rate was reduced to 2°C/min as the temperature approached homogenization (i.e., when the vapor bubble was very small). For the smallest fluid inclusions, where phase changes were difficult to observe, the homogenization temperature was bracketed using the temperature cycling approach of Goldstein and Reynolds (1993). The microthermometric data were then interpreted quantitatively using the computer program of Steele-MacInnis et al. (2012). The melting temperature (T_m) of the fluid inclusions were also attempted, but the inclusions were unable to be frozen during these analyses (at temperatures down to –175°C).

3.8. Rock deformation experiments

3.8.1. Starting material

Carrara marble (CM) and Solnhofen limestone (SL) were used as the experimental materials for this study. Cylindrical specimens, 45 mm in length and 15 mm in diameter, of each lithology were prepared for axisymmetric shortening experiments. Samples of CM were cored in an arbitrary but constant direction (designated the *a*-direction in this block), whereas samples of SL were cored normal to bedding. Axisymmetric extension

experiments were conducted on “dog-bone” shaped samples that were waisted to 13 mm in diameter over a central length of 16 mm. Samples of CM were oven-dried at 60°C, whereas samples of SL were air-dried at a relative humidity of 60%, in each case resulting in a constant sample mass. The strength of CM is unaffected by ambient water vapour pressure, whereas the unconfined compressive strength (C_0) of SL in the oven-dried (100° C) state is reduced by ~30% through water saturation at room temperature or when exposed to the atmosphere at laboratory relative humidity (60%) (Rutter, 1972). French et al. (2022) reported that the ultimate strength of “nominally dry” Solnhofen limestone was unaffected by wetting, which would be expected if “nominally” dry means air-dry.

Carrara marble, with a mean grain size of 98.4 μm ± 72.7 μm and 0.2% porosity, is a medium-grade metamorphic rock from the Tuscany region of Italy. CM comprises >99.9 wt% $CaCO_3$ and includes rare muscovite, quartz, dolomite, and graphite grains (Rutter, 1995; Pieri et al. 2001; Kandula et al. 2019; Rybacki et al. 2021; Rutter et al. 2022). Grain boundaries range from straight to gently curving with slightly sutured edges. The calcite crystals are equant, lack optical strain features, are free from crystallographic preferred orientation, and possess only low densities of lamellar twinning (Rutter, 1995; de Raadt et al. 2014). The CM used for this study was derived from a block of “Lorano Bianco” statutory marble that was collected as a laboratory standard by D. Olgaard and M. Pieri (ETH Zürich, Switzerland), and M. Coli (University of Florence, Italy).

Solnhofen limestone, with a mean grain size of 3.8 μm ± 0.3 μm and 4.2% porosity, is a pelagic mudstone from the Bavaria region of Germany. SL comprises 99.1 wt% $CaCO_3$ and includes minor detrital quartz grains with a mean grain size of 20 μm as a secondary phase. Minor impurities (e.g., organic matter, oxide particles, clay minerals) also occur along the grain boundaries (Schmid et al. 1977; Rutter et al. 1994). Llana-Fúnez and Rutter (2005) demonstrated that the calcite in SL has a weak crystallographic preferred orientation of c-axes parallel to bedding. The anisotropy of *P*-wave velocities in SL (4.92%

faster normal to bedding) is, thus, analogous to that of an individual calcite crystal (e.g., Khazanehdari et al. 1998).

3.8.2. Experimental design

Samples of CM and SL were held in a ¼ mm thick, annealed copper jacket and deformed using a rock deformation apparatus. Following deformation, the copper jacket holds the specimen together to facilitate subsequent thin-sectioning and microstructural analyses, particularly in the case of tensile failure. Each copper jacket was heat-treated to ~600°C to remove crystal dislocations, quenched in water, and cleaned with nitric acid. Cylindrical steel split-cones, with an included angle of 70°, were placed at each end of the jacket to grip the specimen. Heat-shrink synthetic rubber tubing was then placed around the specimen and the loading piston assembly to prevent ingress of the confining fluid.

The deformation apparatus used for this study allows experiments in both axisymmetric extension and shortening to be carried out, the former owing to a bayonet-style connector on the bottom loading piston that engages with the top of the internal load cell assembly. Once the loading piston assembly is inserted into the pressure vessel, it is sealed, and confining fluid is pumped into the vessel to apply radial pressure to the exterior of the specimen (up to ~300 MPa). The confining fluid is dioctyl sebacate synthetic ester, which has a low rate of change of viscosity with pressure (Rutter and Mecklenburgh, 2018). Confining pressure measurements were made using a 700 MPa Heise Bourdon tube pressure gauge, with an accuracy of 0.1 MPa, that was also used to calibrate all the other electronic pressure transducers. Experiments were conducted at room temperature (20°C) and an axial displacement rate of 3.3×10^{-3} mm s^{-1}. This corresponds to a strain rate of 2.1×10^{-4} s^{-1} over the waisted portion of the specimen in extension tests and 7.4×10^{-5} s^{-1} over the full length of the specimen in shortening tests. Forty-seven axisymmetric extension experiments and 16 axisymmetric shortening experiments were conducted, typically at 10 MPa intervals of confining pressure across the range of stress conditions. In extension, true

tensile stresses could be achieved because the specimen diameter was smaller than that of the moving piston (19.0 mm) where it passes through the pressure seal. The maximum tensile force that can be applied to the specimen is given by the difference between its cross-sectional area and that of the moving piston, multiplied by the confining pressure.

Although most tests were conducted without pore pressure, the apparatus allows pore pressure tests to be carried out. Two tests were run with an elevated pore pressure of argon gas that was generated by a servo-controlled pressure generator. Confining pressure was controlled by a similar but larger servo-controlled pressure generator. As the axial loading piston is displaced into or withdrawn from the pressure vessel, the volume change in the vessel causes an increase or decrease in confining pressure, respectively. Hence, the servo-controller compensates for this to maintain a constant confining pressure during a test.

Experiments were terminated at different values of bulk strain, depending on the failure mode identified by the stress/strain behaviour during the experiment. The piston assembly was then unloaded, and the vessel was depressurized to recover the specimen.

3.8.3. Calibrations, data processing, and jacket strength correction

In this type of rock deformation apparatus, the total displacement of the axial column was measured using a linear displacement transducer that was mounted outside the pressure vessel. The total displacement includes both the deformation of the specimen and the axial distortion of the apparatus. The latter was determined by calibration tests, using a steel specimen, over a range of confining pressures. Strain measurements in the specimen were determined to be accurate to ± 0.1%. The axial load on the specimen was measured using a Heard (1963)-type semi-internal load cell that was mounted inside the pressure medium directly below the specimen assembly. This was calibrated against a 25,000 kg load cell over a range of confining pressures, in axisymmetric extension and shortening. Stress measurements in the specimen were determined to be accurate to ± 1.0 MPa. Given that the axial column is long, induced flexural forces can contribute to the stress state in the

sample (Mackwell and Paterson, 2002), which influences the apparent differential stress at failure. Nevertheless, the largest source of uncertainty in the measurements of stress and strain arise from the natural variability between different rock specimens.

Data processing involved the correction of the measured axial load for (1) the effects of confining pressure on the load cell calibration and (2) the subtraction of machine axial distortion from the measured displacement and thus, the total axial strain. The axial force on the sample was calculated using the load cell calibration. Next, the axial differential stress was calculated, taking into account the change in the cross-sectional area of the specimen arising from axial strain, assuming homogeneous constant volume deformation. The axial force that was supported by the annealed copper jacket was also removed.

In low temperature experiments, the copper jacket can support a significant fraction of the total axial load, particularly at low mean pressures when the rock is very weak or fails in tension. The analysis of results particularly requires the load supported by the copper jacket at the point of tensile failure or shear failure (ultimate strength) to be determined and subtracted from the total load at failure. To this end, the stress/strain behaviour of an annealed specimen that was fabricated from a solid copper bar was measured. The yield stress of copper is 31.0 MPa, after which rapid strain hardening begins. The strain in the jacket and the rock are the same, but the smaller cross-sectional area of the jacket reduces the load it supports by ~90%. From the known stress/strain behaviour of the jacket and the measured strain at failure, the load supported by the jacket at failure was determined for each test. This was inferred to correspond to the formation of the first tensile crack.

Using only a synthetic rubber jacket, measured to be of negligible strength, the formation of the first tensile crack splits the specimen into two pieces that are no longer able to support an axial differential load. In contrast, localized strain hardening of the copper jacket stabilizes the first crack, allowing a succession of several cracks to form in locations where strain hardening has not yet occurred. Each of these cracks are stabilized by the local strain of the copper jacket at the periphery of the crack. This avoids jacket

rupture in extension and the flooding of the specimen with hydraulic fluid, which would complicate subsequent petrographical study.

3.8.4. Microstructural analyses

Microstructural observations were made on optical thin-sections cut parallel to the specimen cylinder axis and oriented to capture the maximum failure surface angle. For shortening tests, these angles are specified by the angle between the failure surface and the specimen axis (σ_1), and between the failure surface and the plane normal to the specimen axis (σ_1) for extension tests. Samples were vacuum impregnated with blue-stained epoxy resin and prepared as 20 μm thick sections. The jacketing material was removed, and the section was polished on its upper surface. Polished sections were examined under plane-polarized light and between crossed-polars using a Nikon Eclipse LV100N POL microscope. Six representative samples of SL that cover the full range of failure modes were analysed by scanning electron microscopy using a Thermo Fisher Scientific Quanta 650 FEG instrument and backscattered electron imaging was conducted at an accelerating voltage of 15.0 kV.

References

Anderson, N.T., Kelson, J.R., Kele, S., Daëron, M., Bonifacie, M., Horita, J., Mackey T.J., John C.M., Kluge T., Petschnig, P., Jost, A.B., Huntington, K.W., Bernasconi, S.M., Bergmann, K.D., 2021. A unified clumped isotope thermometer calibration (0.5–1,100 C) using carbonate-based standardization. Geophysical Research Letters, 48(7), e2020GL092069.

Bernasconi, S.M., Daëron, M., Bergmann, K.D., Bonifacie, M., Meckler, A.N., Affek, H.P., Anderson, N., Bajnai, D., Barkan, E., Beverly, E., Blamart, D., Burgener, L., Calmels, D., Chaduteau, C., Clog, M., Davidheiser-Kroll, B., Davies, A., Dux, F., Eiler, J., Elliott, B., Fetrow, A.C., Fiebig, J., Goldberg, S., Hermoso, M., Huntington, K.W., Hyland, E., Ingalls, M., Jaggi, M., John, C.M., Jost, A.B., Katz, S., Kelson, J., Kluge, T., Kocken, I.J., Laskar, A., Leutert, T.J., Liang, D., Lucarelli, J., Mackey, T.J., Mangenot, X., Meinicke, N., Modestou, S.E., Müller, I.A., Murray, S., Neary, A., Packard, N., Passey, B.H., Pelletier, E., Petersen, S., Piasecki, A., Schauer, A., Snell,

K.E., Swart, P.K., Tripati, A., Upadhyay, D., Vennemann, T., Winkelstern, I., Yarian, D., Yoshida, N., Zhang, N., Ziegler, M., 2021. InterCarb: a community effort to improve inter-laboratory standardization of the carbonate clumped isotope thermometer using carbonate standards. Geochemistry, Geophysics, Geosystems, 22(5), e2020GC009588.

Brand, W.A., Assonov, S.S., Coplen, T.B., 2010. Correction for the ^{17}O interference in $\delta^{13}C$ measurements when analyzing CO_2 with stable isotope mass spectrometry (IUPAC Technical Report). Pure and Applied Chemistry, 82, 1719-1733.

Davies, A.J., John, C.M., 2017. Reducing contamination parameters for clumped isotope analysis: The effect of lowering Porapak™ Q trap temperature to below -50 C. Rapid Communications in Mass Spectrometry, 31(16), 1313-1323.

de Raadt, W.S., Burlini, L., Kunze, K., Spiers, C.J., 2014. Effect of pre-existing crystallographic preferred orientation on the rheology of Carrara marble. Journal of Structural Geology, 68, 44-57.

Dickson, J.A.D., 1965. A modified staining technique for carbonates in thin section. Nature, 205(4971), 587-587.

Dickson, J.A.D., 1966. Carbonate identification and genesis as revealed by staining. Journal of Sedimentary Research, 36(2), 491-505.

French, M.E., Zhu, W., Xiao, X., Evans, B., Prior, D.J., 2022. Thermally Enhanced Water Weakening of the Solnhofen Limestone. Journal of Geophysical Research: Solid Earth, 127(3), e2021JB022742.

Heard, H.C., 1963. Effect of large changes in strain rate in the experimental deformation of Yule marble. The Journal of Geology, 71(2), 162-195.

Howell, D., Griffin, W.L., Pearson, N.J., Powell, W., Wieland, P., O'Reilly, S.Y., 2013. Trace element partitioning in mixed-habit diamonds. Chemical Geology, 355, 134-143.

Kandula, N., Cordonnier, B., Boller, E., Weiss, J., Dysthe, D.K., Renard, F., 2019. Dynamics of microscale precursors during brittle compressive failure in Carrara marble. Journal of Geophysical Research: Solid Earth, 124(6), 6121-6139.

Khazanehdari, J., Rutter, E.H., Casey, M., Burlini, L., 1998. The role of crystallographic fabric in the generation of seismic anisotropy and reflectivity of high strain zones in calcite rocks. Journal of Structural Geology, 20(2-3), 293-299.

Kruse, F.A., Lefkoff, A.B., Boardman, J.W., Heidebrecht, K.B., Shapiro, A.T., Barloon, P.J., Goetz, A.F.H., 1993. The spectral image processing system (SIPS) – interactive

visualization and analysis of imaging spectrometer data. Remote sensing of environment, 44(2-3), 145-163.

Kurz, T.H., Buckley, S.J., Howell, J.A., 2013. Close-range hyperspectral imaging for geological field studies: Workflow and methods. International Journal of Remote Sensing, 34(5), 1798-1822.

Kurz, T.H., Buckley, S.J., Howell, J.A., Schneider, D., 2011. Integration of panoramic hyperspectral imaging with terrestrial lidar data. The Photogrammetric Record, 26(134), 212-228.

Gasparrini, M., Bechstädt, T., Boni, M., 2006. Massive hydrothermal dolomites in thesouthwestern Cantabrian Zone (Spain) and their relation to the Late Variscan evolution. Marine and Petroleum Geology, 23, 543-568.

Goldsmith, J.R., Graf, D.L., 1958. Structural and compositional variations in some natural dolomites. The Journal of Geology, 66(6), 678-693.

Goldstein, R.H., Reynolds, T.J., 1994: *Systematics of fluid inclusions in diagenetic minerals*. Short Course 31, Society of Economic Paleontologists and Mineralogists, Tulsa, 199 p.

Gregg, J.M., Bish, D.L., Kaczmarek, S.E., Machel, H.G., 2015. Mineralogy, nucleation and growth of dolomite in the laboratory and sedimentary environment: a review. Sedimentology, 62(6), 1749-1769.

Jochum, K.P., Weis, U., Stoll, B., Kuzmin, D., Yang, Q., Raczek, I., Jacob, D.E., Stracke, A., Birbaum, K., Frick, D.A., Günther, D., Enzweiler, J., 2011. Determination of reference values for NIST SRM 610–617 glasses following ISO guidelines. Geostandards and Geoanalytical Research, 35(4), 397-429.

Jochum, K.P., Garbe-Schönberg, D., Veter, M., Stoll, B., Weis, U., Weber, M., Lugli, F., Jentzen, A., Schiebel, R., Wassenburg, J.A., Jacob, D.E., Haug, G.H., 2019. Nano-powdered calcium carbonate reference materials: Significant progress for microanalysis?. Geostandards and Geoanalytical Research, 43(4), 595-609.

John, C.M., Bowen, D., 2016. Community software for challenging isotope analysis: First applications of ‘Easotope’ to clumped isotopes. Rapid Communications in Mass Spectrometry, 30(21), 2285-2300.

Jones, B., Luth, R.W., MacNeil, A.J., 2001. Powder X-ray diffraction analysis of homogeneous and heterogeneous sedimentary dolostones. Journal of Sedimentary Research, 71(5), 790-799.

Llana-Fúnez, S., Rutter, E.H., 2005. Distribution of non-plane strain in experimental compression of short cylinders of Solnhofen limestone. Journal of Structural Geology, 27(7), 1205-1216.

Lumsden, D.N., 1979. Discrepancy between thin-section and X-ray estimates of dolomite in limestone. Journal of Sedimentary Research, 49(2), 429-435.

Lypaczewski, P., Rivard, B., 2018. Estimating the Mg# and AlVI content of biotite and chlorite from shortwave infrared reflectance spectroscopy: Predictive equations and recommendations for their use. International journal of applied earth observation and geoinformation, 68, 116-126.

Lypaczewski, P., Rivard, B., Gaillard, N., Perrouty, S., Piette-Lauzière, N., Bérubé, C.L., Linnen, R.L., 2019. Using hyperspectral imaging to vector towards mineralization at the Canadian Malartic gold deposit, Québec, Canada. Ore Geology Reviews, 111, 102945.

Machel, H.G., Burton, E.A., 1991. Factors governing cathodoluminescence in calcite and dolomite, and their implications for studies of carbonate diagenesis. In: Barker, C.E., Kopp, O.C., (Eds.), Luminescence microscopy and spectroscopy - Qualitative and quantitative applications. Society for Sedimentary Geology Short Course, No. 25. 37-57.

Mackwell, S.J., Paterson, M.S., 2002. New developments in deformation studies: high-strain deformation. In: Karato, S.I., Wenk, H.R., (Eds.) *Plastic deformation of minerals and rocks*. Reviews in Mineralogy and Geochemistry, 51(1), 1-19.

Murphy, R.J., Taylor, Z., Schneider, S., Nieto, J., 2015. Mapping clay minerals in an open-pit mine using hyperspectral and LiDAR data. European Journal of Remote Sensing, 48(1), 511-526.

Nielsen, P., Swennen, R., Muchez, P., Keppens, E., 1998. Origin of Dinantian zebra dolomites south of the Brabant-Wales Massif, Belgium. Sedimentology, 45, 727-743.

Paton, C., Hellstrom, J., Paul, B., Woodhead, J., Hergt, J., 2011. Iolite: Freeware for the visualisation and processing of mass spectrometric data. Journal of Analytical Atomic Spectrometry, 26(12), 2508-2518.

Petersen, S.V., Defliese, W.F., Saenger, C., Daëron, M., Huntington, K.W., John, C.M., Kelson, J.R., Bernasconi, S.M., Colman, A.S., Kluge, T., Olack, G.A., Schauer, A.J., Bajnai, D., Bonifacie, M., Breitenbach, S.F.M., Fiebig, J., Fernandez, A.B., Henkes, G.A., Hodell, D., Katz, A., Kele, S., Lohmann, K.C., Passey, B.H., Peral, M.Y., Petrizzo, D.A., Rosenheim, B.E., Tripati, A., Venturelli, R., Young, E.D., Winkelstern, I.Z., 2019. Effects of improved ^{17}O correction on interlaboratory

agreement in clumped isotope calibrations, estimates of mineral-specific offsets, and temperature dependence of acid digestion fractionation. Geochemistry, Geophysics, Geosystems, 20(7), 3495-3519.

Pieri, M., Burlini, L., Kunze, K., Stretton, I., Olgaard, D.L., 2001. Rheological and microstructural evolution of Carrara marble with high shear strain: results from high temperature torsion experiments. Journal of Structural Geology, 23(9), 1393-1413.

Rogge, D.M., Rivard, B., Zhang, J., Sanchez, A., Harris, J., Feng, J., 2007. Integration of spatial–spectral information for the improved extraction of endmembers. Remote Sensing of Environment 110, 287-303.

Rogge, D.M., Rivard, B., 2010. Iterative spatial filtering for reducing intra-class spectral variability and noise. IEEE GRSS Workshop on Hyperspectral Image and Signal Processing: Evolution in Remote Sensing, Reykjavik, Iceland, June 14-16, 1-4.

Rogge, D., Bachmann, M., Rivard, B., Feng, J., 2012. Spatial sub-sampling using local endmembers for adapting OSP and SSEE for large-scale hyperspectral surveys. IEEE Journal of Selected Topics in Applied Earth Observations and Remote Sensing 5, 183-195.

Rosenbaum, J., Sheppard, S.M.F., 1986. An isotopic study of siderites, dolomites and ankerites at high temperatures. Geochimica et cosmochimica acta, 50(6), 1147-1150.

Rutter, E.H., 1972. The influence of interstitial water on the rheological behaviour of calcite rocks. Tectonophysics, 14, 13-33.

Rutter, E.H., 1995. Experimental study of the influence of stress, temperature, and strain on the dynamic recrystallization of Carrara marble. Journal of Geophysical Research: Solid Earth, 100(B12), 24651-24663.

Rutter, E.H., Casey, M., Burlini, L., 1994. Preferred crystallographic orientation development during the plastic and superplastic flow of calcite rocks. Journal of Structural Geology, 16(10), 1431-1446.

Rutter, E.H., Mecklenburgh, J., 2018. Influence of normal and shear stress on the hydraulic transmissivity of thin cracks in a tight quartz sandstone, a granite, and a shale. Journal of Geophysical Research: Solid Earth, 123(2), 1262-1285.

Rutter, E.H., Wallis, D., Kosiorek, K., 2022. Application of Electron Backscatter Diffraction to Calcite-Twinning Paleopiezometry. Geosciences, 12(6), 222.

Rybacki, E., Niu, L., Evans, B., 2021. Semi-brittle deformation of Carrara marble: Hardening and twinning induced plasticity. Journal of Geophysical Research: Solid Earth, 126, e2021JB022573.

Schmid, S.M., Boland, J.N., Paterson, M.S., 1977. Superplastic flow in finegrained limestone. Tectonophysics, 43(3-4), 257-291.

Sibley, D.F., Gregg, J.M., 1987. Classification of dolomite rock textures. Journal of sedimentary Research, 57(6), 967-975.

Steele-MacInnis, M., Lecumberri-Sanchez, P., Bodnar, R.J., 2012. Short note: HokieFlincs_H2O-NaCl: A Microsoft Excel spreadsheet for interpreting microthermometric data from fluid inclusions based on the PVTX properties of H2O-NaCl. Computers & Geosciences, 49, 334-337.

Vandeginste, V., Swennen, R., Gleeson, S.A., Ellam, R.M., Osadetz, K., Roure, F., 2005. Zebra dolomitization as a result of focused fluid flow in the Rocky Mountains Fold and Thrust Belt, Canada. Sedimentology, 52, 1067-1095.

Woodhead, J.D., Hellstrom, J., Hergt, J.M., Greig, A., Maas, R., 2007. Isotopic and elemental imaging of geological materials by laser ablation inductively coupled plasma-mass spectrometry. Geostandards and Geoanalytical Research, 31(4), 331-343.

Blank page

Shortwave infrared hyperspectral imaging as a novel method to elucidate multi-phase dolomitization, recrystallization, and cementation in carbonate sedimentary rocks

Cole A. McCormick [1,*], Hilary Corlett [2], Jack Stacey [1], Cathy Hollis [1], Jilu Feng [3], Benoit Rivard [3], Jenny E. Omma [4]

1. Department of Earth and Environmental Sciences, The University of Manchester, Manchester, M13 9PL, United Kingdom.

2. Department of Physical Sciences, MacEwan University, Edmonton, Alberta, T5J 4S2, Canada.

3. Department of Earth and Atmospheric Sciences, University of Alberta, Edmonton, Alberta, T6G 2E3, Canada.

4. Scottish Universities Environmental Research Council, East Kilbride, Glasgow, G75 0QF, United Kingdom.

* Corresponding author: Cole McCormick - cole.mccormick@manchester.ac.uk

McCormick, C.A., Corlett, H., Stacey, J., Hollis, C., Feng, J., Rivard, B., Omma, J.E., 2021. Shortwave infrared hyperspectral imaging as a novel method to elucidate multi-phase dolomitization, recrystallization, and cementation in carbonate sedimentary rocks. Scientific reports, 11(1), 1-16.

Abstract

Carbonate sedimentary rocks undergo low-temperature, post-depositional changes, including mineral precipitation, dissolution, or recrystallisation (diagenesis). Unravelling the sequence of these events is time-consuming, expensive, and relies on destructive analytical techniques, yet such characterization is essential to understand their post-depositional history for mineral and energy exploitation and carbon storage. Conversely, hyperspectral imaging offers a rapid, non-destructive method to determine mineralogy, while also providing compositional and textural information. It is commonly employed to differentiate lithology, but it has never been used to discern complex diagenetic phases in a largely monomineralic succession. Using spatial-spectral endmember extraction, we explore the efficacy and limitations of hyperspectral imaging to elucidate multi-phase dolomitization and cementation in the Cathedral Formation (Western Canadian Sedimentary Basin). Spectral endmembers include limestone, two replacement dolomite phases, and three saddle dolomite phases. Endmember distributions were mapped using Spectral Angle Mapper, then sampled and analyzed to investigate the controls on their spectral signatures. The absorption-band position of each phase reveals changes in %Ca (molar Ca/(Ca + Mg)) and trace element substitution, whereas the spectral contrast correlates with texture. The ensuing mineral distribution maps provide meter-scale spatial information on the diagenetic history of the succession that can be used independently and to design a rigorous sampling protocol.

4.1. Introduction

Hyperspectral imaging involves the collection and analysis of reflectance data in the form of many, narrow and contiguous, spectral bands (Cloutis, 1996; van der Meer et al, 2012). Laboratory-, field-, and satellite-based spectroscopy are well-established methods with numerous geological applications, including lithological mapping (Rivard et al. 2009; Feng et al. 2018), mineral prospectivity (Turner et al. 2003; Krupnik and Khan, 2019; Lypaczewski et al. 2019), and environmental monitoring (Bellante et al. 2013; Zabcic et al. 2014). The application of such methods to carbonate sedimentary rocks, however, is limited, with previous research largely focusing on the measurement of the laboratory-based spectral characteristics of minerals (Hunt and Salisbury, 1971; Gaffey, 1986, 1987; van der Meer, 1995) and their abundances in rocks (Zaini et al. 2012, 2014; Green and Schodlok, 2016). The few studies that have applied hyperspectral imaging to carbonate sedimentary rocks in the field have largely focused on up-scaling and accelerating the identification of lithological heterogeneities (Kurz et al. 2012; Beckert et al. 2018).

Previous studies on the reflectance of carbonate minerals have recognized up to seven absorption-bands, from 1600 to 2550 nm, caused by the vibration of the carbonate ion (Hunt and Salisbury, 1971; Gaffey, 1986, 1987; van der Meer, 1995). The positions, depths, and asymmetries of these bands reflect the mineral structure and properties of the substituted cations (van der Meer, 2004; Zaini et al. 2014). Calcite (Ca^{+2} mass = 40.078 amu; radius = 100 pm) has an absorption-band at ~2335 nm, whereas the same band for magnesite (Mg^{+2} mass = 24.305 amu; radius = 72 pm) is at ~2300 nm (Gaffey, 1986, 1987). This absorption-band for dolomite, centered at ~2315 nm, is not equidistant between the calcite and magnesite band positions because the Mg–O bond is shorter than the Ca–O bond in dolomite (Gaffey, 1986). Several studies have effectively used absorption-band positions to differentiate carbonate minerals (Windeler and Lyon, 1991; van der Meer, 1996; Zaini et al. 2014; Beckert et al. 2018), but this method has not been used to discern multiple diagenetic phases in a largely monomineralic carbonate system.

Furthermore, the textural properties of minerals (e.g., crystal size, shape, orientation) affect the surface and volume scattering of light (Crowley, 1986; Gaffey, 1986, 1987; van der Meer, 1995; Zaini et al. 2012) and can, thus, be used to further discern individual phases in carbonate sedimentary rocks.

This study is based on the shortwave infrared (SWIR) hyperspectral imaging of an exposure of variably dolomitized limestone that belongs to the Cathedral Formation (Middle Cambrian; 509 to 497 Ma) in the Western Canadian Sedimentary Basin (WCSB). Non-stratabound dolomite bodies originate from normal-to-transtensional faults and include several diagenetic mineral phases that have distinct compositions and textures. Given that the timing and mechanism of dolomitization are well-constrained (Koeshidayatullah et al. 2020a, 2020b, 2021; Stacey et al. 2021), this succession is ideal to test whether hyperspectral imaging can be used to identify and map multiple, visibly indistinguishable, phases of dolomite in outcrop. In particular, this methodological study investigates the extent to which dolomite stoichiometry and texture can be determined by hyperspectral imaging. Consequently, the mineral distribution map products facilitate the validation and/or revision of existing fault-controlled dolomitization models (Koeshidayatullah et al. 2020a, 2020b, 2021; Stacey et al. 2021).

4.2. Geological setting

The WCSB is a southwest-thickening wedge of sedimentary rocks, up to ~18 km thick in the southern Rocky Mountains, that extends from the southwest corner of the Northwest Territories to the north-central United States and includes four unconformity-bounded packages of strata (Bond and Kominz, 1984; Desjardins et al. 2010). The (1) Purcell Supergroup (Mesoproterozoic) records deposition and volcanic activity in an intracratonic basin, whereas the (2) Windermere Supergroup (Neoproterozoic) records the rifting of northwest Laurentia that waned in the Cryogenian to Ediacaran (Bond and Kominz, 1984; Li et al. 2008; Desjardins et al. 2010). (3) Lower Cambrian (541 to 509 Ma) to Triassic

strata were deposited on a passive margin. Episodic basement reactivation and renewed rifting in the Cambrian gave rise to regional thermal subsidence with evidence that heat flow and tectonic activity remained high (Powell et al. 2006; Johnston et al. 2009; Stacey et al. 2021). (4) Jurassic to Paleocene strata were deposited in a foreland basin that developed during the Columbian (Jurassic to Early Cretaceous) and Laramide (Late Cretaceous to Paleocene) orogenies. The Cathedral Formation outcrops at Whirlpool Point (52°00′07.5″N, 116°28′13.5″W), the focus of this study, in the Bourgeau Thrust (Fig. 4.1A, B).

Middle Cambrian strata in the southern Rocky Mountains record a series of northeast-transgressing carbonate-mudrock cycles that comprise regional facies belts (Fig. 4.1C). The Cathedral Formation was deposited on a carbonate platform that developed with its margin proximal to the Kicking Horse Rim; an elevated paleotopographic feature that formed due to the syn-depositional reactivation of deep-rooted basement faults (Aitken, 1971; Collom et al. 2009). The formation is up to ~365 m thick and comprises a central shoal complex that grades laterally to proximal slope facies to the southwest and intrashelf basin facies to the northeast (Fig. 4.1D; Aitken, 1997; Pratt, 2002). At Whirlpool Point, the Cathedral Formation overlies the Mount Whyte Formation and is unconformably overlain by the Stephen Formation; host to the Burgess Shale lagerstätte (Collom et al. 2009; Johnston et al. 2009).

4.3. Overview of the diagenetic features in the Cathedral Formation

In the southern Rocky Mountains, the Cathedral Formation consists of light-grey limestone, medium-grey to tan finely-crystalline replacement dolomite (RD), and white coarsely-crystalline saddle dolomite (SD). Dolomitization is most pervasive proximal to the Cambrian platform margin and dolomite grades laterally to limestone towards the northeast (Fig. 4.1D; Stacey et al. 2021). Such dolomite bodies are typically non-stratabound (inclined-to-bedding) at their cores, with stratabound (bedding-parallel)

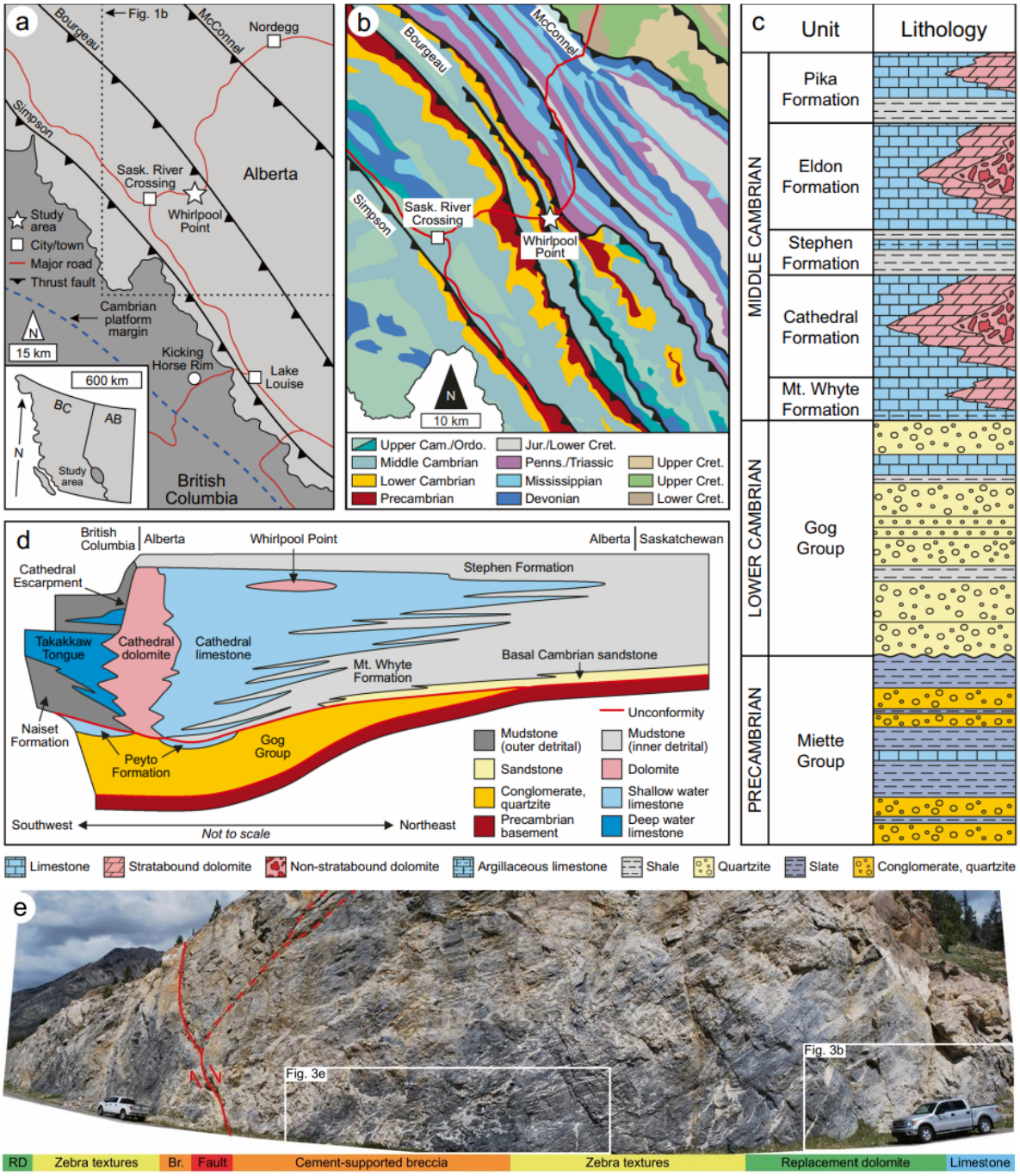

Figure 4.1. (A) Location of the study area in Alberta, Canada showing the major thrust faults and the Cambrian platform margin (modifed from Stacey et al. 2021; based on Vandeginste et al. 2005). **(B)** Geological map of the study area (modifed from Stacey et al. 202; based on the Alberta Geological Survey Interactive Minerals Map: https://ags.aer.ca/publication/iam-001). **(C)** Stratigraphy of the southern Rocky Mountains (based on Aitken, 1971, 1997). **(D)** Schematic cross-section of the Cathedral carbonate platform in the southern Rocky Mountains (modifed from Stacey et al. 2021; based on Aitken, 1971, 1997). **(E)** Photomosaic of the Cathedral Formation at Whirlpool Point showing the diagenetic facies in relation to a normal-to-transtensional fault. Note that the scale changes throughout the photomosaic. Vehicle = 5.0 m in length.

margins (Koeshidayatullah et al. 2020b, 2021; Stacey et al. 2021). Cement-supported breccias and zebra textures are widespread in the Kicking Horse Rim area, with local occurrences of talc, magnesite, and Mississippi Valley-type (MVT) minerals (Powell et al. 2006; Vandeginste et al. 2007; Johnston et al. 2009). These minerals are absent to the northeast, but zebra textures and cement-supported breccias are locally common (Vandeginste et al. 2005; Stacey et al. 2021).

This study focuses on an outcrop, 240 m in width and 40 m in height, at Whirlpool Point that includes a fault-controlled dolomite body in the Cathedral Formation. The outcrop contains a fault that is oriented at 028/52, has a normal offset of 30 cm, and intersects the formation 100 m from the east end (Fig. 4.1E). At the core of the dolomite body, coarsely-crystalline breccias extend 25 m into the hanging-wall, 5 m into the footwall, and are limited to the fault damage zone. Proximal to the fault, the hanging-wall (146/32) comprises cement-supported breccias and bedding-inclined zebra textures. The medial part of the hanging-wall includes fabric-retentive dolomitized microbial bindstone with bedding-parallel and rare bedding-inclined zebra textures. At the margin of the dolomite body, the hanging-wall includes fabric-retentive, finely-crystalline dolomitized peloidal wackestone with rare bedding-parallel zebra textures. The lower part of the Cathedral Formation includes a sharp, bedding-parallel contact with a 2 m thick bed of limestone. In the footwall (179/25), the upper part of the formation is similar to the hanging-wall, but cement-supported breccias and bedding-inclined zebra textures are rare. The medial part of the footwall includes fabric-retentive dolomitized microbial bindstone with bedding-parallel zebra textures that grade laterally to fabric-retentive, finely-crystalline dolomite at the margin (Fig. 4.1E).

4.4. Methods

4.4.1. Collection and processing of the infrared reflectance data

A set of four SWIR (930 to 2508 nm) spectral images were acquired on June 12, 2018 between 11 am and 2 pm using a Specim SisuROCK hyperspectral scanner (a linescan imager) that is mounted on a rotary stage for wall rock imaging. Integration time varied from 5 to 10 ms depending on the time of acquisition and it required 30 s for the stage to rotate 90°. The scanner contains a 256 spectral by 320 spatial pixels mercury-cadmium-telluride detector array that acquires data at a 6.3 nm sampling interval and a 10 nm spectral bandwidth. Two Spectralon panels of 2% and 99% reflectance were positioned in each scene. Data were acquired under clear sky conditions and the sun directly illuminated the outcrop. For each scene, radiance data was obtained by applying appropriate gain and offset and conversion to reflectance, then an empirical line correction was applied based on the known reflectance of the Spectralon panels relative to their measured radiance spectrum. The latter were obtained as the mean radiance spectrum for a 20 × 20 pixel area over the panel (nominal pixel size of the acquired imagery = 5 cm). The empirical line method has the advantage of correcting for the influence of the atmosphere on the target radiance (Kurz et al. 2011, 2013; Murphy et al. 2015). In contemporaneous studies with the same camera (Lypaczewski and Rivard, 2018; Lypaczewski et al. 2019), the wavelength position of SWIR absorptions of a National Institute of Standards and Technology (NIST) referenced Mylar standard were accurate within 1 nm.

Following calibration of the spectral data to reflectance, bands with the poorest signal to noise (e.g., 930 to 991, 1295 to 1435, 1735 to 1998, and 2461 to 2508 nm) were removed from the ensuing analysis. The four images were then spatially co-registered using tie points, resulting in a single image for further analysis. Next, an iterative spatial spectral filter was used to compare the spectral similarity of spatially adjacent pixels within a 3 × 3 pixel window (Rogge et al. 2007, 2012; Rogge and Rivard, 2010). When the spectral signatures were within a predefined similarity threshold, an average spectrum was

substituted for the original data, thereby reducing the intra-class spectral variability. Lastly, areas in shadow and the calibration panels were masked.

Mineralogical and lithological information in the imagery was obtained by the extraction of endmember spectra and their distributions were mapped. To derive an image endmember set, spatial-spectral endmember extraction (SSEE) was used to divide the image into equal spatial subsets (each subset = 7 × 7 pixels; Rogge et al. 2007, 2012; Rogge and Rivard, 2010). This method is designed to discern spectrally similar endmembers that occupy different portions of the scene. The endmember set derived from SSEE was clustered and labelled to derive final endmember sets for mapping. For clustering, we used a tree cluster that recursively merges a pair of clusters based on a similarity measurement. To start, each endmember was treated as an individual cluster and endmembers that are most similar were successively merged. In this study, the Spectral Angle (SA) between two endmembers was used as the measure of similarity. A minimum SA threshold was defined to stop the merging process that took place when all pairwise clusters had a similarity greater than the threshold. To address the spectral variability of the extracted endmembers, the tree cluster tool was applied twice on the given data. The first time, using all endmembers, a SA threshold of 0.2 radians produced clusters that capture the broad material classes, namely non-geological (e.g., panels, vegetation, weathering) and geological. The next level of clustering focused on the geological class to capture subclasses and define multiple geological endmember clusters. In this case, a smaller SA threshold (0.05 radians) was used because these endmembers are more spectrally similar. Clustered endmembers were then averaged to obtain an individual endmember that represents the given class, contributing to an endmember set of thirteen geological endmembers. This clustering process was data-driven.

After accounting for the spectral similarity between classes, these thirteen endmembers were condensed into four groups (Fig. 4.2A, B): limestone (Lst), two groups of replacement dolomite (RDa, RDb), and saddle dolomite (SD). Groups were labelled

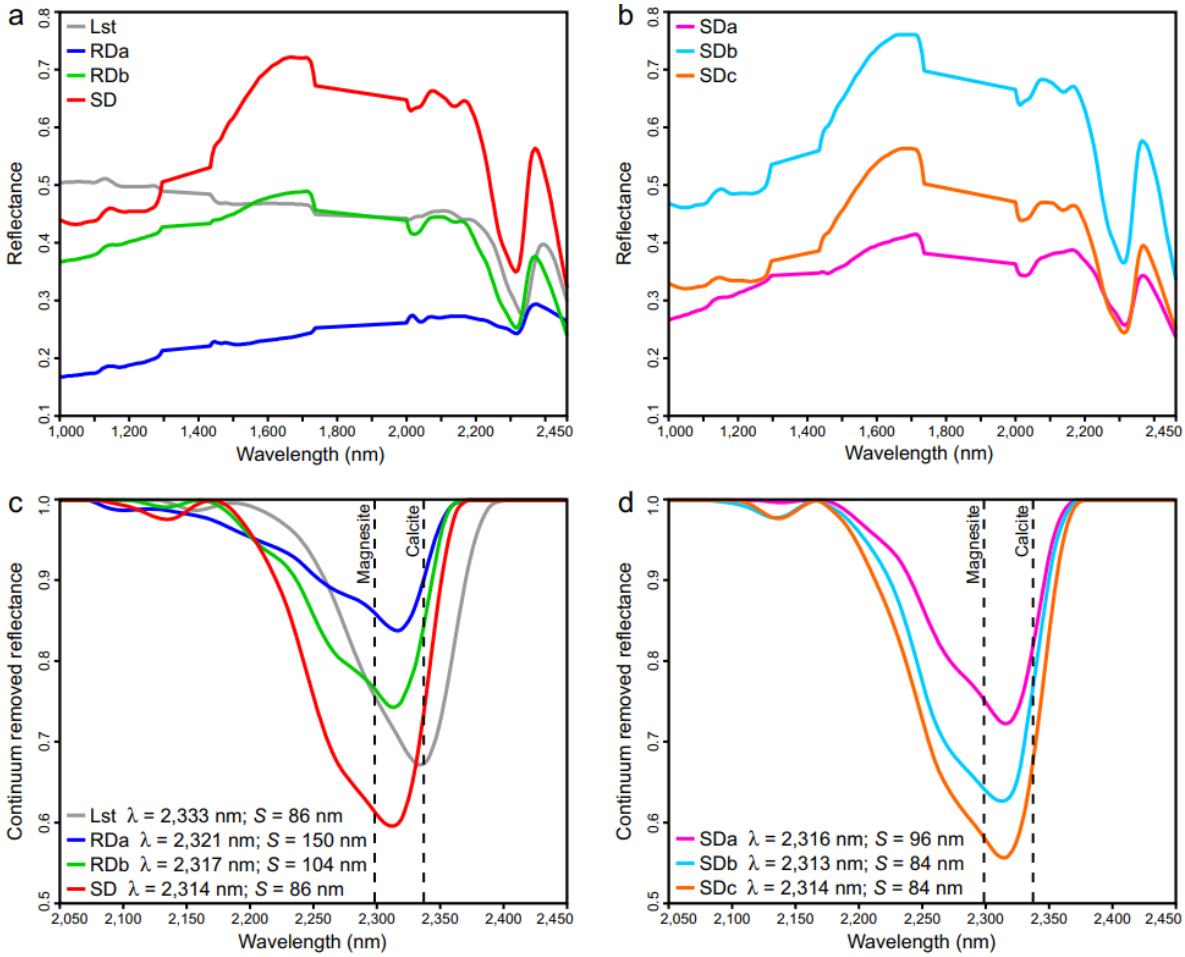

Figure 4.2. Reflectance spectra for **(A)** limestone (Lst), replacement dolomite a (RDa), replacement dolomite b (RDb), and saddle dolomite (SD). **(B)** Endmember SD consists of saddle dolomite a (SDa), saddle dolomite b (SDb), and saddle dolomite c (SDc). **(C)** Continuum removed reflectance for the ~2315 nm absorption-band showing Lst, RDa, RDb, and SD. **(D)** Continuum removed reflectance for the ~2315 nm absorption-band showing SDa, SDb, and SDc. Absorption-band positions (λ) were calculated using the linear interpolation method of van der Meer (2004; his Fig. 2). Absorption-band asymmetry (S) is calculated as A – B, where A is the width from the short-wavelength shoulder to the absorption-band position and B is the width from absorption-band position to the long-wavelength shoulder (van der Meer, 2004).

based on spectral interpretations that were supported by field and petrographical observations. Group Lst was defined by all pixels with a carbonate absorption-band position > 2330 nm and was validated in the field using dilute hydrochloric acid. Group RDa includes the spectral endmembers that correspond to light- and medium- grey replacement dolomite. Endmembers that corresponded to clasts, bedding, and bedding-parallel fractures within the RDa intervals were also included. Group RDb includes the endmembers that correspond to light-brown replacement dolomite and the alteration rims

along the margins of the saddle dolomite intervals. Group SD includes three subgroups (SDa, SDb, SDc), labelled based on their paragenesis, that correspond to white, coarsely crystalline, saddle dolomite. Their paragenesis was determined by the relative positions of each endmember in macro-pores that were validated by petrographical analyses.

4.4.2. Distribution maps of the spectral endmembers

Mapping of the endmember spectra resulted in two image products. The first examined the distributions of limestone (Lst), replacement dolomite (RDa, RDb), and saddle dolomite (SD) and is suited for a synoptic view of the outcrop. The second, more detailed image product, examined the distribution of the saddle dolomite subgroups (SDa, SDb, SDc). In both instances, mapping the distribution of each endmember was conducted using a spectral angle mapper (SAM) algorithm that treats spectra as multidimensional vectors and computes the angle between spectral pairs (Kruse et al. 1993). For this purpose, the spectrum from each pixel of the image after processing was compared to that of each endmember. Spectra with the smallest SAM angles indicate the greatest similarity. In the first image product, the SAM results for RDa, RDb, and SD are presented as a red-green-blue composite where a higher color hue corresponds to a higher spectral similarity to the given endmember. If two or more of the endmembers predominate within a given pixel, then a color other than RGB is seen. In the second image product, the SAM results for SDa, SDb and SDc are classified in such a way that the endmember of highest similarity to that of the given pixel is assigned to that pixel. Consequently, only the colors that were assigned to the endmembers are seen in the second image product and when the SAM angle exceeds 5 degrees the pixel is not classified.

4.4.3. Sampling, petrography, and geochemical analyses

Fieldwork and sampling were conducted over two field seasons. Prior to obtaining the hyperspectral reflectance data, Stacey et al. (2021) collected 72 samples from the Cathedral Formation in the Whirlpool Point area; 35 of these samples were systematically taken from

the roadcut at ~2 m intervals along a 62 m logged section. After processing the hyperspectral data, an additional 33 samples were taken from the roadcut to support the analysis of the reflectance data and to evaluate specific features and trends within the mineral distribution maps. Samples were impregnated with blue epoxy and prepared as polished sections that were partially stained with alizarin red-S and potassium ferricyanide (Dickson, 1965). Polished sections were examined under plane- and cross-polarized light and then analysed using a CITL Mk5 cold cathodoluminescence (CL) system (operating conditions = 15 to 20 kV and 350 to 450 μA) that is mounted on a Nikon Eclipse LV100N POL microscope. Dolomite crystal textures are described according to Sibley and Gregg (1987).

Thirty-eight representative samples from endmembers RDa, RDb, and SD were analysed for mineralogical composition by powder X-ray diffraction (XRD) using a Bruker D8 Advance diffractometer. Silicon was added as a standard and samples were scanned at 40 kV and 30 mA from 5° to 70° 2θ in 0.02° increments. %Ca is calculated based on Lumsden (1979) and degree of ordering is based on Goldsmith and Graf (1958). Two polished mounts that included each of the SD subgroups (SDa, SDb, SDc) were analysed by quantitative evaluation of minerals by scanning electron microscopy (QEMSCAN) and energy-dispersive X-ray (EDX) spectroscopy using an FEI Aspex eXstreme equipped with Bruker 5030 EDX detectors and an iExplorer software suite. An initial 10 × 10 mm mineral map was created for each sample at a stepping interval of 50 μm and 4 × 4 mm areas of interest were mapped at a stepping interval of 4 μm. An X-ray spectrum was generated for each point, matched against a standard library, and the map was created by assigning the library mineral to each point.

Twenty-four representative samples from endmembers RDa, RDb, and SD were analysed for trace elements by inductively coupled plasma mass spectrometry (ICP-MS) using an Agilent 7700× at the Advanced Isotope Geochemistry and Cosmochemistry Suite, The University of Manchester. Two polished sections that included each of the SD

subgroups (SDa, SDb, SDc) were analysed by electron probe micro-analysis (EPMA) using a Cameca SX100 at The University of Manchester. An initial 2 × 10 mm map was created at a stepping interval of 10 μm and 1.536 × 1.536 mm areas of interest were mapped at a stepping interval of 3 μm. Ca (Kα; PET) and Mg (Kα; TAP) were analysed at 15 kV, 10 nA, and a dwell time of 100 ms using calcite ($CaCO_3$) and magnesite ($MgCO_3$) as standards, whereas Fe (Kα; LLIF) and Mn (Kα; LLIF) were analysed at 15 kV, 200 nA, and a dwell time of 200 ms using fayalite (Fe_2SiO_4) and tephroite (Mn_2SiO_4) as standards.

4.5. Results

4.5.1. SWIR hyperspectral imaging

Each of the endmembers can be discerned based on their absorption-band positions and spectral contrast (the difference between the peaks and the valleys in the spectrum). Phase Lst presents an absorption-band position of 2333 nm, akin to calcite and unique among all endmembers. RDa, RDb, and SD have absorption-band positions of 2321, 2317, and 2314 nm, respectively, and display increasing spectral contrast (Fig. 4.2C). Phase SD includes SDa, SDb, and SDc that have absorption-band positions of 2316, 2313, and 2314 nm, respectively, and display increasing spectral contrast (Fig. 4.2D). The absorption-band asymmetry for Lst, RDa, RDb, and SD are 86, 150, 104, and 86 nm, respectively (Fig. 4.2C) and the asymmetry for SDa, SDb, and SDc are 96, 84, and 84 nm, respectively (Fig. 4.2D).

At the margin of the fault-controlled dolomite body, a sharp, bedding-parallel contact occurs between Lst, RDa, and RDb (Fig. 4.3A, B). Scattered RDa pixels are located below the limestone-dolomite contact but RDb and SD are absent. Phase Lst is absent above this contact and throughout the remainder of the hanging-wall and the footwall. The distal parts of the hanging-wall comprise a mixture of RDa and RDb, the contacts between which follow the bedding (Fig. 4.3B, C). Phase SD is rare in the distal parts of the hanging-wall and is typically restricted to isolated beds of bioturbated wackestone. The spatial

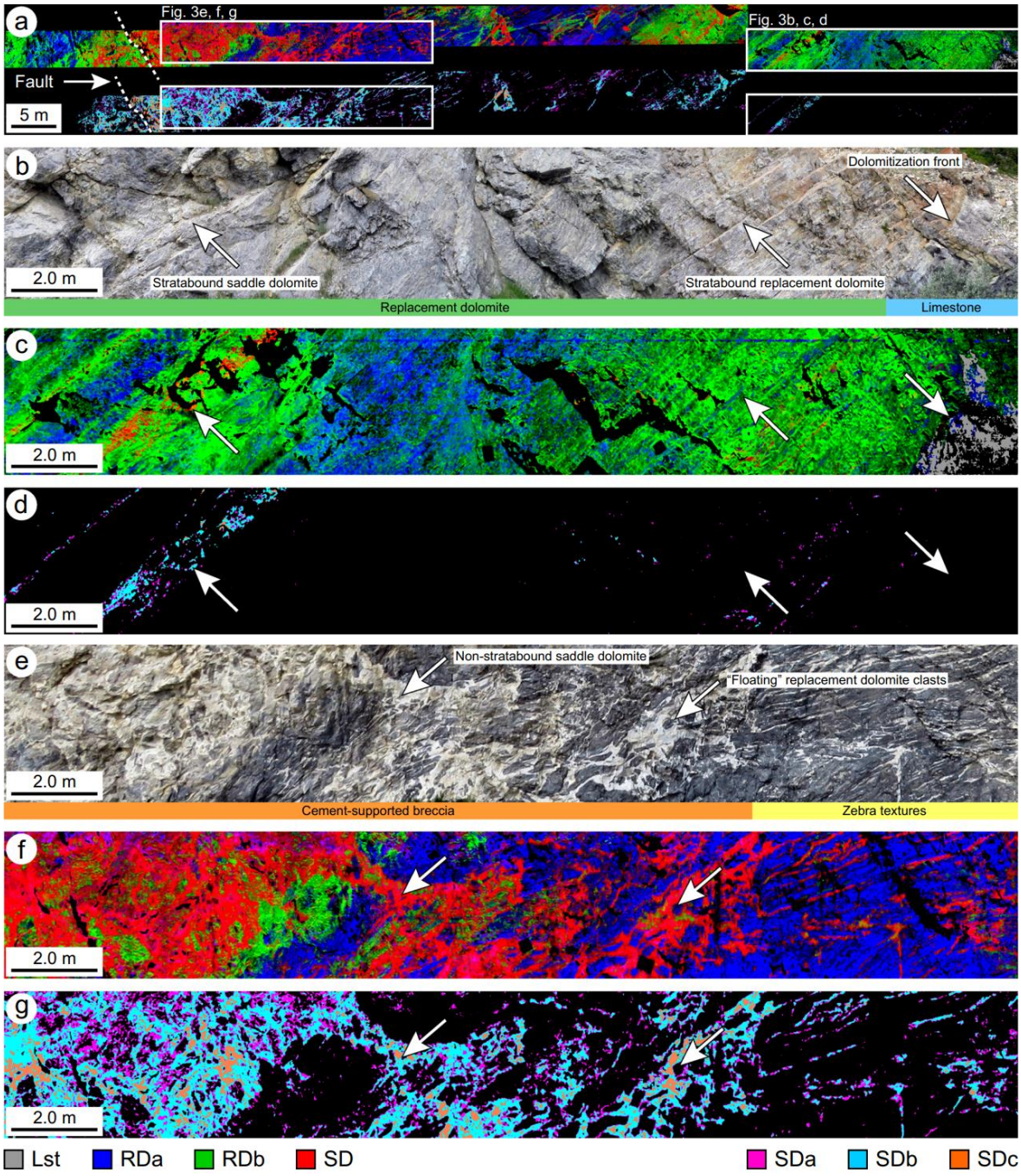

Figure 4.3. Endmember mineral distribution maps of the Cathedral Formation at Whirlpool Point showing **(A)** an overview of the acquired imagery illustrating the spatial distributions of each diagenetic phase (upper panels show Lst, RDa, RDb, and SD; lower panels show SDa, SDb, and SDc). Lst was mapped by retaining all pixels with a carbonate absorption-band position >2330 nm. **(B)** The distal part of the fault-controlled dolomite body (white box in A) showing the abundant stratabound dolomite at the dolomitization front (limestone-dolomite contact) accompanied by **(C)** the corresponding Lst, RDa, RDb, and SD mineral distribution map, as well as **(D)** the SDa, SDb, and SDc mineral distribution map. **(E)** The proximal part of the fault-controlled dolomite body (white box in A) showing the abundant non-stratabound dolomite, cement-supported breccias, and zebra textures accompanied by **(F)** the corresponding Lst, RDa, RDb, and SD mineral map, as well as **(G)** the SDa, SDb, and SDc mineral map.

distribution of RDb pixels correlate with the occurrence of SD pixels, whereas RDa pixels are typically not in contact with SD pixels (Fig. 4.3B, C). This isolated SD bed illustrates the paragenetic sequence of each of the constituent SD phases. SDa lines the margins of the SD intervals and is post-dated by SDb. SDc is rare, but this phase is located at the centers of the SD intervals (Fig. 4.3B, D).

At the core of the dolomite body, the hanging-wall largely comprises cement-supported breccias and zebra textures (Fig. 4.3E). Consequently, phase SD is more abundant at the core of the dolomite body relative to at the margins. Isolated clasts of RDa and RDb are suspended and fully surrounded by SD (Fig. 4.3E, F). Typically, RDb pixels are located adjacent to SD pixels, but contacts between RDa and SD are locally common (Fig. 4.3E, F). The spatial distributions of the constituent phases of SD correlate with fault proximity. SDa and SDb are located throughout the hanging-wall but increase in abundance towards the core of the dolomite body (Fig. 4.3E, G). SDc post-dates these phases and is located at the centers of macro-pores such as breccias, fractures, zebra textures, and bedding planes. SDc increases in abundance towards the fault (Fig. 4.3E, G).

4.5.2. Petrography

Petrographical analysis of samples from the Cathedral Formation identified several diagenetic phases based on their crystal size, texture, fluid inclusions, CL properties, and mineral associations (Table 4.1). In addition to the host limestone, two phases of RD and three phases of SD were identified. RDa includes finely-crystalline (20 to 150 μm), planar-e to planar-s dolomite with dull-purple luminescent cores and bright-orange to dull-red luminescent rims (Fig. 4.4A, B). RDb includes medium-crystalline (100 to 400 μm), planar-s to non-planar-a dolomite with dull-red luminescent cores and dull- to moderate-red luminescent rims (Fig. 4.4A, B). The crystal size distribution in RDa has a normal distribution with a mode of 84 μm, a mean of 86 μm, and a standard deviation (±) of 24 μm (Fig. 4.4C). The crystal size distribution in RDb is broader than RDa and has a slight

Diagenetic phase		Crystal size (μm)	Texture	Inclusions	CL	Other features
Matrix calcite (host limestone)	Lst	~25	Blocky	Turbid	Unzoned, mottled dark-purple to dull-orange	Detrital quartz, clay minerals, organic matter, and pyrite common
Replacement dolomite (RD)	RDa	20–150, mean = 86	Planar-e to planar-s	Turbid	Concentric zoning, dull-purple cores, bright-orange to dull-red rims	Fabric-retentive. Detrital quartz, clay minerals, organic matter, and pyrite locally common
	RDb	100–400, mean = 267	Planar-s to nonplanar-a	Limpid, rare inclusions	Weak blotchy zoning, dull-red cores, dull-red to moderate-red rims	Fabric-destructive. Locally associated with stylolites. Detrital quartz, clay minerals, and organic matter rare
Saddle dolomite (SD)	SDa	250–550, mean = 400	Nonplanar (saddle)	Limpid, rare inclusions	Unzoned, dull-red to medium-red	Fabric-destructive. Form syntaxial layers on RDb. Detrital quartz and clay minerals rare
	SDb	250–2500 wide, up to 4500 long, mean = 2000	Nonplanar (saddle)	Limpid	Unzoned, dull-red to medium-red	Breccia and fracture fill. Elongate crystals normal to cavity walls, crystal size increases to center
	SDc	250–1250 thick rims, crystals up to 4500, mean = 2000	Nonplanar (saddle)	Limpid	Oscillatory zoning, dull-red to bright-red, dull-orange to bright-orange	Breccia and fracture fill. Commonly form rims nucleated on SDb. Associated with Pb–Zn-Fe–Mn-Cu sulphides/oxides

Table 4.1. Summary table of the microscopic features of the diagenetic phases in the Cathedral Formation at Whirlpool Point, southern Rocky Mountains based on transmitted light, cathodoluminescence (CL), and scanning electron microscopy (SEM).

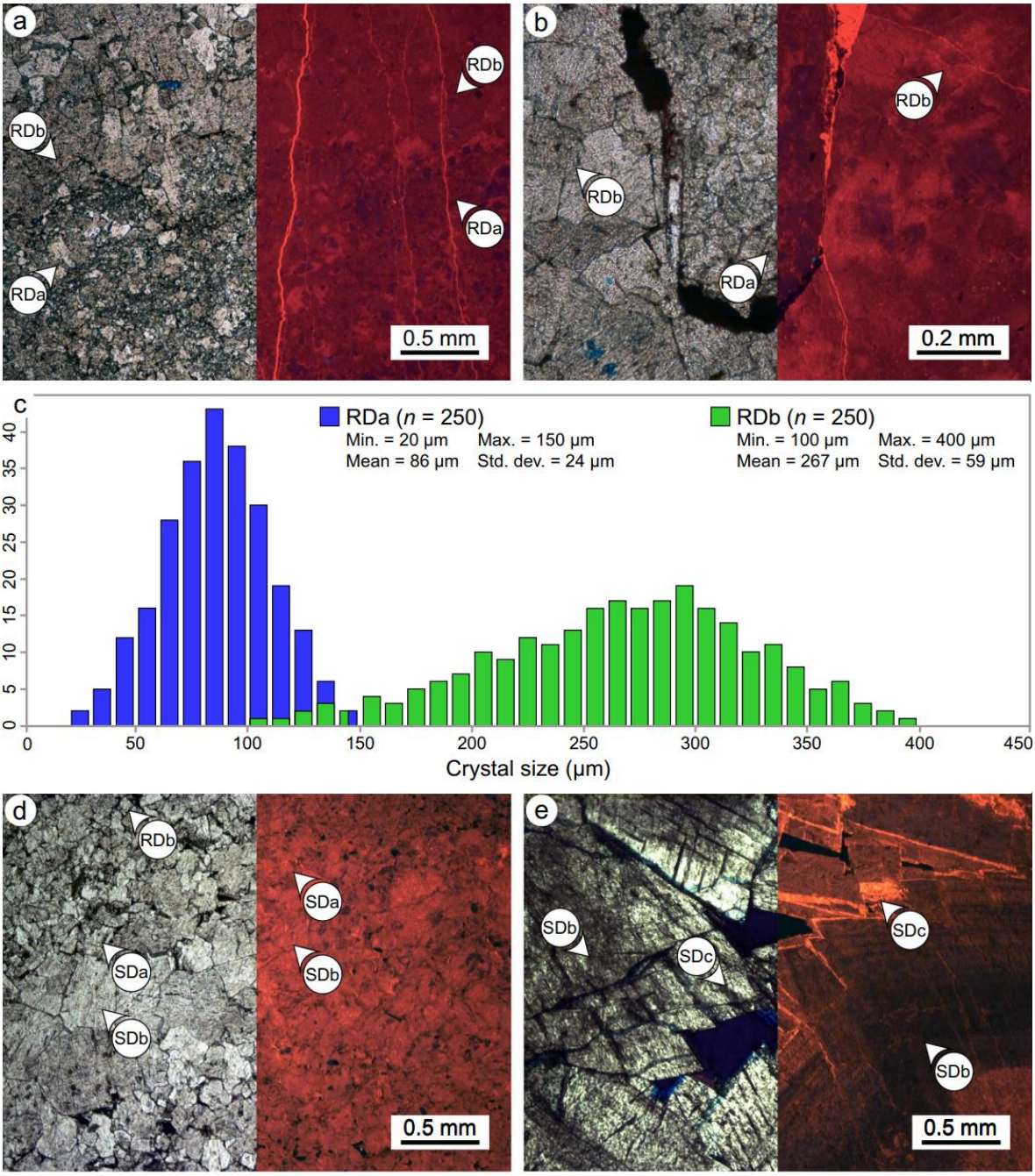

Figure 4.4. Transmitted light (PPL; left) and cathodoluminescence (CL; right) photomicrographs of the replacement dolomite (RD) and saddle dolomite (SD) phases in the Cathedral Formation. **(A)** The contact between RDa and RDb showing their respective microscopic features. **(B)** RDa and RDb located above and below a bedding-parallel stylolite, respectively. **(C)** Crystal size histogram for RDa and RDb showing their mean crystal size, range, and standard deviation. Note that the histogram for RDb has a negative skew (–0.3). **(D)** Bedding-parallel zebra texture showing the gradational increase in crystal size between SDa and SDb and their respective microscopic features. Note that SDa and SDb have similar CL signatures. **(E)** SDc, which commonly form rims nucleated on SDb, comprises alternating zones of dull-red to bright-red luminescent dolomite.

negative skew (–0.3). The modal crystal size of RDb is 284 μm with a mean of 267 μm (± 59 μm; Fig. 4.4C). RDa includes trace clay minerals, detrital quartz, organic matter, and pyrite that are rare in RDb. Phase SD consists of three separate phases of non-planar (saddle) dolomite that have different petrographical characteristics (Table 4.1).

SDa includes medium-crystalline (250 to 550 μm), non-planar dolomite that typically grew syntaxially on RDb (Fig. 4.4D). SDb includes coarsely-crystalline (up to 4500 μm), non-planar dolomite crystals that are abundant in cement-supported breccias, zebra textures, and fractures (Fig. 4.4D, E). SDb crystals are elongate, oriented normal to the cavity wall, and are polymodal in size depending on the size of the cavity in which they were precipitated. SDa and SDb are unzoned with a dull- to medium-red luminescence. SDc includes coarsely-crystalline, non-planar dolomite that are largely indistinguishable from SDb based on their textural properties. SDc crystals, however, have a characteristic dull- to bright-red and dull- to bright-orange oscillatory zonation (Fig. 4.4E). SDc typically form rims (250 to 1250 μm thick) that are nucleated on SDb crystals in zebra textures and fractures. Individual SDc crystals (up to 4500 μm) are common in the central parts of cement-supported breccias.

4.5.3. Geochemistry

Overall, QEMSCAN indicates that the RD phases comprise 97.87% dolomite, 1.67% clay minerals (trace illite) and muscovite, 0.41% quartz, 0.02% calcite, 0.01% pyrite, and 0.02% other minerals (Fig. 4.5A, B). In contrast, phase SD comprises 99.91% dolomite, 0.06% clay minerals and muscovite, 0.02% pyrite, and 0.01% calcite (Fig. 4.5A, C). Although RDb and SDa are clearly discernible in outcrop and in hand-samples due to their color and crystallinity, EDX spectroscopy indicates that there is minimal contrast in the abundances of Ca, Mg, and Fe between these phases (Fig. 4.5D, E, F). In contrast, SDb and SDc cannot be confidently distinguished in outcrop and in hand-samples, but they are clearly distinguished by their composition (Fig. 4.5G, H, I).

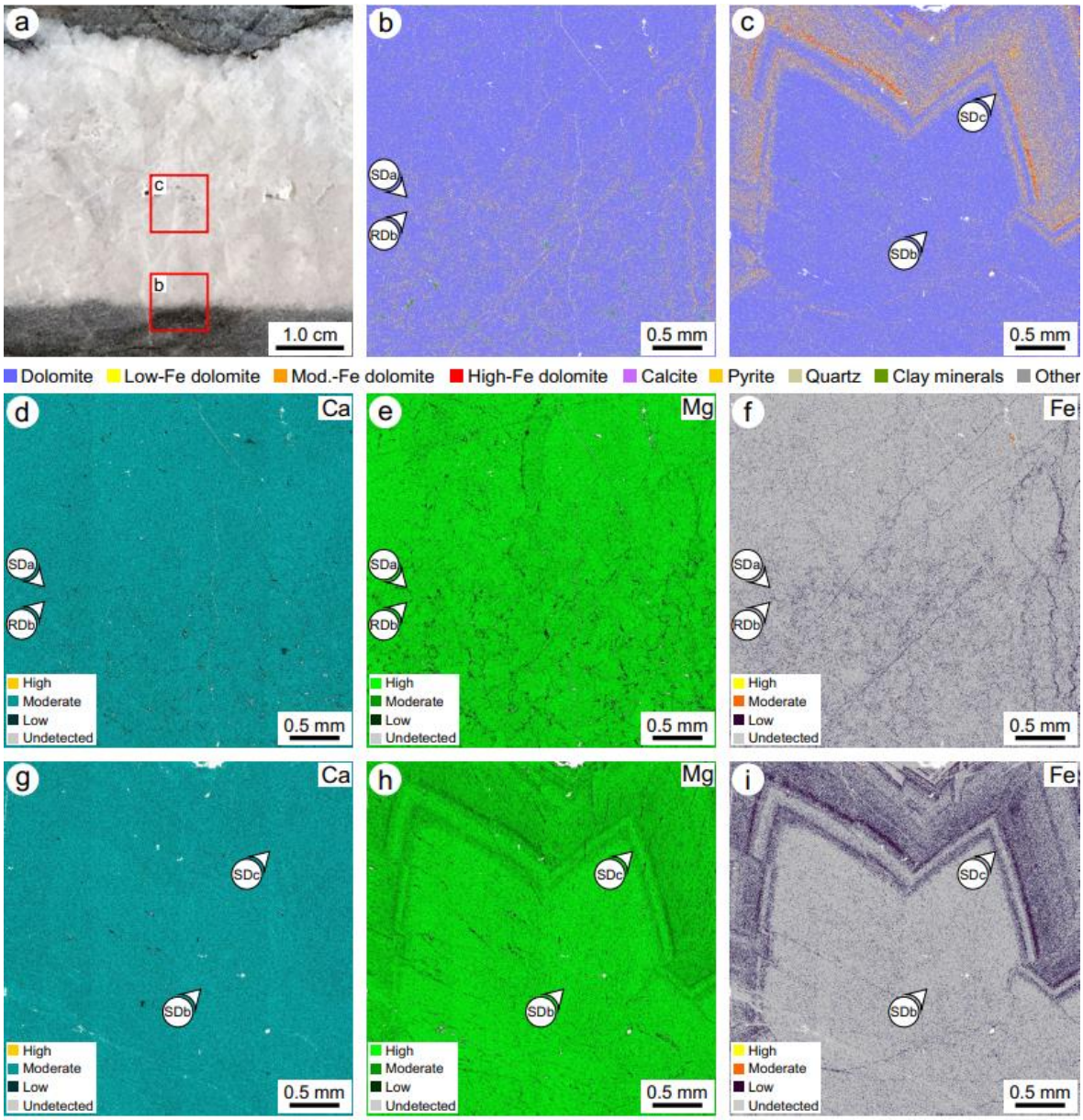

Figure 4.5. (A) Photograph of a sample from the Cathedral Formation showing the locations of the quantitative evaluation of minerals by scanning electron microscopy (QEMSCAN) and energy-dispersive X-ray (EDX) spectroscopy images. **(B)** QEMSCAN image showing the contact between RDb and SDa. **(C)** QEMSCAN image showing the contact between SDb and SDc. **(D, E, F)** EDX spectroscopy images showing the relative abundances of Ca, Mg, and Fe across the contact between RDb and SDa. **(G, H, I)** EDX spectroscopy images showing the relative abundances of Ca, Mg, and Fe across the contact between SDb and SDc. Stepping interval = 4.0 μm.

Each of the RD phases are stoichiometric with %Ca = 50.21 (± 0.471) and 49.79 (± 0.404) for RDa and RDb, respectively (Table 4.2). Phase SD has %Ca = 49.65 (± 0.540), however, the range (48.8 to 50.6%Ca) and standard deviation are markedly higher relative to each of the RD phases. Dolomite ordering increases from RDa (0.920 ± 0.088) to RDb (1.00 ± 0.232). [Sr] decreases from RDa (171 ± 168 ppm) to RDb (18.1 ± 6.70 ppm). [Fe]

Phase	X-ray diffraction (XRD)	Inductively coupled plasma mass spectrometry (ICP-MS)		
	%Ca	Sr (ppm)	Fe (ppm)	Mn (ppm)
Replacement dolomite a (RDa)	*XRD (n = 9)*			*ICP-MS (n = 5)*
Min	49.27	24.7	958.0	38.6
Mean	50.21	171.3	2,407.1	182.7
Max	50.72	377.7	6,057.1	546.5
SD	0.471	167.8	2,097.6	212.7
Replacement dolomite b (RDb)	*XRD (n = 12)*			*ICP-MS (n = 13)*
Min	49.12	11.3	1444.5	101.4
Mean	49.79	18.1	4907.1	340.4
Max	50.30	37.5	11,006.0	813.3
SD	0.404	6.7	3649.7	218.3
Saddle dolomite (SD)	*XRD (n = 17)*			*ICP-MS (n = 6)*
Min	48.79	11.5	2026.1	183.6
Mean	49.65	20.2	7571.8	552.9
Max	50.57	26.8	12,290.0	813.6
SD	0.540	5.8	4272.9	278.4
	Electron probe microanalysis (EPMA)			
Phase	Ca (wt%)	Mg (wt%)	Fe (ppm)	Mn (ppm)
Saddle dolomite a (SDa)	*Mean %Ca = 49.92*			
Min	15.92	8.42	0	0
Mean	21.07	12.82	2170	290
Max	26.22	16.46	4910	630
SD	2.209	1.751	1420	140
Saddle dolomite b (SDb)	*Mean %Ca = 49.67*			
Min	16.13	8.85	0	0
Mean	21.06	12.94	3310	380
Max	25.99	17.03	5040	710
SD	2.202	1.744	1590	180
Saddle dolomite c (SDc)	*Mean %Ca = 50.53*			
Min	14.77	7.53	0	0
Mean	20.45	12.14	12,130	1190
Max	26.13	16.75	36,740	2030
SD	2.261	1.822	2030	660

Table 4.2. Major and trace element concentrations of the diagenetic phases in the Cathedral Formation at Whirlpool Point, southern Rocky Mountains. %Ca = molar Ca / (Ca+Mg).

increases from RDa (2410 ± 2100 ppm), to RDb (4910 ± 3650 ppm), to SD (7570 ± 4270 ppm) and the [Mn] correlates with the [Fe] in each of these phases of dolomite (Table 4.2).

Each of the constituent phases of SD were further analysed by EPMA (Table 4.2). SDa has %Ca = 49.92, SDb has %Ca = 49.67, and SDc has %Ca = 50.53. SDa has similar [Fe] (2170 ± 1420 ppm) and [Mn] (290 ± 140 ppm) relative to SDb ([Fe] = 3310 ± 1590 ppm; [Mn] 380 ± 180 ppm). SDc is markedly enriched in [Fe] (12100 ± 2030 ppm) and [Mn] (1190 ± 660 ppm) relative to each of the RD and the other SD phases (Table 4.2).

4.6. Interpretations

4.6.1. Paragenesis of the Cathedral Formation at Whirlpool Point

Petrographical observations, compositional changes, and hyperspectral imaging were used to establish the paragenesis of the Cathedral Formation. Stacey et al. (2021) documented micritized grains, post-dated by a blocky calcite cement that is consistent with cementation at or below the seafloor. Cross-cutting relationships between RDa and RDb are absent, but RDb is interpreted to have formed by the recrystallization of RDa due to (1) increasing crystal size, (2) decreasing %Ca, (3) decreasing [Sr], and (4) increasing [Fe + Mn] (Table 4.1, 4.2). Recrystallization is associated with a change from planar-e to planar-s dolomite in RDa to planar-s to non-planar-a dolomite in RDb (Fig. 4.4A, B). Given that RDa and RDb are cross-cut by low-amplitude, bedding-parallel stylolites, replacement dolomitization is interpreted to have occurred during shallow burial (cf. Martín-Martín et al. 2018; Stacey et al. 2021).

Saddle dolomite (SD) grows within pores in RDa and RDb and, therefore, post-dates them. SDa is consistently located at the margins of these pores and is overgrown and postdated by SDb (Fig. 4.4D). In thin-section, SDa forms a syntaxial rim that is in optical continuity with RDb; a common feature of cavity-filling cements with the same mineralogy as the cavity-wall (Vandeginste et al. 2005). SDa and SDb have similar compositions, gradational contacts, and were likely derived from a similar fluid-flow

event. SDb crystals are an order of magnitude larger than SDa (Table 4.1) due to competitive crystallization; a process by which favourably-oriented crystals obstruct the growth of poorly-oriented crystals (Wallace and Hood, 2018). Although SDc is not present throughout the outcrop, it consistently nucleates on and, thus, postdates SDb. SDc is restricted to the central parts of vugs, fractures, zebra textures, and cementsupported breccias (Fig. 4.3).

4.6.2. Spatial distribution of each diagenetic phase

Dolomitization fronts in the Cathedral Formation and the underlying Mount Whyte Formation at Whirlpool Point are interpreted to have "retreated" over time due to the occlusion of porosity from repeated fluid-pulses (Koeshidayatullah et al. 2020a, 2020b, 2021; Stacey et al. 2021). In this model, the core of the dolomite body is younger than the margins; with each successive fluid-pulse contributing to the recrystallization of earlier phases during the cementation of the dolomite body (Koeshidayatullah et al. 2020a, 2020b, 2021; Stacey et al. 2021). This retreating dolomitization front is associated with increased dolomite stoichiometry and ordering towards the core of the dolomite body (Koeshidayatullah et al. 2020b). The cement-supported breccias and associated zebra textures that were imaged in this study are largely restricted to the core of the dolomite body, and are interpreted to have formed as a final event when the occlusion of porosity gave rise to high pore-fluid pressures and the rupturing of the formation during seismic valving (Stacey et al. 2021).

The mineral distribution maps, derived from the hyperspectral data, reveal outcrop-scale heterogeneities that provide evidence of how fault-controlled dolomitization in the Cathedral Formation progressed and terminated. Each paragenetic stage increases in abundance from the margin of the dolomite body to the core and their spectral signatures indicate that the %Ca decreases between each phase (Fig. 4.6). At the margin, the dolomitization front (contact between Lst and RDa) is sharp and bed-parallel (Fig. 4.3B,

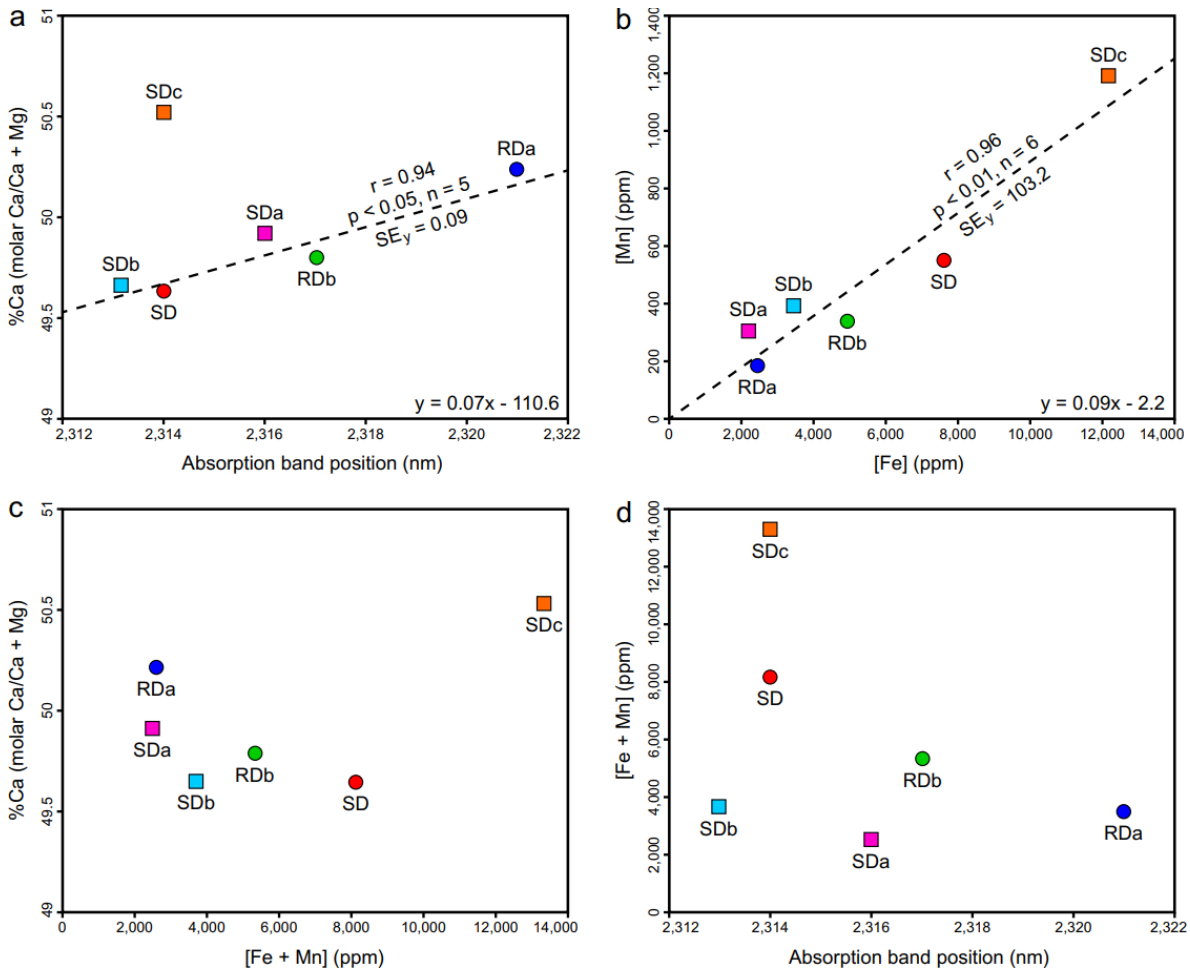

Figure 4.6. Scatterplots showing the relationships between: **(A)** %Ca versus the position of the ~2315 nm absorption-band, **(B)** the [Mn] versus the [Fe], **(C)** %Ca versus the [Mn + Fe], and **(D)** the [Mn + Fe] versus the position of the ~2315 nm absorption-band. r = correlation coefcient. SE_y=standard error of the y-estimate. Note that the r and SE_y for Fig. 4.6A omit phase SDc.

C). RDa grades laterally to RDb and the phases have a patchy distribution throughout the outcrop. Bedding planes can be identified by the distribution of RDa and RDb (Fig. 4.3B, C), which suggests that that they acted as permeability pathways that circulated the initial dolomitizing fluids during replacement dolomitization (Budd and Park, 2018). RDb has a pronounced spatial relationship to SD, which suggests that recrystallization occurred during the later fluid-pulses that also precipitated SD (Fig. 4.3). Consequently, there are textural changes from the nonstoichiometric RDa (concentrically zoned, poorly-ordered, planar-e to planar-s dolomite) that is present at the margins of the dolomite body to the more stoichiometric RDb (weakly zoned, well-ordered, planar-s to nonplanar-a dolomite) that is present at the core.

SD is present throughout the dolomite body, but it is more abundant at the core relative to at the margins and in the hanging-wall of the fault relative to in the footwall (Fig. 4.3A). Each of the constituent phases of SD, which are indistinguishable in visible light, also increase in abundance from the margin of the dolomite body to the core (Fig. 4.3A). SDa occurs as isolated pixels in RDa and RDb, and lines the margins of vugs, zebra textures, and cement-supported breccias (Fig. 4.3D, G). SDb has a gradational contact with SDa and is restricted to the central parts of these rock textures. Finally, SDc precipitated in macro-pores that were proximal to the fault (Fig. 4.3G), but occasionally occurs along fractures, stylolites, and bedding planes that were likely the few remaining permeability pathways after brecciation and cementation (Martín-Martín et al. 2018). Consequently, the back-stepping and paragenesis of the SD subgroups could only be resolved using hyperspectral imaging because the endmembers are indistinguishable at the outcrop-scale and thin-sections are at too small a scale to capture their spatial distributions.

4.6.3. Compositional characteristics derived from the reflectance spectra

The position of the 2315 to 2335 nm absorption-band is commonly used to differentiate dolomite from calcite in the laboratory (Hunt and Salisbury, 1971; Gaffey, 1986) and in remotely-sensed imagery (van der Meer, 1996; Beckert et al. 2018; Beirami and Tangestani, 2020). Van der Meer (1995) suggested that this absorption-band has a linear relationship with the degree of dolomitization and Zaini et al. (2012, 2014) applied this approach to track the band positions of synthetic mixtures of calcite and dolomite. This method, however, has not been used to infer the %Ca of multiple phases of dolomite with varying compositions. RDa is the most calcium-rich phase of dolomite identified in the Cathedral Formation (%Ca = 50.21; Table 4.2) and has an absorption-band positioned at the longest wavelength (λ = 2321 nm; Fig. 4.2C). In contrast, SDb is the most magnesium-rich phase (%Ca = 49.67; Table 4.2), with an absorption-band positioned at the shortest wavelength (λ = 2313 nm; Fig. 4.2D). Excluding SDc, the phases with intermediate

compositions plot along a linear trendline with a slope of 0.07%Ca/nm and a correlation coefficient (r) of 0.94, $p < 0.05$, $n = 5$ (Fig. 4.6A).

SDc deviates from this trend because it includes substantial trace element substitution for Mg ([Fe + Mn] = 13320 ppm; Fig. 4.6B, C). Increased [Fe + Mn], each with a mass greater than Ca and a radius between Mg and Ca, shift the carbonate absorption-bands to longer wavelengths (Gaffey, 1986; Green and Schodlok, 2016). The [Fe + Mn], however, has a poor correlation ($r = 0.50$, $p > 0.05$, $n = 6$) with the position of the ~2315 nm absorption-band of each of the dolomite phases in the Cathedral Formation (Fig. 4.6D). In the laboratory, Gaffey (1986) documented a broad Fe^{2+} absorption-band at 1200 nm and Mn^{2+} bands from 300 to 800 nm, but these features are difficult to identify in the field due to spectral range limitations of the equipment (Kurz et al. 2012). Strontium, which substitutes for Ca in dolomite (Vahrenkamp and Swart, 1990), reveals the recrystallization pathway from RDa (%Ca = 50.21; [Sr] = 171.3 ppm) to RDb (%Ca = 49.79; [Sr] = 18.1 ppm). The effect of [Sr] on the position of the ~2315 nm absorption-band, however, has not been systematically investigated in dolomite and is equivocal (Gaffey, 1987).

Although each of the RD and SD phases are >97% dolomite, the asymmetry of the ~2315 nm absorption-band generally relates to the volume of non-carbonate grains identified in thin-section. RDa ($S = 150$ nm) and RDb ($S = 104$ nm) include trace clay minerals and detrital quartz that are absent in each SD phase ($S = 84$ to 96 nm). QEMSCAN indicates that RD includes 1.67% clay minerals and muscovite, whereas they are negligible in SD (Fig. 4.5B, C). Clay minerals in RD reflect the composition of the precursor limestone, whereas their absence in SD is consistent with it being precipitated as a void-filling cement. A muscovite absorption feature at ~2200 nm could not be distinguished, and it is unclear if non-carbonate minerals affect the absorption-band asymmetry of each phase.

4.6.4. Influence of textural characteristics on the reflectance spectra

Several laboratory-based studies have demonstrated that the textural properties of minerals and rocks impact the surface scattering and volume scattering of light (Crowley, 1986; Gaffey, 1986; van der Meer, 1995; Zaini et al. 2014). Gaffey (1986) and Zaini et al. (2012), for example, studied the reflectance of powdered carbonate minerals that were sieved to various sizes, typically <500 μm, and showed that finer powders have a higher overall reflectance with shallower absorption features, whereas coarser powders have a lower overall reflectance with deeper absorption features. The degree of compaction in rocks relative to powders, as well as porosity occlusion, can minimize these differences and it is not always possible to infer the grain or crystal size of rocks from their spectra.

In the Cathedral Formation, the endmembers present three broad groups based on their spectral contrast (Fig. 4.2). RDa, with a mean crystal size of 86 μm, has the lowest overall reflectance and absorption-band depths (Fig. 4.2A, C). Organic matter (OM), which reduces the reflectance of a sample and attenuates its absorption bands (van der Meer, 1995), is locally common in RDa and rare in RDb (Fig. 4.3A, B). Consequently, the presence of OM in RDa may contribute to its low overall reflectance. RDb and SDa (mean crystal size = 267 μm and 400 μm, respectively) have similar overall reflectance and absorption-band depths (Fig. 4.2). These phases are more coarsely crystalline than RDa and their spectral contrasts are intermediate between RDa and the remaining SD phases. SDb and SDc have the largest crystals (mean size = 2000 μm), roughly five times larger than SDa, and they display the highest overall reflectance and absorption-band depths (Fig. 4.2B, D). In this case, it is likely that the specular reflectance from crystal facets dominates over volume scattering, thus, explaining their high reflectance (van Ginneken et al. 1998).

4.7. Discussion

The results of this work demonstrate that hyperspectral imaging is an invaluable tool that reveals mineralogy, composition, and texture in carbonate sedimentary rocks at a

macro-scale. Nevertheless, care must be taken to consider the scale of observation, or spatial resolution, because each imaged pixel comprises several phases that contribute to the reflectance (Woodcock and Strahler, 1987; van der Meer, 2012). The diagenetic phases that are present in the Cathedral Formation, for example, comprise crystals that are below the image resolution (5 cm). Although each of the phases of dolomite are monomineralic, they are represented by an endmember because they are compositionally and texturally distinct. RDa and RDb co-exist in samples at the thin-section scale and their spectral signatures are, therefore, a linear average of their relative surface abundances. For this reason, applying the laboratory-based spectra of a single dolomite endmember to our field-based imagery would not have captured the compositional and textural diversity that is present at the outcrop-scale without petrographical and geochemical calibration. Similarly, Beckert et al. (2018) cautioned against the over-reliance on published spectral libraries, which are based on pure, end-member, minerals (i.e., stoichiometric well-ordered dolomite), to discriminate carbonate sedimentary rocks in the field. Given that most sedimentary dolomite is nonstoichiometric with 48.0 to 62.5%Ca (Lumsden, 1979; Jones et al. 2001), consists of different crystal shapes and boundaries (Sibley and Gregg, 1987), and includes different volumes of substituted trace elements, the application of a single dolomite endmember to field- or satellite-based imagery without calibration should be treated with caution.

Initial observations of the Cathedral Formation suggests that the succession comprises only limestone, a single phase of RD, and a single phase of SD. Detailed petrographical and geochemical analyses (Stacey et al. 2021), however, revealed that the succession includes several diagenetic phases. Accordingly, this study examined the extent to which hyperspectral imaging can be used to map multiple phases of dolomite at the outcrop-scale and to determine their cross-cutting relationships; features that have traditionally only been revealed petrographically. The method presented here yields a map that illustrates the spatial distribution of each diagenetic phase in an outcrop; a feat that could not be achieved

with photogrammetry or Lidar, even if supported by a dense sampling campaign (Kurz et al. 2012; Beckert et al. 2018). As a result, hyperspectral imaging provides a geological toolkit that facilitates systematic sampling and improves confidence that all of the phases in the paragenetic history have been sampled, thereby allowing for macro-scale fluid flow pathways to be determined. This has economic implications because structurally-controlled deposits of magnesite (e.g., Mount Brussilof) and MVT-minerals (e.g., Kicking Horse, Monarch) are associated with "hydrothermal sparry dolomite" in the Cathedral Formation (Powell et al. 2006; Paradis and Simandl, 2017a, 2017b). Their effective exploitation, therefore, requires a robust understanding of the spatial distributions of each of the SD subgroups and their relationship to mineralization.

The methodological study presented here, with a wavelength accuracy greater than 1 nm (Lypaczewski and Rivard, 2018; Lypaczewski et al. 2019), tested whether hyperspectral imaging can be used to discriminate a narrow range of dolomite stoichiometries and textures that are present in the Middle Cambrian strata in the WCSB. We distinguished five phases of dolomite, ranging from 49.67 to 50.21%Ca, that are approaching a stoichiometric, well-ordered endmember following 100's of millions of years of diagenesis and several kilometers of burial (Koeshidayatullah et al. 2020a, 2020b, 2021; Stacey et al. 2021). The progressive recrystallization of dolomite over geological time is driven by mineralogical stabilization during burial that increases dolomite stoichiometry and cation ordering (Manche and Kaczmarek, 2021). Consequently, this methodology has profound transferability to other, younger, successions that have not been subject to such burial, recrystallization, and mineralogical stabilization. This includes the Cenozoic "island-type" dolomite bodies that have a wider range of dolomite stoichiometries (Budd, 1997; Ren and Jones, 2018; Wang et al. 2021). With careful calibration, hyperspectral imaging can provide an upscaled view of the distribution of each of these diagenetic phases in an outcrop, akin to a geocellular model, that cannot be replicated by conventional geological methods.

4.8. Conclusions

Exposures of Middle Cambrian strata in the WCSB offer an unparalleled natural laboratory to unravel the extent and timing of dolomitization, recrystallization, and cementation in carbonate sedimentary rocks. Hyperspectral imaging, in conjunction with the detailed analysis of samples from a fault-controlled dolomite body, has led to the following important conclusions:

- The position of the ~2315 nm absorption-band is an effective analogue for the %Ca of dolomite and this can be used to map outcrop-scale variations in dolomite stoichiometry.
- The relationship between %Ca and absorption-band positions is convoluted in dolomite with high trace element substitution (SDc; %Ca = 50.53; [Fe + Mn] = 13320 ppm), therefore, non-stoichiometric dolomite can be distinguished using hyperspectral imaging.
- The spectral contrast of the reflectance profile, which accounts for overall reflectance and absorption-band depths, correlates with the textural properties (e.g., crystal size, boundary-shape) of each dolomite phase, thus, enabling their discrimination and mapping.
- The paragenesis and spatial distributions of the RD and SD phases in the Cathedral Formation support the prior interpretation that the dolomitization front "retreated" towards the fluid source during the ensuing recrystallization and cementation of the dolomite body.

The results of this study demonstrate that SWIR hyperspectral imaging is capable of discerning subtle diagenetic heterogeneities in carbonate sedimentary rocks, beyond the routine identification of calcite and dolomite. Consequently, robust multi-scale studies can be conducted through the targeted sampling of individual diagenetic phases for further petrographical and geochemical analyses.

Acknowledgements

This research was made possible by an infrastructure grant from the Canadian Foundation for Innovation under the John R. Evans Leaders Fund – Funding for research infrastructure (Project 22222) and by the National Science and Engineering Research Council of Canada (Discovery grant to B. Rivard). The authors acknowledge the Natural Environment Research Council funded Nanoscale Imaging and Analysis Facility for Environmental Materials in the Williamson Research Centre for Molecular Environmental Science, The University of Manchester (NERCCC042). Additional support to C.A. McCormick came from the Society for Sedimentary Geology Foundation (Student Research Grant), the International Association of Sedimentologists (Postgraduate Research Grant), the British Sedimentological Research Group (Trevor Elliot Memorial Grant), and the American Association of Petroleum Geologists Foundation (Classen Family Named Grant). We are grateful to Alberta Tourism, Parks, and Recreation for the Research and Collection Permit to sample in the Kootenay Plains Ecological Reserve. We are indebted to Tyler Hauck and Jesse Peterson (Alberta Geological Survey), who provided logistical assistance in the field; John Waters (The University of Manchester) who conducted the XRD; Paul Lythgoe (The University of Manchester) who ran the ICP-MS; Jonathan Fellows (The University of Manchester) who conducted the EPMA; and Christine Gopon and Aukje Benedictus (Rocktype Ltd.), who ran the QEMSCAN and EDX spectroscopy.

References

Aitken, J.D., 1971. Control of lower Paleozoic sedimentary facies by the kicking horse rim, southern Rocky Mountains, Canada. Bulletin of Canadian Petroleum Geology, 19(3), 557-569.

Aitken, J.D., 1997. Stratigraphy of the Middle Cambrian platformal succession, southern Rocky Mountains. Geological Survey of Canada Bulletin, 398, 1-322.

Beckert, J., Vandeginste, V., McKean, T.J., Alroichdi, A., John, C.M., 2018. Ground-based hyperspectral imaging as a tool to identify different carbonate phases in natural cliffs. International Journal of Remote Sensing, 39(12), 4088-4114.

Beirami, M.R., Tangestani, M.H., 2020. A new band ratio approach for discriminating calcite and dolomite by ASTER imagery in arid and semiarid regions. Natural Resources Research, 29(5), 2949-2965.

Bellante, G.J., Powell, S.L., Lawrence, R.L., Repasky, K.S., Dougher, T.A.O., 2013. Aerial detection of a simulated CO2 leak from a geologic sequestration site using hyperspectral imagery. International Journal of Greenhouse Gas Control, 13, 124-137.

Bond, G.C., Kominz, M.A., 1984. Construction of tectonic subsidence curves for the early Paleozoic miogeocline, southern Canadian Rocky Mountains: Implications for subsidence mechanisms, age of breakup, and crustal thinning. Geological Society of America Bulletin, 95(2), 155-173.

Budd, D.A., 1997. Cenozoic dolomites of carbonate islands: their attributes and origin. Earth-Science Reviews, 42(1-2), 1-47.

Budd, D.A., Park, A.J., 2018. Formation of bed-scale spatial patterns in dolomite abundance during early dolomitization: Part I. Mechanisms and feedbacks revealed by reaction–transport modelling. Sedimentology, 65(1), 209-234.

Cloutis, E.A., 1996. Review article hyperspectral geological remote sensing: evaluation of analytical techniques. International Journal of Remote Sensing, 17(12), 2215-2242.

Collom, C.J., Johnston, P.A., Powell, W.G., 2009. Reinterpretation of 'Middle' Cambrian stratigraphy of the rifted western Laurentian margin: Burgess Shale Formation and contiguous units (Sauk II megasequence), Rocky Mountains, Canada. Palaeogeography, Palaeoclimatology, Palaeoecology, 277(1-2), 63-85.

Crowley, J.K., 1986. Visible and near-infrared spectra of carbonate rocks: Reflectance variations related to petrographic texture and impurities. Journal of Geophysical Research: Solid Earth, 91(B5), 5001-5012.

Desjardins, P.R., Buatois, L.A., Pratt, B.R., Mangano, M.G., 2010. Stratigraphy and sedimentary environments of the Lower Cambrian Gog Group in the southern Rocky Mountains of Western Canada: Transgressive sandstones on a broad continental margin. Bulletin of Canadian Petroleum Geology, 58(4), 403-439.

Dickson, J.A.D., 1965. A modified staining technique for carbonates in thin section. Nature, 205(4971), 587-587.

Feng, J., Rogge, D., Rivard, B., 2018. Comparison of lithological mapping results from airborne hyperspectral VNIR-SWIR, LWIR and combined data. International journal of applied earth observation and geoinformation, 64, 340-353.

Gaffey, S.J., 1986. Spectral reflectance of carbonate minerals in the visible and near infrared (0.35-2.55 microns); calcite, aragonite, and dolomite. American Mineralogist, 71(1-2), 151-162.

Gaffey, S.J., 1987. Spectral reflectance of carbonate minerals in the visible and near infrared (0.35–2.55 um): Anhydrous carbonate minerals. Journal of Geophysical Research: Solid Earth, 92(B2), 1429-1440.

Goldsmith, J.R., Graf, D.L., 1958. Structural and compositional variations in some natural dolomites. The Journal of Geology, 66(6), 678-693.

Green, D., Schodlok, M., 2016. Characterisation of carbonate minerals from hyperspectral TIR scanning using features at 14 000 and 11 300 nm. Australian Journal of Earth Sciences, 63(8), 951-957.

Hunt, G.R., Salisbury, J.W., 1971. Visible and near-infrared spectra of minerals and rocks: II. Carbonates. Modern Geology, 2, 23-30.

Johnston, P.A., Johnston, K.J., Collom, C.J., Powell, W.G., Pollock, R.J., 2009. Palaeontology and depositional environments of ancient brine seeps in the Middle Cambrian Burgess Shale at The Monarch, British Columbia, Canada. Palaeogeography, Palaeoclimatology, Palaeoecology, 277(1-2), 86-105.

Jones, B., Luth, R.W., MacNeil, A.J., 2001. Powder X-ray diffraction analysis of homogeneous and heterogeneous sedimentary dolostones. Journal of Sedimentary Research, 71(5), 790-799.

Koeshidayatullah, A., Corlett, H., Hollis, C., 2021. An overview of structurally-controlled dolostone-limestone transitions in the stratigraphic record. Earth-Science Reviews, 220, 103751.

Koeshidayatullah, A., Corlett, H., Stacey, J., Swart, P.K., Boyce, A., Robertson, H., Whitaker, F., Hollis, C., 2020a. Evaluating new fault-controlled hydrothermal dolomitisation models: Insights from the Cambrian Dolomite, Western Canadian Sedimentary Basin. Sedimentology, 67, 2945-2973.

Koeshidayatullah, A., Corlett, H., Stacey, J., Swart, P.K., Boyce, A., Hollis, C., 2020b. Origin and evolution of fault-controlled hydrothermal dolomitization fronts: A new insight. Earth and Planetary Science Letters, 541, 116291.

Krupnik, D., Khan, S., 2019. Close-range, ground-based hyperspectral imaging for mining applications at various scales: Review and case studies. Earth-science reviews, 198, 102952.

Kruse, F.A., Lefkoff, A.B., Boardman, J.W., Heidebrecht, K.B., Shapiro, A.T., Barloon, P.J., Goetz, A.F.H., 1993. The spectral image processing system (SIPS) – interactive

visualization and analysis of imaging spectrometer data. Remote sensing of environment, 44(2-3), 145-163.

Kurz, T.H., Buckley, S.J., Howell, J.A., 2013. Close-range hyperspectral imaging for geological field studies: Workflow and methods. International Journal of Remote Sensing, 34(5), 1798-1822.

Kurz, T.H., Buckley, S.J., Howell, J.A., Schneider, D., 2011. Integration of panoramic hyperspectral imaging with terrestrial lidar data. The Photogrammetric Record, 26(134), 212-228.

Kurz, T.H., Dewit, J., Buckley, S.J., Thurmond, J.B., Hunt, D.W., Swennen, R., 2012. Hyperspectral image analysis of different carbonate lithologies (limestone, karst and hydrothermal dolomites): the Pozalagua Quarry case study (Cantabria, North-west Spain). Sedimentology, 59(2), 623-645.

Li, Z.X., Bogdanova, S., Collins, A.S., Davidson, A., De Waele, B., Ernst, R.E., Fitzsimons, I.C.W., Fuck, R.A., Gladkochub, D.P., Jacobs, J. Karlstrom, K.E., Lu, S., Natapov, L.M., Pease, V., Pisarevsky, S.A., Thrane, K., Vernikovsky, V., 2008. Assembly, configuration, and break-up history of Rodinia: a synthesis. Precambrian research, 160(1-2), 179-210.

Lumsden, D.N., 1979. Discrepancy between thin-section and X-ray estimates of dolomite in limestone. Journal of Sedimentary Research, 49(2), 429-435.

Lypaczewski, P., Rivard, B., 2018. Estimating the Mg# and AlVI content of biotite and chlorite from shortwave infrared reflectance spectroscopy: Predictive equations and recommendations for their use. International journal of applied earth observation and geoinformation, 68, 116-126.

Lypaczewski, P., Rivard, B., Gaillard, N., Perrouty, S., Piette-Lauzière, N., Bérubé, C.L., Linnen, R.L., 2019. Using hyperspectral imaging to vector towards mineralization at the Canadian Malartic gold deposit, Québec, Canada. Ore Geology Reviews, 111, 102945.

Manche, C.J., Kaczmarek, S.E., 2021. A global study of dolomite stoichiometry and cation ordering through the Phanerozoic. Journal of Sedimentary Research, 91(5), 520-546.

Martín-Martín, J.D., Gomez-Rivas, E., Gómez-Gras, D., Travé, A., Ameneiro, R., Koehn, D., & Bons, P.D., 2018. Activation of stylolites as conduits for overpressured fluid flow in dolomitized platform carbonates. Geological Society, London, Special Publications, 459(1), 157-176.

Murphy, R.J., Taylor, Z., Schneider, S., Nieto, J., 2015. Mapping clay minerals in an open-pit mine using hyperspectral and LiDAR data. European Journal of Remote Sensing, 48(1), 511-526.

Paradis, S., Simandl, G.J., 2017a. Is there a genetic link between the SEDEX and MVT deposits of the Canadian Cordillera? In: Rogers, N., (Ed.). Targeted Geoscience Initiative: 2016 Report of Activities, Geological Survey of Canada, Open File 8199, 107-113. http://doi.org/10.4095/299573

Paradis, S., Simandl, G.J., 2017b. Are there genetic links between carbonate-hosted barite-zinc-lead sulphide deposits and magnesite mineralization in southeast British Columbia? In: Rogers, N., (Ed.). Targeted Geoscience Initiative: 2017 Report of Activities, Geological Survey of Canada, Open File 8358, 217-227. http://doi.org/10.4095/306391

Powell, W.G., Johnston, P.A., Collom, C.J., Johnston, K.J., 2006. Middle Cambrian brine seeps on the Kicking Horse Rim and their relationship to talc and magnesite mineralization and associated dolomitization, British Columbia, Canada. Economic Geology, 101(2), 431-451.

Pratt, B.R., 2002. Tepees in peritidal carbonates: origin via earthquake-induced deformation, with example from the Middle Cambrian of western Canada. Sedimentary Geology, 153(3-4), 57-64.

Ren, M., Jones, B., 2018. Genesis of island dolostones. Sedimentology, 65(6), 2003-2033.

Rivard, B., Zhang, J., Feng, J., & Sanchez-Azofeifa, G. A. (2009). Remote predictive lithologic mapping in the Abitibi Greenstone Belt, Canada, using airborne hyperspectral imagery. Canadian Journal of Remote Sensing, 35, S95-S105.

Rogge, D.M., Rivard, B., Zhang, J., Sanchez, A., Harris, J., Feng, J., 2007. Integration of spatial–spectral information for the improved extraction of endmembers. Remote Sensing of Environment 110, 287-303.

Rogge, D.M., Rivard, B., 2010. Iterative spatial filtering for reducing intra-class spectral variability and noise. IEEE GRSS Workshop on Hyperspectral Image and Signal Processing: Evolution in Remote Sensing, Reykjavik, Iceland, June 14-16, 1-4.

Rogge, D., Bachmann, M., Rivard, B., Feng, J., 2012. Spatial sub-sampling using local endmembers for adapting OSP and SSEE for large-scale hyperspectral surveys. IEEE Journal of Selected Topics in Applied Earth Observations and Remote Sensing 5, 183-195.

Sibley, D.F., Gregg, J.M., 1987. Classification of dolomite rock textures. Journal of sedimentary Research, 57(6), 967-975.

Stacey, J., Corlett, H., Holland, G., Koeshidayatullah, A., Cao, C., Swart, P., Crowley, S., Hollis, C., 2021. Regional fault-controlled shallow dolomitization of the Middle Cambrian Cathedral Formation by hydrothermal fluids fluxed through a basal clastic aquifer. GSA Bulletin, 133(11-12), 2355-2377.

Turner, W.A., Laamrani, A., Rivard, B., 2003. Laboratory reflectance spectra of hydrothermally altered carbonate facies, Pine Point mining camp, NWT, Canada. Geochemistry: Exploration, Environment, Analysis, 3(4), 369-379.

Vahrenkamp, V.C., Swart, P.K., 1990. New distribution coefficient for the incorporation of strontium into dolomite and its implications for the formation of ancient dolomites. Geology, 18(5), 387-391.

van der Meer, F., 1995. Spectral reflectance of carbonate mineral mixtures and bidirectional reflectance theory: Quantitative analysis techniques for application in remote sensing. Remote Sensing Reviews, 13(1-2), 67-94.

van der Meer, F., 1996. Classification of remotely-sensed imagery using an indicator kriging approach: Application to the problem of calcite-dolomite mineral mapping. International journal of remote sensing, 17(6), 1233-1249.

van Der Meer, F., 2004. Analysis of spectral absorption features in hyperspectral imagery. International journal of applied earth observation and geoinformation, 5(1), 55-68.

van der Meer, F., 2012. Remote-sensing image analysis and geostatistics. International Journal of Remote Sensing, 33(18), 5644-5676.

van der Meer, F.D., van der Werff, H.M., van Ruitenbeek, F.J., Hecker, C.A., Bakker, W.H., Noomen, M.F., van der Meijde, M., Carranza, E.J.M., de Smeth, J.B., Woldai, T., 2012. Multi-and hyperspectral geologic remote sensing: A review. International Journal of Applied Earth Observation and Geoinformation, 14(1), 112-128.

van Ginneken, B., Stavridi, M., Koenderink, J.J., 1998. Diffuse and specular reflectance from rough surfaces. Applied optics, 37(1), 130-139.

Vandeginste, V., Swennen, R., Gleeson, S.A., Ellam, R.M., Osadetz, K., Roure, F., 2005. Zebra dolomitization as a result of focused fluid flow in the Rocky Mountains Fold and Thrust Belt, Canada. Sedimentology, 52(5), 1067-1095.

Vandeginste, V., Swennen, R., Gleeson, S.A., Ellam, R.M., Osadetz, K., Roure, F., 2007. Geochemical constraints on the origin of the Kicking Horse and Monarch Mississippi Valley-type lead-zinc ore deposits, southeast British Columbia, Canada. Mineralium Deposita, 42(8), 913-935.

Wallace, M.W., v.S. Hood, A., 2018. Zebra textures in carbonate rocks: fractures produced by the force of crystallization during mineral replacement. Sedimentary Geology, 368, 58-67.

Wang, R., Yu, K., Jones, B., Jiang, W., Xu, S., Fan, T., Zhang, Y., 2021. Dolomitization micro-conditions constraint on dolomite stoichiometry: A case study from the Miocene Huangliu Formation, Xisha Islands, South China Sea. Marine and Petroleum Geology, 133, 105286.

Windeler, D.S., Lyon, R.J., 1991. Discriminating dolomitization of marble in the Ludwig Skarn near Yerington, Nevada using high-resolution airborne infrared imagery. Photogrammetric engineering and remote sensing, 57(9), 1171-1177.

Woodcock, C.E., Strahler, A.H., 1987. The factor of scale in remote sensing. Remote sensing of Environment, 21(3), 311-332.

Zabcic, N., Rivard, B., Ong, C., Müller, A., 2014. Using airborne hyperspectral data to characterize the surface pH and mineralogy of pyrite mine tailings. International Journal of Applied Earth Observation and Geoinformation, 32, 152-162.

Zaini, N., Van der Meer, F., Van der Werff, H., 2012. Effect of grain size and mineral mixing on carbonate absorption features in the SWIR and TIR wavelength regions. Remote sensing, 4(4), 987-1003.

Zaini, N., Van der Meer, F., Van der Werff, H., 2014. Determination of carbonate rock chemistry using laboratory-based hyperspectral imagery. Remote sensing, 6(5), 4149-4172.

Blank page

An experimental study of the transition from tensile failure to shear failure in Carrara marble and Solnhofen limestone: Does "hybrid failure" exist?

Cole A. McCormick [1,*], Ernest H. Rutter [1]

1. Department of Earth and Environmental Sciences, The University of Manchester, Manchester, M13 9PL, United Kingdom.

* Corresponding author: Cole McCormick - cole.mccormick@manchester.ac.uk

McCormick, C.A., Rutter, E.H., 2022. An experimental study of the transition from tensile failure to shear failure in Carrara marble and Solnhofen limestone: Does "hybrid failure" exist?. Tectonophysics, 844, 229623.

Abstract

Failure of brittle rocks under axisymmetric extensional loading, when the minimum principal stress is tensile, results in the formation of one or more opening-mode cracks that are oriented normal to the extension axis. When all the principal stresses are compressive, failure occurs through the formation of numerous, grain-scale tensile cracks, which coalesce into a shear-mode fault that is inclined at >20° to the maximum principal stress. There have been few attempts to study the transition between these failure modes, particularly those that incorporate microstructural analyses. A transitional mode of failure, termed “hybrid failure”, is often proposed to describe the orientation of faults between these end-member loading conditions, but this concept has traditionally been based on a parabolic, “Griffith-type” failure envelope that describes the growth of the single most critically-oriented crack. By integrating axisymmetric rock deformation experiments with microstructural analyses, it can be shown that failure under these transitional conditions involves the formation of several, transgranular tensile cracks, which coalesce into a shear-mode fault that is inclined at <10° to the maximum principal stress. The stress intensity at the tip of each crack interacts with adjacent cracks to produce a stair-step geometry along the failure surface. These are what may be appropriately considered “hybrid faults”, the angle of which systematically increase as the maximum principal stress, and thus the differential stress increases. There is, however, no evidence of a distinct “hybrid failure” mode, which involves the in-plane propagation of a single crack that is subject to a combined shear stress and tensile normal stress. The results of this experimental study provide novel insights into the mechanical behaviour of carbonate rocks and into the interpretation of meso-scale natural examples of failure under mixed stress-states.

5.1. Introduction

Experimental rock mechanics, which forms the foundation for interpreting natural examples of brittle failure in modern and ancient geological settings (Ferrill et. al. 2012; Busetti et al. 2014; Peacock et al. 2021), comprises a great number of rock mechanical studies of brittle failure that have been carried out over a wide range of confining pressures. Most experimental studies have been conducted under axisymmetric shortening, where the principal stresses $\sigma_1 > \sigma_2 = \sigma_3$, and $\sigma_2 = \sigma_3$ is the hydraulic confining pressure. Fewer studies have been reported under polyaxial compressive stress states ($\sigma_1 > \sigma_2 > \sigma_3$) (e.g., Handin et al. 1967; Mogi, 1967, 1971; Haimson and Chang, 2000; Colmenares and Zoback, 2002; Haimson and Rudnicki, 2010; Chang and Haimson, 2012; Feng et al. 2016), but the variation in σ_2 typically does not cover the whole range of stress conditions from axisymmetric shortening to extension. Similarly, few investigations have been reported on brittle rocks under confined, axisymmetric extensional loading ($\sigma_1 = \sigma_2 > \sigma_3$) (e.g., Heard, 1960; Brace, 1964; Ramsey and Chester, 2004; Hackston and Rutter, 2016; Lan et al. 2019), but only Bobich (2005) and Huang et al. (2022) reported experiments spanning the transition from true tensile failure to shear failure in both axisymmetric extension and shortening.

It is generally considered that tensile failure and shear failure represent the end-members of a continuous spectrum of brittle failure (Fig. 5.1A) (Brace, 1964; Hancock, 1985; Engelder, 1999; Ramsey and Chester, 2004). Tensile failure occurs when the minimum principal stress (σ_3) is negative and results in the formation of one or more opening-mode cracks that are oriented normal to σ_3 and in the plane of $\sigma_1 = \sigma_2$ (Brace, 1960; Coviello et al. 2005; Lan et al. 2019). Conversely, shear failure occurs when all of the principal stresses are positive and it involves the precursory formation of numerous, grain-scale, tensile cracks that are oriented parallel to σ_1 and that coalesce into a shear-mode fault, inclined at >20° to σ_1 (Heard, 1960; Reches and Lockner, 1994; Wibberley et al. 2000). Due to a wide array of experimental challenges, there have been relatively few

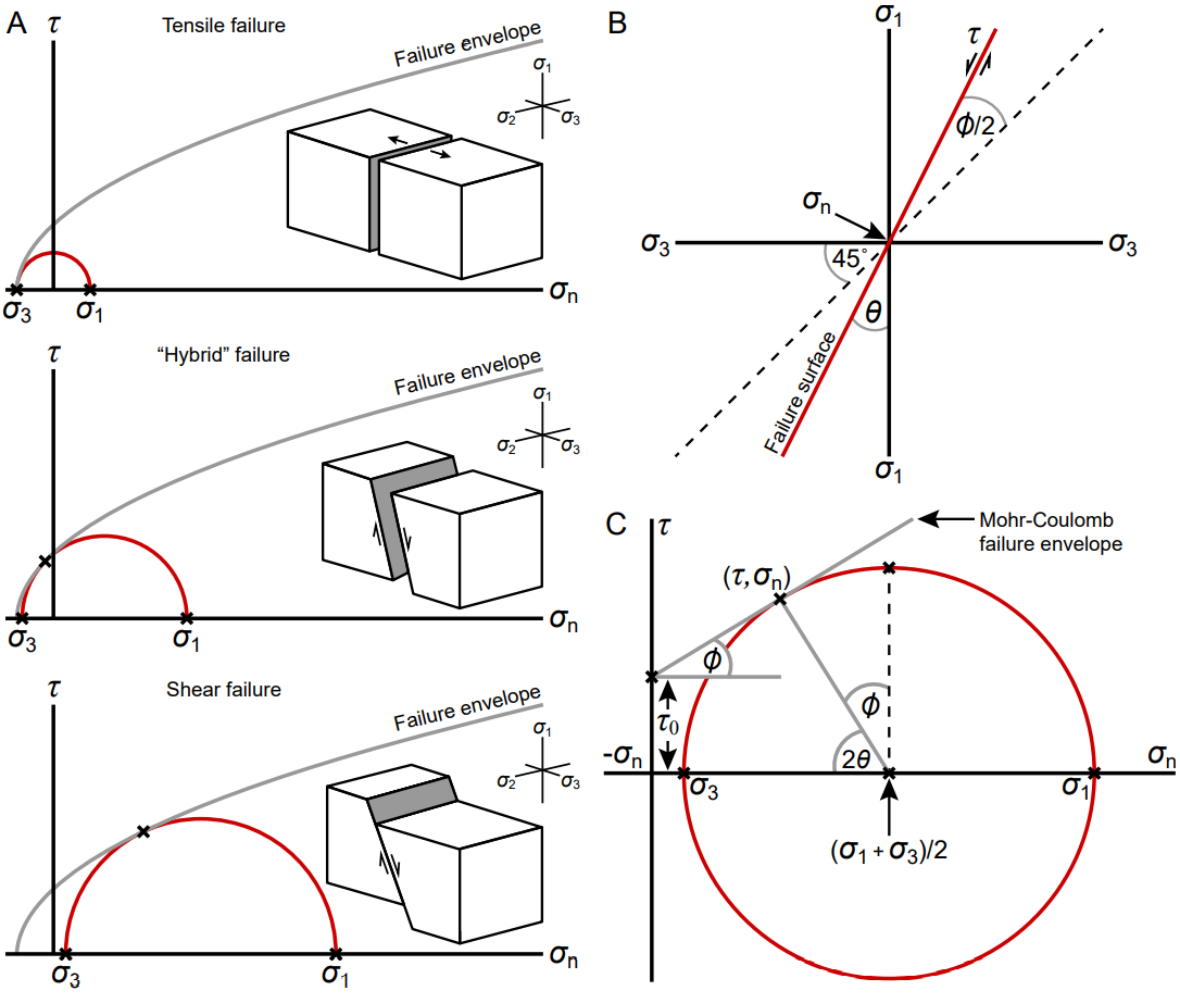

Figure 5.1. (A) Conceptual model for the transition from tensile failure to shear failure (modified from Ferrill et al. 2012, their Fig. 1) using a parabolic failure envelope based on Hoek and Brown (1988). **(B)** Diagram illustrating the material parameters in the σ_1 versus σ_3 coordinate frame and their linear transformations to **(C)** a Mohr diagram in the τ versus σ_n coordinate frame.

attempts to study the transition between these two end-member failure modes, particularly those that incorporate microstructural analyses. A transitional mode of dilatant shear failure, termed "hybrid failure" (Fig. 5.1A), is often proposed to describe a progressive transition in the orientation of the macroscopic failure surfaces from tensile failure to shear failure (Ramsey and Chester, 2004; Bobich, 2005; Ferrill et al. 2012; Huang and Zhu, 2018; Huang et al. 2022). Nevertheless, a Griffith (1921)-type failure envelope is commonly invoked to describe this transition, despite the approach being applicable only to the growth of the single-most critically-oriented flaw in the material.

In this study, we investigate failure through this transitional region in two markedly different carbonate rocks, Carrara marble (CM) and Solnhofen limestone (SL), both of which have been widely used in previous experimental studies. Using a single rock deformation apparatus, we examine (i) the stress conditions at failure over a wide range of stress states, alongside (ii) the microstructural evolution from true tensile failure to shear failure in both axisymmetric extension and shortening. A series of experiments were initially conducted on SL, but additional tests on CM were incorporated as an independent comparison and validation of works by Ramsey (2003), Ramsey and Chester (2004), and Rodriguez (2005).

5.2. Outline of the Mohr-Coulomb criterion for failure

The Mohr-Coulomb criterion, which is a description of shear failure under axisymmetric shortening, is the most widely applied criterion to the brittle failure of geological materials. This description represents the starting point for this study, and its main features are outlined below. Although it does not have to be assumed to be linear, a simple linear relationship is typically applied to relate the principal stresses at failure (Hoek and Martin, 2014):

$$\sigma_1 = m\sigma_3 + C_0 \tag{5.1}$$

where the slope (m) and the unconfined compressive strength (C_0) are material parameters. Furthermore, it is commonly assumed that failure produces a shear fault that is inclined at the angle θ to the maximum principal stress (σ_1), so that the maximum resolved normal stress (σ_n) and shear stress (τ) on the failure surface satisfy the relationships (Fig. 5.1B, C):

$$\sigma_n = \frac{\sigma_1+\sigma_3}{2} \pm \left(\frac{\sigma_1-\sigma_3}{2}\cos 2\theta\right) \tag{5.2}$$

$$\tau = \pm\frac{\sigma_1-\sigma_3}{2}\sin 2\theta \tag{5.3}$$

The Mohr-Coulomb failure criterion can be transformed into the τ versus σ_n coordinate frame:

$$\tau = \sigma_n \tan\phi + \tau_0 \tag{5.4}$$

where $\phi = (90 - 2\theta)$, $C_0 = 2\tau_0\sqrt{m}$, and $m = (1 + \sin\phi)/(1 - \sin\phi)$. The result is a linear envelope to the family of Mohr circles that represent a succession of stress states at failure, each having the diameter ($\sigma_1 - \sigma_3$). When failure occurs, the limited combination of σ_n and τ within the material are given by the tangent points on each of the Mohr circles where they intersect the failure envelope, represented by the coordinates (σ_n, τ) (Fig. 5.1B, C). The Mohr-Coulomb description of failure in the compressive domain is commonly linked and extended into the tensile domain such that the cohesive strength (0, τ_0) is connected to the tensile strength (T, 0) by a segment of the failure envelope that is assumed to be parabolic in form:

$$\sigma_n = T\left(\frac{\tau}{\tau_0}\right)^2 - 1 \qquad (5.5)$$

where T is the uniaxial tensile strength of the rock. This parabolic form is empirical, but it is often compared to the form of the Griffith (1921) criterion that assumes failure arises from the propagation of the single most unfavourably oriented crack in the material. Sometimes the above criteria are a good description of experimental data, but in many cases the relationships between the observed orientation of the failure surface and the orientation implied by the stress states along the Mohr envelope do not conform well to these empirical descriptions.

The Mohr-Coulomb criterion is two dimensional, which assumes that the intermediate principal stress has no influence on failure, and that it always lies in the plane of the resulting failure surface. Many experimental studies have demonstrated that the intermediate principal stress affects failure, producing significant departures from the Mohr-Coulomb criterion, especially when σ_2 is midway between σ_1 and σ_3. Consequently, the conventional, two-dimensional Mohr-Coulomb failure criterion is not adequate for polyaxial loading conditions and other empirically derived failure criteria, typically based on functions of stress invariants, have had to be devised (e.g., Colmenares and Zoback 2002; Chang and Haimson, 2012).

5.3. Methods

5.3.1. Starting material

Carrara marble (CM) and Solnhofen limestone (SL) were used as the experimental materials for this study (Table 5.1; Fig. 5.2A). Cylindrical specimens, 45 mm in length and 15 mm in diameter, of each lithology were prepared for axisymmetric shortening experiments. Samples of CM were cored in an arbitrary but constant direction (designated the *a*-direction in this block), whereas samples of SL were cored normal to bedding. Axisymmetric extension experiments were conducted on "dog-bone" shaped samples that were waisted to 13 mm in diameter over a central length of 16 mm. Samples of CM were oven-dried at 60°C, whereas samples of SL were air-dried at a relative humidity of 60%, in each case resulting in a constant sample mass. The strength of CM is unaffected by ambient water vapour pressure, whereas the unconfined compressive strength (C_0) of SL in the oven-dried (100° C) state is reduced by ~30% through water saturation at room temperature or when exposed to the atmosphere at laboratory relative humidity (60%) (Rutter, 1972). French et al. (2022) reported that the ultimate strength of "nominally dry" Solnhofen limestone was unaffected by wetting, which would be expected if "nominally" dry means air-dry.

Carrara marble, with a mean grain size of 98.4 μm (± 72.7 μm; standard deviation of the grain size distribution) and 0.2% porosity, is a medium-grade metamorphic rock from the Tuscany region of Italy (Table 5.1; Fig. 5.2B, C). CM comprises >99.9 wt% $CaCO_3$ and includes rare muscovite, quartz, dolomite, and graphite grains (Rutter, 1995; Pieri et al. 2001; Kandula et al. 2019; Rybacki et al. 2021; Rutter et al. 2022). Grain boundaries range from straight to gently curving with slightly sutured edges. The calcite crystals are equant, lack optical strain features, are free from crystallographic preferred orientation, and possess only low densities of lamellar twinning (Rutter, 1995; de Raadt et al. 2014). The CM used for this study was derived from a block of "Lorano Bianco" statutory marble that

Experimental material	Composition (from XRD)	Grain size (μm)	Porosity (%)	*P*-wave velocity (m/s) (Axial)	(Radial)	Anisotropy $2(V_A - V_R)/(V_A + V_R)$
Carrara marble (CM)	Calcite (100%)	98.4 ± 72.7	0.2 ± 0.11	4574.3 ± 8.6	4705.4 ± 34.7	-2.82
Solnhofen limestone (SL)	Calcite (99.1%) Quartz (0.9%)	3.8 ± 0.3	4.2 ± 0.37	5815.4 ± 28.1	5536.4 ± 48.9	4.92

Table 5.1. Summary table showing the mineralogy (from X-ray diffraction), grain size, porosity, and *P*-wave velocities of the experimental material used in this study.

was collected as a laboratory standard by D. Olgaard and M. Pieri (ETH Zürich, Switzerland), and M. Coli (University of Florence, Italy).

Solnhofen limestone, with a mean grain size of 3.8 μm (± 0.3 μm; standard deviation on measurements of the mean) and 4.2% porosity, is a pelagic mudstone from the Bavaria region of Germany (Table 5.1; Fig. 5.2D, E). SL comprises 99.1 wt% $CaCO_3$ and includes minor detrital quartz grains with a mean grain size of 20 μm as a secondary phase. Minor impurities (e.g., organic matter, oxide particles, clay minerals) also occur along the grain boundaries (Schmid et al. 1977; Rutter et al. 1994). Llana-Fúnez and Rutter (2005, their Fig. 2) demonstrated that the calcite in SL has a weak crystallographic preferred orientation of c-axes parallel to bedding. The anisotropy of *P*-wave velocities in SL (4.92% faster normal to bedding) is, therefore, analogous to that of an individual calcite crystal (e.g., Khazanehdari et al. 1998).

5.3.2. Experimental design

Samples of CM and SL were held in a ¼ mm thick, annealed copper jacket and deformed using an axisymmetric rock deformation apparatus. Following deformation, the copper jacket holds the specimen together to facilitate subsequent thin-sectioning and microstructural analyses, particularly in the case of tensile failure. Each copper jacket was heat-treated to ~600°C to remove crystal dislocations, quenched in water, and cleaned with nitric acid. Cylindrical steel split-cones, with an included angle of 70°, were placed at each end of the jacket to grip the specimen (Fig. 5.3). Heat-shrink synthetic rubber tubing was

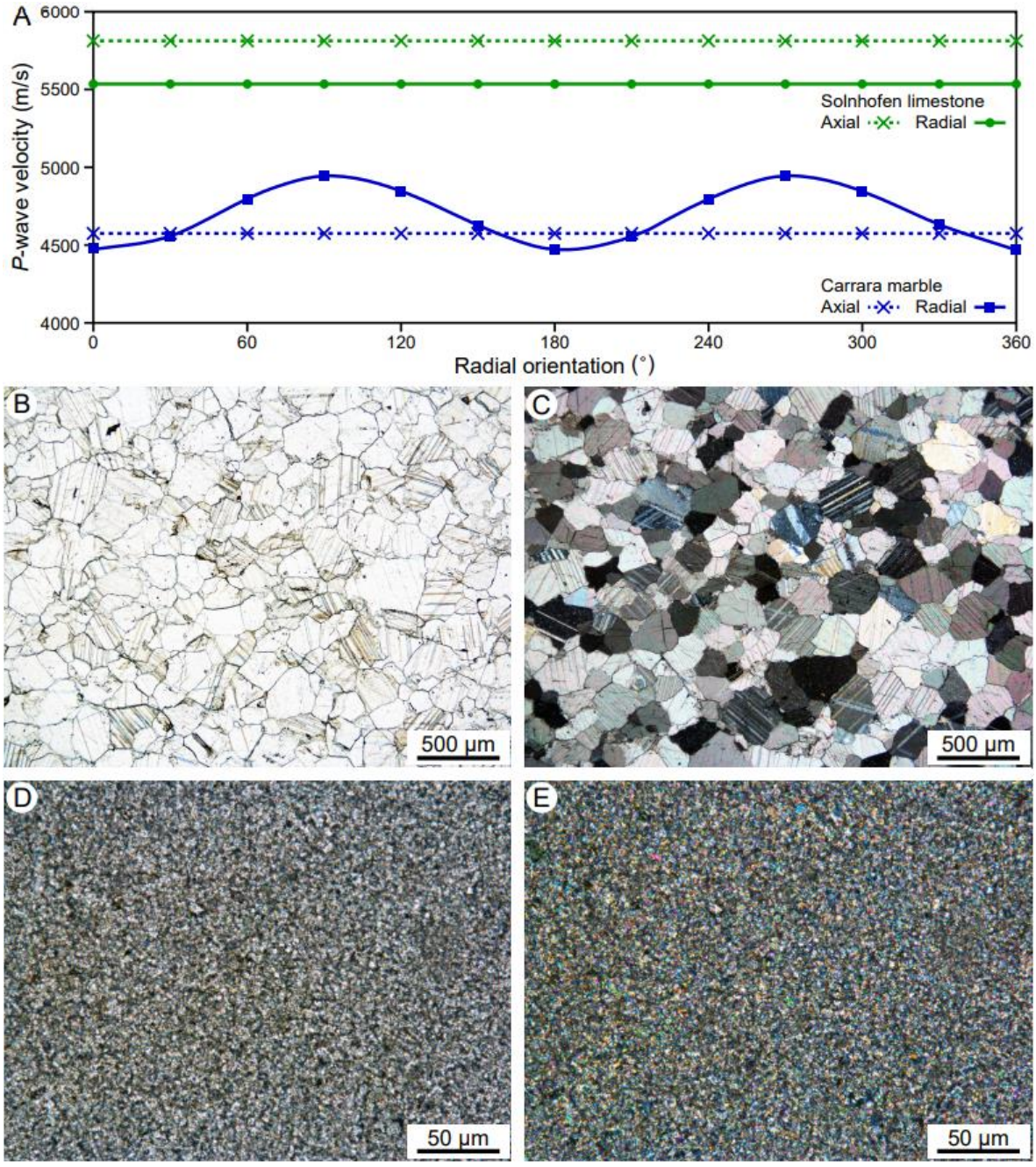

Figure 5.2. (A) Axial and radial *P*-wave velocities of Carrara marble and Solnhofen limestone showing the velocity anisotropy of each lithology. **(B, C)** Transmitted light photomicrographs of Carrara marble showing its representative petrography in plane-polarized light (left) and between crossed-polars (right). **(D, E)** Transmitted light photomicrographs of Solnhofen limestone showing its representative petrography in plane-polarized light (left) and between crossed-polars (right).

then placed around the specimen and the loading piston assembly to prevent ingress of the confining fluid.

The deformation apparatus used for this study allows experiments in both axisymmetric extension and shortening to be carried out, the former owing to a bayonet-

style connector on the bottom loading piston that engages with the top of the internal load cell assembly (Fig. 5.3). Once the loading piston assembly is inserted into the pressure vessel, it is sealed, and confining fluid is pumped into the vessel to apply radial pressure to the exterior of the specimen (up to ~300 MPa). The confining fluid is dioctyl sebacate synthetic ester, which has a low rate of change of viscosity with pressure (Rutter and Mecklenburgh, 2018). Confining pressure measurements were made using a 700 MPa Heise Bourdon tube pressure gauge, with an accuracy of 0.1 MPa, that was also used to calibrate all the other electronic pressure transducers. Experiments were conducted at room temperature (20°C) and an axial displacement rate of 3.3×10^{-3} mm s^{-1}. This corresponds to a strain rate of 2.1×10^{-4} s^{-1} over the waisted portion of the specimen in extension tests and 7.4×10^{-5} s^{-1} over the full length of the specimen in shortening tests. Forty-seven axisymmetric extension experiments (CM = 12, SL = 35) and 16 axisymmetric shortening experiments (CM = 8, SL = 8) were conducted, typically at 10 MPa intervals of confining pressure across the range of stress conditions. In extension, true tensile stresses could be achieved because the specimen diameter was smaller than that of the moving piston (19.0 mm) where it passes through the pressure seal. The maximum tensile force that can be applied to the specimen is given by the difference between its cross-sectional area and that of the moving piston, multiplied by the confining pressure.

Although most tests were conducted without pore pressure, the apparatus allows pore pressure tests to be carried out. Two tests were run with an elevated pore pressure of argon gas that was generated by a servo-controlled pressure generator. Confining pressure was controlled by a similar but larger servo-controlled pressure generator. As the axial loading piston is displaced into or withdrawn from the pressure vessel, the volume change within the vessel causes an increase or decrease in confining pressure, respectively. Accordingly, the servo-controller compensates for this to maintain a constant confining pressure during a test.

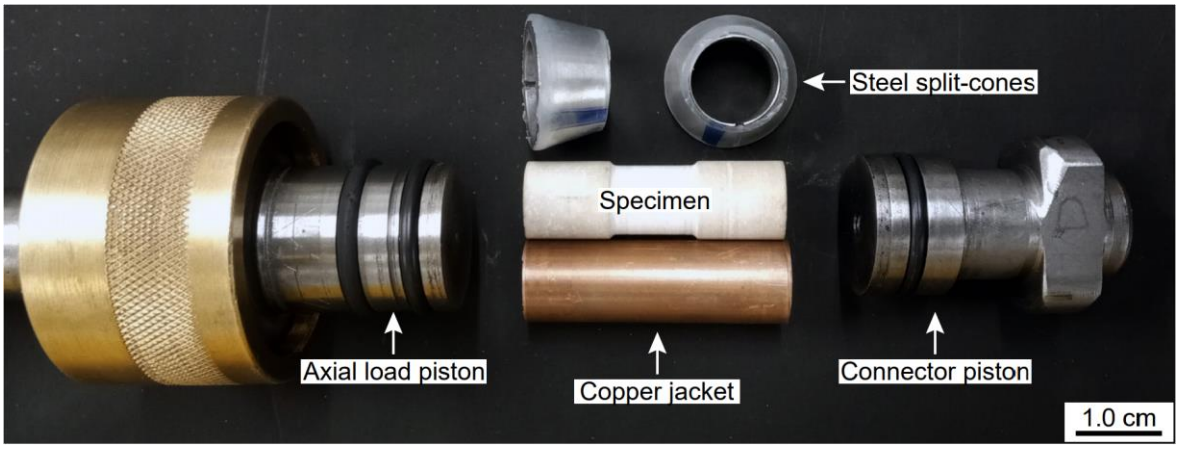

Figure 5.3. Loading piston assembly showing the specimen (in this case, Solnhofen limestone), the annealed copper jacket, and the steel split-cones that grip the ends of the specimen in axisymmetric extension. Note that in extension, the bayonet-style connector piston rotates 90° to engage with the top of the internal load cell assembly.

Experiments were terminated at different values of bulk strain, depending on the failure mode that was identified by the stress/strain behaviour during the experiment. The piston assembly was then unloaded, and the vessel was depressurized to recover the specimen.

5.3.3. Calibrations, data processing, and jacket strength correction

In this type of rock deformation apparatus, the total displacement of the axial column was measured using a linear displacement transducer that was mounted outside the pressure vessel. The total displacement includes both the deformation of the specimen and the axial distortion of the apparatus. The latter was determined by calibration tests, using a steel specimen, over a range of confining pressures. Strain measurements in the specimen were determined to be accurate to ± 0.1%. The axial load on the specimen was measured using a Heard (1963)-type semi-internal load cell that was mounted inside the pressure medium directly below the specimen assembly. This was calibrated against a 25,000 kg load cell over a range of confining pressures, both in axisymmetric extension and shortening. Stress measurements in the specimen were determined to be accurate to ± 1.0 MPa. Given that the axial column is long, induced flexural forces can contribute to the

stress state in the sample at the point of rock failure (Mackwell and Paterson, 2002) and this can influence the apparent differential stress at failure. However, the largest source of uncertainty in the measurements of stress and strain arise from the natural variability between different rock specimens.

Data processing involved the correction of the measured axial load for (1) the effects of confining pressure on the load cell calibration and (2) the subtraction of machine axial distortion from the total measured displacement and thus, the total axial strain. The axial force on the sample was calculated using the load cell calibration. Next, the axial differential stress was calculated, taking into account the change in the cross-sectional area of the specimen arising from axial strain, assuming homogeneous deformation at constant volume. The axial force that was supported by the annealed copper jacket was also removed.

In low temperature experiments, the copper jacket can support a significant fraction of the total axial load, particularly at low mean pressures when the rock is very weak or fails in tension. The analysis of results particularly requires the load supported by the copper jacket at the point of tensile failure or shear failure (ultimate strength) to be determined and subtracted from the total load at failure. To this end, the stress/strain behaviour of an annealed specimen that was fabricated from a solid copper bar was measured. The yield stress of copper is 31.0 MPa, after which rapid strain hardening begins. The strain in the jacket and the rock are the same, but the smaller cross-sectional area of the jacket reduces the load it supports by ~90%. From the measured strain at failure and the known stress/strain behaviour of the jacket, the load supported by the jacket at the onset of failure was determined for each test. This was inferred to correspond to the formation of the first tensile crack.

Using only a synthetic rubber jacket, measured to be of negligible strength, the formation of the first tensile crack splits the specimen into two pieces that are no longer able to support an axial differential load. In contrast, localized strain hardening of the

copper jacket stabilizes the first crack, allowing a succession of several cracks to form in locations where strain hardening has not yet occurred. Each of these cracks are stabilized by the local strain of the copper jacket at the periphery of the crack. This avoids jacket rupture in extension and the flooding of the specimen with hydraulic fluid, which would complicate subsequent petrographical study.

5.3.4. Microstructural analyses

Microstructural observations were made on optical thin-sections cut parallel to the specimen cylinder axis and oriented to capture the maximum failure surface angle. For shortening tests, these angles are specified by the angle between the failure surface and the specimen axis (σ_1), and between the failure surface and the plane normal to the specimen axis (σ_1) for extension tests. Samples were vacuum impregnated with blue-stained epoxy resin and prepared as 20 μm thick sections. The jacketing material was removed, and the section was polished on its upper surface. Polished sections were examined under plane-polarized light and between crossed-polars using a Nikon Eclipse LV100N POL microscope. Six representative samples of SL that cover the full range of failure modes were analysed by scanning electron microscopy using a Thermo Fisher Scientific Quanta 650 FEG instrument and backscattered electron imaging was conducted at an accelerating voltage of 15.0 kV.

5.4. Mechanical behaviour of Carrara marble and Solnhofen limestone

5.4.1. Stress-strain behaviour

Differential stress (σ_1 - σ_3) and axial strain were measured during each rock deformation experiment by the internal force gauge and the axial displacement transducer, respectively. The confining pressure is $\sigma_1 = \sigma_2$ in extension tests, and it is $\sigma_2 = \sigma_3$ in shortening tests. Compressive stress components are shown as positive and tensile stresses as negative.

In axisymmetric extension, for both CM and SL, the differential stress at failure increases as the confining pressure ($\sigma_1 = \sigma_2$) is increased, whereas the bulk strain at failure decreases (becomes more negative) (Fig. 5.4A, B). At the lowest of confining pressures, and when the value of σ_3 is very small or negative, the support of the copper jacket (strain-hardening) causes the stress-strain curve to have a flat post-yield stage, as a succession of tension cracks form along the length of the specimen. Consequently, the specimen can be deformed to an apparent bulk extensional strain of ~-8% before the jacket will rupture. At the highest of confining pressures, the post-yield differential stress increases, and the copper jacket will eventually tear at a lower bulk strain due to sliding on the failure surface. In CM, this transition from extensional cracking to shear failure occurs at a confining pressure of 60 MPa (Fig. 5.4A), whereas the transition occurs at a confining pressure of 100 MPa in SL (Fig. 5.4B).

In axisymmetric shortening, for both CM and SL, the differential stress at failure increases with increasing confining pressure (σ_3), as does the bulk strain at failure (Fig. 5.4C, D). The post-faulting frictional sliding stress also increases with increasing confining pressure. CM shows clear evidence of ductile (distributed) deformation above a confining pressure of 20 MPa (Fig. 5.4C), whereas SL shows more subtle evidence of ductility above 40 MPa (Fig. 5.4D). Consequently, CM can accommodate a larger magnitude of strain before fault localization relative to SL, both in axisymmetric extension and shortening (Fig. 5.4A, B, C, D).

5.4.2. Maximum principal stress vs. minimum principal stress at failure

Results from the rock deformation experiments on CM and SL are summarized in Table 5.2. For CM in axisymmetric extension, the average σ_3 at failure for samples deformed at the lowest confining pressures ($\sigma_1 < 40$ MPa) is -2.9 ± 0.5 MPa ($n = 2$; Table 5.2). Up to a confining pressure of 50 MPa, σ_3 at failure displays a slight negative deflection (Fig. 5.5A). The point where this negative deflection changes orientation

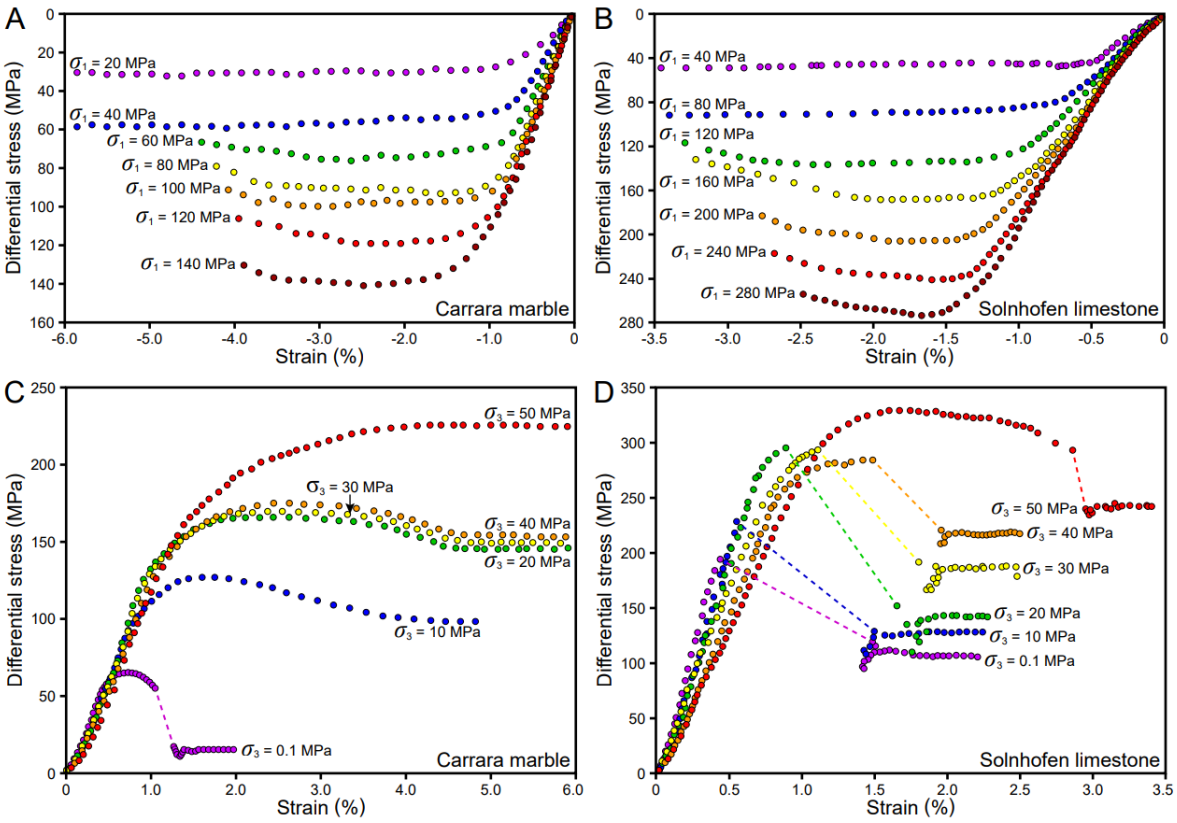

Figure 5.4. Differential stress versus axial strain curves showing the results from the **(A)** axisymmetric extension experiments on Carrara marble, **(B)** extension experiments on Solnhofen limestone, **(C)** shortening experiments on Carrara marble, and **(D)** shortening experiments on Solnhofen limestone. Note that to emphasise the distinction between the two types of test, differential stresses in the extensional tests are plotted downwards and shortening tests are plotted upwards. Axial strains are shown as negative in extensional tests and as positive in shortening tests.

towards the positive domain coincides with the point at which inclination of the failure surface away from normal to the specimen axis was first observed (Table 5.2; Fig. 5.5A). From a confining pressure of 60 to 140 MPa, σ_3 at failure has a near-linear relationship to σ_1 (Fig. 5.5A). Data points from the extension tests with a compressive σ_3 at failure are coincident (within experimental error) with the results of the shortening tests (Fig. 5.5A). In axisymmetric shortening, σ_1 at failure has a near-linear relationship to σ_3, up to a confining pressure of 20 MPa. Extrapolating the values below σ_3 = 20 MPa (n = 12; Table 5.2), the CM used in this study has an unconfined compressive strength (C_0) of 72.8 MPa and a slope ($d\sigma_1/d\sigma_3$) of 4.34 (Fig. 5.5A).

Lithology	Axial displacement	Sample ID	σ_1 (MPa)	σ_3 (MPa)	$\sigma_1 - \sigma_3$ (MPa)	Failure angle (°)	τ (MPa)	σ_n (MPa)
CM	Extension	CM_E01	20.0	-2.4	22.4	0	0	-2.4
CM	Extension	CM_E04	30.0	-3.4	33.4	0	0	-3.4
CM	Extension	CM_E02	40.0	-6.8	46.8	0	0	-6.8
CM	Extension	CM_E05	50.0	-5.7	55.7	0	0	-5.7
CM	Extension	CM_E03	60.0	–	–	–	–	Faulty test
CM	Extension	CM_E12	60.0	-4.2	64.2	2.0	2.2	-4.1
CM	Extension	CM_E10	70.0	-2.5	72.5	5.0	6.3	-2.0
CM	Extension	CM_E06	80.0	-0.2	80.2	6.0	8.3	0.7
CM	Extension	CM_E11	90.0	5.2	84.8	14.0	19.9	10.1
CM	Extension	CM_E07	100.0	10.9	89.1	16.0	23.6	17.6
CM	Extension	CM_E08	120.0	14.7	105.3	22.0	36.6	29.5
CM	Extension	CM_E09	140.0	16.7	123.3	26.0	48.6	40.4
CM	Shortening	CM_S07	59.5	0.1	59.4	22.0	20.6	8.4
CM	Shortening	CM_S06	93.5	5.0	88.5	26.0	34.9	22.0
CM	Shortening	CM_S01	130.2	10.0	120.2	32.0	54.0	43.7
CM	Shortening	CM_S05	146.7	15.0	131.7	33.0	60.1	54.1
CM	Shortening	CM_S02	178.1	20.0	158.1	34.0	73.3	69.4
CM	Shortening	CM_S03	189.8	30.0	159.8	38.0	77.5	90.6
CM	Shortening	CM_S04	206.9	40.0	166.9	36.0	79.4	97.7
CM	Shortening	CM_S08	256.2	50.0	206.2	37.0	99.1	124.7
SL	Extension	SL_E30	20.0	-3.9	23.9	0	0	-3.9
SL	Extension*	SL_E01	30.0	-0.5	30.5	0	0	-0.5
SL	Extension*	SL_E02	30.0	-1.9	31.9	0	0	-1.9
SL	Extension	SL_E03	40.0	-0.8	40.8	0	0	-0.8
SL	Extension	SL_E04	40.0	-0.1	40.1	0	0	-0.1
SL	Extension	SL_E31	50.0	-2.2	52.2	0	0	-2.2
SL	Extension	SL_E29	60.0	-1.9	61.9	0	0	-1.9
SL	Extension	SL_E32	70.0	0.2	69.8	0	0	0.2
SL	Extension	SL_E07	80.0	2.1	77.9	0	0	2.1
SL	Extension	SL_E33	90.0	0.7	89.3	0	0	0.7
SL	Extension	SL_E05	100.0	3.7	96.3	4.0	6.7	4.2
SL	Extension	SL_E34	110.0	-0.3	110.3	3.0	5.8	0
SL	Extension	SL_E18	120.0	-2.3	122.3	2.0	4.3	-2.1
SL	Extension	SL_E35	130.0	1.5	128.5	3.5	7.8	2.0
SL	Extension	SL_E10	140.0	0.9	139.1	3.0	7.3	1.3
SL	Extension	SL_E06	150.0	–	–	–	–	Faulty test
SL	Extension	SL_E12	150.0	-0.6	150.6	3.5	9.2	-0.1
SL	Extension	SL_E11	160.0	2.2	157.8	4.3	11.7	3.0
SL	Extension	SL_E09	170.0	6.1	163.9	4.3	12.1	7.0
SL	Extension	SL_E15	180.0	-0.3	180.3	5.3	16.4	1.2
SL	Extension	SL_E16	190.0	-3.5	193.5	5.5	18.5	-1.7
SL	Extension	SL_E08	200.0	0.8	199.2	6.0	20.7	3.0
SL	Extension	SL_E25	210.0	-3.1	213.1	6.5	24.0	-0.4
SL	Extension	SL_E24	220.0	2.9	217.1	6.5	24.4	5.7
SL	Extension	SL_E21	230.0	–	–	–	–	Faulty test
SL	Extension	SL_E27	230.0	-0.5	230.5	3.5	14.0	0.4
SL	Extension	SL_E26	240.0	6.8	233.2	8.0	32.1	11.3
SL	Extension	SL_E13	250.0	4.1	245.9	10.3	43.1	11.9
SL	Extension	SL_E28	260.0	10.0	250.0	10.0	42.8	17.5
SL	Extension	SL_E14	270.0	11.6	258.4	11.0	48.4	21.0
SL	Extension	SL_E17	280.0	15.3	264.7	11.0	49.6	24.9
SL	Extension	SL_E19	300.0	20.4	279.6	13.0	61.3	34.5
SL	Extension	SL_E20	300.0	–	–	–	–	Faulty test
SL	Extension	SL_E22	300.0	–	–	–	–	Faulty test
SL	Extension	SL_E23	300.0	–	–	–	–	Faulty test
SL	Shortening	SL_S01	211.4	5.0	206.4	14.5	50.0	17.9
SL	Shortening	SL_S07	246.6	10.0	236.6	16.0	62.7	28.0
SL	Shortening	SL_S05	298.0	20.0	278.0	15.0	69.5	38.6
SL	Shortening	SL_S08	312.9	25.0	287.9	16.5	78.4	48.2
SL	Shortening	SL_S06	297.1	30.0	267.1	17.5	76.6	54.1
SL	Shortening	SL_S02	400.8	40.0	360.8	16.0	95.6	67.4
SL	Shortening	SL_S04	360.1	50.0	310.1	20.0	99.7	86.3
SL	Shortening	SL_S03	376.8	60.0	316.8	19.5	99.7	95.3

Table 5.2. Results from the deformation experiments conducted in axisymmetric extension and shortening on Carrara marble (CM) and Solnhofen limestone (SL). Experiments with an asterisk (*) were conducted with 10 MPa of pore pressure and Terzaghi (1923) effective stresses are shown.

For SL in axisymmetric extension, the average σ_3 at failure for samples deformed at the lowest confining pressures (σ_1 < 100 MPa) is -0.8 ± 1.6 MPa (n = 10; Table 5.2). Inclination of the failure surface was first observed at a confining pressure of 100 MPa, which coincides with the point at which σ_3 at failure is distinctly compressive (Table 5.2; Fig. 5.5B). The negative deflection in the data trend that was observed for CM in the tensile region is not present for SL, which has a near vertical trend of the σ_1 versus σ_3 data up to a confining pressure of 210 MPa (Table 5.2; Fig. 5.5A, B). From a confining pressure of 210 to 300 MPa, σ_3 at failure has a near-linear relationship to σ_1 (Fig. 5.5B). As with CM, data points from the extension tests on SL with a compressive σ_3 at failure are coincident with the results of the shortening tests (Fig. 5.5B). In axisymmetric shortening, σ_1 at failure has a near-linear relationship to σ_3, up to a confining pressure of 40 MPa. Extrapolating the values below σ_3 = 40 MPa (n = 21; Table 5.2), the SL used in this study has an C_0 of 210.0 MPa and a slope ($d\sigma_1/d\sigma_3$) of 3.93 (Fig. 5.5B).

5.4.3. Failure surface angle

The two carbonate lithologies that were investigated in this study show clear differences in terms of the failure surface angles (θ) that were produced, which is the maximum angle measured between the σ_1 direction and the failure plane (Table 5.2; Fig. 5.5C). Both CM and SL show a trend of increasing θ with increasing differential stress, and they both display a degree of discontinuity between the failure surface angles that were produced in axisymmetric extension and in shortening (Fig. 5.5C). This apparent discontinuity, however, could be argued in each case to lie within experimental uncertainty. In axisymmetric extension, θ in CM ranges from 0 to 26.0°, whereas θ ranges from 0 to 13.0° in SL (Table 5.2; Fig. 5.5C). In axisymmetric shortening, θ in CM ranges from 22.0 to 37.0°, whereas θ ranges from 14.5 to 20.0° in SL (Table 5.2; Fig. 5.5C). In the transitional region between tensile failure and shear failure, there is a distinct change in the rate at which θ increases with increasing differential stress (Fig. 5.5C). This change occurs

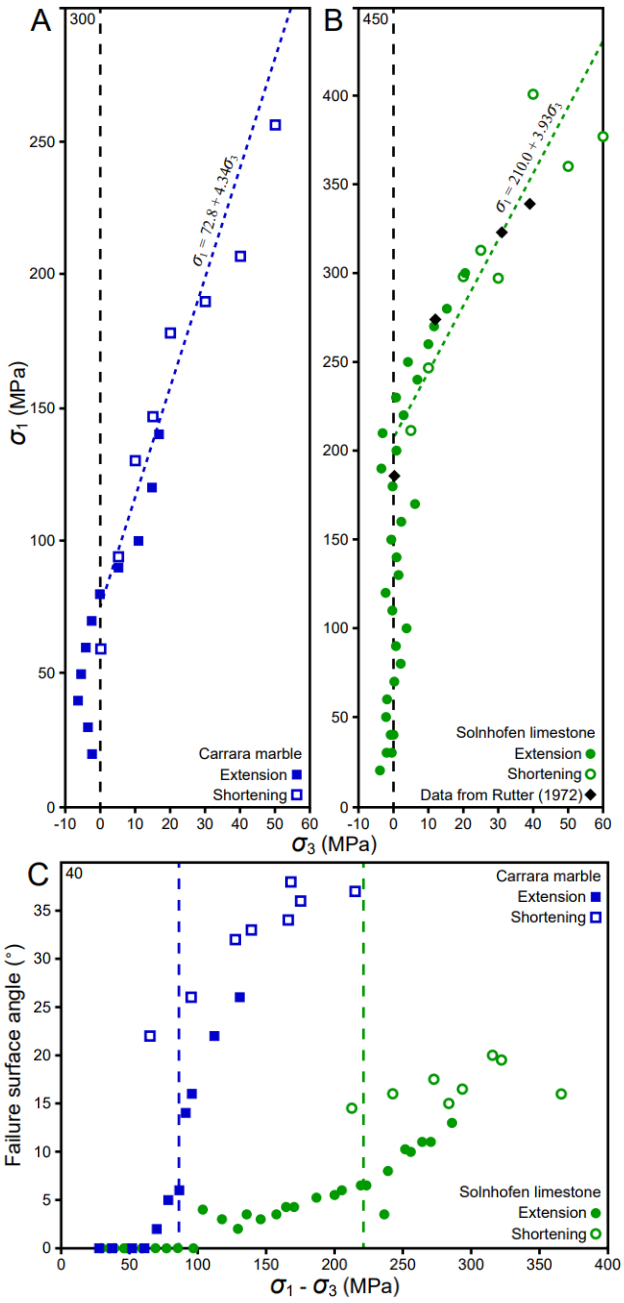

Figure 5.5. (A) Maximum principal stress (σ_1) versus minimum principal stress (σ_3) plots showing the experimental results on Carrara marble and **(B)** Solnhofen limestone. **(C)** Failure surface angle versus differential stress (σ_1 - σ_3) plot for Carrara marble and Solnhofen limestone. Note the rapid increase in the failure surface angle where σ_3 has a shift into the compressive domain, which occurs at a slightly higher differential stress than the unconfined compressive strength.

at a slightly higher differential stress than the C_0 for each lithology (σ_1 - σ_3 = σ_1 = C_0), which is also where the σ_3 at failure has a marked excursion into the compressive (positive) domain, and thus a more rapid rate of increase in the values of θ (Fig. 5.5A, B, C).

5.5. Petrographical characterization of failure

5.5.1. Macrostructural characterization of failure

From a macroscopic perspective, the results of this study are largely analogous to the failure characteristics that have been documented in previous works (cf. Brace, 1964; Hancock, 1985; Reches and Lockner, 1994; Wibberley et al. 2000; Ramsey and Chester,

2004). In both CM and SL, tensile failure results in a one or more discrete cracks, which are oriented parallel to σ_1, with displacement normal to the crack surface (Fig. 5.6A). Although these cracks have a measured angle of 0°, their surfaces are commonly undulating at the grain-scale with areas of reflective intragranular cleavages and plumose markings. In contrast, shear failure on an inclined surface results in a fault with displacement parallel to the fault surface (Fig. 5.6B, C, D). The failure surface is typically covered by a fine powder of comminuted grains (fault gouge) and the surface has small mechanical wear grooves that are oriented parallel to the line of slip (slickenlines). As the confining pressure increases, the failure surface angle (θ) progressively increases with respect to σ_1, and this occurs both in axisymmetric extension and shortening.

In the transitional region between tensile failure and shear failure, the shear faults that are formed have intermediate characteristics between these two endmembers. In both CM and SL, these petrographical characteristics include isolated patches of reflective, intragranular cleavages between areas of comminuted grains with slip lineations (slickenlines). At lower confining pressures (σ_1), the failure surfaces have a higher proportion of cleaved grains relative to comminuted grains. In contrast, the failure surfaces at higher confining pressures have a higher proportion of comminuted grains relative to the proportion of cleaved grains.

Ramsey (2003), Ramsey and Chester (2004), and Rodriguez (2005) presented detailed petrographical studies of the transition from tensile failure to shear failure in CM. Thus, the following microstructural analyses focus on the behaviour of SL.

5.5.2. Microstructural characterization of tensile failure in Solnhofen limestone

In sections cut parallel to the specimen axis, tensile failure in SL involves a series of discrete cracks with negligible strain present in the regions between cracks (Fig. 5.7A). These long, transgranular cracks are consistently oriented parallel to σ_1 and normal to σ_3. The cracks typically cleave and propagate through numerous calcite grains, but rarely

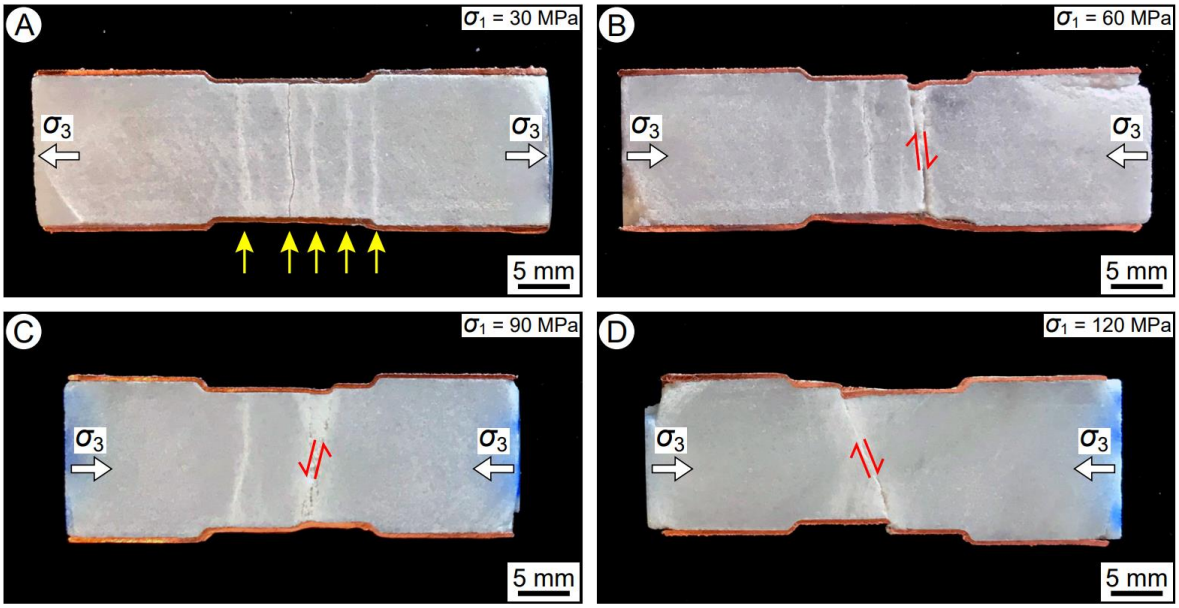

Figure 5.6. Photographs of longitudinally-cut samples of Carrara marble tested in axisymmetric extension, illustrating the transition from tensile failure to shear failure with increasing confining pressure ($\sigma_1 = \sigma_3$). **(A)** CM_E04 (failure angle = 0°), **(B)** CM_E12 (failure angle = 2°), **(C)** CM_E11 (failure angle = 14°), and **(D)** CM_E08 (failure angle = 22°). Note that The local strain-hardening of the jacket allows multiple cracks to develop in Fig. 5.6A. σ_3 is tensile in Fig. 5.6A, but it is compressive in Fig. 5.6B, C, D. Yellow arrows = extensional cracks. Red arrows = shear sense.

propagate through quartz grains (Fig. 5.7B). Under plane-polarized light, a thin, discoloured region is typically present in the region that is adjacent to the macroscopic crack surface (Fig. 5.7A). Given that there are no grain-scale cracks adjacent to the macroscopic crack (Fig. 5.7B), this discoloration is due to the epoxy resin that was able to enter the matrix intergranular porosity by permeation from the crack.

5.5.3. Microstructural characterization of shear failure in Solnhofen limestone

In extension, shear failure in SL involves the coalescence of multiple tensile cracks into a shear-mode fault (Fig. 5.7C, D). These tensile cracks are typically short, but transgranular, and have numerous grain-scale tensile cracks and comminuted grains that are located in-between them (Fig. 5.7D). The abundances of the grain-scale tensile cracks and the comminuted grains are heterogeneously distributed throughout the rock matrix (Fig. 5.7D). The failure surface has a pronounced stair-step pattern that links these short transgranular cracks (Fig. 5.7C).

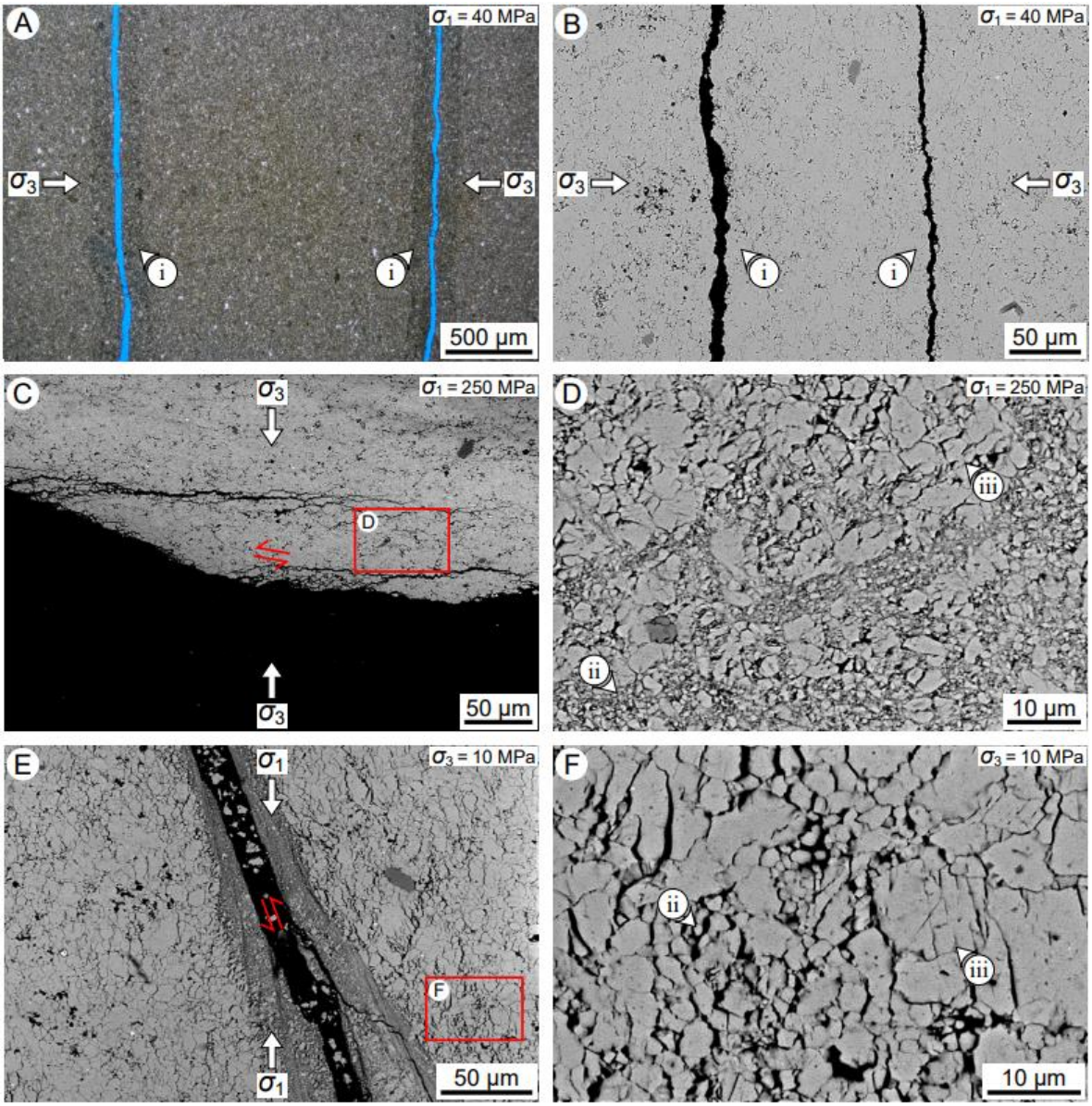

Figure 5.7. (A) Transmitted light photomicrograph and **(B)** back-scattered electron (BSE) photomicrograph showing tensile failure in Solnhofen limestone (sample ID = SL_E04). Note that (i) there are no grain-scale cracks adjacent to the macroscopic crack. **(C, D)** BSE photomicrographs showing shear failure in axisymmetric extension in Solnhofen limestone (sample ID = SL_E13). **(E, F)** BSE photomicrographs showing shear failure in axisymmetric shortening in Solnhofen limestone (sample ID = SL_S07). Note the (ii) grain-scale cracks and (iii) comminuted grains.

In shortening, shear failure in SL involves the coalescence of numerous, grain-scale, tensile cracks into a shear-mode fault (Fig. 5.7E, F). The longer, transgranular, tensile cracks that were present in axisymmetric extension are strikingly absent in shortening. Adjacent to the macroscopic failure surface, comminuted grains are notably more abundant in axisymmetric shortening relative to in extension (Fig. 5.7E). In contrast, the grain-scale

tensile cracks are largely homogenously distributed throughout the rock matrix (Fig. 5.7E, F). At higher confining pressures ($\sigma_3 \geq 40$ MPa), ductile deformation (e.g., intracrystalline twinning, dislocation glide, distributed cataclastic flow) is the dominant mechanism by which strain is accommodated within the specimen. In particular, differential stresses above 350 MPa are required to induce deformation twinning in SL at room temperature, as compared to 90 MPa in CM (Rowe and Rutter 1990; Rutter et al. 2022).

5.5.4. The transition from tensile failure to shear failure in Solnhofen limestone

In the region of transition between tensile failure and shear failure in SL, failure involves the coalescence of relatively few, long tensile cracks into a shear-mode fault (Fig. 5.8A, B, C, D). With increasing confining pressure (σ_1), these tensile cracks systematically become shorter and more tightly spaced as the failure surface angle (θ) increases (Fig. 5.8B, D). At lower confining pressures, the tensile cracks are widely spaced, and they are linked by a low angle failure surface that has a faint stair-step pattern (Fig. 5.8B). In contrast, the tensile cracks are more tightly spaced at higher confining pressures, and they are linked by a moderate angle failure surface that has a more pronounced stair-step pattern (Fig. 5.8D). The discolouration adjacent to the macroscopic failure surface (Fig. 5.8A, C) is due to the infiltration of the epoxy resin into the dilated region that includes these grain-scale and transgranular cracks.

It is challenging to investigate the role of stepped tensile cracks and their contribution to brittle failure within the throughgoing macroscopic fault because there has been a loss of fragmented and incohesive material from the fault region during shearing prior to fabrication of the section. In the matrix of the sample, however, there are numerous examples of these stepped cracks where the rock has accommodated less bulk strain (Fig. 5.8E, F). These long tensile cracks are consistently oriented parallel to σ_1, normal to σ_3, and terminate laterally within the sample where no faulting has developed. Their apertures are greatest at the mid-point of the crack, and they decrease laterally until the crack tips (Fig.

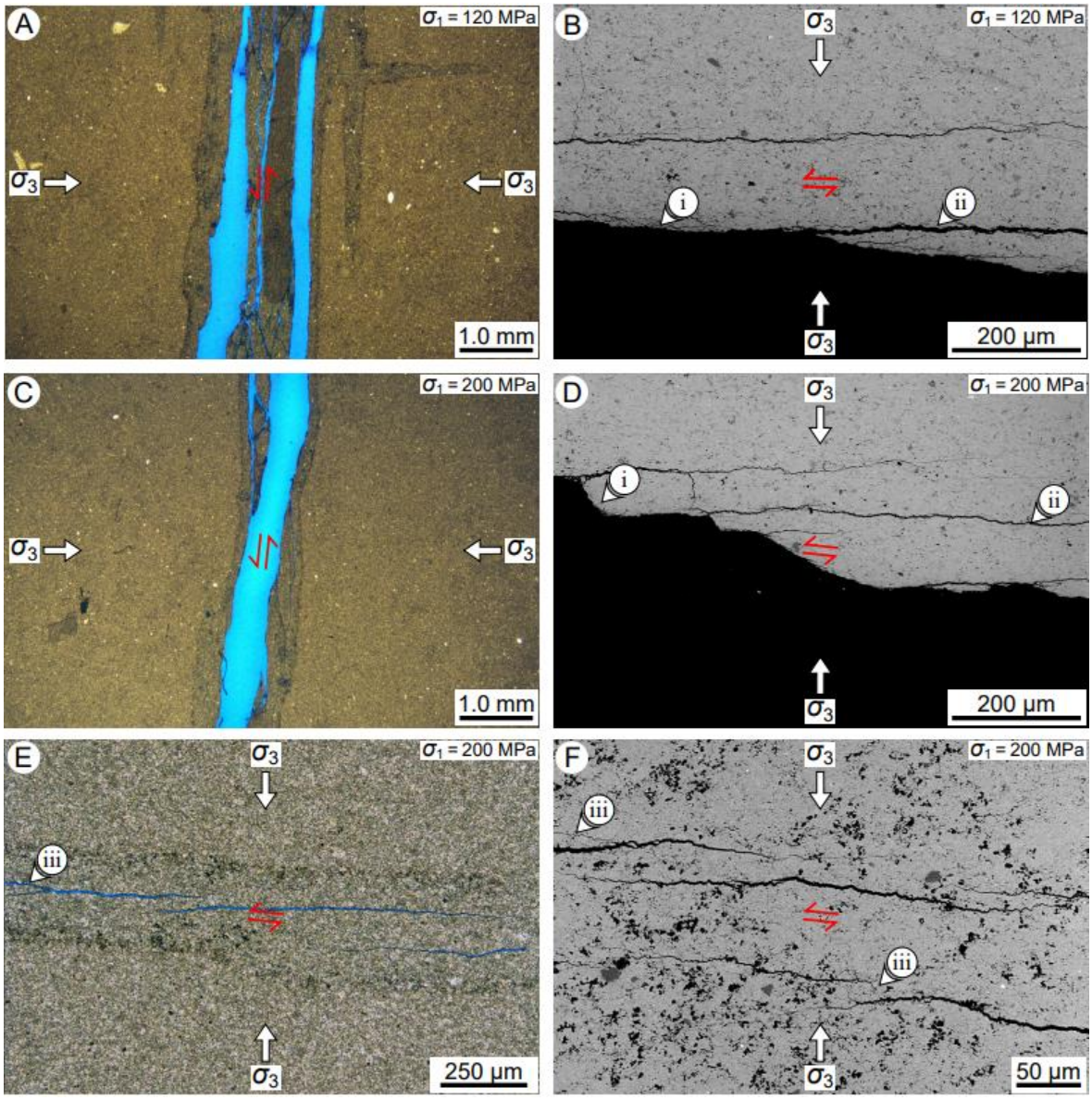

Figure 5.8. (A, C) Transmitted light photomicrographs and **(B, D)** BSE photomicrographs showing the transition between tensile failure and shear failure in Solnhofen limestone (sample IDs = SL_E18 and SL_E08). Note the orientation of the (i) inclined failure surface between the (ii) transgranular tensile cracks. **(E)** Transmitted light photomicrograph and **(F)** BSE photomicrograph showing the nucleation of stepped cracks in Solnhofen limestone (sample ID = SL_E08). Note the (iii) nascent, inclined cracks at the margins of the transgranular tensile cracks (i.e., wing cracks) that probably imply incipient sliding along the extensional cracks.

5.8F). Smaller, nascent cracks (i.e., wing cracks) have formed at the margins of these larger tensile cracks and are typically inclined at a similar angle as the risers of the stepped macroscopic failure surface (Fig. 5.8F).

Based on their petrographical characteristics, it is unfeasible to distinguish samples that were deformed in the upper part of the tensile failure regime from those that were

deformed in the lower part of a theoretical "hybrid failure" regime. Similarly, it is unfeasible to differentiate samples that were deformed in the upper part of this "hybrid failure" regime from those that were deformed in the lower part of the shear failure regime.

5.6. Interpretation of the experimental data

5.6.1. Compatibility of tests in axisymmetric extension vs. shortening

Figure 5.5 shows the results of experiments performed under axisymmetric extension and shortening. These are the end-members of polyaxial deformation, with $\sigma_1 = \sigma_2 > \sigma_3$ in extension and $\sigma_1 > \sigma_2 = \sigma_3$ in shortening. It is widely considered that σ_1 and σ_3 are the main controls on brittle failure, but σ_2 also affects the mean $((\sigma_1 + \sigma_2 + \sigma_3)/3)$ and differential stress at failure, as well as the failure surface angle (Handin et al. 1967; Colmenares and Zoback, 2002; Haimson and Rudnicki, 2010). Volume expansion, due to the creation and opening of microcracks, requires mechanical work to be done against the mean stress on the rock. It is therefore to be anticipated that higher values of σ_2, as well as of σ_3, will result in higher values of mean, and thus of differential stress at failure. For both CM and SL, the data at the axisymmetric extension and shortening end-members are, considering the limits of experimental error, contiguous (Fig. 5.5A, B). Therefore, no corrections to the data are necessary in this respect. Bobich (2005) found that the same was true for Berea sandstone.

Colmenares and Zoback (2002) examined data from Mogi (1967, 1971), Takahashi and Koide (1989), and Chang and Haimson (2000) for failure of several lithologies, across a range of true triaxial conditions, using seven different failure criteria (typically based on functions of stress invariants). For all lithologies, the main strengthening effect of σ_2 occurs when it lies approximately halfway between σ_1 and σ_3. For SL, however, only the Mogi (1971) criterion and the modified Lade criterion (Lade, 1977; Ewy, 1999) describe the mechanical behaviour fairly well across the range of stress conditions. The Mogi (1971) criterion also predicts no difference between the strengths at the axisymmetric extension and shortening end-members, as is observed in our data (Fig. 5.5). Figure 5.9

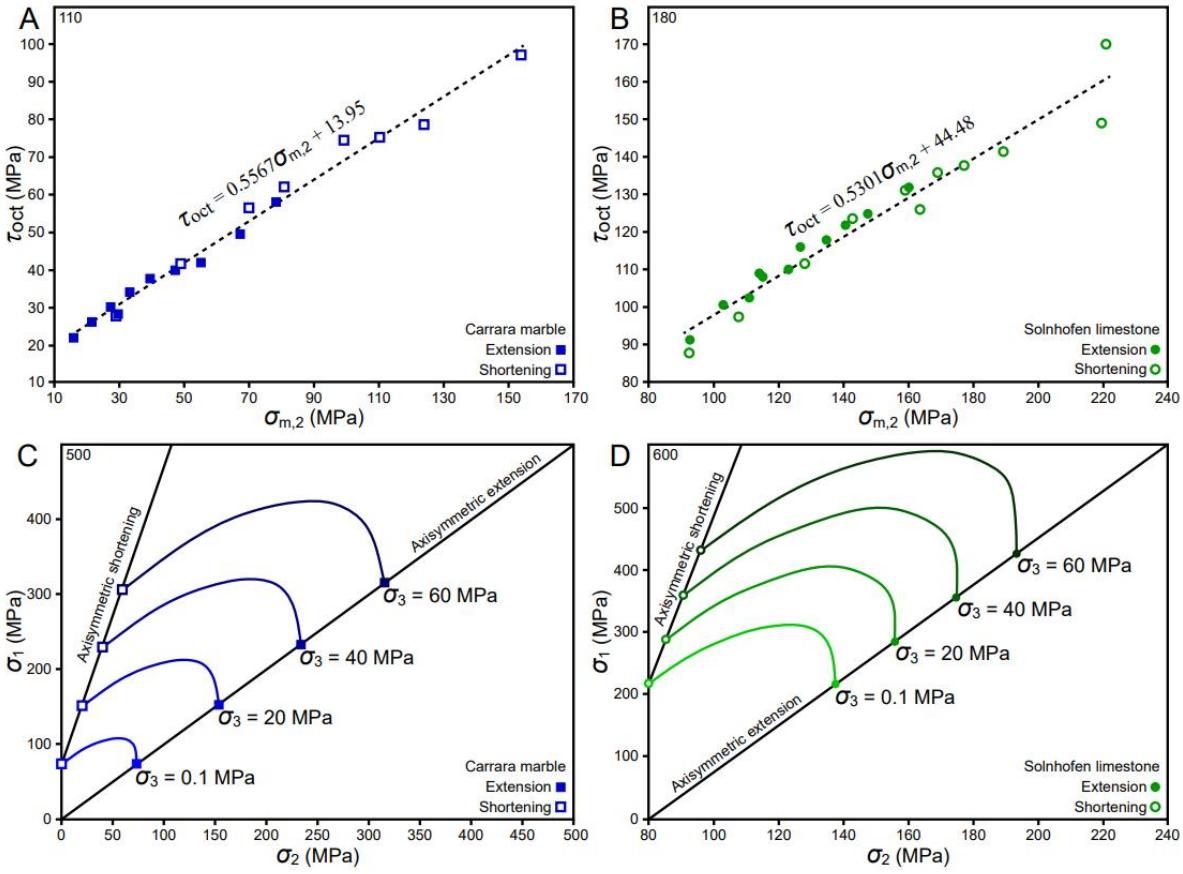

Figure 5.9. Application of the Mogi (1971) criterion to our data on **(A)** Carrara marble (n = 18) and **(B)** Solnhofen limestone (n = 22). **(C, D)** Such a criterion allows polyaxial behaviour to be predicted by using axisymmetric extension and shortening data to plot σ_1 versus σ_2 for a series of constant values of σ_3. Note that the fits do not include data from the parabolic part of the failure envelope, and they do not include data from the highest confining pressures, where intracrystalline plasticity and deformation twinning are significant.

shows the application of the Mogi (1971) criterion to our experiments on SL and CM, demonstrating the expected strengthening for intermediate values of σ_2. The application of the Mogi (1971) criterion facilitates the prediction of polyaxial behaviour, while satisfying the empirical constraint that the differential stress is the same at both the axisymmetric shortening and extension ends of the curves for constant values of σ_3 (Fig. 5.9).

Mogi (1971) proposed that the octahedral shear stress (τ_{oct}) at failure is a function of the mean of the maximum and minimum principal stresses ($\sigma_{m,2} = (\sigma_1 + \sigma_3)/2$). The function can be linear, a power function, or a polynomial. The justification for using $\sigma_{m,2}$ rather than $\sigma_{m,3}$ ($(\sigma_1 + \sigma_2 + \sigma_3)/3$) is that the failure plane is expected to contain the σ_2 axis,

hence the mean stress should be independent of σ_2. Thus, the Mogi (1971) polyaxial criterion is given by:

$$\tau_{\mathrm{oct}} = \frac{1}{3}\sqrt{(\sigma_1 - \sigma_2)^2 + (\sigma_2 - \sigma_3)^2 + (\sigma_3 - \sigma_1)^2} = f\left(\sigma_{\mathrm{m},2}\right) \quad (5.6)$$

The octahedral shear stress is related to the second stress invariant by:

$$\tau_{\mathrm{oct}} = \sqrt{\frac{2J_2}{3}} \quad (5.7)$$

Assuming a linear form for $f(\sigma_{\mathrm{m},2})$, the criterion becomes:

$$\tau_{\mathrm{oct}} = m\frac{(\sigma_1+\sigma_3)}{2} + b \quad (5.8)$$

where *m* and *b* are empirical coefficients from the ploted experimental data (Fig. 5.9A, B).

5.6.2. Fitting a function to shear stress vs. normal stress on the failure surface

The maximum values of resolved normal stress (σ_{n}) and shear stress (τ) on the observed failure surfaces from each experiment, calculated using Eq. 5.2 and 5.3, are summarized in Table 5.2. For each lithology, a parabola provides an ideal fit to the data (Fig. 5.10A, B). For CM and SL, the least-squares best fit parabolic functions plotted in Fig. 5.10A and B are:

$$\sigma_{\mathrm{n}} = 0.0144\tau^2 - 2.9 \quad (5.9)$$

for Carrara marble, and:

$$\sigma_{\mathrm{n}} = 0.0085\tau^2 - 0.8 \quad (5.10)$$

for Solnhofen limestone. For CM, the standard errors in σ_{n} and τ are 6.8 and 6.2 MPa, whereas they are 3.1 and 5.5 MPa for SL (Fig. 5.10A, B). The tensile strengths (*T*) are not well constrained by the curve fitting because the uncertainties of the measured values of *T* are commensurate with the values themselves. The values of *T* depend on the difference between two similarly sized numbers, the applied confining pressure and the measured differential stress. Thus, the values of *T* used to constrain the curve fitting were taken to be -2.9 MPa (*n* = 2; Table 5.2) and -0.8 MPa (*n* = 10; Table 5.2) for CM and SL, respectively. These are the averages of the measured values for the samples that were deformed at the

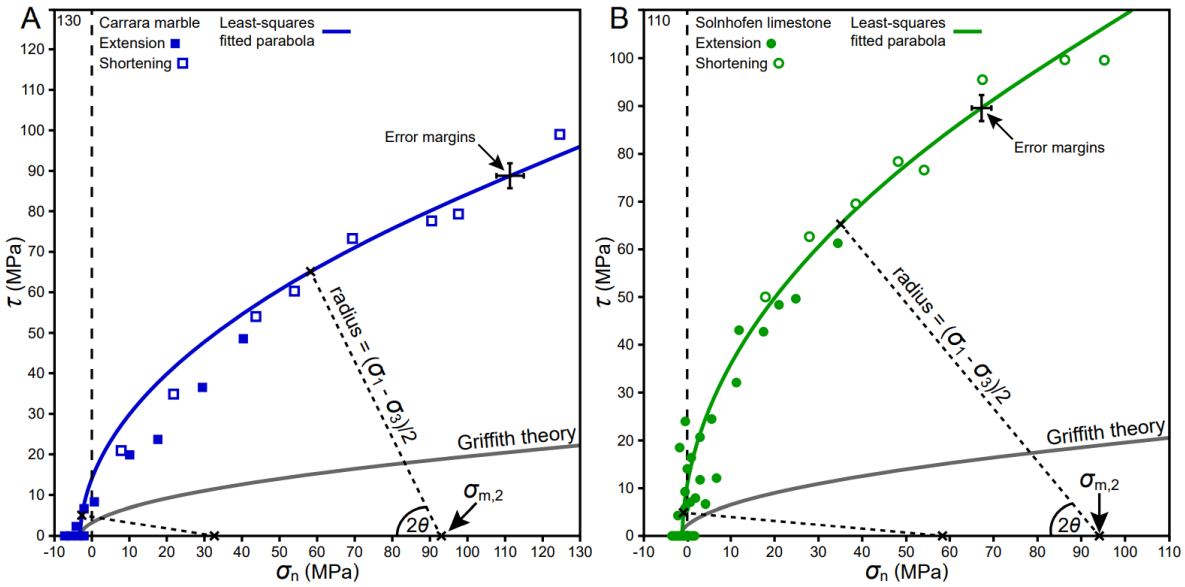

Figure 5.10. Least-squares fitted parabolas for the experimental results on **(A)** Carrara marble (Eq. 5.9) and **(B)** Solnhofen limestone (Eq. 5.10) plotted in the τ versus σ_n coordinate frame. Note that the mechanical strengths are higher than predicted by the Griffith (1921) criterion for the observed tensile strengths. The radii of Mohr circles (dashed lines, tangent to the parabolic curves) are to illustrate how the circles correspond to failure surface angles θ, according to the classical Mohr-Coulomb theory outlined in section 5.2, and hence how θ is observed to increase with increasing σ_n.

lowest of confining pressures, and that underwent tensile failure. According to the above measurements, the apparent T of CM is greater than that of SL. This is to be expected because the greater brittleness of the latter implies a lower fracture toughness (K_{1c}). Atkinson (1979) reports K_{1c} for SL to be 0.8 MPa√m and Spagnioli et al. (2015) report 1.3 MPa√m for CM. Xu et al (2018), following Zhang (2002), compared tensile strength with fracture toughness for a wide range of rock types and concluded that tensile strength increases linearly with fracture toughness, albeit with a wide scatter.

The classical application of the Mohr analysis can involve two different approaches to obtain a Mohr failure criterion from a suite of experimental data. The first method involves fitting a function to the values of σ_n and τ on the observed failure surfaces, calculated from the measured values of σ_1, σ_3, and θ; as has been done above. At any given value of σ_n and τ, the expected failure surface angle (θ), and values of the mean stress ($\sigma_{m,2}$), σ_1, and σ_3 can be calculated from a line that is normal to the best-fit parabola (radius of the Mohr circle at

that point; Fig. 5.10A, B). The radii of these circles intersect the parabola at tangent points that are given by Eq. 5.11 and 5.12 for CM and SL, respectively:

$$\frac{\mathrm{d}\sigma_\mathrm{n}}{\mathrm{d}\tau} = 0.0288\tau = \tan 2\alpha \tag{5.11}$$

$$\frac{\mathrm{d}\sigma_\mathrm{n}}{\mathrm{d}\tau} = 0.0170\tau = \tan 2\alpha \tag{5.12}$$

where α is the orientation of the failure surface relative to the observed (σ_n, τ), assuming that the Mohr circle is precisely tangent to the parabola. In this case $\alpha = \theta$. The measured values of θ are compared to the back-calculated angle α in Fig. 5.11. For CM, $\alpha = 0.93\theta$, but for SL $\alpha = 1.60\theta$ (Fig. 5.11A, B, C). The difference between α and θ is insignificant for CM, within the limits of experimental error, but it is substantial in the case of SL. Thus, the Mohr circles that are based on the observed differential stresses for SL lie beyond the Mohr failure criterion that was calculated from the observed failure angles, and the Mohr envelope to these circles will lie above the above parabola from Eq. 5.10 (Fig. 5.11C).

5.6.3. Fitting an envelope to a series of Mohr circles

The second approach to the Mohr analysis and the description of failure involves fitting an enveloping curve, in this case a different parabola, to the tangents to a series of Mohr circles drawn using the measured values of σ_1 and σ_3 (e.g., Lisle and Strom, 1982; Bland, 1983). The enveloping curve is expected to have the same tensile strength intercept ($-T$) on the σ_n axis, but the previous parabola (Eq. 5.9, 5.10) will intersect any Mohr circle (defined by the measured values σ_1 and σ_3) in two points (Fig. 5.11B, C). Writing these equations in general terms, $\sigma_\mathrm{n} = a\tau^2 + b$, where parameter b equals the tensile strength intercept. Decreasing the parameter a by a multiplier n to become $a' = an$, which expands the parabola vertically, will cause the two intercepts of the circle on the parabola to move together. The two intercepts become one at the point (σ_n, τ), when the circle is tangent to the parabola, and the condition for one intercept is given by:

$$\left(2a'\sigma_{\mathrm{m},2} - 1\right)^2 = 4a'^2r^2 + 4a'b \tag{5.13}$$

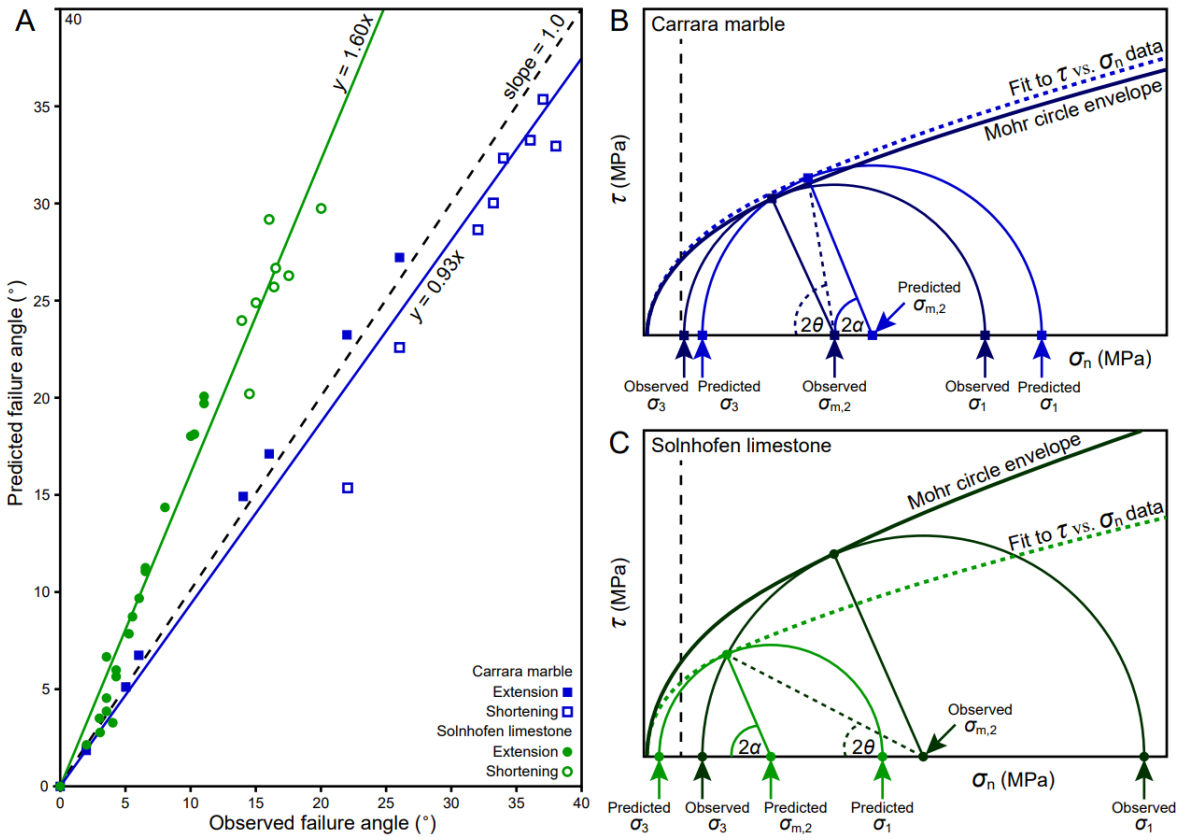

Figure 5.11. (A) Relationship between the failure surface angles that are predicted from an envelope to a series of Mohr circles relative to the observed failure surface angles. **(B, C)** Conceptual diagrams showing the two different methods to obtain Mohr envelopes from the suite of experimental data on Carrara marble and Solnhofen limestone, respectively.

where r is the radius of the Mohr circle. The two roots of this equation (a') are equal and of opposite sign, and they correspond to the two arms of the parabola, reflected across $\tau = 0$.

A single parabolic Mohr envelope will not lie precisely as tangent to all of the Mohr circles, which are defined by the values of σ_1 and σ_3 from the experimental data. A best fit parabola must be found. This can be done by calculating the tangent point coordinates to a parabola for each Mohr circle, then carrying out a least-squares analysis to obtain the best fit enveloping parabola to the entire set of Mohr circles, in the same way as was done in section 6.2. The coordinates of the points (σ_n, τ) to be fitted to this parabolic envelope are given by:

$$\sigma_n = \sqrt{\frac{(\sigma_1+\sigma_3)}{2} - \left(\frac{1}{2}a'\right)} \qquad (5.14)$$

$$\tau = \sqrt{(\sigma_1 - \sigma_3)^2 - \left(\frac{1}{2}a'\right)^2} \quad (5.15)$$

Thus, the parabolas that best describe the envelopes to the Mohr circles are given by:

$$\sigma_n = 0.0145\tau^2 - 2.9 \quad (5.16)$$

$$\sigma_n = 0.0064\tau^2 - 0.8 \quad (5.17)$$

for CM and SL, respectively. For CM, there is no significant difference between the parabola that describes failure in terms of the resolved σ_n and τ on the observed failure surfaces and the parabola that is an envelope to a series of Mohr circles (Fig. 5.11B). There is also no significant difference between the two parabolas after transformation to the σ_1 versus σ_3 coordinate frame (Fig. 5.12B). For SL however, the difference between the two parabolas is pronounced in the τ versus σ_n coordinate frame (Fig. 5.12A) and when they are transformed into σ_1 versus σ_3 and compared with the experimental data (Fig. 5.12C). For CM, the standard errors in σ_3 and σ_1 are 3.5 and 12.9 MPa, whereas they are 3.7 and 14.4 MPa for SL (Fig. 5.12B, C).

5.6.4. Evolution of the failure surface angle with increasing differential stress

Following the Mohr-Coulomb model outlined in section 2, the slope of the failure envelope in the positive stress quadrant is commonly assumed to be linear. The coefficient of internal friction (μ_c) is in this instance a constant value, and it implies that the deviatoric stress state (i.e., the relative value of the intermediate principal stress) is irrelevant. Therefore, the orientation of the localized shear failure surface (θ) is expected to be constant and given by:

$$\theta = \frac{\pi}{4} - \frac{1}{2}\tan^{-1}\mu_c \quad (5.18)$$

In a plot of τ versus σ_n, the angle 2θ is subtended by a line that is normal to the failure envelope $f(\sigma_n, \tau)$ that intersects the abscissa at ($\sigma_{m,2}$, 0). Our experimental results for CM and SL show that the Mohr-Coulomb model is an inadequate descriptor because μ_c is not

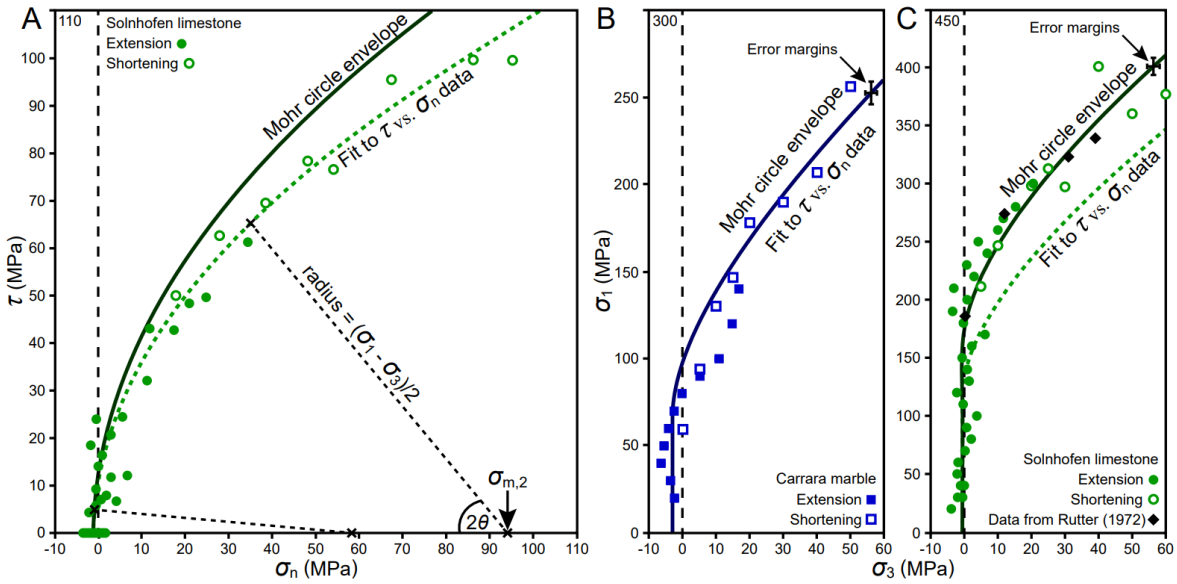

Figure 5.12. (A) Relationship between the two types of Mohr envelopes for Solnhofen limestone (for Carrara marble there is negligible difference between the two parabolas). **(B, C)** Relationships between the plots of the observed σ_1 versus σ_3 data and the corresponding curves arising from the two types of parabolic Mohr envelopes for Carrara marble and Solnhofen limestone, respectively.

constant. For CM, however, the failure surface angle does appear to be related to the local orientation of the normal to the parabolic failure envelope (Fig. 5.10A, 5.11A, B).

Following the Rudnicki and Rice (1975) analysis of the failure of dilatant materials using bifurcation theory, Rudnicki and Olsson (1998) investigated the controls on the localization of deformation into shear bands. For the orientation of failure surfaces with respect to the direction of maximum principal stress, Rudnicki and Olsson (1998) suggested that:

$$\theta = \frac{\pi}{4} - \frac{1}{2}\sin^{-1}\alpha \tag{5.19}$$

where

$$\alpha = \frac{\frac{2}{3}(1+\nu)(\beta+\mu) - N(1-2\nu)}{\sqrt{4-3N^2}} \tag{5.20}$$

in which ν is Poisson's ratio and β is the dilatancy angle. The dilatancy angle is given by the rate of change of volumetric strain with respect to the shear strain at the point of failure. In brittle rocks at low confining pressures, the volumetric strain is dilatant. The

term μ is the local slope of the yield curve in a plot of von-Mises equivalent stress (σ_{vm}) against the mean stress ($\sigma_{m,3} = (\sigma_1 + \sigma_2 + \sigma_3)/3$), and the von-Mises equivalent stress (σ_{vm}) is given by:

$$\sigma_{vm} = \frac{1}{\sqrt{3}}\sqrt{\frac{(\sigma_1-\sigma_2)^2+(\sigma_1-\sigma_3)^2+(\sigma_2-\sigma_3)^2}{2}} \quad (5.21)$$

N describes the deviatoric stress state and is the ratio of the intermediate principal deviatoric stress to σ_{vm} ($N = (\sigma_2 - \sigma_{m,3})/\sigma_{vm}$). *N* ranges from $-1/\sqrt{3}$ in axisymmetric extension to $1/\sqrt{3}$ in shortening, and it is implied that failure surface angles are smaller in extension than in shortening. *N* is zero for deviatoric pure shear. Anisotropy, including preferentially-oriented microcracks, impacts the values of the above parameters at failure (Rudnicki, 1977). Planar crack arrays develop in axisymmetric extension, but in shortening they are oriented radially and intersect in the maximum compressive stress orientation. These differences between axisymmetric extension and shortening are not considered here, but constraints on the values of all the above listed parameters are discussed by Rudnicki and Olsson (1998).

The values of these parameters are rarely available from experimental studies, but see Haimson and Rudnicki (2010), Ingraham et al. (2013), and Ma et al. (2017) for siliciclastic rocks. Rybacki et al. (2021) and Edmond and Paterson (1972) provide volumetric strain data for CM and SL, respectively, but not to sufficient resolution for the purposes required. We can, however, examine semi-quantitatively how reasonable values predict the failure surface angles compared to those that were measured in this study. von-Mises equivalent stresses were plotted against values of mean stress for both CM and SL (Fig. 5.13A, B). From their slopes, which decrease as the mean stress increases, a function $\mu = f(\sigma_n)$ is obtained. Next, the observed failure surface angles were plotted against the respective angles that were calculated using Eq. 5.19 (Fig. 5.13C, D). Estimated values for Poisson's ratio (ν) and dilatancy angle (β) were used to obtain a reasonable match to the observed fault angles. The dilatancy angle was first assumed be equal to the friction angle (ϕ), and

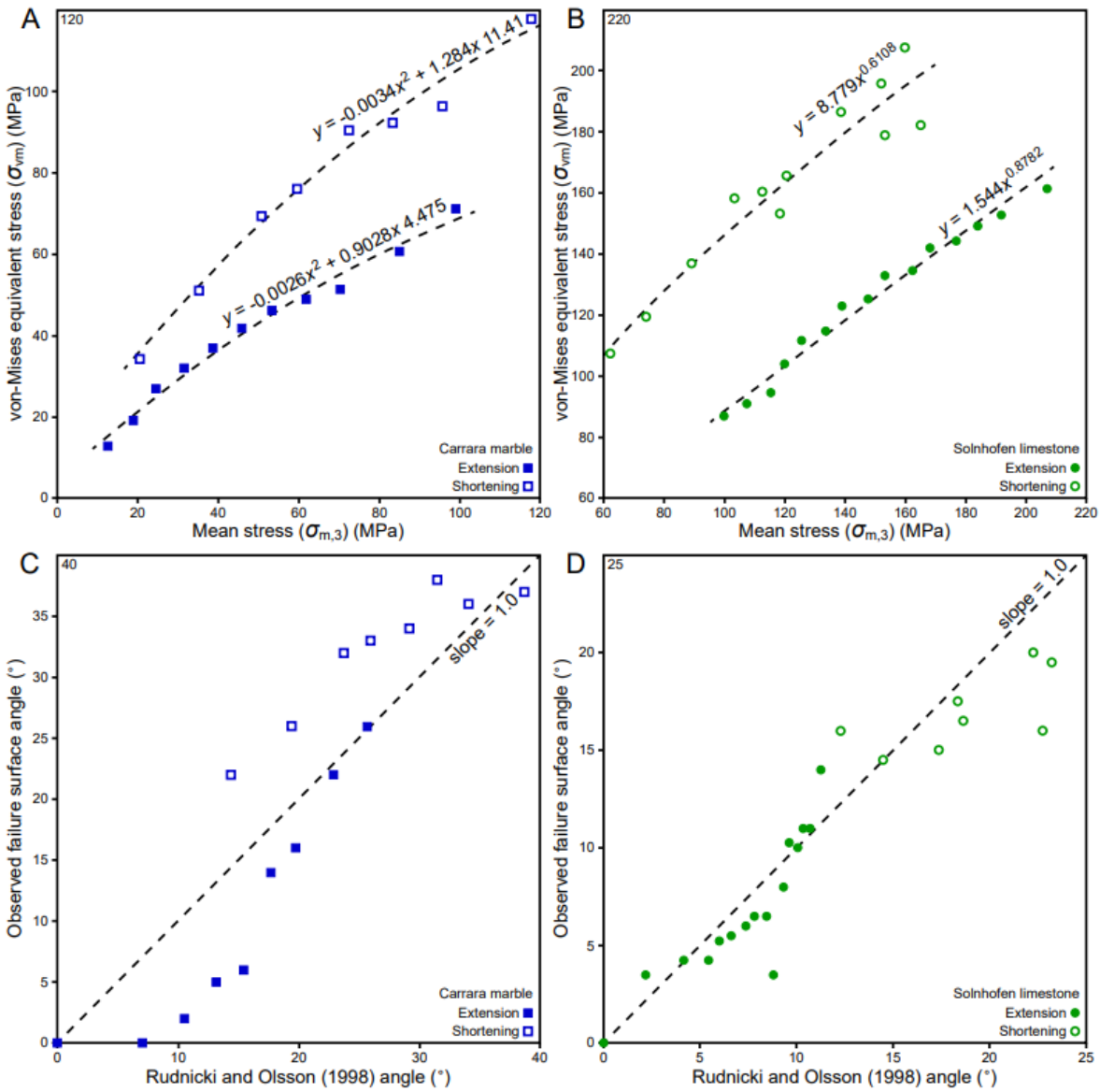

Figure 5.13. (A) von-Mises equivalent stress (σ_{vm}) versus mean stress ($\sigma_{m,3}$) for Carrara marble and **(B)** Solnhofen limestone. From their slopes, the predicted failure surface angles were calculated from Eq. 5.19 (Rudnicki and Olsson, 1998) and plotted against the observed failure surface angles for **(C)** Carrara marble and **(D)** Solnhofen limestone.

then iteratively modified by a multiplier of 1.25×. Linking β to ϕ means that the former decreases with increasing mean stress, as is expected given that dilatancy is progressively suppressed by elevation of the mean pressure (Edmond and Paterson, 1972; Rybacki et al. 2021). Equation 5.19 explains the observed trend that the failure surface angle increases with increasing mean pressure, and that the trend is continuous from axisymmetric extension to shortening (Fig. 5.13C, D). Therefore, there appears to be no reason to believe

that the orientation of the failure surface should be predictable simply from the local orientation of the normal to the Mohr failure envelope, as it also depends on other factors.

5.7. Discussion

5.7.1. Evolution of the failure surface angle with increasing differential stress

For both CM and SL, a progressive increase of the failure surface angle with increasing differential stress was observed to occur. For CM the observed variation was in accordance with the with the normal to the envelope of Mohr circles, but this was not the case for SL, for which observed failure angles were consistently smaller than predicted. Studies by other authors, mainly on siliciclastic rocks, have demonstrated variations in failure surface angles with differential stress also occur. Back-analysis of the data of Ma et al. (2017) data for Coconino sandstone shows that the behaviour is very similar to that of our results for CM. Our SL data also show that the failure surface angles evolve markedly with the differential stress at failure, but the resolved σ_n and τ on the failure surfaces for SL are systematically much less than at the tangent point of each Mohr circle with the envelope of those circles (Fig. 5.11A, C). The same applies to the SL (1.5% porosity) data that was reported by Heard (1960) and to two siltstone samples from the Taiwan Chelungpu Fault Drilling Project (Haimson and Rudnicki, 2010). Similarly, Dansereau et al. (2019) carried out numerical simulations of damage accumulation in a theoretical elasto-damageable material that predicted faults can occur along orientations that are different from the Mohr-Coulomb maximum stress prediction. Their results are congruent with previous works by Girard et al. (2010), Kaus (2010), and Finzi et al. (2013). Thus, while the Mohr envelope is a widely used criterion for failure and the prediction of failure surface orientation, it does not always accurately predict the latter.

5.7.2. Evolution of the failure mechanism with increasing differential stress

Although Griffith theory and the empirical Mohr-Coulomb criterion provide a first-order approximation of the stress conditions that give rise to failure and the general failure

mode, the mechanistic sequence by which tensile microcracking transitions into mesoscopic shear faulting is equivocal. Thus, a "hybrid failure" mode has long been hypothesized as a transitional regime between these end-members failure modes and their respective criteria (Brace, 1964; Hancock, 1985; Engelder, 1999; Ramsey and Chester, 2004). According to Hancock (1985), this transitional failure mode occurs from $4T < \sigma_1 - \sigma_3 < 8T$; a range commonly repeated in more recent works (Ferrill et al. 2012, 2017). Our experiments on CM and SL demonstrate that the transition from tensile failure to shear failure occurs at a much higher differential stress than previously suggested. Based on the fitted parabola for CM (T = -2.9 MPa), the differential stress at failure when $\sigma_n = 0$ is 75.0 MPa, thus $\sigma_1 - \sigma_3 = 25.9T$ (Fig. 5.10A). Based on the parabola for SL (T = -0.8 MPa), the differential stress at failure when $\sigma_n = 0$ is 119.1 MPa, thus $\sigma_1 - \sigma_3 = 148.9T$ (Fig. 5.10B). Attributing a definitive range of stress conditions to a "hybrid failure" mode, however, is imprecise because our mechanical and petrographical data suggests that the transitions between failure modes are part of a continuous spectrum. There is neither a single experiment that defines the boundary between tensile failure and a theoretical "hybrid failure" mode, nor is there an experiment that defines the boundary between "hybrid failure" and shear failure. There are also clear lithological controls on characteristics of the failure surface that are not captured by variations in T.

The first experiments investigating the transition from tensile failure to shear failure are those of Brace (1964), but poor experimental reproducibility led Ramsey and Chester (2004) to improve the Brace (1964) sample and jacketing arrangement. Next, Rodriguez (2005) examined the microstructure of the CM samples from Ramsey and Chester (2004), and Bobich (2005) investigated this region of the failure envelope in Berea sandstone. Such works attempted to extrapolate a Griffith-type failure envelope into the tensile field but found that the observed failure surface angles were systematically less than predicted and the mechanical strengths of CM and Berea sandstone were not consistent with a description based on Griffith theory (Ramsey and Chester, 2004; Bobich, 2005). Although

Ramsey and Chester (2004) did not propose a revised criterion, they noted that a continuous, parabolic failure envelope was not an ideal fit to their σ_1 versus σ_3 data. In the τ versus σ_n coordinate frame, however, back-analysis of the Ramsey and Chester (2004) data for CM shows that the behaviour is largely analogous to our results. More recent experimental results (Cen and Huang, 2017; Lan et al. 2019; Huang et al. 2022) and numerical modelling studies (Zhu, 2017; Huang and Zhu, 2018; Boyce et al. 2020) expanded on the work by Ramsey and Chester (2004) in attempt to propose a new failure criterion. Each of these studies noted that there is smooth and continuous transition between tensile failure and shear failure, but a "hybrid failure" mode was arbitrarily, and somewhat inconsistently placed between these end-members. A failure criterion based on a single parabolic function, as is applied here, (i) justifies a smooth transition between failure modes and (ii) can be scaled based on material properties of different lithologies.

Stepped (en-echelon) opening-mode crack arrays have been widely noted to play a role in the transition from tensile failure to shear failure (Engelder, 1999; Ramsey and Chester, 2004; Cen and Huang, 2017), but the failure criteria that are applied and described are typically not rooted in such microstructural observations. Our observations note that tensile failure involves the formation of one or more, discrete, sample-traversing tensile cracks, whereas shear failure involves the formation of numerous, grain-scale tensile cracks that coalesce into a shear-mode fault. A smooth and continuous transition between these end-member failure modes is facilitated by a gradual change in the lengths, spacing, and apertures of the precursory tensile cracks, illustrated schematically in Fig. 5.14. Failure in this transitional region involves the formation of several transgranular, tensile cracks that coalesce into a shear-mode fault. As the confining pressure and differential stress at failure increases, the lengths and spacing of these transgranular cracks gradually become shorter as the failure surface angle increases (Fig. 5.14). The most pronounced differences between the two lithologies that were investigated in this study is that CM is stronger than SL in tensile failure, but SL is stronger than CM in shear failure. Even at the lowest

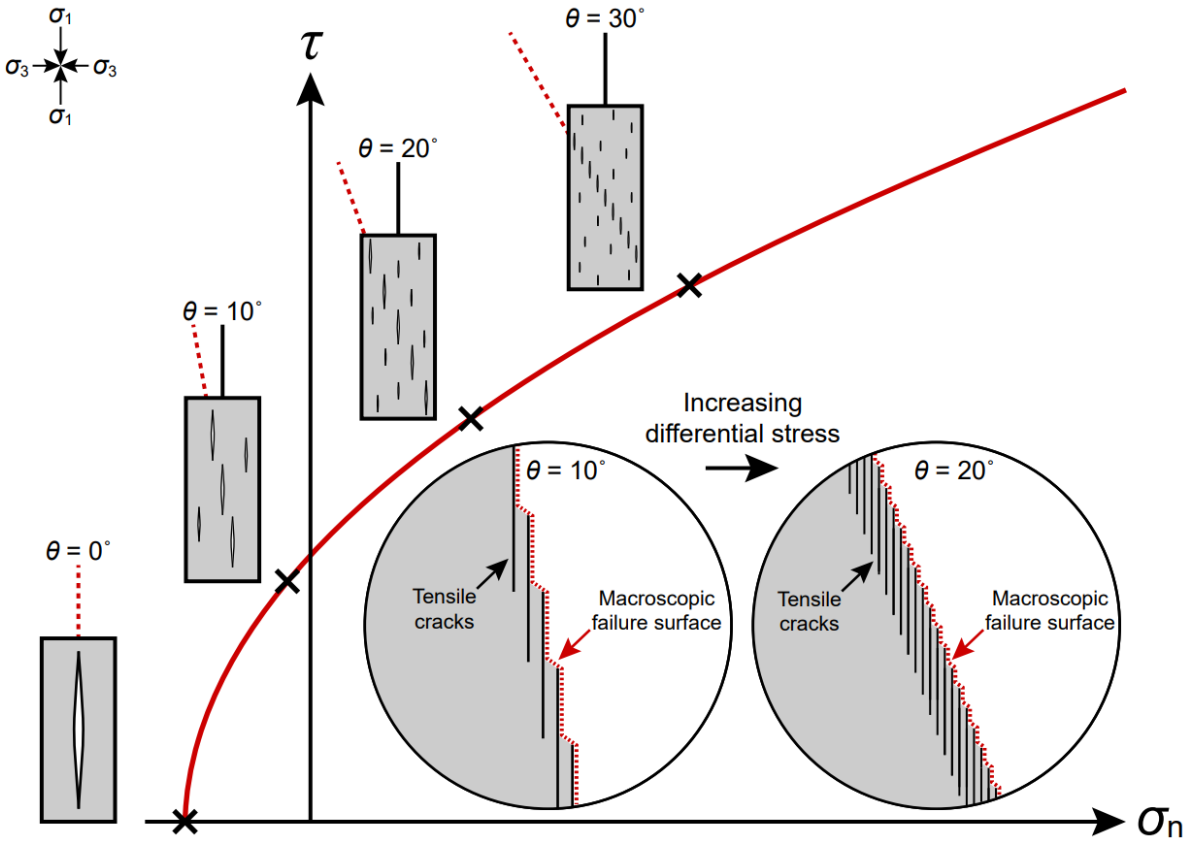

Figure 5.14. Conceptual diagram showing the relative frequencies of the transgranular and grain-scale tensile cracks that were observed in experiments spanning the transitional region from true tensile failure to shear failure. Note the observed trend that the lengths, spacing, and apertures of these precursory tensile cracks decrease with increasing differential stress.

confining pressures, such differences between their mechanical strengths are largely attributed to the pronounced grain size differences and the fact that CM is much more ductile than SL (Schmid et al. 1977; Rutter et al. 1994, 2022; Rybacki et al. 2021). In tensile failure, it requires a larger magnitude of σ_3 (more negative) to nucleate and propagate cracks in CM relative to the more brittle SL. With increasing confining pressure, ductile deformation mechanisms (e.g., intracrystalline twinning, dislocation glide, distributed cataclastic flow) contribute to failure in CM at lower confining pressures relative to in SL.

5.7.3. Irregularities in the form of the failure envelope when σ_3 is tensile

Huang et al. (2022) investigated the mechanical behaviour of a granite (from Hubei, China) and recognized a phase of negative deflection where the σ_3 decreases with

increasing confining pressure in the tensile failure regime, reaches a maximum negative value, then increases as the confining pressure increases in shear failure. Such a distinct negative deflection was noted for CM (Ramsey and Chester, 2004) and our data for CM also show the same effect in the σ_1 versus σ_3 coordinate frame (Fig. 5.5A, 5.12B). Such a phenomenon, however, is not present in our data for SL (Fig. 5.5B, 5.12C). The effect seems to be relatively minor for more brittle lithologies, including Berea sandstone (Bobich, 2005), Longmaxi shale (Lan et al. 2019), and Hubei granite (Huang et al. 2022). Huang et al. (2022) attributed this phenomenon to variation in the frictional force between grains and in the shear stress between the grains as the failure surface angle increases. These factors are impacted by grain size and shape, porosity, and the ductility of the rock. Clearly, increasing the differential stress also increases the mean stress, which in turn increases the frictional forces and inhibits loss of cohesion between the grains. Such a phenomenon would likely be manifested as an increased resistance to the formation of the precursory tensile cracks with increasing differential stress and mean stress.

It should be noted that the negative deflection observed in the σ_1 versus σ_3 coordinate frame is less apparent when the data are transformed into the τ versus σ_n coordinate frame. This occurs due to the corresponding increase in the failure surface angle (θ), which implies that there is an increase in the inter-granular frictional forces. In a similar way to our results on CM and SL, back-analysis of the experiments on CM (Ramsey and Chester, 2004), Berea sandstone (Bobich, 2005), Longmaxi shale (Lan et al. 2019), and Hubei granite (Huang et al. 2022) suggests that a parabolic failure envelope in the τ versus σ_n coordinate frame describes their mechanical behaviour fairly well across the range of stress conditions investigated.

5.7.4. Influence of boundary conditions on failure

Experimental studies of rock failure are most frequently carried out under conditions of lateral confinement by a hydraulic fluid (stress boundary conditions), thus there is no

constraint on lateral displacements. Brittle failure under such loading conditions typically involves the formation of a single tensile crack or shear fault. In nature however, a rock at depth is constrained by an elastic solid in all directions. Together with the effects of polyaxial loading, this can lead to a greater variety of failure geometries, including polymodal faulting, to satisfy the displacement boundary conditions (Reches and Dieterich, 1983; Healy et al. 2015). As a result, natural examples of "hybrid failure" are rare and evidence for this mode of failure in the field can be somewhat ambiguous (Engelder, 1999; Blenkinsop et al. 2020). Ferrill and Morris (2003), for example, documented shear-mode faults in mechanically layered strata where the failure surface angles of the faults in less competent units (10 to 39°) were significantly larger than in more competent units (1 to 9°). Other potential candidates include pinnate joints and en-echelon fractures that are associated with shear-mode faults, as well as veins with oblique crystal growth orientations (Engelder, 1999; Belayneh and Cosgrove, 2010; Bons et al. 2012). Similarly, bedding-inclined zebra textures in fault-controlled dolomite bodies are potential natural examples of low-angle, "hybrid", shear-mode faulting (Vandeginste et al. 2005; McCormick et al. 2021). It is unclear however, whether these rock textures were initiated as such or if the mineralized fractures simply record their post-failure displacement. Such examples of mineralized fractures with oblique crystal growth orientations may involve slow, time-dependent processes and are not definitive evidence of a brittle failure mechanism (Price, 1966; Price and Cosgrove, 1990; Belayneh and Cosgrove, 2010; Bons et al. 2012).

Price (1966) paid particular attention to the occurrence of "semi-brittle" shear zones that, when occurring in conjugate pairs of opposite shear sense inferred to be bisected by the maximum principal stress direction, often subtend a low dihedral angle between them (10 to 20°). Such shear zones are often characterized by an array of dilatant, extensional mineral veins inferred to lie normal to σ_3. These occurrences can be interpreted to imply shear failure under conditions of low differential stress, potentially with a negative effective σ_3. At depths of a few kilometers to mid-crustal depths, the failure of brittle rock

under such low differential stress conditions is likely only to occur if pore-fluid pressures are exceptionally high, close to the least principal stress (σ_3). Such elevated pore-fluid pressures may be produced by a combination of pore compaction, the influx of pressurized fluids expelled from greater depths (e.g., seismic pumping), or diagenetic to low-grade metamorphic dewatering.

5.8. Conclusions

Rock deformation experiments were carried out at room temperature (20°C) on samples of Carrara marble (CM) and Solnhofen limestone (SL) using a rock deformation apparatus that is capable of loading under axisymmetric extension and shortening. This study aimed to investigate the transition from failure under true tensile loading conditions to compressive loading under high effective confining pressures (up to 300 MPa), while also observing the evolution of the peak strength, the orientation of the failure surfaces, and their microstructural characteristics. The results of 63 experiments, which were conducted at an axial strain rate of 2.1×10^{-4} s^{-1} in axisymmetric extension and 7.4×10^{-5} s^{-1} in axisymmetric shortening, are reported. The key conclusions of this study are as follows:

- At low differential stresses, and when σ_3 is tensile, failure results in the formation of one or more opening-mode cracks that are oriented normal to σ_3 and parallel to σ_1.
- At moderate differential stresses, as σ_3 shifts towards the compressive domain, failure involves the formation of several, transgranular tensile cracks that coalesce into a shear-mode fault; typically oriented at <10° to σ_1.
- At high differential stresses, and when all the principal stresses are fully compressive, failure involves the formation of numerous, grain-scale tensile cracks that coalesce into a shear-mode fault, typically oriented in the range of 10 to 30° to σ_1 and with θ increasing as the differential stress increases.

- A continuous parabolic failure envelope, defined by the resolved shear stress and normal stress on the failure surfaces, fits the mechanical behaviours of both lithologies and such a function is rooted in the observation that the lengths, spacing, and apertures of the precursory tensile cracks decrease with increasing differential stress and mean stress.
- Furthermore, the failure surface angle with respect to σ_1 increases for both lithologies as the differential stress increases. Hence, the region often described as "hybrid" failure appears to be nothing other than part of the progressive evolution of the failure angles associated with a continuously curving Mohr failure description in the τ versus σ_n coordinate frame.
- The failure criterion can also be expressed in terms of an envelope of the Mohr circles at failure. For CM, this envelope coincides with the parabola defined by fitting a function to σ_n and τ. In the case of SL, the Mohr envelope parabola is much larger, and the failure surface angles are consistently smaller than those predicted by the "classical" Mohr envelope approach. This discrepancy accords with the application of bifurcation theory by Rudnicki and Olsson (1998) to the prediction of shear fault angles in brittle rocks.

Critically, the mechanical behaviours of CM and SL demonstrate that the transition from tensile failure to shear failure follows a smooth, parabolic failure envelope. This transition occurs when σ_3 at failure displays a marked shift towards, or into, the compressive domain, which is accompanied by the onset of inclination of the failure surface away from being parallel to σ_1 and the development of shear offset. A smooth, parabolic failure envelope is supported by microstructural observations of the number, lengths, and spacing of the precursory tensile cracks that contribute to failure. Whilst there is no evidence of a distinct "hybrid failure" mode, the low-angle shear-mode faults that are produced in this transitional region of the failure envelope may still be considered "hybrid faults" for descriptive purposes.

Acknowledgements

This work was conducted as part of C.A. McCormick's doctoral research that was funded by the President's Doctoral Scholar Award (The University of Manchester). The authors acknowledge the Natural Environment Research Council funded Nanoscale Imaging and Analysis Facility for Environmental Materials in the Williamson Research Centre for Molecular Environmental Science, The University of Manchester (NERC CC042). We are indebted to Dr. John Waters (The University of Manchester) who conducted the XRD, and to Experimental Officer Lee Paul for equipment maintenance, the development of techniques, and general laboratory assistance. We are also grateful for the helpful discussions provided by Dr. Julian Mecklenburgh and Dr. Cathy Hollis on an earlier version of this manuscript.

References

Atkinson, B. K. (1984). Subcritical crack growth in geological materials. Journal of Geophysical Research: Solid Earth, 89(B6), 4077-4114.

Belayneh, M., Cosgrove, J.W., 2010. Hybrid veins from the southern margin of the Bristol Channel Basin, UK. Journal of Structural Geology, 32(2), 192-201.

Bland, J.A., 1983. Fitting failure envelopes by the method of least squares. Quarterly Journal of Engineering Geology, 16(2), 143-147.

Blenkinsop, T.G., Rowland, J.V., Baker, T., 2020. Mechanical Regimes of Hydrothermal Gold Mineralization. In: Rowland, J.V., Rhys, D.A. (Eds.). *Applied Structural Geology of Ore-Forming Hydrothermal Systems*, Reviews in Economic Geology, Society of Economic Geologists, 205-214.

Bobich, J.K., 2005. Experimental analysis of the extension to shear fracture transition in Berea Sandstone. Unpublished M.Sc. thesis. Texas A&M University, College Station, p. 52.

Bons, P.D., Elburg, M.A., Gomez-Rivas, E., 2012. A review of the formation of tectonic veins and their microstructures. Journal of structural geology, 43, 33-62.

Boyce, S., Lei, Z., Euser, B., Knight, E.E., Rougier, E., Stormont, J.C., Reda Taha, M.M., 2020. Simulation of mixed-mode fracture using the combined finite-discrete element method. Computational Particle Mechanics, 7(5), 1047-1055.

Brace, W.F., 1964. Brittle fracture of rocks. In: Judd, W.R., (Ed.). *State of Stress in Earth's Crust*. Elsevier, New York, 111-180.

Busetti, S., Jiao, W., Reches, Z.E., 2014. Geomechanics of hydraulic fracturing microseismicity: Part 1. Shear, hybrid, and tensile events. American Association of Petroleum Geologists Bulletin, 98(11), 2439-2457.

Cen, D., Huang, D., 2017. Direct shear tests of sandstone under constant normal tensile stress condition using a simple auxiliary device. Rock Mechanics and Rock Engineering, 50(6), 1425-1438.

Chang, C., Haimson, B., 2000. True triaxial strength and deformability of the German Continental Deep Drilling Program (KTB) deep hole amphibolite. Journal of Geophysical Research: Solid Earth, 105(B8), 18999-19013.

Chang, C., Haimson, B., 2012. A failure criterion for rocks based on true triaxial testing. Rock Mechanics and Rock Engineering, 45(6), 1007-1010.

Colmenares, L.B., Zoback, M.D., 2002. A statistical evaluation of intact rock failure criteria constrained by polyaxial test data for five different rocks. International Journal of Rock Mechanics and Mining Sciences, 39(6), 695-729.

Coviello, A., Lagioia, R., Nova, R., 2005. On the measurement of the tensile strength of soft rocks. Rock Mechanics and Rock Engineering, 38(4), 251-273.

Dansereau, V., Démery, V., Berthier, E., Weiss, J., Ponson, L., 2019. Collective damage growth controls fault orientation in quasibrittle compressive failure. Physical review letters, 122(8), 085501.

de Raadt, W.S., Burlini, L., Kunze, K., Spiers, C.J., 2014. Effect of pre-existing crystallographic preferred orientation on the rheology of Carrara marble. Journal of Structural Geology, 68, 44-57.

Edmond, J.M., Paterson, M.S., (1972). Volume changes during the deformation of rocks at high pressures. In: International Journal of Rock Mechanics and Mining Sciences & Geomechanics Abstracts, 9(2), 161-182.

Engelder, T., 1999. Transitional-tensile fracture propagation: a status report. Journal of Structural Geology, 21(8-9), 1049-1055.

Ewy, R.T., 1999. Wellbore-stability predictions by use of a modified Lade criterion. SPE Drilling & Completion, 14(02), 85-91.

Feng, X.T., Zhang, X., Kong, R., Wang, G., 2016. A novel Mogi type true triaxial testing apparatus and its use to obtain complete stress-strain curves of hard rocks. Rock Mechanics and Rock Engineering, 49(5), 1649-1662.

Ferrill, D.A., McGinnis, R.N., Morris, A.P., Smart, K.J., 2012. Hybrid failure: Field evidence and influence on fault refraction. Journal of Structural Geology, 42, 140-150.

Ferrill, D.A., Morris, A.P., 2003. Dilational normal faults. Journal of structural geology, 25(2), 183-196.

Ferrill, D.A., Morris, A.P., McGinnis, R.N., Smart, K.J., Wigginton, S.S., Hill, N.J., 2017. Mechanical stratigraphy and normal faulting. Journal of Structural Geology, 94, 275-302.

Finzi, Y., Muhlhaus, H., Gross, L., Amirbekyan, A., 2013. Shear band formation in numerical simulations applying a continuum damage rheology model. Pure and Applied Geophysics, 170(1), 13-25.

French, M.E., Zhu, W., Xiao, X., Evans, B., Prior, D.J., 2022. Thermally Enhanced Water Weakening of the Solnhofen Limestone. Journal of Geophysical Research: Solid Earth, 127(3), e2021JB022742.

Girard, L., Amitrano, D., Weiss, J., 2010. Failure as a critical phenomenon in a progressive damage model. Journal of Statistical Mechanics: Theory and Experiment, 2010(01), P01013.

Griffith, A.A., 1921. The phenomena of rupture and flow in solids. Philosophical transactions of the royal society of London (Series A), 163-198.

Hackston, A., Rutter, E., 2016. The Mohr-Coulomb criterion for intact rock strength and friction-a re-evaluation and consideration of failure under polyaxial stresses. Solid Earth, 7(2), 493-508.

Haimson, B., Chang, C., 2000. A new true triaxial cell for testing mechanical properties of rock, and its use to determine rock strength and deformability of Westerly granite. International Journal of Rock Mechanics and Mining Sciences, 37(1-2), 285-296.

Haimson, B., Rudnicki, J.W., 2010. The effect of the intermediate principal stress on fault formation and fault angle in siltstone. Journal of Structural Geology, 32(11), 1701-1711.

Hancock, P.L., 1985. Brittle microtectonics: principles and practice. Journal of structural geology, 7(3-4), 437-457.

Handin, J., Heard, H.A., Magouirk, J.N., 1967. Effects of the intermediate principal stress on the failure of limestone, dolomite, and glass at different temperatures and strain rates. Journal of geophysical research, 72(2), 611-640.

Healy, D., Blenkinsop, T.G., Timms, N.E., Meredith, P.G., Mitchell, T.M., Cooke, M.L., 2015. Polymodal faulting: Time for a new angle on shear failure. Journal of Structural Geology, 80, 57-71.

Heard, H.C., 1960. Chapter 7: Transition from brittle fracture to ductile flow in Solenhofen limestone as a function of temperature, confining pressure, and interstitial fluid pressure. In: Griggs, D.T., Handin, J., (Eds.). *Rock Deformation*, Geological Society of America Memoirs, 79, 193-226.

Heard, H.C., 1963. Effect of large changes in strain rate in the experimental deformation of Yule marble. The Journal of Geology, 71(2), 162-195.

Hoek, E., Brown, E.T., 1988. The Hoek-Brown failure criterion - a 1988 update. In: Curran, J., (Ed.) *Proceedings of the 15th Canadian Rock Mechanics Symposium*, University of Toronto, Toronto, Canada, 31-38.

Hoek, E., Martin, C.D., 2014. Fracture initiation and propagation in intact rock - a review. Journal of Rock Mechanics and Geotechnical Engineering, 6(4), 287-300.

Huang, D., Liu, Y., Cen, D., Zeng, B., Wu, Z., Yang, Y., 2022. Effect of confining pressure on deformation and strength of granite in confined direct tension tests. Bulletin of Engineering Geology and the Environment, 81(3), 1-20.

Huang, D., Zhu, T.T., 2018. Experimental and numerical study on the strength and hybrid fracture of sandstone under tension-shear stress. Engineering Fracture Mechanics, 200, 387-400.

Kandula, N., Cordonnier, B., Boller, E., Weiss, J., Dysthe, D.K., Renard, F., 2019. Dynamics of microscale precursors during brittle compressive failure in Carrara marble. Journal of Geophysical Research: Solid Earth, 124(6), 6121-6139.

Kaus, B.J., 2010. Factors that control the angle of shear bands in geodynamic numerical models of brittle deformation. Tectonophysics, 484(1-4), 36-47.

Khazanehdari, J., Rutter, E.H., Casey, M., Burlini, L., 1998. The role of crystallographic fabric in the generation of seismic anisotropy and reflectivity of high strain zones in calcite rocks. Journal of Structural Geology, 20(2-3), 293-299.

Ingraham, M.D., Issen, K.A., Holcomb, D.J., 2013. Response of Castlegate sandstone to true triaxial states of stress. Journal of Geophysical Research: Solid Earth, 118(2), 536-552.

Lade, P.V., 1977. Elasto-plastic stress-strain theory for cohesionless soil with curved yield surfaces. International journal of solids and structures, 13(11), 1019-1035.

Lan, H., Chen, J., Macciotta, R., 2019. Universal confined tensile strength of intact rock. Scientific reports, 9(1), 1-9.

Lisle, R.J., Strom, C.S., 1982. Least-squares fitting of the linear Mohr envelope. Quarterly Journal of Engineering Geology and Hydrogeology, 15(1), 55-56.

Llana-Fúnez, S., Rutter, E.H., 2005. Distribution of non-plane strain in experimental compression of short cylinders of Solnhofen limestone. Journal of Structural Geology, 27(7), 1205-1216.

Ma, X., Rudnicki, J.W., Haimson, B.C., 2017. Failure characteristics of two porous sandstones subjected to true triaxial stresses: applied through a novel loading path. Journal of Geophysical Research: Solid Earth, 122(4), 2525-2540.

Mackwell, S.J., Paterson, M.S., 2002. New developments in deformation studies: high-strain deformation. In: Karato, S.I., Wenk, H.R., (Eds.) *Plastic deformation of minerals and rocks*. Reviews in Mineralogy and Geochemistry, 51(1), 1-19.

McCormick, C.A., Corlett, H., Stacey, J., Hollis, C., Feng, J., Rivard, B., Omma, J.E., 2021. Shortwave infrared hyperspectral imaging as a novel method to elucidate multi-phase dolomitization, recrystallization, and cementation in carbonate sedimentary rocks. Scientific reports, 11(1), 1-16.

Mogi, K., 1967. Effect of the intermediate principal stress on rock failure. Journal of Geophysical Research, 72(20), 5117-5131.

Mogi, K., 1971. Effect of the triaxial stress system on the failure of dolomite and limestone. Tectonophysics, 11(2), 111-127.

Peacock, D.C.P., Sanderson, D.J., Leiss, B., 2021. Use of Mohr Diagrams to Predict Fracturing in a Potential Geothermal Reservoir. Geosciences, 11(12), 501.

Pieri, M., Burlini, L., Kunze, K., Stretton, I., Olgaard, D.L., 2001. Rheological and microstructural evolution of Carrara marble with high shear strain: results from high temperature torsion experiments. Journal of Structural Geology, 23(9), 1393-1413.

Price, N.J., 1966. *Fault and Joint Development in Brittle and Semi-brittle Rock*. Pergamon Press, Oxford, 176 p.

Price, N.J., Cosgrove, J.W., 1990. *Analysis of Geological Structures*. Cambridge University Press, Cambridge.

Ramsey, J.M., 2003. Experimental Study of the transition from brittle shear fractures to joints. Unpublished M.Sc. thesis, Texas A&M University, College Station. 291 p.

Ramsey, J.M., Chester, F.M., 2004. Hybrid fracture and the transition from extension fracture to shear fracture. Nature, 428(6978), 63-66.

Reches, Z.E., Dieterich, J.H., 1983. Faulting of rocks in three-dimensional strain fields I. Failure of rocks in polyaxial, servo-control experiments. Tectonophysics, 95(1-2), 111-132.

Reches, Z.E., Lockner, D.A., 1994. Nucleation and growth of faults in brittle rocks. Journal of Geophysical Research: Solid Earth, 99(B9), 18159-18173.

Rodriguez, E., 2005. A microstructural study of the extension-to-shear fracture transition in Carrara Marble. Unpublished M.Sc. thesis. Texas A&M University, College Station, p. 62.

Rowe, K.J, Rutter, E.H., 1990. Palaeostress estimation using calcite twinning: experimental calibration and application to nature. Journal of Structural Geology, 12(1), 1-17.

Rudnicki, J.W., 1977. The effect of stress-induced anisotropy on a model of brittle rock failure as localization of deformation. In: *The 18th U.S. Symposium on Rock Mechanics (USRMS)*, Energy Resources and Excavation Technology, 1-8.

Rudnicki, J.W., Olsson, W.A., 1998. Reexamination of fault angles predicted by shear localization theory. In: *Proceedings of Third North American Rock Mechanics Symposium (NARMS'98)*, Rock Mechanics in Mining, Petroleum and Civil Works, 3-5 June, 1998, Cancun, Mexico. Extended Abstract in International Journal of Rock Mechanics and Mining Sciences 35(415), 512-513.

Rudnicki, J.W., Rice, J.R., 1975. Conditions for the localization of deformation in pressure sensitive dilatant materials. Journal of the Mechanics and Physics of Solids, 23(6), 371-394.

Rutter, E.H., 1972. The influence of interstitial water on the rheological behaviour of calcite rocks. Tectonophysics, 14, 13-33.

Rutter, E.H., 1995. Experimental study of the influence of stress, temperature, and strain on the dynamic recrystallization of Carrara marble. Journal of Geophysical Research: Solid Earth, 100(B12), 24651-24663.

Rutter, E.H., Casey, M., Burlini, L., 1994. Preferred crystallographic orientation development during the plastic and superplastic flow of calcite rocks. Journal of Structural Geology, 16(10), 1431-1446.

Rutter, E.H., Mecklenburgh, J., 2018. Influence of normal and shear stress on the hydraulic transmissivity of thin cracks in a tight quartz sandstone, a granite, and a shale. Journal of Geophysical Research: Solid Earth, 123(2), 1262-1285.

Rutter, E.H., Wallis, D., Kosiorek, K., 2022. Application of Electron Backscatter Diffraction to Calcite-Twinning Paleopiezometry. Geosciences, 12(6), 222.

Rybacki, E., Niu, L., Evans, B., 2021. Semi-brittle deformation of Carrara marble: Hardening and twinning induced plasticity. Journal of Geophysical Research: Solid Earth, 126, e2021JB022573.

Schmid, S.M., Boland, J.N., Paterson, M.S., 1977. Superplastic flow in finegrained limestone. Tectonophysics, 43(3-4), 257-291.

Spagnoli, A., Carpinteri, A., Vantadori, S., 2015. Interpreting experimental fracture toughness results of quasi-brittle natural materials through multi-parameter approaches. Frattura ed Integrità Strutturale, 9(33), 80-88.

Takahashi, M., Koide, H., 1989. Effect of the intermediate principal stress on strength and deformation behavior of sedimentary rocks at the depth shallower than 2000 m. In: Maury, V., Fourmaintraux, D., (Eds.). *Rock at Great Depth*, vol. 1. Rotterdam: Balkema, 19-26.

Terzaghi, K., 1923. Die Berechnung der Durchlässigkeitsziffer des Tones aus dem Verlauf der hydrodynamischen Spannungserscheinungen (in German). Sitzungsber. Akad. Wissen. Wien Math-Naturwiss. Kl. Abt. IIa. 132, 105-124.

Vandeginste, V., Swennen, R., Gleeson, S.A., Ellam, R.M., Osadetz, K., Roure, F., 2005. Zebra dolomitization as a result of focused fluid flow in the Rocky Mountains Fold and Thrust Belt, Canada. Sedimentology, 52(5), 1067-1095.

Wibberley, C.A., Petit, J.P., Rives, T., 2000. Micromechanics of shear rupture and the control of normal stress. Journal of Structural Geology, 22(4), 411-427.

Xu, X., Wu, S., Jin, A., Gao, Y., 2018. Review of the relationships between crack initiation stress, mode I fracture toughness and tensile strength of geo-materials. International Journal of Geomechanics, 18(10), 04018136.

Zhang, Z.X., 2002. An empirical relation between mode I fracture toughness and the tensile strength of rock. International journal of rock mechanics and mining sciences, 39(3), 401-406.

Zhu, Q.Z., 2017. A new rock strength criterion from microcracking mechanisms which provides theoretical evidence of hybrid failure. Rock Mechanics and Rock Engineering, 50(2), 341-352.

Blank page

Basin-scale fluid-flow, dolomitization patterns, and diagnostic rock textures in fault-controlled dolomite bodies: Insights from the Western Canadian Sedimentary Basin

Cole A. McCormick [1,*], Hilary Corlett [2], Matthieu Clog [3], Adrian J. Boyce [3], Romain Tartese [1], Matthew Steele-MacInnis [4], Cathy Hollis [1]

1. Department of Earth and Environmental Sciences, The University of Manchester, Manchester, M13 9PL, United Kingdom.

2. Department of Earth Sciences, Memorial University of Newfoundland, St. John's, Newfoundland, A1C 5S7, Canada.

3. Scottish Universities Environmental Research Council, East Kilbride, Glasgow, G75 0QF, United Kingdom.

4. Department of Earth and Atmospheric Sciences, University of Alberta, Edmonton, Alberta, T6G 2E3, Canada.

* Corresponding author: Cole McCormick - cole.mccormick@manchester.ac.uk

Abstract

Structurally-controlled dolomitization typically involves the interaction of high-pressure (P), high-temperature (T) fluids with the surrounding host-rock. Such reactions are accompanied by dolomite cementation and recrystallization, and the resulting dolomite bodies include several “diagnostic” rock textures. Zebra textures, in particular, are widely considered to reflect elevated P/T conditions, and they are commonly associated with cement-supported breccias and boxwork textures. Although there is a consensus that fracturing is involved in their formation, the processes that control the geographical and temporal evolution of these rock textures are still poorly understood. Through detailed petrographical and geochemical analyses of fault-controlled dolomite bodies, hosted in the Middle Cambrian strata in the Western Canadian Sedimentary Basin, this study demonstrates that a single conceptual model cannot be applied to all the textural characteristics that are observed in these rock textures. Instead, a wide array of sedimentological, tectonic, and metasomatic processes contribute to their formation, and the relative importance of each process is geographically and temporally variable. Distal to the source of the dolomitizing fluid, the strata comprise bedding-parallel zebra textures that formed by dilatational fracturing and the precipitation of saddle dolomite as a cement. Proximal to the fluid-source, however, the strata comprise bedding-inclined zebra textures, cement-supported breccias, and boxwork textures that have been affected by recrystallization. Consequently, the metasomatic evolution of these rock textures reflects the timing, depth, and temperature of dolomitization, as well as the proximity to the source of the dolomitizing fluid. These rock textures are closely associated with faults and carbonate-hosted ore deposits (e.g., magnesite, rare earth element, and Mississippi Valley-type mineralization), which suggests that they provide invaluable information regarding the hydrogeological evolution of the basin and the metasomatism of carbonate sedimentary rocks under elevated P/T conditions.

6.1. Introduction

Fault-controlled, hydrothermal dolomitization is an important metasomatic reaction in the earth's upper crust that involves the replacement of $CaCO_3$ by $CaMg(CO_3)_2$, mediated by an aqueous solution that is of higher temperature than the ambient host-rock (Machel and Lonnee, 2002; Davies and Smith, 2006). The resulting hydrothermal dolomite (HTD) bodies are economically significant as they can form reservoirs for energy exploitation, carbon storage, and commonly host Mississippi Valley-type (MVT) mineralization (Duggan et al. 2001; Vandeginste et al. 2007; Paradis and Simandl, 2017). Fault-controlled dolomitization is also accompanied by multiple phases of cementation and recrystallization that can fingerprint the evolving fluid composition of a sedimentary basin as well as the timing, depth, and temperature that contributed to these reactions (Lonnee and Machel, 2006; Koeshidayatullah et al. 2020b; Stacey et al. 2021). Certain "diagnostic" rock textures (e.g., zebra textures, boxwork textures, cement-supported breccias) are commonly found in fault-controlled dolomite bodies; often defining them as HTD because their presence has been considered evidence of elevated P/T conditions during their formation (Nielsen et al. 1998; Boni et al. 2000; Vandeginste et al. 2005). Nevertheless, HTD can form without these rock textures (Hendry et al. 2015; Hollis et al. 2017; Rustichelli et al. 2017; Hirani et al. 2018), and there is still controversy as to their actual genesis (Wallace and Hood, 2018, and references therein).

Zebra textures comprise alternating, mm- to cm-scale, bands of replacement dolomite (RD) and saddle dolomite (SD) that form symmetrical RD-SD-SD-RD patterns. These rock textures are closely associated with boxwork textures that form similarly banded textures with highly irregular orientations, as well as cement-supported breccias that include floating clasts of RD that are fully surrounded and supported by SD. Earlier works interpreted a precursor sedimentological control on the formation of zebra textures (Beales and Hardy, 1980; Fontboté and Gorzawski, 1990; Morrow, 2014), whereas it is now widely accepted that fracturing plays a critical role in their development (Wallace et al.

1994; Nielsen et al. 1998; Wallace and Hood, 2018). Consequently, these rock textures are commonly considered indicative of a particular tectonic setting, even though they are reported in a wide range of compressional (Gasparrini et al. 2006; Sharp et al. 2010; Kareem et al. 2019), transtensional (López-Horgue et al. 2010; Swennen et al. 2012; Dewit et al. 2014), and extensional (Boni et al. 2000; Shelton et al. 2019; Stacey et al. 2021) environments. It has also been suggested that geochemical self-organization contributes to the formation of zebra textures (Merino et al. 2006; Merino and Canals, 2011; Kelka et al. 2015, 2017). Given the wide disparities between these models, it becomes unclear as to what exactly these rock textures are "diagnostic" of.

This study aims to elucidate the genesis of zebra textures, cement-supported breccias, and boxwork textures and through the detailed characterization of a series of HTD bodies that are hosted in the Cathedral Formation and the Eldon Formation (Middle Cambrian; 509 to 497 Ma; Miaolingian Epoch) in the Western Canadian Sedimentary Basin (WCSB). These vertically and laterally extensive outcrops offer an unparalleled natural laboratory to unravel the geographical and temporal controls on basin-scale, fault-controlled fluid-flow and the resulting dolomitization patterns. By integrating a suite of sedimentological, structural, and geochemical data, this study investigates the (i) timing, temperature, and mechanism of dolomitization, (ii) the source(s) of the dolomitizing fluid(s), as well as their migration pathways, and (iii) controls on the formation of diagnostic rock textures in HTD bodies.

6.2. Geological setting

6.2.1. Tectonic setting

The WCSB includes a southwest-thickening wedge of sedimentary rocks, up to ~18 km thick, that extend from the southwest corner of the Northwest Territories to the north-central United States (Fig. 6.1A, B). In the southern Rocky Mountains, the WCSB includes four unconformity-bounded packages of strata that are informally divided based on their

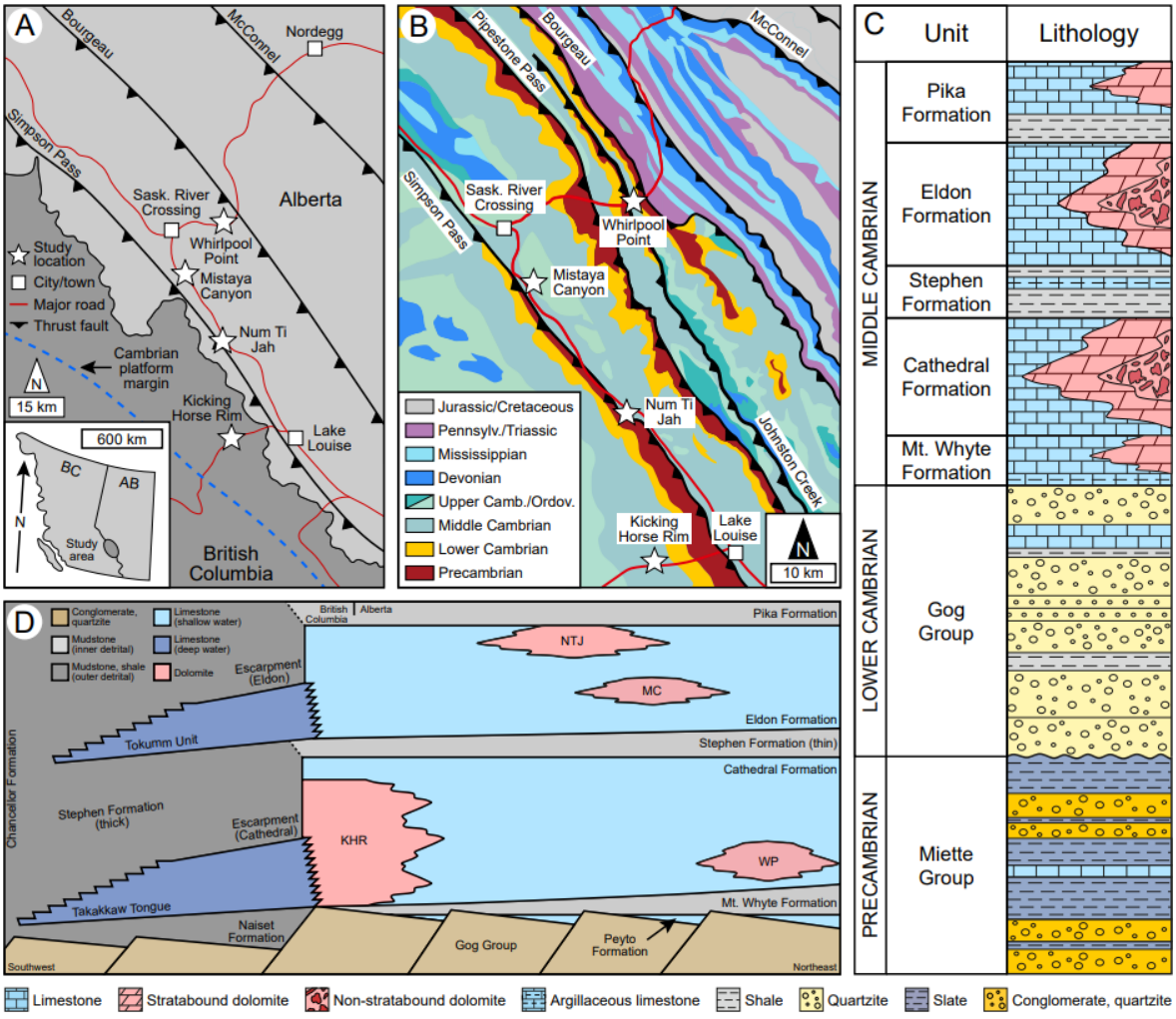

Figure 6.1. (A) Location of the study area in the southern Rocky Mountains (Western Canadian Sedimentary Basin) showing the major thrust faults and the Cambrian platform margin (modified from Stacey et al. 2021; based on Wheeler et al. 1996). **(B)** Geological map of the study area (modified from Stacey et al. 2021; based on the Alberta Geological Survey Interactive Minerals Map: https://ags.aer.ca/publication/iam-001). **(C)** Stratigraphy of the southern Rocky Mountains (based on Aitken, 1997). **(D)** Schematic cross-section of the Middle Cambrian strata in the southern Rocky Mountains (modified from Collom et al. 2009; based on Aitken, 1997). WP = Whirlpool Point, MC = Mistaya Canyon, NTJ = Num Ti Jah, KHR = Kicking Horse Rim.

tectonic settings. The Purcell Supergroup (Mesoproterozoic) records deposition in an intracratonic basin, whereas the Windermere Supergroup (Neoproterozoic) records the rifting of Laurentia. Lower Cambrian (541 to 509 Ma; Terreneuvian Epoch - Series 2) to Triassic strata were deposited on what was considered a passive margin (Bond and Kominz, 1984; Aitken, 1989; Slind et al. 1994), although tectonic activity and heat flow likely remained high during the Cambrian (Bond et al. 1985; Powell et al. 2006; Johnston

et al. 2009). Jurassic to Paleocene strata record the transition to a foreland basin during the Columbian and Laramide orogenies.

The modern structure of the southern Rocky Mountains is dominated by E-NE verging thrust faults that formed during the Antler, Columbian, and Laramide orogenies (Price, 1981; Root, 2001; McMechan, 2022). However, there are several pre-orogenic structural elements in the southern Rocky Mountains, including NE-SW trending normal and transtensional faults that intersect Middle Cambrian strata (Davies and Smith, 2006; Stacey et al. 2021). The most important of these early structural features is the Kicking Horse Rim (oriented N-NW), an elevated paleotopographic feature that formed due to the syn-depositional reactivation of deep-rooted basement faults and influenced the position of the carbonate platform margin during the Cambrian and Ordovician (Aitken, 1971, 1989, 1997; Collom et al. 2009).

6.2.2. Stratigraphy

Middle Cambrian strata in the southern Rocky Mountains record a series of northeast-transgressing carbonate-mudrock cycles that comprise regionally extensive facies belts (Fig. 6.1C; Aitken, 1989, 1997). These cycles comprise a central carbonate platform-shoal complex that grades laterally into proximal slope facies to the southwest and into intrashelf basin facies to the northeast (Fig. 6.1D; Aitken, 1989, 1997; Pratt, 2002). Throughout the middle Cambrian, each of the carbonate platform-shoal complexes were paleogeographically confined by the tectonically active Kicking Horse Rim (Aitken, 1971), and the development of each platform terminated due to the collapse of its basinward margin, platform drowning, and burial by siliciclastic sediment (Aitken, 1989; Collom et al. 2009; Johnston et al. 2009).

At the Kicking Horse Rim (KHR; 51°26′11.5″N, 116°22′48.5″W), the Cathedral Formation (limestone, stratabound and non-stratabound dolomite) overlies the Gog Group (quartzite, shale), whereas it overlies the Mount Whyte Formation (argillaceous limestone,

shale, stratabound dolomite) at Whirlpool Point (WP; 52°00′07.5″N, 116°28′13.5″W) (Aitken, 1997; Koeshidayatullah et al. 2020a). The Cathedral Formation is up to 610 m thick at its platform margin on Mount Stephen, thinning rapidly to the northeast (Aitken, 1997). The Cathedral Formation outcrops at WP as part of the Bourgeau Thrust, whereas it outcrops at the KHR as part of the Simpson Pass (Fig. 6.1B). The Cathedral Formation is overlain by the Stephen Formation (shale, argillaceous limestone), which is 103 m thick at its type section on Mount Bosworth (Aitken, 1997). The Stephen Formation is overlain by the Eldon Formation (limestone, stratabound and non-stratabound dolomite), which is up to 488 m thick at its platform margin (Aitken, 1997). The Eldon Formation, outcropping at Mistaya Canyon (MC; 51°55′09.5″N, 116°43′23.5″W) and Num Ti Jah (NTJ; 51°39′13.0″N, 116°29′59.0″W), is overlain by the Pika Formation (argillaceous limestone, shale, stratabound dolomite). The Eldon Formation outcrops at MC and NTJ as part of the Pipestone Pass (Fig. 6.1B).

6.2.3. Spatial and temporal evolution of HTD bodies

Over the past several years, considerable progress has been made in the understanding of the spatial and temporal evolution of fault-controlled, HTD bodies (Benjakul et al. 2020; Yao et al. 2020; Koeshidayatullah et al. 2021; Humphrey et al. 2022). Of particular relevance to the Middle Cambrian strata in the WCSB is the recognition that dolomitization is self-limiting due to the (i) abrupt depletion of the Mg/Ca ratio at the dolomitization front and (ii) decreased permeability proximal to source of the dolomitizing fluid (Koeshidayatullah et al. 2020b). In these systems, the dolomitization front "retreats" over time due to the recrystallization of the earlier paragenetic stages from repeated fluid-pulses, which occludes porosity and results in the core of the HTD body being younger than its margins (Koeshidayatullah et al. 2020b; 2021). Not only can this phenomenon be recognized by the spatial distributions of each paragenetic stage in the strata (McCormick et al. 2021), but also by a systematic increase in the dolomitization temperature and

$\delta^{18}O_{fluid}$ values towards the core of the HTD body (Koeshidayatullah et al. 2020b). Recrystallization also coincides with the shift from zoned, planar-e dolomite (distal to the fluid-source) to unzoned, planar-s to nonplanar-a dolomite (proximal to the fluid-source). Such relationships have been established at the outcrop-scale (Koeshidayatullah et al. 2020b, 2021; Stacey et al. 2021; McCormick et al. 2021), but whether they hold true at the basin-scale is equivocal. Furthermore, the relationship between these dolomitization patterns and the resulting rock textures has not been investigated.

6.3. Methods

Ninety-two representative samples were collected from the WP (*n* = 35), MC (*n* = 30), NTJ (*n* = 9), and KHR (*n* = 18) localities. Transmitted-light petrography was established on polished sections, prepared from samples impregnated with blue-stained resin, that were stained with alizarin red S and potassium ferricyanide (Dickson, 1966). These 30 μm thick sections were examined under plane-polarized light, between crossed-polars, and then analysed using a CITL Mk5 cold cathodoluminescence (CL) system (operating conditions = 15 to 20 kV and 350 to 450 μA) that is mounted on a Nikon Eclipse LV100N POL microscope. Dolomite crystal textures are described according to Sibley and Gregg (1987).

Five polished sections, which include each of the identified paragenetic stages, were analysed for their major and trace element compositions by electron probe micro-analysis (EPMA) using a Cameca SX100 at The University of Manchester. To obtain an overview of each sample, an initial 2 x 10 mm map was created at a stepping-interval of 10 μm. Based on these low-resolution elemental maps, 1.536 x 1.536 mm areas of interest were mapped at a stepping interval of 3 μm. Ca (Kα; PET) and Mg (Kα; TAP) were analysed at 15 kV, 10 nA, and a dwell time of 100 ms using calcite ($CaCO_3$) and magnesite ($MgCO_3$) as standards, whereas Fe (Kα; LLIF) and Mn (Kα; LLIF) were analysed at 15 kV, 200 nA, and a dwell time of 200 ms using fayalite (Fe_2SiO_4) and tephroite (Mn_2SiO_4) as standards.

These same sections were analyzed for their rare earth element (REE) compositions using a Teledyne Photon Machines Analyte Excite+ 193 nm ArF Excimer laser ablation (LA) system with a HelEx II active 2-volume ablation cell that is coupled to an Agilent 8900 inductively coupled mass spectrometer (ICP-MS). Ablation of NIST 612 glass was used to tune the instrument, optimize signal intensities, and maintain low levels of oxide formation ($^{232}ThO/^{232}Th < 0.25\%$) and a U/Th ratio that is close to unity. NIST 612 glass was used as the primary reference material, whereas the JCp-1 NP reference carbonate was treated as a quality control secondary reference material. The accuracy of measurements on the secondary standard was typically within ± 20% of the recommended values for JCp1-NP. For all carbonate analyses, a spot diameter of 50 μm, a fluence of 3 $J.cm^{-2}$, and a repetition rate of 5 Hz was used. Each analysis lasted 40 s and was preceded by 20 s counting time of a gas blank, used to correct the signal intensities from background contributions. The trace element data reduction scheme from the Iolite4 software (Woodhead et al. 2007; Paton et al. 2011) was applied using known [Ca] of the reference materials (Jochum et al., 2011, 2019) and the samples (measured by EPMA) as internal standards. Results are reported with their respective 2 standard error and detection limit calculated according to Howell et al. (2013).

The $\delta^{13}C$ and $\delta^{18}O$ stable isotopic composition of dolomite (n = 101) was analyzed at the Scottish Universities Environmental Research Centre (SUERC) using an Analytical Precision AP2003 mass spectrometer that is equipped with a separate acid injector system. To isolate each paragenetic stage, samples were micro-drilled (50 μm diameter bit) under a binocular microscope. These ~5 mg powders were digested in 105% H_3PO_4 under a helium atmosphere at 70°C. Measured $\delta^{13}C$ and $\delta^{18}O$ values are reported relative to Vienna PeeDee Belemnite (VPDB) using conventional delta (δ) notation. Analytical reproducibility, based on replicates of the internal SUERC standard MAB-2 (Carrara marble), is ± 0.2‰ for both $\delta^{13}C$ and $\delta^{18}O$. MAB-2 was extracted from the same quarry as

the IAEA-CO-1 international standard, each sample having equivalent $\delta^{13}C$ and $\delta^{18}O$ values of –2.5 and 2.4 VPDB, respectively.

Carbonate clumped isotope (Δ_{47}) measurements were performed at SUERC using a manual extraction line and an Thermo Fisher 253 Isotope Ratio Mass Spectrometer (IRMS). Samples were digested for 30 min in >103% H_3PO_4 at 90°C in an acid bath. The produced CO_2 was transferred to a calibrated volume attached to a strain gauge, thawed until it reached room temperature, and the volume yield was measured. The CO_2 was then diverted to the IRMS, where the intensities of masses 44 to 48 were recorded. The intensity of mass 48 was used to screen for contamination of the gas and exclude replicates when the Δ_{48} offset was >0.5‰ (Davies and John, 2017). Data reduction was conducted using the Easotope software (John and Bowen, 2016), the IUPAC parameters (Brand et al. 2010, Petersen et al. 2019), and the ^{18}O acid fractionation of Rosenbaum and Sheppard (1986) for dolomite. The values from Bernasconi et al. (2021) for the ETH1 to ETH4 carbonate standards were used to define the empirical transfer function from the measured Δ_{47} to the absolute reference frame. Analytical uncertainties on Δ_{47} were calculated as the larger of the standard error on replicates of each sample or the standard error of the ETH standards. The reprojected Δ_{47} values were used to calculate apparent crystallization temperatures using the calibration of Anderson et al. (2021). Based on these temperatures, $\delta^{18}O_{fluid}$ values were calculated according to Horita (2014).

Following the criteria described by Goldstein and Reynolds (1993), petrographical analysis of all samples was conducted to identify the presence of primary fluid inclusion assemblages in each paragenetic stage. Fluid inclusion microthermometry was conducted using a Linkam THMS600 heating and freezing stage that is mounted on an Olympus BX53 petrographical microscope. The stage temperature was calibrated using synthetic fluid inclusions, according to the triple point of CO_2 (–56.6°C), the triple point of H_2O (0°C), and the critical point of H_2O (373.9°C). Accuracy and precision of the measurements are ± 0.5°C at temperatures above 100°C. For the smallest fluid inclusions,

where phase changes were difficult to observe, the homogenization temperature was bracketed using the temperature cycling approach of Goldstein and Reynolds (1993). The microthermometric data were then interpreted quantitatively using the computer program of Steele-MacInnis et al. (2012).

6.4. Field and petrographical observations

6.4.1. Field observations

At WP (Fig. 6.2A, B, C), the lower part of the Cathedral Formation includes (i) thinly-bedded (2 to 12 cm), microbial-peloid mudstone and bindstone, and (ii) highly bioturbated, ooid-peloid mudstone and wackestone (Fig. 6.2D, E). Such facies represent a platform interior environment (Aitken, 1989; Pratt, 2002). The outcrop is intersected by a transtensional fault with a normal offset of 30 cm (Fig. 6.2B). The HTD body is stratabound at its margins (distal to the fault) and non-stratabound at its core (proximal to the fault). In the hangingwall, the HTD body extends laterally from the fault for 85 m, where it has a sharp, bedding-parallel contact with limestone. In the footwall, the HTD body extends for >140 m. Zebra textures (Fig. 6.2F, G) are present up to 70 m from the fault in the hangingwall and up to 120 m in the footwall. Zebra textures are bedding-parallel in the microbial bindstone facies and bedding-inclined (discordant to bedding) in the bioturbated mudstone facies. Cement-supported breccias (Fig. 6.2H, I) are present up to 25 m from the fault in the hangingwall and up to 5 m from the fault in the footwall. The breccias comprise floating clasts of RD that have corroded margins, are surrounded by SD, and include dilatational fractures occluded by SD. In zebra textures, the quantity of SD ranges from 10% to 30% of the rock volume, whereas it can be up to 60% in cement-supported breccias, with evidence of dilatation of the surrounding strata (Fig. 6.2C, H).

At MC and NTJ (Fig. 6.3A, B, C, D), the Eldon Formation largely comprises bioturbated ooid-peloid mudstone. Horizontal burrows are common, but the bioturbation intensity of each unit varies significantly. At MC, a narrow (8 to 12 m wide) fracture

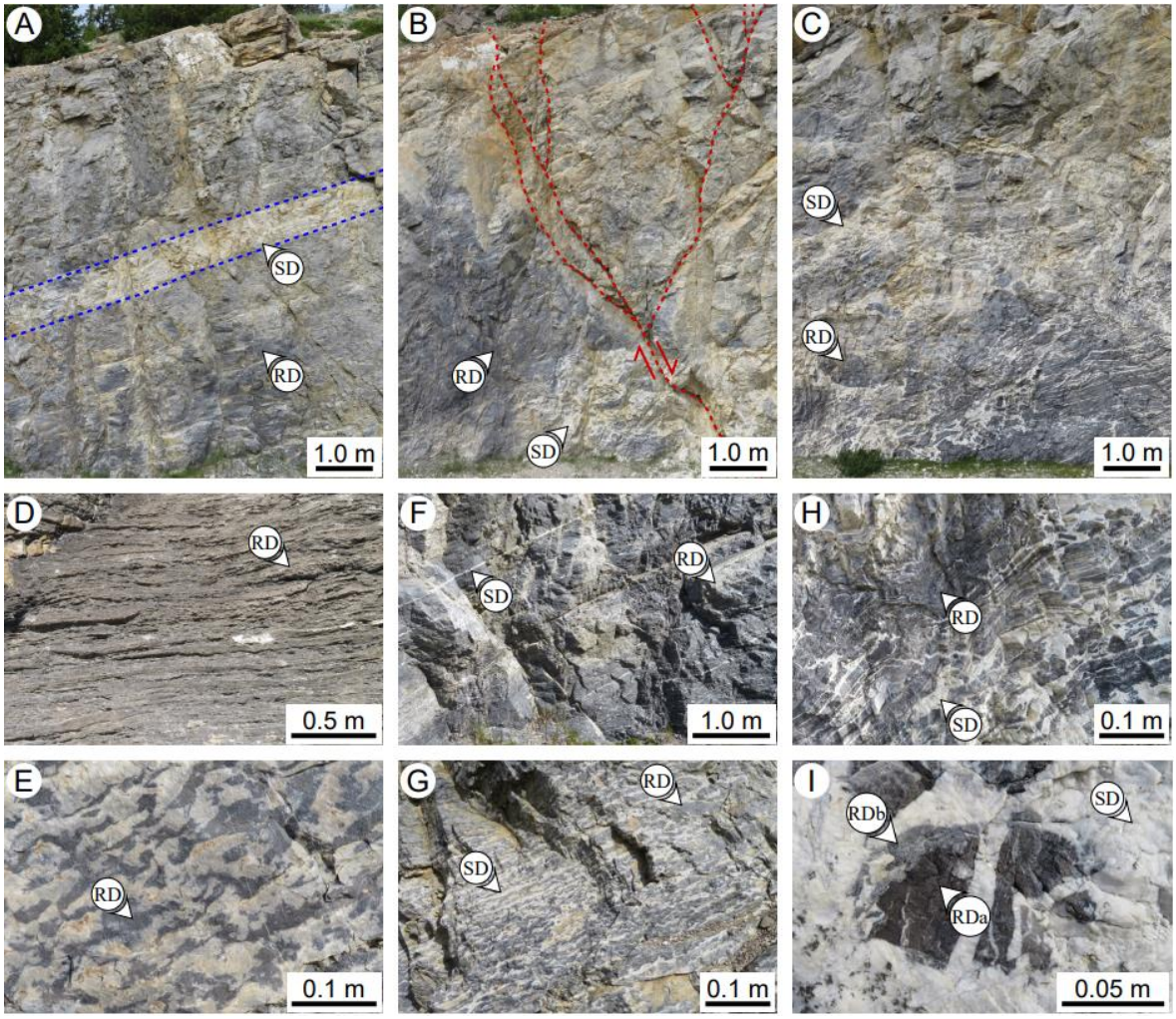

Figure 6.2. Field photographs of the HTD at Whirlpool Point showing the **(A)** footwall that includes bedding-parallel zebra textures, **(B)** transtensional fault with associated negative flower structure, and **(C)** hangingwall that includes cement-supported breccias and bedding-inclined zebra textures. The precursor lithologies at WP include **(D)** microbial bindstone and **(E)** bioturbated peloidal mudstone. The rock textures at WP include **(F, G)** Bedding-parallel zebra textures. **(H, I)** cement-supported breccias. RD = replacement dolomite. SD = saddle dolomite.

corridor intersects the outcrop to the southwest of the road, where the strata are highly eroded. The HTD body is stratabound distal to the fracture corridor and non-stratabound proximal to the fracture corridor. To the northeast of the road, the HTD body is >10 m thick and extends for >300 m as the contacts with limestone are inaccessible. The strata comprise alternating units of RD and SD that either lack rock textures, or include bedding-inclined zebra textures, respectively (Fig. 6.3A, B). The angles of these zebra textures are variable, ranging from 5 to 35° relative to bedding. At the north end of the outcrop, the strata comprise RD with rare occurrences of SD that is localized in burrows (Fig. 6.3E, F).

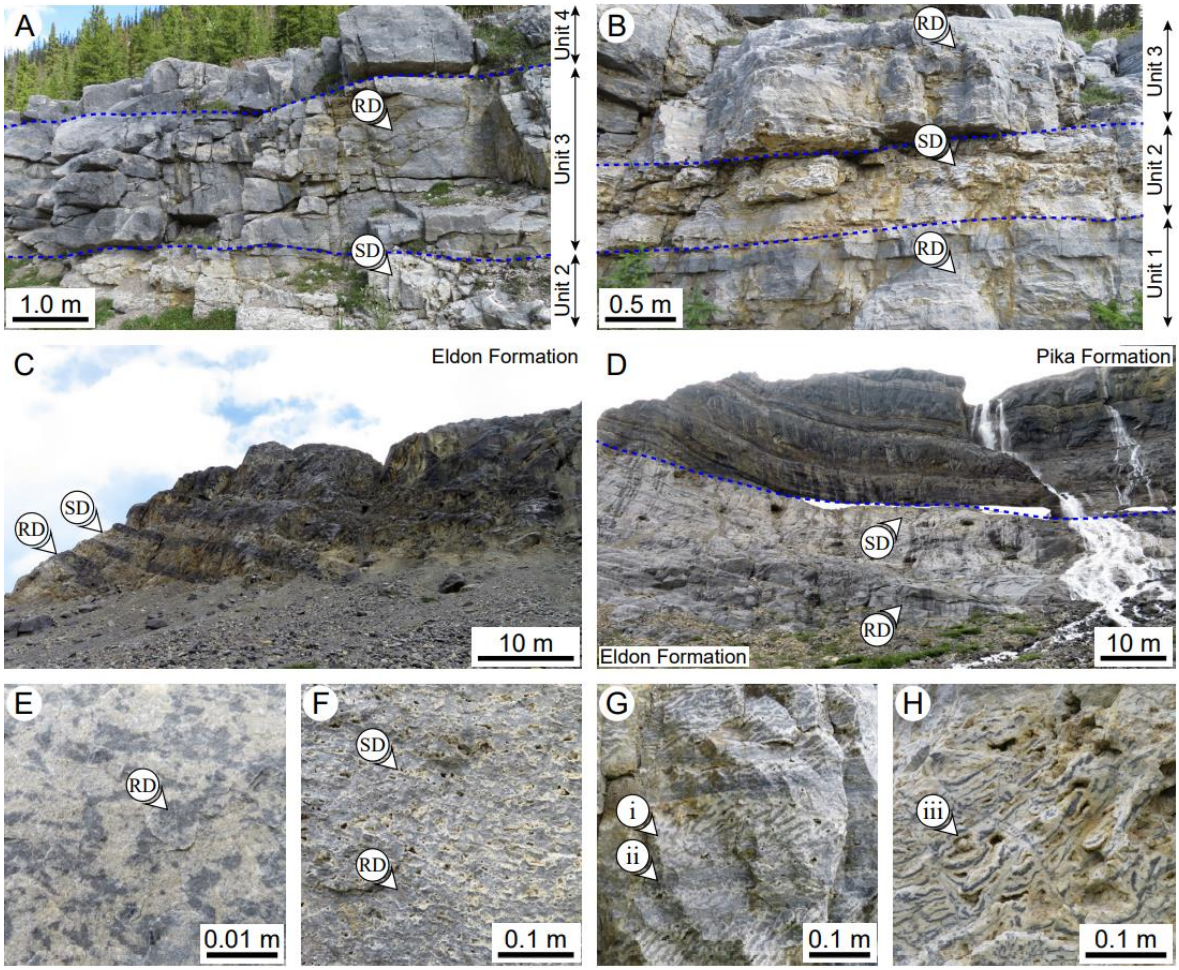

Figure 6.3. Field photographs of the HTD at **(A, B)** Mistaya Canyon and **(C, D)** Num Ti Jah. Note the increase in the abundance of SD proximal to the contact between the Eldon Formation and the Pika Formation. There is a progressive shift from **(E)** precursor bioturbated mudstone, to **(F)** nascent zebra textures, to **(G)** bedding-inclined zebra textures, to **(H)** boxwork textures. Note that the zebra textures are (i) inclined to bedding, and they (ii) comprise stratabound sets that are constrained to individual beds. (iii) Large vugs, >1.0 cm in diameter, are present throughout the most highly altered units in the exposure. RD = replacement dolomite. SD = saddle dolomite.

A striking feature at MC is the development of two scales of periodicity in the zebra textures, including the meso-scale alternation of each RD and SD band, and the macro-scale stratabound alternation of clusters of zebra textures (Fig. 6.3G). Boxwork textures, with irregular orientations, are located proximal to the fracture corridor (Fig. 6.3H). At NTJ, there is no clear evidence of faults that intersect the strata, but there are numerous fractures and zebra textures. Boxwork textures are located proximal to the contact between the Eldon Formation and the Pika Formation. The quantity of SD also increases towards

the contact with the Pika Formation, commonly exceeding 60% of the rock volume, yet there is minimal evidence of dilatation of the overlying strata (Fig. 6.3C, D).

At the KHR (Fig. 6.4A), the upper part of the Cathedral Formation includes (iii) thickly bedded (>10 cm), ooid-pisoid-intraclast wackestone and floatstone. Such facies represent a platform margin environment (Aitken, 1989; Pratt, 2002). The bioturbated mudstone facies is also locally common. There are several faults, 6 to 8 m in length, with normal offsets of 20 to 80 cm, and numerous fractures distributed throughout the outcrop (Fig. 6.4A). These faults do not propagate through the mudstone and shale that is present in the upper 28 to 30 m of the Cathedral Formation, which is not dolomitized. Below this shale bed, the strata comprise beige, non-stratabound dolomite bodies that are sub-vertical to bedding, and grey dolomite that is present throughout the remainder of the succession. The grey dolomite is similar to the successions described at WP, MC, and NTJ, comprising alternating units of RD and SD with zebra textures that are poorly developed (Fig. 6.4B, C). The beige dolomite comprises units of structureless SD with regions that include numerous bedding-inclined zebra textures (Fig. 6.4D, E). These zebra textures include a faint relict of the original RD, which has highly corroded margins. The two scales of periodicity is also present in the zebra textures at the KHR, but there is only a faint relict of the bedding planes that constrain the zebra textures into stratabound sets (Fig. 6.4D). The most striking feature of the succession is that the quantity of SD commonly exceeds 80% of the rock volume, yet the bedding-surfaces are largely undisturbed and there is minimal evidence of dilatation and expansion of the strata (Fig. 6.4A).

6.4.2. Microscopic observations

At WP, the strata include limestone, two phases of RD and three phases of SD (Table 6.1). RDa comprises finely-crystalline (20 to 150 μm) planar-e dolomite with dull-purple luminescent cores and dull-red luminescent rims, whereas RDb comprises medium-crystalline (100 to 400 μm) planar-s dolomite with dull-red luminescent cores and dull- to

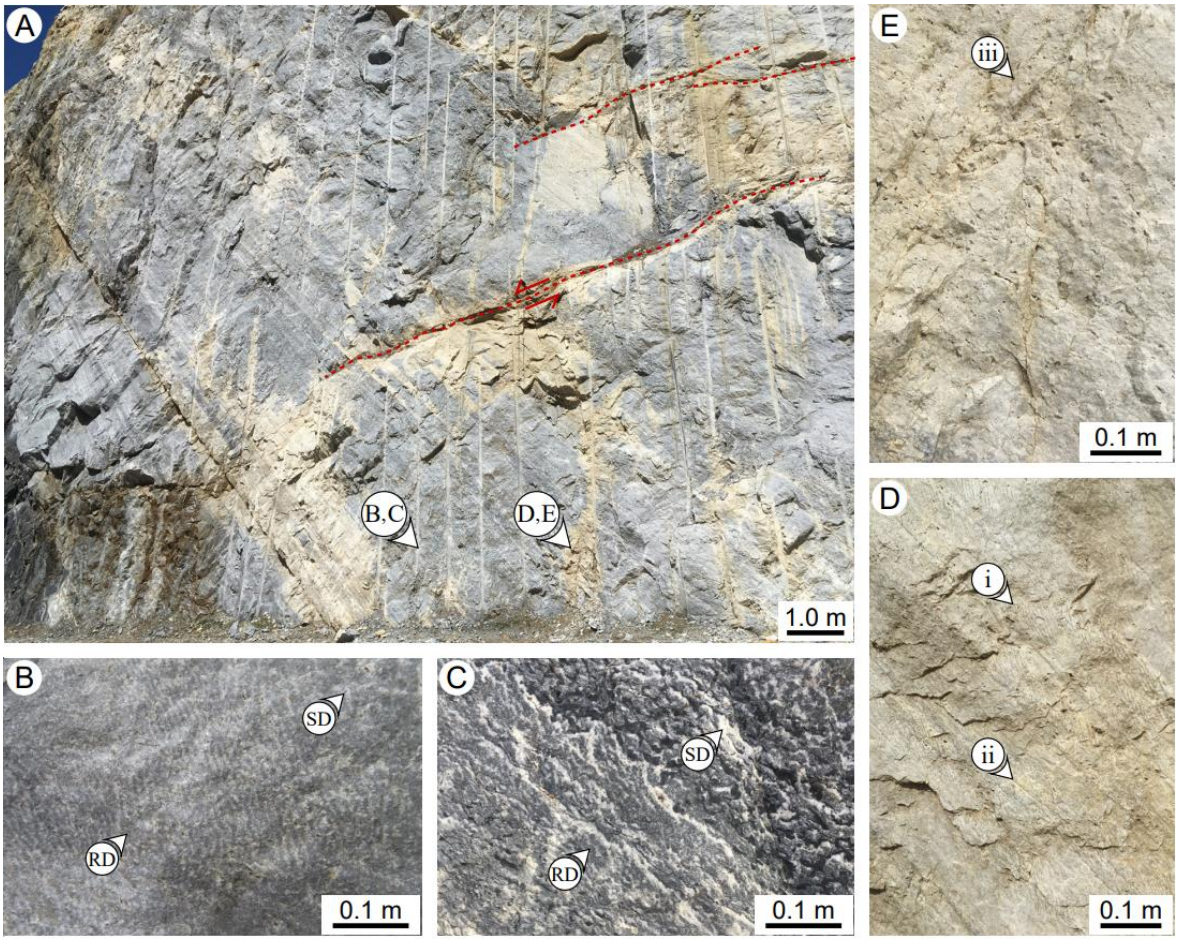

Figure 6.4. (A) Field photograph of the HTD at the Kicking Horse Rim, where zebra textures are present in both the light grey and tan parts of the exposure. **(B, C)** Nascent zebra textures showing their nucleation and progressive shift to **(D, E)** highly recrystallized zebra textures and structureless SD. Note that these rock textures are (i) inclined to bedding, and they (ii) comprise stratabound sets that are constrained to individual beds. (iii) Small vugs, <1.0 cm in diameter, are present in the most highly altered units in the exposure. RD = replacement dolomite. SD = saddle dolomite.

medium-red luminescent rims (Fig. 6.5A). RDa includes clay minerals, detrital quartz, and organic matter that are rare in RDb. SDa is medium-crystalline (250 to 550 μm), forming syntaxial layers that are nucleated on RDb. SDb is coarsely-crystalline, with crystals that gradually become coarser away from the cavity wall (up to 4500 μm). Apart from their crystal sizes, SDa and SDb are indistinguishable based on their textural properties (unzoned, dull- to medium-red luminescent, nonplanar dolomite; Fig. 6.5B). McCormick et al. (2021) suggested that SDa and SDb formed due to competitive crystallization, a process where favourably-oriented crystals obstruct the growth of poorly-oriented crystals. Thus, these phases are grouped as SDa+b for the ensuing geochemical analyses (Table 6.1). Such

Locality	Geometries of the HTD bodies	Predominant rock textures	Paragenetic stage	Dolomite texture	Cathodoluminescence	Other features
Whirlpool Point (WP)	Stratabound distal to faults, non-stratabound proximal to faults. Increased abundance of saddle dolomite in the hanging-wall of faults.	Bedding-parallel zebra textures. Cement-supported breccias in the central ~30 m of the dolomite body.	RDa	Planar-e to planar-s	Concentric zoning, dull-purple cores, dull-red rims.	Fabric-retentive, detrital quartz and organic matter locally common.
			RDb	Planar-s to nonplanar-a	Blotchy zoning, dull-red cores, dull-red to medium-red rims.	Fabric-destructive, locally associated with stylolites. Detrital quartz rare.
			SDa+b	Nonplanar (saddle)	Unzoned, dull-red to medium-red.	Form syntaxial layers on RDb. Elongate crystals normal to cavity wall.
			SDc	Nonplanar (saddle)	Oscillatory zoning, dull-red to bright-red and dull-orange to bright-orange.	Breccia and fracture fill, commonly form rims nucleated on SDb. Pb-Zn-Fe sulphides locally common.
Mistaya Canyon (MC) and Num Ti Jah (NTJ)	Largely stratabound, locally non-stratabound proximal to faults and proximal to the upper contact with the Pika Formation.	Bedding-inclined zebra textures in stratabound units. Boxwork textures locally common proximal to faults and fractures.	RDa	Planar-e to planar-s	Concentric zoning, medium-purple and medium-red cores, dull-red rims.	Fabric-retentive, detrital quartz and organic matter locally common.
			RDb	Planar-s to nonplanar-a	Blotchy zoning, medium-red cores, medium-red rims.	Fabric-destructive, locally associated with stylolites. Detrital quartz rare.
			SDa+b	Nonplanar (saddle)	Unzoned, dull-red to medium-red.	Form syntaxial layers on RDb. Elongate crystals normal to cavity wall.
			SDc	Nonplanar (saddle)	Oscillatory zoning, dull-red to bright-red and dull-orange to bright-orange.	Breccia and fracture fill, commonly form rims nucleated on SDb. Pb-Zn-Fe sulphides locally common.
Kicking Horse Rim (KHR)	Non-stratabound, irregular patterns.	Numerous bedding-inclined zebra textures with scattered patches of structureless saddle dolomite. Rare bedding-parallel zebra textures.	RDb	Nonplanar-a	Unzoned, dull-red to medium-red, irregular patterns.	Fabric-destructive, stylolites common, corroded crystal boundaries. Pb-Zn-Fe sulphides locally common.
			SDa+b	Nonplanar (saddle)	Unzoned, dull-red to medium-red.	Form syntaxial layers on RDb. Elongate crystals normal to cavity wall. Pb-Zn-Fe sulphides locally common.
			SDc	Nonplanar (saddle)	Oscillatory zoning, dull-red to bright-red and dull-orange to bright-orange.	Breccia and fracture fill, commonly form rims nucleated on SDb. Pb-Zn-Fe sulphides locally common.

Table 6.1. Summary table describing the geometries of the HTD bodies, predominant rock textures, and microscopic characteristics of each of the paragenetic stages in the Cathedral Formation (WP, KHR) and the Eldon Formation (MC, NTJ).

classification is also more congruent with previous works (Nielsen et al. 1998; Vandeginste et al. 2005; Wallace and Hood, 2018). SDc includes nonplanar dolomite, with a characteristic dull- to bright- red and orange oscillatory zonation, that form rims (250 to 1250 μm thick) nucleated on SDb crystals (Fig. 6.5C).

At MC and NTJ, the petrographical phases are largely analogous to those described at WP, but limestone is not present (Table 6.1). Stylolites are common and commonly form the boundary between RDa and RDb (Fig. 6.5D). Microfractures, oriented parallel to the maximum principal stress, are also associated with these stylolites. The CL characteristics of RDb and SDa+b are largely homogenous in the zebra textures, and these phases can only be differentiated in transmitted light (Fig. 6.5E). Relative to the Cathedral Formation,

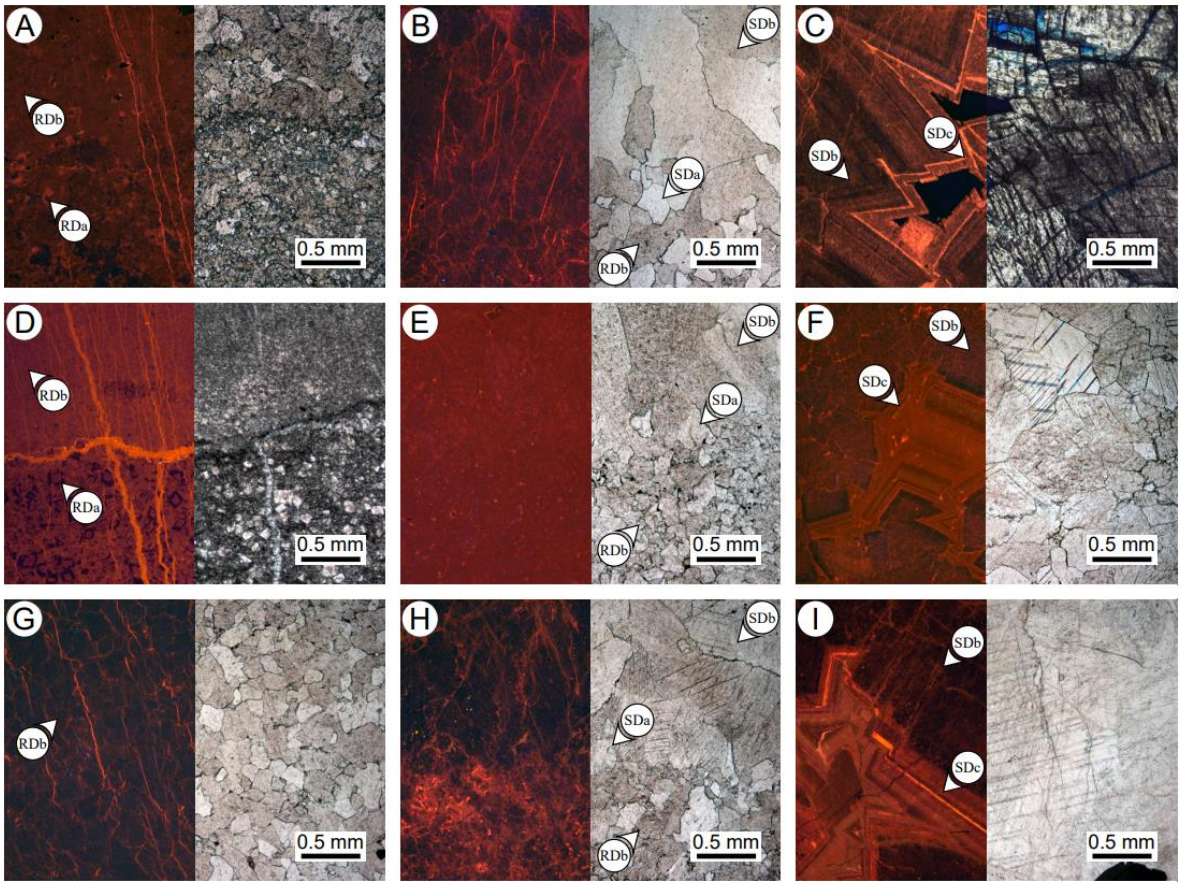

Figure 6.5. Cathodoluminescence (CL; left) and transmitted light (TL; right) photomicrographs showing the different phases of dolomite that are present in **(A-C)** the Cathedral Formation at Whirlpool Point, **(D-F)** the Eldon Formation at Mistaya Canyon and Num Ti Jah, and **(G-I)** the Cathedral Formation at Kicking Horse Rim. RD = replacement dolomite. SD = saddle dolomite. Note that RDa is not present at the KHR location, and that the ferroan dolomite (SDc) increases in abundance from WP to the KHR. RD = replacement dolomite. SD = saddle dolomite.

SDc is less abundant in the Eldon Formation and has duller CL characteristics (Fig. 6.5F). At the KHR (Table 6.1), RDa is not present and RDb comprises medium-crystalline, nonplanar-a dolomite with a dull- to moderate-red luminescence (Fig. 6.5G). Proximal to the zebra textures, however, RDb has a bright-red luminescence, with highly corroded margins, and there is local evidence of grain size reduction along the contact between RDb and SDa+b (Fig. 6.5H). Throughout the zebra textures, the CL characteristics of each petrographical phase is largely homogenous. SDc is more abundant at the KHR, and its CL characteristics are notably brighter (Fig. 6.5I).

6.5. Geochemical results

6.5.1. Major and trace element analyses

Selected results from EPMA are summarized in Table 6.2. RDa, RDb, and SDa+b are formed by near-stoichiometric dolomite, with %Ca (molar Ca/(Ca + Mg)) values that range from 47.8 to 51.4%. SDc is much more variable, with %Ca values that range from 47.2 to 51.6%. %Ca values are relatively consistent in the platform interior at WP (49.8 to 50.5%), MC (50.9 to 51.6%), and NTJ (49.6 to 50.1%), but then decrease at the KHR (47.2 to 48.2%) towards the platform margin. [Si] and [Sr] are higher in RD relative to SD, but the values are typically <100 ppm and, thus, approaching the error margins of the EPMA.

Visualization of μm-scale geochemical variations (Fig. 6.6) is facilitated by high [Fe], which covaries linearly with [Mn] (correlation coefficient >0.95; Table 6.2). The [Fe] and [Mn] are notably higher in the Cathedral Formation relative to the Eldon Formation, and there is an increasing trend from WP ([Fe] = 2407 to 12130 ppm, [Mn] = 183 to 1190 ppm) to the KHR ([Fe] = 6890 to 14300 ppm, [Mn] = 1140 to 2180 ppm). At WP, MC, and NTJ, these trace elements are highly differentiated and SDc has a marked enrichment of Fe and Mn relative to RDa, RDb, and SDa+b (Fig. 6.6A, B, C). In contrast, Fe and Mn are much more homogenously distributed at the KHR (Fig. 6.6D). Based on its CL characteristics (oscillatory zoned, dull- to bright- red), the final paragenetic stage at the KHR was assigned to SDc. This phase, however, has an enigmatic decrease in [Fe] and [Mn] that it is accompanied by an increase in [Mg] (Table 6.2). Accordingly, it should be noted that magnesite has been reported in the vicinity of the KHR (Powell et al. 2006; Vandeginste et al. 2007; Paradis and Simandl, 2017).

6.5.2. Rare earth element analyses

Rare earth element and yttrium (REE + Y) concentrations are shown in Fig. 6.7, with the light (∑LREE), middle (∑MREE), and heavy (∑HREE) REE values summarized in Table 6.2. At WP, limestone has consistent ∑LREE (0.063 ppm), ∑MREE (0.076 ppm),

Locality	Phase		Ca (wt%)	Mg (wt%)	Fe (ppm)	Mn (ppm)	∑LREE (ppm)	∑MREE (ppm)	∑HREE (ppm)	Ce/Ce*	Pr/Pr*	Eu/Eu*	$\delta^{13}C$ (‰, VPDB)	$\delta^{18}O$ (‰, VPDB)	Δ_{47} (‰; CDES)	$T\Delta_{47}$ (°C)	$\delta^{18}O_{fluid}$ (‰, SMOW)	T_h (°C)
Whirlpool Point (WP)	Lst.	Mean	–	–	–	–	0.0628	0.0764	0.0686	0.796	1.11	1.16	-0.68	-11.5	–	–	–	–
		Std. dev.	–	–	–	–	–	–	–	–	–	–	0.029	0.49	–	–	–	–
	RDa	Mean	20.82	12.52	2407	183	0.111	0.186	0.109	0.852	1.07	1.22	-0.59	-11.7	0.371	150	4.6	138
		Std. dev.	2.233	1.785	2098	213	–	–	–	–	–	–	0.154	0.47	0.0101	10.2	–	5.6
	RDb	Mean	21.10	12.91	4907	340	0.122	0.294	0.132	0.885	1.03	1.27	-0.70	-12.5	0.363	158	4.5	139
		Std. dev.	2.205	1.745	3650	218	–	–	–	–	–	–	0.188	0.96	0.0023	12.3	–	5.0
	SDa+b	Mean	21.13	12.92	2740	335	0.0554	0.137	0.0901	0.995	1.01	1.28	-0.73	-13.1	0.362	159	3.9	141
		Std. dev.	2.206	1.748	1505	160	–	–	–	–	–	–	0.107	0.44	0.0160	10.0	–	5.7
	SDc	Mean	20.45	12.14	12130	1190	0.0489	0.462	0.232	0.818	0.916	1.55	-0.78	-14.1	0.364	157	2.8	151
		Std. dev.	2.261	1.822	2030	660	–	–	–	–	–	–	0.046	0.86	0.0174	13.1	–	4.8
Mistaya Canyon (MC)	RDa	Mean	22.21	12.75	1010	164	0.0571	0.0883	0.0466	0.984	1.04	1.25	-0.91	-14.2	0.343	180	4.3	167
		Std. dev.	2.210	1.360	701	112	–	–	–	–	–	–	0.243	1.12	0.0233	16.9	–	4.2
	RDb	Mean	22.13	12.85	1290	215	0.0658	0.103	0.0550	0.994	1.05	1.20	-1.03	-15.1	0.324	204	4.9	176
		Std. dev.	2.331	1.439	740	229	–	–	–	–	–	–	0.205	0.92	0.0306	26.7	–	5.4
	SDa+b	Mean	22.15	12.94	1190	198	0.0305	0.0470	0.0251	0.955	1.00	1.50	-1.03	-15.5	0.336	189	3.6	164
		Std. dev.	2.081	1.324	850	213	–	–	–	–	–	–	0.276	1.13	0.0222	17.1	–	6.0
	SDc	Mean	20.91	11.90	8880	1135	0.0665	0.490	0.129	0.908	0.861	1.64	-1.06	-15.8	0.340	183	2.9	175
		Std. dev.	3.886	2.363	2280	510	–	–	–	–	–	–	0.121	1.44	0.0086	10.2	–	6.3
Num Ti Jah (NTJ)	RDa	Mean	22.68	13.71	984	176	0.0192	0.0363	0.0310	0.931	0.958	1.24	-0.93	-14.8	0.322	207	5.4	179
		Std. dev.	2.330	1.630	721	156	–	–	–	–	–	–	0.071	0.48	0.0234	20.3	–	4.9
	RDb	Mean	22.49	13.79	1280	213	0.0205	0.0380	0.0329	0.928	0.945	1.25	-0.97	-15.4	0.328	199	4.4	177
		Std. dev.	2.290	1.408	1180	197	–	–	–	–	–	–	0.069	0.57	0.0139	11.6	–	4.5
	SDa+b	Mean	22.61	13.93	1030	172	0.0166	0.0322	0.0281	0.969	0.981	1.18	-0.99	-15.5	0.335	190	3.8	164
		Std. dev.	2.872	1.915	910	168	–	–	–	–	–	–	0.104	0.72	0.0131	11.0	–	6.1
	SDc	Mean	21.69	13.20	5525	789	0.0279	0.169	0.0980	0.883	0.919	1.59	-0.95	-15.5	0.338	186	3.4	177
		Std. dev.	4.276	2.889	3205	355	–	–	–	–	–	–	0.100	0.99	0.0095	10.6	–	5.4
Kicking Horse Rim (KHR)	RDb	Mean	21.50	13.99	11875	1935	0.112	0.177	0.128	1.07	0.935	1.19	-0.97	-17.0	0.274	294	7.0	182
		Std. dev.	2.579	1.345	5735	885	–	–	–	–	–	–	0.310	1.64	0.0163	27.6	–	4.7
	SDa+b	Mean	21.66	14.37	14300	2180	0.0647	0.109	0.0816	1.06	0.947	1.15	-1.08	-19.2	0.258	336	6.2	186
		Std. dev.	2.308	1.738	3900	810	–	–	–	–	–	–	0.300	0.82	0.0106	25.5	–	6.8
	SDc	Mean	21.69	14.69	6890	1140	0.171	0.905	0.347	0.879	0.954	1.63	-1.26	-19.8	0.271	301	4.5	192
		Std. dev.	2.387	1.814	2580	450	–	–	–	–	–	–	0.051	0.32	0.0078	26.3	–	6.2

Table 6.2. Selected major, trace, and rare earth element concentrations, as well as the results from stable and clumped isotope, and fluid inclusion analyses on each of the paragenetic stages at WP, MC, NTJ, and the KHR. $T\Delta_{47}$ values were calculated from Anderson et al. (2021), whereas δ_{18}Ofluid values were calculated from Horita (2014).

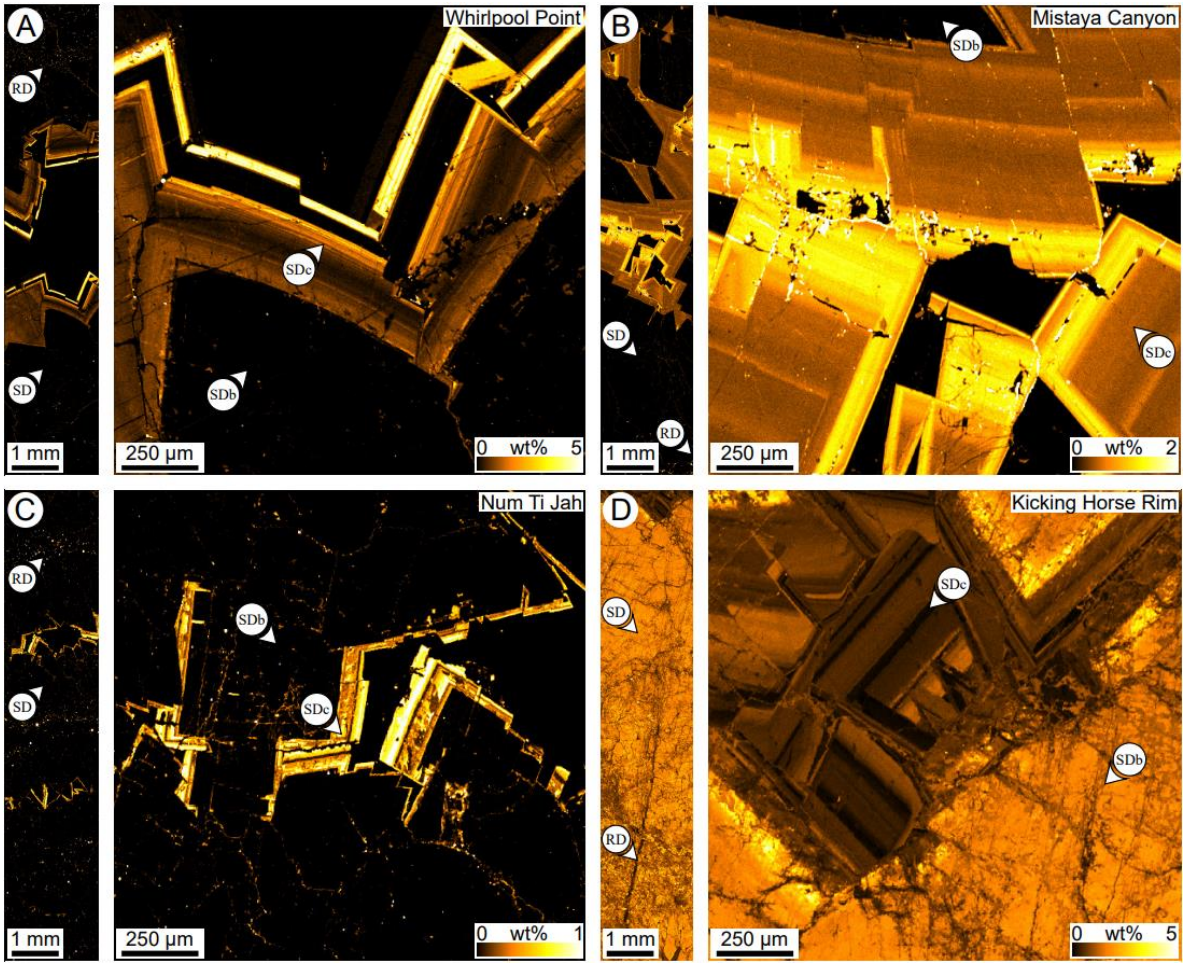

Figure 6.6. Low-resolution (left; 10 µm stepping-interval) and high-resolution (right; 3 µm stepping-interval) electron probe micro-analysis (EPMA) maps showing the spatial distribution of Fe in each of the paragenetic stages at **(A)** Whirlpool Point, **(B)** Mistaya Canyon, **(C)** Num Ti Jah, and **(D)** the Kicking Horse Rim. 1.0 wt% = 10000 ppm.

and ∑HREE (0.069 ppm). RDa has a similar REE profile as limestone, but with enriched ∑LREE (0.11 ppm), ∑MREE (0.19 ppm), and ∑HREE (0.11 ppm). RDb and SDa+b have different REE profiles than limestone, with characteristic ∑MREE enrichment relative to their ∑LREE. This shift is distinct in SDc, which has enriched ∑MREE (0.46 ppm) and ∑HREE (0.23 ppm) relative to its ∑LREE (0.049 ppm). Such depleted ∑LREE values are also characteristic of SDc at MC, NTJ, and the KHR. Overall, the [REE] are higher in the Cathedral Formation relative to the Eldon Formation. RDa, RDb, and SDa+b are also less differentiated at MC and NTJ, plotting in a tight cluster (Fig. 6.7B, C). At the KHR, RDb and SDa+b have similar [REE] as their respective paragenetic stage at WP. Conversely,

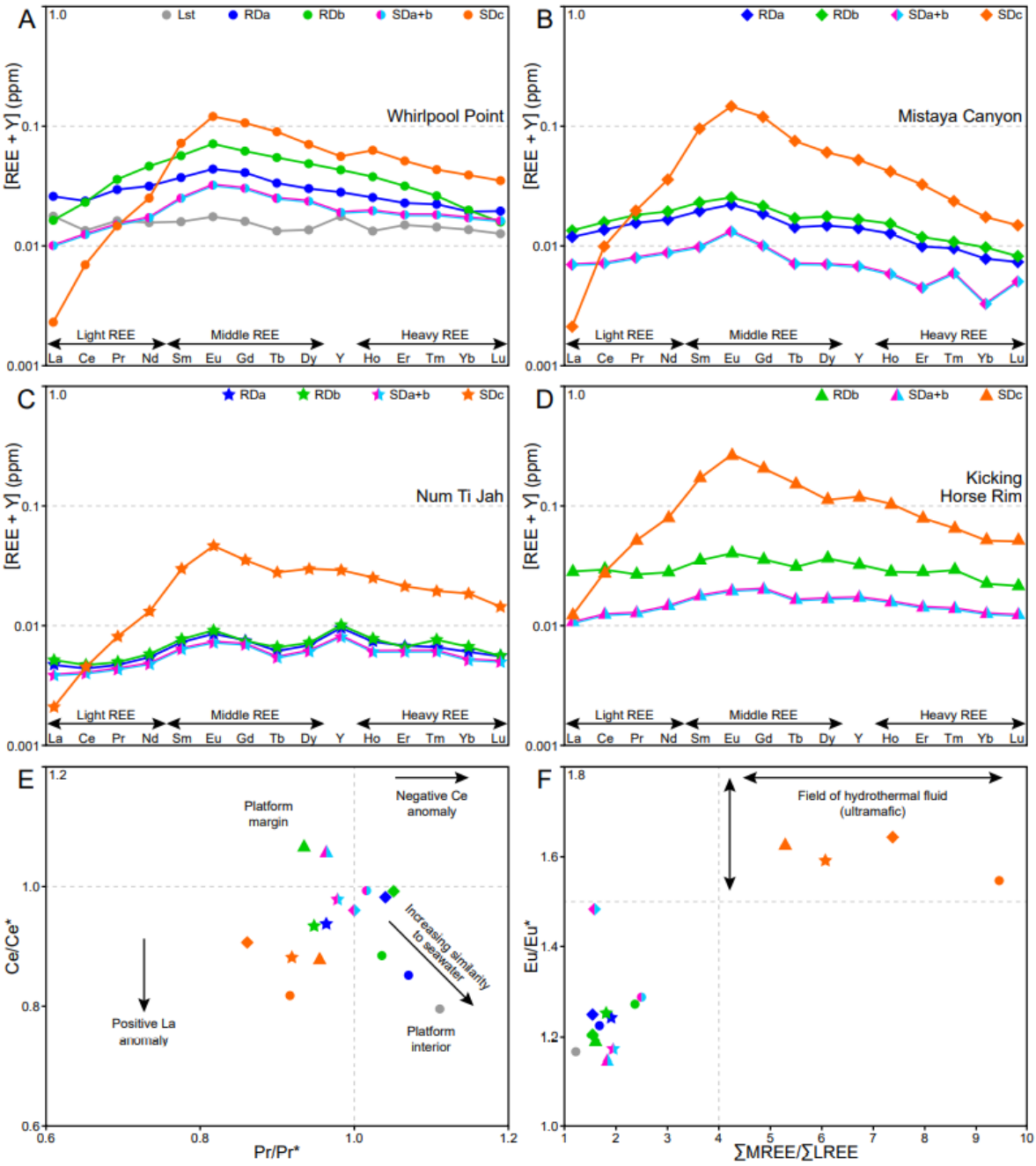

Figure 6.7. Post Archaean Australian Shale (PAAS) normalized (Nance and Taylor, 1976; Taylor and McLennan, 1985) rare earth element (REE) and yttrium (Y) concentrations in each of the paragenetic stages at **(A)** Whirlpool Point, **(B)** Mistaya Canyon, **(C)** Num Ti Jah, and **(D)** the Kicking Horse Rim. **(E)** Ce/Ce* vs. Pr/Pr* plot showing the decrease in the contribution of seawater from the platform interior (WP) to the platform margin (KHR). **(F)** Eu/Eu* vs. ΣMREE/ΣLREE plot that illustrates the marked change in composition that occurs in SDc.

SDc is markedly enriched in ∑LREE (0.17 ppm), ∑MREE (0.91 ppm), and ∑HREE (0.35 ppm) values at the KHR (Fig. 6.7D).

Calculated Ce anomalies (Ce/Ce* = [Ce]/(0.5[La] + 0.5[Pr]), Pr anomalies (Pr/Pr* = [Pr]/(0.5[Ce] + 0.5[Nd]), and Eu anomalies (Eu/Eu* = [Eu]/(0.67[Sm] + 0.33[Tb]) are

shown in Table 6.2. Values >1.0 are positive, whereas values <1.0 are negative. At WP, limestone has a prominent negative Ce/Ce* (0.80) and a positive Pr/Pr* (1.1). With each later paragenetic stage (e.g., RDa, RDb, SDa+b), the Ce/Ce* systematically increases and the Pr/Pr* decreases (Fig. 6.7E; Table 6.2). At MC and NTJ, the Ce/Ce* and the Pr/Pr* of RDa, RDb, SDa+b plot in a narrow range and close to 1.0 (Fig. 6.7E; Table 6.2). Conversely, RDb and SDa+b have positive Ce/Ce* (1.1) and negative Pr/Pr* (0.95) at the KHR (Fig. 6.7E). At each locality, SDc plots separately from these earlier paragenetic stages, with negative Ce/Ce* and Pr/Pr* (Fig. 6.7E; Table 6.2). Such relationship is also clear when the Eu/Eu* is plotted against ΣMREE/ΣLREE, where the values for SDc are markedly higher than RDa, RDb, and SDa+b (Fig. 6.7F; Table 6.2).

6.5.3. Stable and clumped isotope analyses

Carbon and oxygen stable isotope ratios ($\delta^{13}C_{VPDB}$, $\delta^{18}O_{VPBD}$) are plotted in Fig. 6.8A, with the values shown in Table 6.2. At WP, limestone $\delta^{13}C$ and $\delta^{18}O$ values are –0.7‰ and –11.5‰, respectively. Relative to limestone, each later paragenetic stage is increasingly depleted in $\delta^{13}C$ and $\delta^{18}O$ (RDa = –0.6‰, –11.7‰; RDb = –0.7‰, –12.5‰; SDa+b = –0.7‰, –13.1‰; SDc = –0.8‰, –14.1‰). Relative to the WP, the $\delta^{13}C$ and $\delta^{18}O$ values at MC (–0.9 to –1.1‰, –14.2 to –15.8‰) and NTJ (–0.9 to –1.0‰, –14.8 to –15.5‰) are more depleted. Such trend continues towards the KHR, where the $\delta^{13}C$ and $\delta^{18}O$ values of RDb (–1.0‰, –17.0‰), SDa+b (–1.1‰, –19.2‰) and SDc (–1.3‰, –19.8‰) are the most depleted in the study area.

Clumped isotope (Δ_{47}) values are shown in Table 6.2, with crystallization temperatures ($T\Delta_{47}$) calculated according to Anderson et al. (2021) and plotted in Fig. 6.8B. At WP, Δ_{47} values range from 0.362 to 0.371‰, which corresponds to $T\Delta_{47}$ values of 150 to 159°C. At each locality, paragenetic variations are typically within the error margin of each adjacent phase (Fig. 6.8B). Δ_{47} values decrease at MC (0.324 to 0.343‰) and NTJ (0.322 to 0.338‰), corresponding to $T\Delta_{47}$ values of 180 to 204°C and 186 to 207°C,

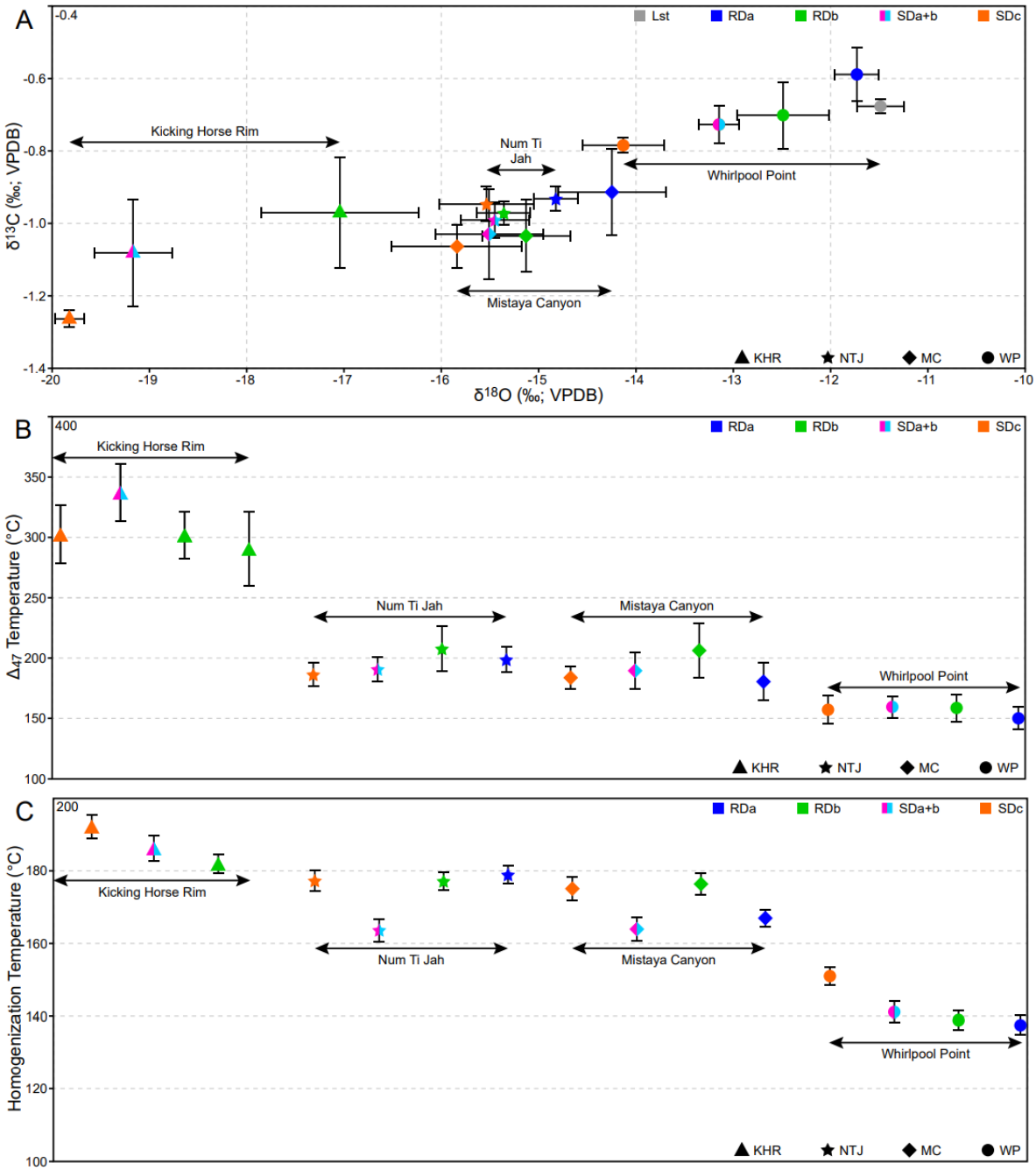

Figure 6.8. (A) $\delta^{13}C_{VPDB}$ vs. $\delta^{18}O_{VPDB}$ plot showing the isotopic depletion from the platform interior (WP) to the platform margin (KHR). Note that Cambrian marine calcite (–10 to –4‰) and dolomite (–7 to –1‰) values plot outside of the region shown (Veizer and Prokoph, 2015; Ryb and Eiler, 2018). VDPB = Vienna Pee Dee Belemnite. **(B)** Clumped isotope crystallization temperatures ($T\Delta_{47}$; Anderson et al. 2021) and **(C)** fluid inclusion homogenization temperatures (T_h) showing the progressive increase in temperature from the platform interior (WP) to the platform margin (KHR).

respectively. Such trend continues towards the KHR, where the Δ_{47} values are 0.258 to 0.274‰ and the $T\Delta_{47}$ values are 294 to 336°C. Based on these $\delta^{18}O$ and $T\Delta_{47}$ values, $\delta^{18}O_{fluid}$ was calculated according to Horita (2014) and shown in Table 6.2 (values reported

in SMOW). $\delta^{18}O_{fluid}$ values range from 2.8 to 4.6‰ at WP, 2.9 to 4.3‰ at MC, 3.4 to 5.4‰ at NTJ, and 4.5 to 7.0‰ at the KHR.

6.5.4. Fluid inclusion analyses

Fluid inclusions in RDa and RDb are sparse, diminutive (2 to 6 μm in diameter), and assemblages were not observed. Consequently, several isolated inclusions, hosted in the same crystal, were analysed to ensure consistency. The fluid inclusions in SDa+b and SDc are 4 to 12 μm in diameter and form primary assemblages within individual crystallographic growth zones. The inclusions analysed were two-phase (~20% vapour, ~80% liquid), but RDa, RDb, and SDa+b also include numerous single-phase inclusions that are entirely vapour or liquid. Conversely, SDc is limpid and lacks single-phase inclusions. Fluid inclusion homogenization temperatures (T_h) are plotted in Fig. 6.8C, with the values shown in Table 6.2. At WP, T_h values range from 138 to 151°C, whereas they range from 164 to 176°C at MC, and 164 to 179°C at NTJ. At the KHR, T_h values range from 182 to 192°C. Melting temperature (T_m) of the fluid inclusions were attempted, but they were not frozen during these analyses (down to –175°C).

6.6. Interpretations

6.6.1. Textural interpretation of the rock textures in HTD bodies

Middle Cambrian strata in the WCSB include two phases of RD and three phases of SD (Fig. 6.9). Evidence for replacement dolomitization includes (i) the fabric-retentive preservation of sedimentological textures, and (ii) the observation that detrital quartz is locally common (Wallace et al. 1994; Vandeginste et al. 2005). RDb is coarser than RDa and is accompanied by the shift from oscillatory-zoned, planar-e dolomite to a poorly-zoned mosaic of planar-s dolomite. Such evidence suggests that RDb, which is spatially associated with the occurrence of SD, formed through recrystallization (Koeshidayatullah et al. 2020b; McCormick et al. 2021). Conversely, there are no sedimentological textures in SD, and it does not include detrital quartz. There is typically a sharp contact between

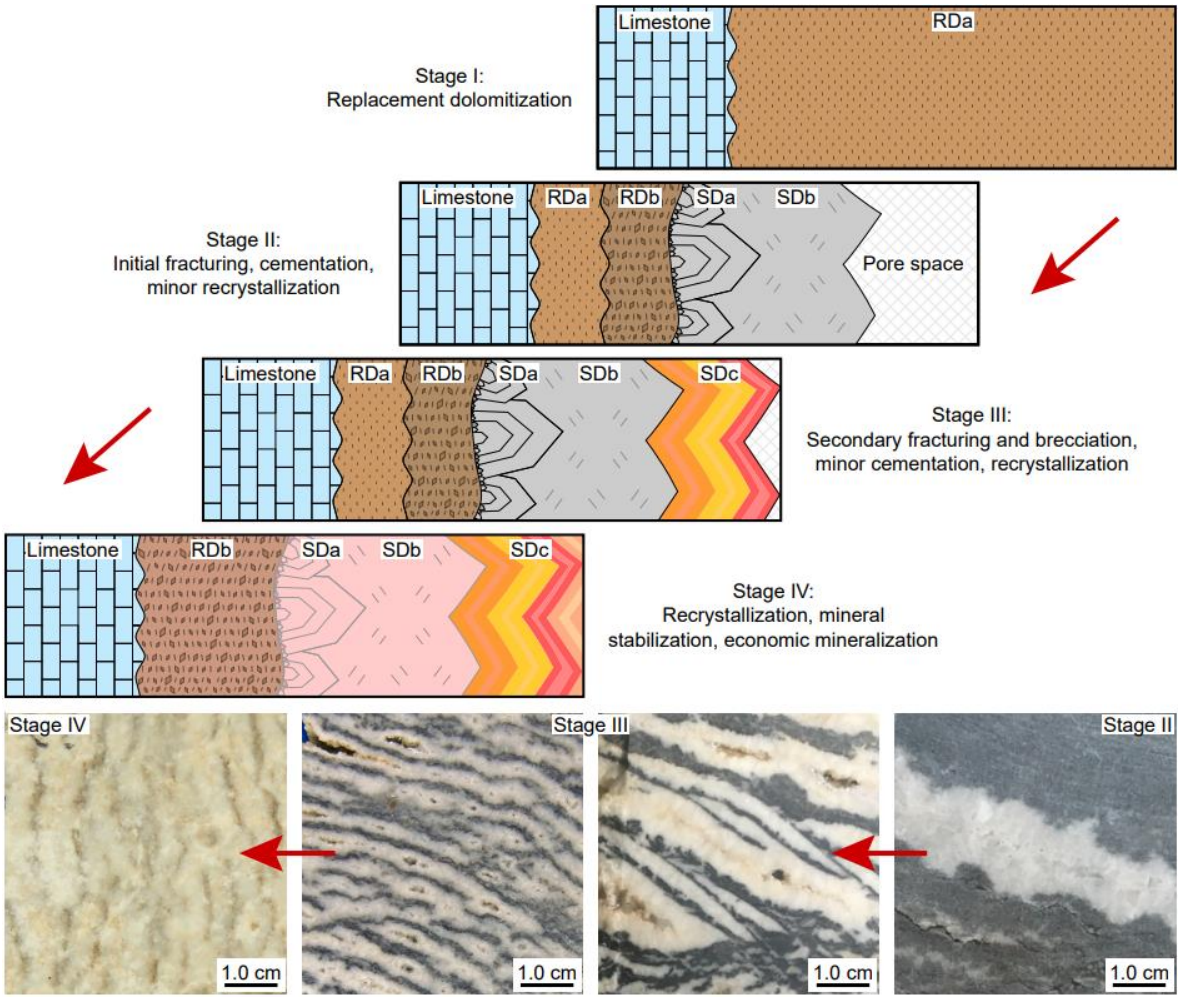

Figure 6.9. Conceptual model illustrating the multi-stage development of rock textures in HTD bodies. Stage I involves replacement dolomitization of the host-rock. Stage II involves fracturing, cementation, and the formation of zebra textures (associated with minor recrystallization). Stage III involves secondary fracturing and the formation of boxwork textures and cement-supported breccias (associated with significant recrystallization). Stage IV involves the final interval(s) of recrystallization, proximal to the fluid-source, that may coincide with economic mineralization.

RD (dark, finely crystalline) and SD (light, coarsely crystalline) in zebra textures, cement-supported breccias, and boxwork textures. In transmitted-light, however, SDa+b is syntaxial and in optical continuity with RDb; a characteristic of cavity-filling cements that have the same mineralogy as the cavity-wall (Wallace and Hood, 2018). Furthermore, the oscillatory zoning of the final paragenetic stage is indicative of crystal growth into a cavity (Nielsen et al. 1998; Gasparrini et al. 2006).

At WP, the zebra textures have textural characteristics that are similar to opening-mode, tensile fractures (cf. Brace, 1964; Ramsey and Chester, 2004). Adjacent fracture

surfaces, for example, are negative images of one another and would fit together if the SD bands were to be removed. Such opening-mode fractures are bedding-parallel, with SD crystals that are elongate perpendicular to the fracture surface (Fig. 6.9). Porosity is preserved between adjacent SD bands (Fig. 6.9), which suggests that the fractures formed by dilatation and cementation, rather than by displacive crystallization (cf. Merino et al. 2006; Merino and Canals, 2011). At WP, there is evidence of dilatation in the strata that corresponds to the proportion of in the zebra textures SD (10 to 30%). Likewise, there is clear evidence of dilatation in the cement-supported breccias (Fig. 6.2H, I). Conversely, there is no evidence of sorting or rotated clasts in these breccias, which suggest that they did not form by collapse. Sedimentological textures are preserved in the RD clasts, they have corroded margins, and they are crosscut by fractures that are now occluded by SD. Such textural evidence suggests that these breccias post-date replacement dolomitization, and that SD was syn-kinematic. A sudden drop in pore-fluid pressure due to fracturing and brecciation caused the rapid precipitation of SD, preserving the RD clasts in their positions (Davies and Smith, 2006; Stacey et al. 2021). Bedding-inclined zebra textures are rare, but they are spatially associated with these breccias, which suggests that elevated pore-fluid pressures and locally variable stress states impact their formation.

At MC and NTJ, the strata include bedding-inclined zebra textures and rare boxwork textures. The fracture angles vary considerably, but each individual zebra texture has a strikingly constant inclination. This increase in the fracture angle reflects the transition from tensile failure to a mode of dilatant shear failure that occurs under low differential stresses (Ramsey and Chester, 2004; McCormick and Rutter, 2022). Such conditions occur when pore-fluid pressures are high and close to the minimum principal stress. The dolomitizing fluid may have been preferentially focused into flow units that had a high lateral permeability relative to their vertical permeability, which resulted in the localization of the zebra textures in individual beds (Fig. 6.3A, B). Thus, the individual RD and SD bands are not bed-parallel, but the zebra textures are stratabound. Conversely, the boxwork

textures are non-stratabound, located proximal to the fracture corridor at MC and the contact between the Eldon Formation and the Pika Formation at NTJ (Fig. 6.3D, H). This strongly suggests that the Pika Formation was as a low permeability seal and reactivity barrier as the fluid entered the Eldon Formation, leading to an increase in the pore-fluid pressure proximal to this contact. Relative to zebra textures, boxwork textures have a characteristic increase in porosity, with highly corroded margins, and evidence of clast rotation (Jacquemyn et al. 2014; Morrow, 2014). The irregular orientations of the RD and SD bands in boxwork textures reflect the several fluid-pulses that entered the strata, which contributed to secondary fracturing and recrystallization (Fig. 6.9).

At the KHR, the strata include a wide array of bedding-inclined zebra textures with scattered patches of structureless SD. These rock textures are typically non-stratabound and comprise a strikingly high volume of SD, locally exceeding 80% of the strata. Nevertheless, the bedding-surfaces at the KHR are largely undisturbed with minimal evidence of dilatation. Such volumetric constraints suggest that dilatational fracturing and cementation was not the predominant mechanism at the KHR (Fig. 6.9). Conversely, there is widespread evidence of recrystallization. Much of the RD is unzoned, forming an interlocking mosaic of nonplanar-a crystals. Apart from their crystal sizes, RDb is largely indistinguishable from SDa+b based on their petrographical characteristics. Under CL, their homogenously dull- to medium-red luminescence indicates that RDb and SDa+b have been recrystallized (Koeshidayatullah et al. 2020b; McCormick et al. 2021). Consequently, these rock textures may have been initiated as fractures, but recrystallization is clearly the prevailing mechanism at the KHR (Fig. 6.9). As was the case for NTJ, the presence of a low permeability caprock also influenced the dolomitization of the strata at the KHR. Faults do not propagate through the argillaceous mudstone and shale in the upper parts of the Cathedral Formation, nor do they intersect the Stephen Formation to circulate the dolomitizing fluid upwards into the Eldon Formation.

6.6.2. Basin-scale fluid-flow and its influence on the rock textures

At a basin-scale, there is a spatial control on the development of these rock textures, which is also reflected in the geochemical data (Table 6.1). At WP, where the strata comprise RD with lesser SD, the $T\Delta_{47}$ values range from 150 to 159°C. $T\Delta_{47}$ values are higher than the T_h values by 5 to 20°C, which is due to pressure differences during the entrapment of the fluid inclusions (Came et al. 2017; Honlet et al. 2018). Conversely, the strata at the KHR comprise SD with lesser RD that have $T\Delta_{47}$ values ranging from 288 to 336°C. $T\Delta_{47}$ values are higher than the T_h values by up to 150°C, which may reflect thermal equilibration of $T\Delta_{47}$ through solid-state reordering due to internal, diffusion-driven isotope exchange reactions in the solid mineral lattice (Ryb et al. 2017; Lloyd et al. 2018; Hemingway and Henkes, 2021). Nevertheless, there is a clear trend of increasing temperature from the platform interior to the platform margin (Fig. 6.8B, C), which reflects the epicenter of rifting and the associated crustal thinning that was in the vicinity of the KHR (Aitken, 1971; Bond and Kominz, 1984; Powell et al. 2006). Such tectonism is also reflected in the composition of the dolomite, which has led previous works to suggest that the dolomitizing fluid(s) were at least partially sourced in the vicinity of the KHR (Powell et al. 2006; Vandeginste et al. 2007; Stacey et al. 2021).

At WP, limestone has the lowest Ce/Ce* (0.796), and these values are consistent with early Paleozoic seawater (Tostevin et al. 2016; Wallace et al. 2017). Ce/Ce* in dolomite may indicate that (i) the values were inherited from limestone, or (ii) dolomitization was partially mediated by seawater. In the latter case, the increasing Ce/Ce* with each paragenetic stage suggests that the fluid was less seawater-dominated over time. Such interpretation is consistent with the $\delta^{18}O_{fluid}$ values (2.8 to 4.6‰) that are between Middle Cambrian seawater (0 to –6‰; Veizer and Prokoph, 2015) and crustal fluids (2.2 to 11.5‰; Schulze et al. 2003). Trace elements at WP are highly differentiated, with SDc, having a marked enrichment of Fe (12130 ppm) and Mn (1190 ppm) relative to the earlier, non-ferroan paragenetic stages. The high Eu/Eu* values for SDc also plot in the field of

hydrothermal fluids that have interacted with ultramafic rocks (Douville et al. 2002). Such change in composition suggests that there was either a contribution from a different fluid-source, or the fluid was subject to increased latency and water-rock interaction prior to dolomitization. These data are consistent with Koeshidayatullah et al. (2020a) and Stacey et al. (2021) who suggested that dolomitization was mediated by seawater mixed with a crustal-sourced, serpentinite-derived brine.

The trend of increasing Ce/Ce* with each paragenetic stage that is present at WP (0.796 to 1.01) continues towards MC (0.908 to 0.993) and NTJ (0.882 to 0.991), which suggests that the fluid had a decreased contribution from seawater. The $\delta^{18}O_{fluid}$ values at MC (2.9 to 4.9‰) and NTJ (3.4 to 5.4‰) are also higher than at WP, which suggests that there was an increased contribution from crustal fluids. However, the spatial relationships between WP, MC, and NTJ are subtle and obscured because they were situated at a different stratigraphic position and, thus, depth at the time of dolomitization (Cathedral Formation vs. Eldon Formation). Nevertheless, these spatial relationships are clear between WP and the KHR, where the HTD bodies are situated in the Cathedral Formation. The KHR has the highest $\delta^{18}O_{fluid}$ (4.5 to 7.0‰) and Ce/Ce* (0.879 to 1.06) values, which suggests that the fluid had the least contribution from seawater (Fig. 6.7E; Table 6.2). At the KHR, the [Fe] (up to 14300 ppm) and [Mn] (up to 2180 ppm) are also significantly higher relative to at WP (Fig. 6.6A, D).

Overall, these geochemical relationships suggest that the fluid was seawater-dominated during the early stages of replacement dolomitization, potentially due to faults breaching the seafloor in the platform interior (cf. Hollis et al. 2017; Stacey et al. 2021). Such faults and fractures, however, did not propagate through the upper parts of the Cathedral Formation and the Stephen Formation at the KHR, where the geochemical data suggests that the fluid was crustal-dominated. These crustal fluids were sourced in the vicinity of the KHR, associated with crustal thinning and an elevated geothermal gradient, and flowed laterally towards the platform interior within the underlying Gog Group

(Stacey et al. 2021). The crustal fluids were then emplaced upwards along faults, mixed with seawater, and distributed by thermal convection cells to dolomitize the Cathedral Formation (cf. Hollis et al. 2017; Benjakul et al. 2020). The dolomitizing fluid also became less seawater-dominated over time, and thus with each later paragenetic stage. This basin-scale hydrogeological system is also reflected in the development of zebra textures, boxwork textures, cement-supported breccias, with fracturing being more prominent at the platform interior (distal to the fluid-source) and recrystallization overprinting these structural controls at the platform margin (proximal to the fluid-source).

6.7. Discussion

Each of the models for the formation of rock textures in HTD bodies fail to explain at least one of their textural characteristics. Models suggesting that zebra textures form through the dissolution-replacement of sedimentological features (Beales and Hardy, 1980; Krebs and Macqueen, 1984; Fontboté and Gorzawski, 1990; Morrow, 2014) fail to explain the non-stratabound components that they are typically associated with. Similarly, models suggesting that zebra textures form through dilatational fracturing and cementation (Nielsen et al. 1998; Vandeginste et al. 2005; Swennen et al. 2012) do not account for the volume expansion and mass-balance constraints required to accommodate such a process. Furthermore, models that invoke geochemical self-organization (Merino et al. 2006; Merino and Canals, 2011; Kelka et al. 2015, 2017) do not provide an explanation for the porosity between adjacent SD bands in the zebra textures. Kelka et al. (2017) suggested that zebra textures form by pressure solution and recrystallization, but stylolites commonly cross-cut entire zebra textures (Vandeginste et al. 2005; Stacey et al. 2021), which suggests that they predate the onset of pressure solution.

Wallace and Hood (2018) succinctly noted that the formation of zebra textures may involve a combination of several of these conceptual models. To systematically assess this, the method of Burgess et al. (2013) was used to construct a decision ranking table to

evaluate the evidence for each of the mechanisms that may be involved in the genesis of rock textures in HTD bodies (Fig. 6.10A). Based on these criteria (Fig. 6.10A), it is immediately obvious that a single genetic model cannot be applied to the Middle Cambrian strata in the WCSB, and that the importance of each process shifts from the platform interior to the platform margin. There are both depositional and structural controls on dolomitization at WP, whereas metasomatic processes (e.g., recrystallization, mineral stabilization) are the predominant mechanism at the KHR (Fig. 6.10A, B). Thus, the ensuing sections discuss these sedimentological, tectonic, and metasomatic controls at the scale of the HTD bodies and at their constituent rock textures.

6.7.1. Sedimentological controls

Numerous studies have recognized the effect of sedimentological parameters on the termination of the dolomitization front (Koeshidayatullah et al. 2020b), as well as on the size, geometry, and distribution of the resulting HTD bodies (Sharp et al. 2010; Humphreys et al. 2022). Such HTD bodies typically have stratabound components, bedding-parallel vertical terminations, and are often facies-restricted with sharp lithological contrasts between adjacent beds (e.g., grain size, texture, porosity). These lithological contrasts likely affected the permeability of the host-rock during replacement dolomitization, which resulted in the flow of the dolomitizing fluid being confined to individual beds. Bedding-parallel stylolites can also baffle fluid-flow during the early stages of replacement dolomitization, but they can be opened by later, highly pressurized fluids (Martín-Martín et al. 2018). These lithological heterogeneities not only affect the permeability of the host-rock, but also its mechanical properties. Relatively incompetent, ductile lithologies typically limit the propagation of faults, which results in the preferential containment of fractures into beds that comprise more competent, brittle lithologies (Bowness et al. 2022). Such depositional and early diagenetic controls, however, are largely overlooked when interpreting the formation of zebra textures.

A	Kicking Horse Rim (platform margin)			Num Ti Jah and Mistaya Canyon			Whirlpool Point (platform interior)		
Observation	Sedimentological	Tectonic	Metasomatic	Sedimentological	Tectonic	Metasomatic	Sedimentological	Tectonic	Metasomatic
Are the orientations of the HTD bodies stratabound?	-0.5	0.5	0.5	0.5	0.5	-0.5	1.0	0.0	-1.0
Is the presence of zebra textures facies dependent?	-1.0	0.5	0.5	1.0	0.5	-0.5	1.0	-0.5	-1.0
Do zebra textures mimic the sedimentary texture?	-0.5	0.5	1.0	0.5	0.0	-0.5	1.0	0.0	-1.0
Does the abundance of zebra textures change with fault proximity?	-1.0	0.0	0.5	-0.5	0.0	0.5	0.5	0.5	-0.5
Does the type of zebra textures change with fault proximity?	-1.0	0.0	0.5	-0.5	0.0	0.5	0.5	0.5	-0.5
Are zebra textures aligned with fractures?	-1.0	0.0	0.0	-0.5	0.5	-0.5	-0.5	1.0	-0.5
Do zebra textures include multi-phase replacement and cementation?	-1.0	-1.0	1.0	0.5	0.5	0.0	1.0	1.0	0.0
Are geochemical signatures differentiated between each paragetetic stage?	-1.0	-0.5	1.0	0.5	0.5	-1.0	0.5	1.0	-1.0
Are clasts in breccias and boxwork textures cement-supported?	-1.0	0.0	-0.5	-1.0	0.5	-0.5	-0.5	0.5	-0.5
Do clasts in breccias and boxwork textures have corroded margins?	-1.0	0.0	1.0	-0.5	0.0	0.5	-0.5	0.0	0.5
Are zebra textures associated with pressure dissolution?	-1.0	0.0	0.5	-0.5	0.0	0.0	-0.5	0.0	0.0
Are zebra textures associated with recrystallization?	-1.0	-0.5	1.0	0.0	0.0	0.5	0.0	0.0	0.5
Are clumped isotope temperatures ($T\Delta_{47}$) >250°C?	-1.0	0.5	1.0	0.0	0.0	-1.0	0.5	0.0	-1.0
Total	-12.0	0.0	8.0	-0.5	3.0	-2.5	4.0	4.0	-6.0

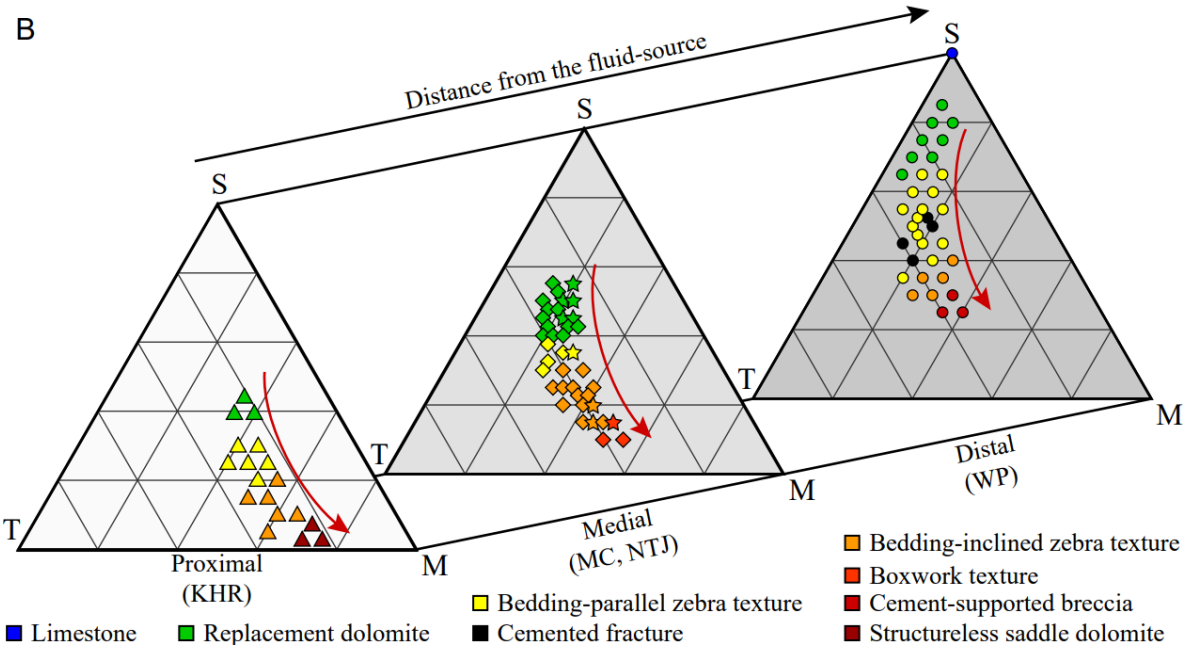

Figure 6.10. (A) Decision ranking table, following the method of Burgess et al. (2013), used to assess the evidence for (1.0) or against (–1.0) each mechanism involved in the formation of rock textures in HTD bodies. **(B)** Ternary diagrams that illustrate the proportion of sedimentological (S), tectonic (T), and metasomatic (M) controls on the genesis of these rock textures. Note the increase in the contribution of metasomatic processes proximal to the source of the dolomitizing fluid.

In the Middle Cambrian strata in the WCSB, bedding-parallel zebra textures are common in the highly anisotropic microbial mud- to bindstone facies (Fig. 6.2D). Conversely, bedding-inclined zebra textures are preferentially hosted in the more isotropic bioturbated mudstone facies (Fig. 6.2E, 6.3E). It has been suggested that zebra textures are constrained to low permeability precursor limestones that had a higher horizontal permeability relative to their vertical permeability prior to dolomitization (Davies and Smith Jr., 2006). In Albian strata from the Basque-Cantabrian Basin (northern Spain), Dewit et al. (2014) suggested that there is no relationship between the precursor texture of the host-rock and the resulting HTD bodies. In the system described by Dewit et al. (2014), however, the host-rock generally comprises low permeability bioclastic wackestones, and the zebra textures were constrained to the central parts of the HTD body (proximal to the fault and, thus, the source of the dolomitizing fluid). Thus, the occurrence and orientation of zebra textures may be a function of both the permeability of the host-rock and the pore-fluid pressure, which naturally suggests that their formation involves both sedimentological and tectonic controls (Fig. 6.10A, B). These sedimentological controls are prominent at WP (4.0), but decrease at MC and NTJ (–0.5), and further decrease towards the KHR (–12.0), proximal to the fluid-source (Fig. 6.10A, B).

6.7.2. Tectonic controls

The influence of tectonic features on dolomitization can vary depending on whether the fluid-flow event(s) were pre-, syn-, or post-kinematic (Kareem et al. 2019; Koeshidayatullah et al. 2022). Faults and fractures, for example, can act as conduits or barriers to fluid-flow. In the WCSB, the geometries of the HTD bodies vary according to their proximity to the faults that intersect the strata (Stacey et al. 2021), and the spatial distributions of each paragenetic stage reflect these tectonic features (McCormick et al. 2021). At WP, the rock textures are increasingly non-stratabound proximal to the fault. This relationship is also evident at a basin-scale, whereby the HTD bodies are increasingly

non-stratabound towards the interpreted source of the dolomitizing fluid, the faulted platform margin at the KHR. Such observations parallel those of Iriarte et al. (2012) for the HTD bodies in the Basque-Cantabrian Basin, who suggested that the increased density of fractures proximal to faults enhanced the permeability of the host-rock and, thus, the flux of the dolomitizing fluid. The lateral change from non-stratabound to stratabound geometries in HTD bodies have also been documented by Yao et al. (2020) and Humphrey et al. (2022) for the Maestrat Basin (eastern Spain). The relationship of HTD bodies with faults and fracture indicates that dolomitization was not pre-kinematic, but these observations are congruent with either a syn- or a post-kinematic interpretation.

The solution to this paradox lies in the "diagnostic" rock textures that are found in HTD bodies. Similar to the geometries of the HTD bodies, these rock textures vary according to their proximity to the source of the dolomitizing fluid (Fig. 6.10B). Distal to the fluid-source, the strata comprise bedding-parallel zebra textures that form by dilatational fracturing and cementation, with local evidence of dissolution-replacement (Wallace and Hood, 2018) or recrystallization along the margin of the fractures (McCormick et al. 2021). Towards the core of the HTD body, the angles of the fractures systematically increase, which reflects an increase in the effective differential stress (Ramsey and Chester, 2004; McCormick and Rutter, 2022). As dolomitization, recrystallization, and cementation progress, matrix porosity and fractures become occluded, and the permeability of the host-rock decreases (Koeshidayatullah et al. 2020b). With each successive fluid-pulse, these tectonic features are re-activated and each paragenetic stage is further restricted to the core of the HTD body. The observation that cement supported breccias and boxwork textures are present proximal to faults is strongly consistent with this interpretation. Stacey et al. (2021) suggested that these breccias form by the expulsion of overpressured fluids, upwards along faults, into a host-rock confined by a low permeability caprock. The presence of a vertical/lateral seal affects the local pore-fluid pressure, which is evidenced by the increasing abundance of non-stratabound rock

textures towards the upper contact with the Pika Formation at NTJ (Fig. 6.3C, D). These tectonic controls are roughly equivalent at WP (4.0) and at MC and NTJ (3.0), but they slightly decrease towards the KHR (0.0), proximal to the fluid-source (Fig. 6.10A, B).

6.7.3. Metasomatic controls

Metasomatism refers to compositional and mineralogical transformations, associated with chemical reactions triggered by the reaction of a fluid, that affect a pre-existing rock (*sensu* Lesher and Spera, 2015). Replacement dolomitization is the ever-present metasomatic process that affects these rock textures, however, the following section will largely focus on recrystallization and the transformation that occurs from WP to the KHR. Recrystallization refers to the replacement of the initial dolomite crystals by new, thermodynamically stable, crystals of the same mineralogy (*sensu* Machel, 1997; Ryan et al. 2022). At the KHR, the zebra textures cannot simply form by fracturing and cementation because SD forms >50% of the rock volume, with is minimal evidence of dilatation in the strata. This model also suggests that zebra textures should be found in any lithology (e.g., limestone, sandstone, granite), regardless of if replacement or recrystallization has occurred (cf. Wallace and Hood, 2018).

As dolomitization progresses, the ensuing fluid-pulses contribute to the recrystallization of pre-existing dolomite in the strata (Koeshidayatullah et al. 2020b; McCormick et al. 2021; Stacey et al. 2021). In zebra textures, cement-supported breccias, and boxwork textures, such recrystallization is denoted by the shift from RDa (concentrically zoned, planar-e to planar-s dolomite) to an interlocking mosaic of RDb (weakly zoned to unzoned, planar-s to nonplanar-a dolomite). The change in texture between RDa and RDb is accompanied by an increase in crystal size because dissolution-precipitation is partially driven by a reduction of surface free energy (Gregg et al. 1992; Machel, 1997; Ryan et al. 2022). The recrystallization from RDa to RDb is spatially associated with SD (McCormick et al. 2021), which strongly suggests that recrystallization

was caused by the fluid-flow event(s) that formed SD. The observation that RDb in has a similar trace element and stable isotopic composition as SDa+b is consistent with recrystallization; an observation that is typical of zebra textures elsewhere (Wallace and Hood, 2018, and references therein). In the platform interior facies, the recrystallization from RDa to RDb is associated with an increase in crystal size. At the KHR, however, there is a narrow region of decreased crystal size along the boundary between RDb and SDa+b (Fig. 6.5H). Such crystal size reduction is characteristic of dynamic recrystallization, a process that is driven by strain energy and surface free energy (Newman and Mitra, 1994, and references therein). As is the case for the effect of solid-state clumped isotope bond reordering, which may have occurred at the KHR, dynamic recrystallization may be particularly relevant in HTD bodies that have been subject to P/T conditions approaching low-grade metamorphism. These metasomatic controls are relatively minor at WP (–6.0), but increase at MC and NTJ (–2.5), and further increase towards the KHR (8.0), proximal to the fluid-source (Fig. 6.10A, B).

6.7.4. Implications for the interpretation of regional tectonics

The rock textures that are hosted in the Cathedral Formation and the Eldon Formation have been interpreted to have formed in both compressional and extensional tectonic settings. Symons et al. (1998) suggested that dolomitization occurred during the Laramide Orogeny (Cretaceous to Paleocene), whereas Vandeginste et al. (2005) suggested that it occurred during the Antler Orogeny (Devonian to Mississippian). Absolute age dating of dolomite, however, has not yet been consistently achieved. Vandeginste et al. (2005), for example, used K-Ar dating on a muscovite phase that post-dates the dolomite to suggest that dolomitization occurred prior to 338 Ma. Conversely, Stacey et al. (2021) interpreted that dolomitization occurred soon after deposition, prior to significant burial, because RD is crosscut by low-amplitude, bedding-parallel stylolites. Such interpretation suggests that dolomitization occurred under extensional tectonic conditions (late syn-rift to early post-

rift) during the middle to late Cambrian (Koeshidayatullah et al. 2020a; Stacey et al. 2021). Further support for this model is provided by a dolomitized megabreccia that has been described in the basinal equivalent of the Cathedral Formation, which is consistent with dolomitization prior to and during the deposition of the Stephen Formation (Powell et al. 2006; Collom et al. 2009; Johnston et al. 2009). These interpretations are similar to those of Shelton et al. (2019) for the Dublin Basin, Ireland, where reworked clasts of zebra textures in Viséan carbonates were re-deposited in a younger, Viséan debrite. Without age constraints on each paragenetic stage, however, the timing of cementation and recrystallization in the WCSB is equivocal.

These problems are exacerbated by model-driven approaches where zebra textures are considered to be "diagnostic" of a particular tectonic setting. In particular, a compressional tectonic origin is often invoked because many HTD bodies are documented in inverted sedimentary basins with known orogenic histories (e.g., Nielsen et al. 1998; Vandeginste et al. 2005; Gasparrini et al. 2006; Swennen et al. 2012). The largely stratabound orientations of these zebra textures are also consistent with the stress states of such compressional settings. It is, however, difficult to reconcile how hydrothermal dolomitization occurs in a compressional basin due to the lack of a proximal heat source, mass-balance constraints, and hydrologic models that fail to explain how the dolomitizing fluid was circulated for prolonged periods of time (Machel and Lonnee, 2002; Whitaker et al. 2004; Hendry et al. 2015). A compressional tectonic origin for the formation of zebra textures is also inconsistent with the rock-buffered marine rare earth and trace element signatures that are common in RD (Hirani et al. 2018; Stacey et al. 2021). Conversely, the higher geothermal gradients in extensional tectonic settings have been invoked to contribute to the formation of HTD bodies (Boni et al. 2000; Hollis et al. 2017; Koeshidayatullah et al. 2020a). The largely stratabound orientations of these zebra textures, however, are inconsistent with such settings, but elevated pore-fluid pressures and a mechanically anisotropic host-rock can locally influence their orientations.

6.8. Conclusions

Rock textures in HTD bodies are petrographical and geochemical archives of multi-phase dolomitization, recrystallization, and cementation. Such reactions fingerprint the geographical and temporal evolution of fluids in a sedimentary basin and provide critical insights into sedimentological, tectonic, and metasomatic processes. Accordingly, this study investigated the formation of zebra textures, cement-supported breccias, and boxwork textures that are hosted in Middle Cambrian strata in the WCSB. The detailed petrographical and geochemical analysis of these HTD bodies has led to the following key conclusions:

(1) Each of the models for the formation of zebra textures fail to explain at least one of their characteristics. However, the general features of these models can be grouped into ternary diagrams that can differentiate a wider array of rock textures.

(2) Sedimentological heterogeneities affect the permeability of the host-rock, which preferentially focuses the dolomitizing fluid(s) into individual stratabound units, and locally influences the pore-fluid pressure during dolomitization and cementation.

(3) There is clear evidence that brittle failure is involved in the formation of these rock textures. Models based solely on fracturing, however, fail to account for the volume expansion and mass-balance constraints required to accommodate such a process.

(4) With each successive pulse of the dolomitizing fluid, these faults and fractures can be reactivated and metasomatically altered (e.g., recrystallization, mineral stabilization, economic mineralization) to form increasingly complex rock textures.

(5) At the outcrop-scale, the relative importance of each process changes with each successive fluid-pulse and, thus, each paragenetic stage. This trend is also present at the basin-scale, with sedimentological and tectonic controls at the platform interior that are increasingly affected by metasomatism towards the platform margin.

In summary, zebra textures, cement-supported breccias, and boxwork textures are "diagnostic" of syn-kinematic conditions, but there is an over-reliance on these rock

textures as unique indicators of a given tectonic setting. Although compressional tectonics are consistent with the orientations of these rock textures, it is challenging to reconcile this with the low geothermal gradients and fluid fluxes. Conversely, extensional tectonics provide elevated heat fluxes, but other mechanisms (e.g., mechanical anisotropy, pore-fluid pressures) are required to justify the fact that the orientations of these rock textures are inconsistent with the local stress field. Thus, the application of "diagnostic" rock textures to postulate tectonic processes require a robust analysis of the timing, depth, and temperature of dolomitization. Such interpretations are critical to predicting the distribution of carbonate-hosted ore deposits and reservoir properties for energy exploitation and carbon storage.

Acknowledgements

This work was conducted as part of C.A. McCormick's doctoral research, funded by the President's Doctoral Scholar Award (The University of Manchester). We are grateful to Parks Canada and Alberta Tourism, Parks, and Recreation for the research and collection permits. $\delta^{13}C$, $\delta^{18}O$, and Δ_{47} analyses were made possible by a National Environmental Isotope Facility grant from the Natural Environment Research Council (NERC). Additional support came from the Society for Sedimentary Geology Foundation (Student Research Grant), the International Association of Sedimentologists (Postgraduate Research Grant), the British Sedimentological Research Group (Trevor Elliot Memorial Grant), and the American Association of Petroleum Geologists Foundation (Classen Family Named Grant). The authors acknowledge the NERC-funded Nanoscale Imaging and Analysis Facility for Environmental Materials in the Williamson Research Centre for Molecular Environmental Science, The University of Manchester (NERC CC042). We are indebted to John Waters (The University of Manchester) who conducted preliminary characterization of samples by X-ray diffraction, and to Jonathan Fellows (The University of Manchester) who conducted the electron-probe micro-analysis.

References

Aitken, J.D., 1971. Control of lower Paleozoic sedimentary facies by the Kicking Horse Rim, southern Rocky Mountains, Canada. Bulletin of Canadian Petroleum Geology, 19, 557-569.

Aitken, J. D., 1989. Birth, growth and death of the Middle Cambrian Cathedral carbonate lithosome, Southern Rocky Mountains. Bulletin of Canadian Petroleum Geology, 37(3), 316-333.

Aitken, J.D., 1997. Stratigraphy of the Middle Cambrian platformal succession, southern Rocky Mountains. Geological Survey of Canada Bulletin, 398, 1-322.

Anderson, N.T., Kelson, J.R., Kele, S., Daëron, M., Bonifacie, M., Horita, J., Mackey T.J., John C.M., Kluge T., Petschnig, P., Jost, A.B., Huntington, K.W., Bernasconi, S.M., Bergmann, K.D., 2021. A unified clumped isotope thermometer calibration (0.5–1,100 C) using carbonate-based standardization. Geophysical Research Letters, 48(7), e2020GL092069.

Beales, F.W., Hardy, J.L., 1980. Criteria for the recognition of diverse dolomite types with an emphasis on studies of host rocks for Mississippi Valley-type ore deposits. In: Zenger, D.H., Dunham, J.B., Ethington, R.L., (Eds.), *Concepts and Models of Dolomitization*. SEPM Special Publication. 28. Society of Economic Paleontologists and Mineralogists, Tulsa, OK, 197-213.

Benjakul, R., Hollis, C., Robertson, H.A., Sonnenthal, E.L., Whitaker, F.F., 2020. Understanding controls on hydrothermal dolomitisation: insights from 3D Reactive Transport Modelling of geothermal convection. Solid Earth Discussions, 1-35.

Bernasconi, S.M., Daëron, M., Bergmann, K.D., Bonifacie, M., Meckler, A.N., Affek, H.P., Anderson, N., Bajnai, D., Barkan, E., Beverly, E., Blamart, D., Burgener, L., Calmels, D., Chaduteau, C., Clog, M., Davidheiser-Kroll, B., Davies, A., Dux, F., Eiler, J., Elliott, B., Fetrow, A.C., Fiebig, J., Goldberg, S., Hermoso, M., Huntington, K.W., Hyland, E., Ingalls, M., Jaggi, M., John, C.M., Jost, A.B., Katz, S., Kelson, J., Kluge, T., Kocken, I.J., Laskar, A., Leutert, T.J., Liang, D., Lucarelli, J., Mackey, T.J., Mangenot, X., Meinicke, N., Modestou, S.E., Müller, I.A., Murray, S., Neary, A., Packard, N., Passey, B.H., Pelletier, E., Petersen, S., Piasecki, A., Schauer, A., Snell, K.E., Swart, P.K., Tripati, A., Upadhyay, D., Vennemann, T., Winkelstern, I., Yarian, D., Yoshida, N., Zhang, N., Ziegler, M., 2021. InterCarb: a community effort to improve inter-laboratory standardization of the carbonate clumped isotope thermometer using carbonate standards. Geochemistry, Geophysics, Geosystems, 22(5), e2020GC009588.

Bond, G.C., Christie-Blick, N., Kominz, M.A., Devlin, W.J., 1985. An early Cambrian rift to post-rift transition in the Cordillera of western North America. Nature, 315(6022), 742-746.

Bond, G.C., Kominz, M.A., 1984. Construction of tectonic subsidence curves for the early Paleozoic miogeocline, southern Canadian Rocky Mountains: Implications for subsidence mechanisms, age of breakup, and crustal thinning. Geological Society of America Bulletin, 95(2), 155-173.

Boni, M., Iannace, A., Bechstädt, T., Gasparrini, M., 2000. Hydrothermal dolomites in SW Sardinia (Italy) and Cantabria (NW Spain): evidence for late-to post-Variscan widespread fluid-flow events. Journal of Geochemical Exploration, 69, 225-228.

Bowness, N.P., Cawood, A.J., Ferrill, D.A., Smart, K.J., Bellow, H.B., 2022. Mineralogy controls fracture containment in mechanically layered carbonates. Geological Magazine, 1-19.

Brace, W.F., 1964. Brittle fracture of rocks. In: Judd, W.R., (Ed.). *State of Stress in Earth's Crust*. Elsevier, New York, 111-180.

Brand, W.A., Assonov, S.S., Coplen, T.B., 2010. Correction for the ^{17}O interference in $\delta^{13}C$ measurements when analyzing CO_2 with stable isotope mass spectrometry (IUPAC Technical Report). Pure and Applied Chemistry, 82, 1719-1733.

Burgess, P.M., Winefield, P., Minzoni, M., Elders, C., 2013. Methods for identification of isolated carbonate buildups from seismic reflection data. American Association of Petroleum Geologists bulletin, 97(7), 1071-1098.

Came, R.E., Azmy, K., Tripati, A., Olanipekun, B.J., 2017. Comparison of clumped isotope signatures of dolomite cements to fluid inclusion thermometry in the temperature range of 73–176 C. Geochimica et Cosmochimica Acta, 199, 31-47.

Collom, C.J., Johnston, P.A., Powell, W.G., 2009. Reinterpretation of 'Middle' Cambrian stratigraphy of the rifted western Laurentian margin: Burgess Shale Formation and contiguous units (Sauk II megasequence), Rocky Mountains, Canada. Palaeogeography, Palaeoclimatology, Palaeoecology, 277, 63-85.

Davies, A.J., John, C.M., 2017. Reducing contamination parameters for clumped isotope analysis: The effect of lowering Porapak™ Q trap temperature to below -50 C. Rapid Communications in Mass Spectrometry, 31(16), 1313-1323.

Davies, G.R., Smith Jr., L.B., 2006. Structurally controlled hydrothermal dolomite reservoir facies: an overview. American Association of Petroleum Geologists bulletin, 90, 1641-1690.

Dewit, J., Foubert, A., El Desouky, H.A., Muchez, P., Hunt, D., Vanhaecke, F., Swennen, R., 2014. Characteristics, genesis and parameters controlling the development of a large stratabound HTD body at Matienzo (Ramales Platform, Basque–Cantabrian Basin, northern Spain). Marine and Petroleum Geology, 55, 6-25.

Dickson, J.A.D., 1966. Carbonate identification and genesis as revealed by staining. Journal of Sedimentary Research, 36, 491-505.

Douville, E., Charlou, J.L., Oelkers, E.H., Bienvenu, P., Colon, C.J., Donval, J.P., Fouquet, Y., Prieur, D., Appriou, P., 2002. The rainbow vent fluids (36 140 N, MAR): the influence of ultramafic rocks and phase separation on trace metal content in Mid-Atlantic Ridge hydrothermal fluids. Chemical Geology, 184, 37-48.

Duggan, J.P., Mountjoy, E.W., Stasiuk, L.D., 2001. Fault-controlled dolomitization at Swan Hills Simonette oil field (Devonian), deep basin west-central Alberta, Canada. Sedimentology, 48(2), 301-323.

Fontboté, L., Gorzawski, H., 1990. Genesis of the Mississippi Valley-type Zn-Pb deposit of San Vicente, central Peru; geologic and isotopic (Sr, O, C, S, Pb) evidence. Economic Geology, 85, 1402-1437.

Gasparrini, M., Bechstädt, T., Boni, M., 2006. Massive hydrothermal dolomites in the southwestern Cantabrian Zone (Spain) and their relation to the Late Variscan evolution. Marine and Petroleum Geology, 23, 543-568.

Goldstein, R.H., Reynolds, T.J., 1994. *Systematics of fluid inclusions in diagenetic minerals*. Short Course 31, Society of Economic Paleontologists and Mineralogists, Tulsa, 199 p.

Gregg, J.M., Howard, S.A., Mazzullo, S.J., 1992. Early diagenetic recrystallization of Holocene (< 3000 years old) peritidal dolomites, Ambergris Cay, Belize. Sedimentology, 39(1), 143-160.

Hemingway, J.D., Henkes, G.A., 2021. A disordered kinetic model for clumped isotope bond reordering in carbonates. Earth and Planetary Science Letters, 566, 116962.

Hendry, J.P., Gregg, J.M., Shelton, K.L., Somerville, I.D., Crowley, S.F., 2015. Origin, characteristics and distribution of fault-related and fracture-related dolomitization: Insights from Mississippian carbonates, Isle of Man. Sedimentology, 62(3), 717-752.

Hirani, J., Bastesen, E., Boyce, A., Corlett, H., Gawthorpe, R., Hollis, C., John, C.M., Robertson, H., Rotevatn, A., Whitaker, F., 2018. Controls on the formation of stratabound dolostone bodies, Hammam Faraun Fault block, Gulf of Suez. Sedimentology, 65(6), 1973-2002.

Hollis, C., Bastesen, E., Boyce, A., Corlett, H., Gawthorpe, R., Hirani, J., Rotevatn, A., Whitaker, F., 2017. Fault-controlled dolomitization in a rift basin. Geology, 45(3), 219-222.

Honlet, R., Gasparrini, M., Muchez, P., Swennen, R., John, C. M., 2018. A new approach to geobarometry by combining fluid inclusion and clumped isotope thermometry in hydrothermal carbonates. Terra Nova, 30(3), 199-206.

Horita, J., 2014. Oxygen and carbon isotope fractionation in the system dolomite–water–CO2 to elevated temperatures. Geochimica et Cosmochimica Acta, 129, 111-124.

Howell, D., Griffin, W.L., Pearson, N.J., Powell, W., Wieland, P., O'Reilly, S.Y., 2013. Trace element partitioning in mixed-habit diamonds. Chemical Geology, 355, 134-143.

Humphrey, E., Gomez-Rivas, E., Martín-Martín, J.D., Neilson, J., Salas, R., Guimerà, J., 2022. Depositional and structural controls on a fault-related dolostone formation (Maestrat Basin, E Spain). Basin Research, 34(2), 961-990.

Iriarte, E., Lopez-Horgue, M.A., Schroeder, S., Caline, B., 2012. Interplay between fracturing and hydrothermal fluid flow in the Asón Valley hydrothermal dolomites (Basque Cantabrian Basin, Spain). Geological Society, London, Special Publications, 370(1), 207–227.

Jacquemyn, C., El Desouky, H., Hunt, D., Casini, G., Swennen, R., 2014. Dolomitization of the Latemar platform: Fluid flow and dolomite evolution. Marine and Petroleum Geology, 55, 43-67.

Jochum, K.P., Weis, U., Stoll, B., Kuzmin, D., Yang, Q., Raczek, I., Jacob, D.E., Stracke, A., Birbaum, K., Frick, D.A., Günther, D., Enzweiler, J., 2011. Determination of reference values for NIST SRM 610–617 glasses following ISO guidelines. Geostandards and Geoanalytical Research, 35(4), 397-429.

Jochum, K.P., Garbe-Schönberg, D., Veter, M., Stoll, B., Weis, U., Weber, M., Lugli, F., Jentzen, A., Schiebel, R., Wassenburg, J.A., Jacob, D.E., Haug, G.H., 2019. Nano-powdered calcium carbonate reference materials: Significant progress for microanalysis?. Geostandards and Geoanalytical Research, 43(4), 595-609.

John, C.M., Bowen, D., 2016. Community software for challenging isotope analysis: First applications of ‘Easotope’ to clumped isotopes. Rapid Communications in Mass Spectrometry, 30(21), 2285-2300.

Johnston, P.A., Johnston, K.J., Collom, C.J., Powell, W.G., Pollock, R.J., 2009. Palaeontology and depositional environments of ancient brine seeps in the Middle

Cambrian Burgess Shale at The Monarch, British Columbia, Canada. Palaeogeography, Palaeoclimatology, Palaeoecology, 277, 86-105.

Kareem, K.H., Al-Aasm, I.S., Mansurbeg, H., 2019. Structurally-controlled hydrothermal fluid flow in an extensional tectonic regime: A case study of Cretaceous Qamchuqa Formation, Zagros Basin, Kurdistan Iraq. Sedimentary Geology, 386, 52-78.

Kelka, U., Koehn, D., Beaudoin, N., 2015. Zebra pattern in rocks as a function of grain growth affected by second-phase particles. Frontiers in Physics, 3, 1-14.

Kelka, U., Veveakis, M., Koehn, D., Beaudoin, N., 2017. Zebra rocks: compaction waves create ore deposits. Scientific Reports, 7(1), 1-9.

Koeshidayatullah, A., Al-Sinawi, N., Swart, P. K., Boyce, A., Redfern, J., Hollis, C., 2022. Coevolution of diagenetic fronts and fluid-fracture pathways. Scientific Reports, 12(1), 1-11.

Koeshidayatullah, A., Corlett, H., Hollis, C., 2021. An overview of structurally-controlled dolostone-limestone transitions in the stratigraphic record. Earth-Science Reviews, 220, 103751.

Koeshidayatullah, A., Corlett, H., Stacey, J., Swart, P.K., Boyce, A., Robertson, H., Whitaker, F., Hollis, C., 2020a. Evaluating new fault-controlled hydrothermal dolomitisation models: Insights from the Cambrian Dolomite, Western Canadian Sedimentary Basin. Sedimentology, 67, 2945-2973.

Koeshidayatullah, A., Corlett, H., Stacey, J., Swart, P.K., Boyce, A., Hollis, C., 2020b. Origin and evolution of fault-controlled hydrothermal dolomitization fronts: A new insight. Earth and Planetary Science Letters, 541, 116291.

Krebs, W., Macqueen, R., 1984. Sequence of diagenetic and mineralization events, Pine Point lead-zinc property, Northwest Territories, Canada. Bulletin of Canadian Petroleum Geology, 32, 434-464.

Lesher, C.E., Spera, F.J., 2015. Thermodynamic and transport properties of silicate melts and magma. In: Sigurdsson, H., Houghton, B., McNutt, S.R., Rymer, H., Stix, J., (Eds.), *The encyclopedia of volcanoes*. Academic Press, 113-141.

Lloyd, M.K., Ryb, U., Eiler, J.M., 2018. Experimental calibration of clumped isotope reordering in dolomite. Geochimica et Cosmochimica Acta, 242, 1-20.

Lonnee, J., Machel, H.G., 2006. Pervasive dolomitization with subsequent hydrothermal alteration in the Clarke Lake gas field, Middle Devonian Slave Point Formation, British Columbia, Canada. American Association of Petroleum Geologists bulletin, 90(11), 1739-1761.

López-Horgue, M.A., Iriarte, E., Schröder, S., Fernández-Mendiola, P.A., Caline, B., Corneyllie, H., Frémont, J., Sudrie, M., Zerti, S., 2010. Structurally controlled hydrothermal dolomites in Albian carbonates of the Asón valley, Basque Cantabrian Basin, Northern Spain. Marine and Petroleum Geology, 27(5), 1069-1092.

Machel, H.G., 1997. Recrystallization versus neomorphism, and the concept of 'significant recrystallization' in dolomite research. Sedimentary Geology, 113(3-4), 161-168.

Machel, H.G., Lonnee, J., 2002. Hydrothermal dolomite—A product of poor definition and imagination. Sedimentary geology, 152(3-4), 163-171.

Martín-Martín, J.D., Gomez-Rivas, E., Gómez-Gras, D., Travé, A., Ameneiro, R., Koehn, D., Bons, P.D., 2018. Activation of stylolites as conduits for overpressured fluid flow in dolomitized platform carbonates. Geological Society, London, Special Publications, 459(1), 157-176.

McCormick, C.A., Corlett, H., Stacey, J., Hollis, C., Feng, J., Rivard, B., Omma, J.E., 2021. Shortwave infrared hyperspectral imaging as a novel method to elucidate multi-phase dolomitization, recrystallization, and cementation in carbonate sedimentary rocks. Scientific reports, 11(1), 1-16.

McCormick, C.A., Rutter, E.H., 2022. An experimental study of the transition from tensile failure to shear failure in Carrara marble and Solnhofen limestone: Does "hybrid failure" exist?. Tectonophysics, 844, 229623.

McMechan, M.E., 2022. Structural geometry and kinematic history of the southern Kicking Horse Rim Cambrian carbonate platform: out-of-sequence thrust faulting in the southern Canadian Rocky Mountains. Bulletin of Canadian Petroleum Geology, 69(1), 51-72.

Merino, E., Canals, À., 2011. Self-accelerating dolomite-for-calcite replacement: Self-organized dynamics of burial dolomitization and associated mineralization. American Journal Science, 311(7), 573-607.

Merino, E., Fletcher, R., Canals, À., 2006. Genesis of self-organized zebra textures in burial dolomites: displacive veins, induced stress, and dolomitization. Geologica Acta, 4, 383-393.

Morrow, D.W., 2014. Zebra and boxwork fabrics in hydrothermal dolomites of northern Canada: Indicators for dilational fracturing, dissolution or in situ replacement? Sedimentology, 61, 915-951.

Nance, W.B., Taylor, S.R., 1976. Rare earth element patterns and crustal evolution–I. Australian post-Archean sedimentary rocks. Geochimica et Cosmochimica Acta, 40(12), 1539-1551.

Nielsen, P., Swennen, R., Muchez, P., Keppens, E., 1998. Origin of Dinantian zebra dolomites south of the Brabant-Wales Massif, Belgium. Sedimentology, 45, 727-743.

Newman, J., Mitra, G., 1994. Fluid-influenced deformation and recrystallization of dolomite at low temperatures along a natural fault zone, Mountain City window, Tennessee. Geological Society of America Bulletin, 106(10), 1267-1280.

Paradis, S., Simandl, G.J., 2017. Are there genetic links between carbonate-hosted barite-zinc-lead sulphide deposits and magnesite mineralization in southeast British Columbia? In: Rogers, N. (Ed.). Targeted Geoscience Initiative: 2017 Report of Activities, Geological Survey of Canada, Open File 8358, 217-227.

Paton, C., Hellstrom, J., Paul, B., Woodhead, J., Hergt, J., 2011. Iolite: Freeware for the visualisation and processing of mass spectrometric data. Journal of Analytical Atomic Spectrometry, 26(12), 2508-2518.

Petersen, S.V., Defliese, W.F., Saenger, C., Daëron, M., Huntington, K.W., John, C.M., Kelson, J.R., Bernasconi, S.M., Colman, A.S., Kluge, T., Olack, G.A., Schauer, A.J., Bajnai, D., Bonifacie, M., Breitenbach, S.F.M., Fiebig, J., Fernandez, A.B., Henkes, G.A., Hodell, D., Katz, A., Kele, S., Lohmann, K.C., Passey, B.H., Peral, M.Y., Petrizzo, D.A., Rosenheim, B.E., Tripati, A., Venturelli, R., Young, E.D., Winkelstern, I.Z., 2019. Effects of improved ^{17}O correction on interlaboratory agreement in clumped isotope calibrations, estimates of mineral-specific offsets, and temperature dependence of acid digestion fractionation. Geochemistry, Geophysics, Geosystems, 20(7), 3495-3519.

Powell, W.G., Johnston, P.A., Collom, C.J., Johnston, K.J., 2006. Middle Cambrian brine seeps on the Kicking Horse Rim and their relationship to talc and magnesite mineralization and associated dolomitization, British Columbia, Canada. Economic Geology, 101, 431-451.

Pratt, B.R., 2002. Teepees in peritidal carbonates: origin via earthquake-induced deformation, with example from the Middle Cambrian of western Canada. Sedimentary Geology, 153, 57-64.

Price, R., 1981. The Cordilleran foreland thrust and fold belt in the southern Canadian Rocky Mountains. Geological Society, London, Special Publications, 9(1), 427-448.

Ramsey, J.M., Chester, F.M., 2004. Hybrid fracture and the transition from extension fracture to shear fracture. Nature, 428(6978), 63-66.

Root, K.G., 2001. Devonian Antler fold and thrust belt and foreland basin development in the southern Canadian Cordillera: implications for the Western Canada Sedimentary Basin. Bulletin of Canadian Petroleum Geology, 49(1), 7-36.

Rosenbaum, J., Sheppard, S.M.F., 1986. An isotopic study of siderites, dolomites and ankerites at high temperatures. Geochimica et cosmochimica acta, 50(6), 1147-1150.

Rustichelli, A., Iannace, A., Tondi, E., Di Celma, C., Cilona, A., Giorgioni, M., Parente, M., Girundo, M., Invernizzi, C., 2017. Fault-controlled dolomite bodies as palaeotectonic indicators and geofluid reservoirs: New insights from Gargano Promontory outcrops. Sedimentology, 64(7), 1871-1900.

Ryan, B.H., Kaczmarek, S.E., Rivers, J.M., Manche, C.J., 2022. Extensive recrystallization of Cenozoic dolomite during shallow burial: A case study from the Palaeocene–Eocene Umm er Radhuma formation and a global meta-analysis. Sedimentology.

Ryb, U., Eiler, J.M., 2018. Oxygen isotope composition of the Phanerozoic ocean and a possible solution to the dolomite problem. Proceedings of the National Academy of Sciences, 115(26), 6602-6607.

Ryb, U., Lloyd, M.K., Stolper, D.A., Eiler, J.M., 2017. The clumped-isotope geochemistry of exhumed marbles from Naxos, Greece. Earth and Planetary Science Letters, 470, 1-12.

Schulze, D.J., Harte, B., Valley, J.W., Brenan, J.M., Dominic, M.D.R., 2003. Extreme crustal oxygen isotope signatures preserved in coesite in diamond. Nature, 423(6935), 68-70.

Sharp, I., Gillespie, P., Morsalnezhad, D., Taberner, C., Karpuz, R., Vergés, J., Horbury, A., Pickard, N., Garland, J., Hunt, D. 2010. Stratigraphic architecture and fracture-controlled dolomitization of the Cretaceous Khami and Bangestan groups: an outcrop case study, Zagros Mountains, Iran. In: Van Buchem, F.S.P., Gerdes, K.D., Esteban, M., (Eds.), *Mesozoic and Cenozoic Carbonate Systems of the Mediterranean and the Middle East: Stratigraphic and Diagenetic Reference Models*. Geological Society, London, Special Publications, 329(1), 343-396.

Shelton, K.L., Hendry, J.P., Gregg, J.M., Truesdale, J.P., Somerville, I.D., 2019. Fluid Circulation and Fault- and Fracture-related Diagenesis in Mississippian Syn-rift Carbonate Rocks on the Northeast Margin of the Metalliferous Dublin Basin, Ireland. Journal of Sedimentary Research, 89(6), 508-536.

Sibley, D.F., Gregg, J.M., 1987. Classification of dolomite rock textures. Journal of Sedimentary Research, 57, 967-975.

Slind, O.L., Andrews, G.D., Murray, D.L., Norford, B.S., Paterson, D.F., Salas, C.J. and Tawadros, E.E., 1994. Middle Cambrian to Lower Ordovician strata of the Western Canada Sedimentary Basin. In: Mossop, G., Shetsen, I., (Eds.), *Geological Atlas of the*

Western Canada Sedimentary Basin. Canadian Society of Petroleum Geologists and Alberta Research Council, Special Report, 4, 87-108.

Stacey, J., Corlett, H., Holland, G., Koeshidayatullah, A., Cao, C., Swart, P., Crowley, S., Hollis, C., 2021. Regional fault-controlled shallow dolomitization of the Middle Cambrian Cathedral Formation by hydrothermal fluids fluxed through a basal clastic aquifer. Geological Society of America Bulletin. 133(11-12), 2355-2377.

Steele-MacInnis, M., Lecumberri-Sanchez, P., Bodnar, R.J., 2012. Short note: HokieFlincs_H2O-NaCl: A Microsoft Excel spreadsheet for interpreting microthermometric data from fluid inclusions based on the PVTX properties of H2O-NaCl. Computers & Geosciences, 49, 334-337.

Swennen, R., Dewit, J., Fierens, E., Muchez, P., Shah, M., Nader, F., Hunt, D., 2012. Multiple dolomitization events along the Pozalagua Fault (Pozalagua Quarry, Basque–Cantabrian Basin, Northern Spain). Sedimentology, 59, 1345-1374.

Symons, D.T.A., Lewchuk, M.T., Sangster, D.F., 1998. Laramide orogenic fluid flow into the Western Canada sedimentary basin; evidence from paleomagnetic dating of the Kicking Horse mississippi valley-type ore deposit. Economic Geology, 93(1), 68-83.

Taylor, S.R., McLennan, S.M., 1985. *The continental crust: its composition and evolution*. Blackwell, Oxford, 312 pp.

Tostevin, R., Shields, G.A., Tarbuck, G.M., He, T., Clarkson, M.O., Wood, R.A., 2016. Effective use of cerium anomalies as a redox proxy in carbonate-dominated marine settings. Chemical Geology, 438, 146-162.

Vandeginste, V., Swennen, R., Gleeson, S.A., Ellam, R.M., Osadetz, K., Roure, F., 2005. Zebra dolomitization as a result of focused fluid flow in the Rocky Mountains Fold and Thrust Belt, Canada. Sedimentology, 52, 1067-1095.

Vandeginste, V., Swennen, R., Gleeson, S.A., Ellam, R.M., Osadetz, K., Roure, F., 2007. Geochemical constraints on the origin of the Kicking Horse and Monarch Mississippi Valley-type lead-zinc ore deposits, southeast British Columbia, Canada. Mineralium Deposita, 42(8), 913-935.

Veizer, J., Prokoph, A., 2015. Temperatures and oxygen isotopic composition of Phanerozoic oceans. Earth-Science Reviews, 146, 92-104.

Wallace, M.W., Both, R., Morales-Ruano, S., Hach-Ali, P.F., Lees, T., 1994. Zebra textures from carbonate-hosted sulfide deposits: sheet cavity networks produced by fracture and solution enlargement. Economic Geology, 89, 1183-1191.

Wallace, M.W., Hood, A.vS., 2018. Zebra textures in carbonate rocks: Fractures produced by the force of crystallization during mineral replacement. Sedimentary Geology, 368, 58-67.

Wallace, M.W., Hood, A.vS., Shuster, A., Greig, A., Planavsky, N.J., Reed, C.P., 2017, Oxygenation history of the Neoproterozoic to early Phanerozoic and the rise of land plants. Earth and Planetary Science Letters, 466, 12-19.

Wheeler, J.O., Hoffman, P.F., Card, K.D., Davidson, A., Sanford, B.V., Okulitch, A.V., Roest, W.R., 1996. Geological map of Canada. Geological Survey of Canada, "A" Series Map, 1860A.

Whitaker, F.F., Smart, P.L., Jones, G.D., 2004. Dolomitization: from conceptual to numerical models. Geological Society, London, Special Publications, 235(1), 99-139.

Woodhead, J.D., Hellstrom, J., Hergt, J.M., Greig, A., Maas, R., 2007. Isotopic and elemental imaging of geological materials by laser ablation inductively coupled plasma-mass spectrometry. Geostandards and Geoanalytical Research, 31(4), 331-343.

Yao, S., Gomez-Rivas, E., Martín-Martín, J.D., Gómez-Gras, D., Travé, A., Griera, A., Howell, J.A., 2020. Fault-controlled dolostone geometries in a transgressive–regressive sequence stratigraphic framework. Sedimentology, 67(6), 3290-3316.

Blank page

Local hardening mechanisms in the laboratory and in nature: implications for the formation of closely spaced meso-fractures in fault-controlled dolomite bodies

Cole A. McCormick [1,*], Ernest H. Rutter [1], Hilary Corlett [2], Cathy Hollis [1]

1. Department of Earth and Environmental Sciences, The University of Manchester, Manchester, M13 9PL, United Kingdom.

2. Department of Earth Sciences, Memorial University of Newfoundland, St. John's, Newfoundland, A1C 5S7, Canada.

* Corresponding author: Cole McCormick - cole.mccormick@manchester.ac.uk

Abstract

Dolomitization in structurally-controlled environments typically involves the formation of rock textures that reflect the interaction of high-temperature, pressurized fluids with the surrounding host-rock. Recent works have investigated the dimensions of the dolomite bodies, the timing of dolomitization, and the origin of the dolomitizing fluid. Nevertheless, the localization of strain during fault-controlled dolomitization has received limited attention. By integrating the conventional analytical techniques that are used to study carbonate diagenesis with axisymmetric rock deformation experiments, novel insights can be made into the governing processes that control the formation of rock textures in fault-controlled dolomite bodies. This study integrates the analysis of natural geological samples from Middle Cambrian strata in the Western Canadian Sedimentary Basin with laboratory-based rock deformation experiments. The samples include zebra textures, comprising alternating bands of replacement dolomite (RD) and saddle dolomite (SD) that form symmetrical RD-SD-SD-RD patterns. Fragmented sheets of RD are commonly entrained in the SD bands of the zebra textures, and petrographical analyses suggest that the SD bands comprise elongate crystals that were syntaxially built by a succession of crack-seal increments. To model this process, rock deformation experiments were conducted on three lithologies with different grain-sizes and porosities, Carrara marble (98 μm; <1%), Solnhofen limestone (4 μm; 4%), and Portland limestone (350 μm; 14%). To simulate strain-hardening and the formation of crack-seal textures, samples were held in an annealed copper jacket and deformed in axisymmetric extension. Textural heterogeneities between each lithology support field observations that strain is localized into discrete fractures in mudstones and wackestones whereas it is widely distributed in grainstones and rudstones. The experimental results also demonstrate the need for a local hardening mechanism to propagate multiple, closely spaced fractures in the laboratory and in nature. In fault-controlled dolomite bodies, mechanisms such as dilatancy hardening and precipitation hardening contribute to the formation of zebra textures.

"Such a system, although it may originally be quite homogeneous, may later develop a pattern or structure due to an instability of the homogeneous equilibrium, which is triggered off by random disturbances" – Alan M. Turing (1952; p. 37).

7.1. Introduction

Natural geological systems, which are rarely homogenous, include a wide range of patterns and structures that signify a deviation from equilibrium, triggered off by predictable disturbances. There are numerous examples of these rhythmic structures in geological systems, including ladder veins (Green et al. 1982; Hodgson, 1989), deformation bands (Fossen et al. 2007; Rutter and Glover, 2012), fracture swarms (Bai and Pollard, 2000; Olson, 2004), and zebra dolomite textures (Wallace and Hood, 2018; McCormick et al. Chapter VI). The formation of these closely spaced structures requires a local stress perturbation and/or a local hardening mechanism to prevent additional strain from localizing in their vicinity (Rutter and Glover, 2012; Wallace and Hood, 2018). Zebra textures comprise alternating, mm- to cm-scale, bands of replacement dolomite (RD) and saddle dolomite (SD) that form symmetrical RD-SD-SD-RD patterns (Fig. 7.1). It is widely accepted that fracturing plays a critical role in their development (Wallace and Hood, 2018; McCormick et al. Chapter VI), but the impact of local hardening mechanisms during fault-controlled dolomitization is still poorly understood.

In the laboratory, experimental rock mechanics can provide invaluable insights into these processes, facilitating the interpretation of failure mechanisms in natural geological systems. In axisymmetric extension, and when σ_3 is negative, tensile failure results in the formation of a single opening-mode fracture that is oriented normal to σ_3 and in the plane of $\sigma_1 = \sigma_2$ (Brace, 1960; Ramsey and Chester, 2004; McCormick and Rutter, 2022). A single fracture forms because there is no mechanism to prevent the continued increase of its aperture. An annealed copper jacket, however, can be used to promote the formation of

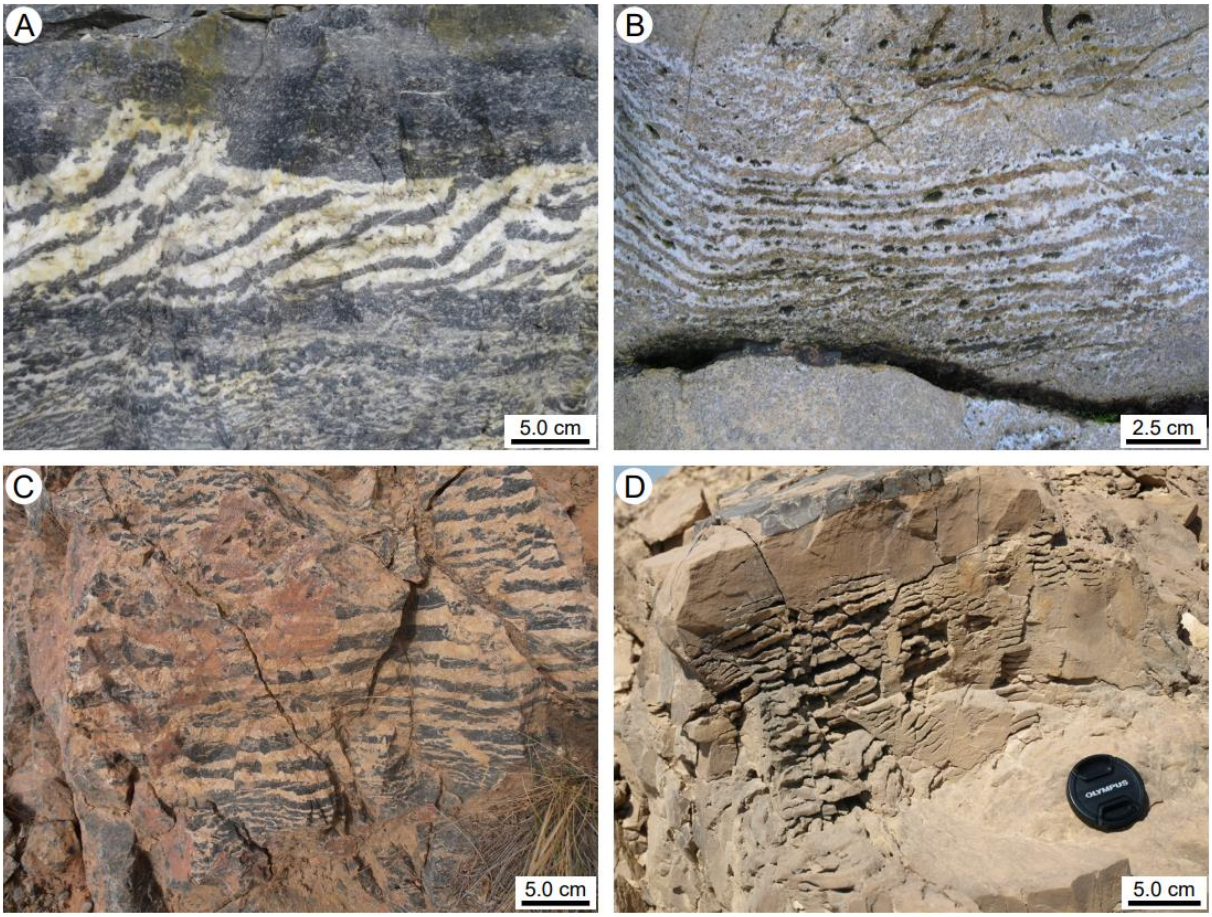

Figure 7.1. Closely spaced meso-fractures that are commonly found in fault-controlled dolomite bodies (i.e., zebra textures). These zebra textures are hosted in the **(A)** Eldon Formation (Middle Cambrian, western Canada), **(B)** Pier Dolomite Formation (Mississippian, northern Wales), **(C)** Lujar-Gador unit (Triassic, southern Spain), and **(D)** Thebes Formation (Eocene, northeast Egypt).

several fractures because the jacket locally strain-hardens as dislocations are introduced into the copper upon deformation. Accordingly, this study tests the hypothesis that a local hardening mechanism is required to nucleate and stabilize multiple, closely spaced, fractures in the laboratory. Petrographical analyses of zebra dolomite textures from the Western Canadian Sedimentary Basin (WCSB; Fig. 7.1A) were then conducted to determine whether there is evidence of strain-hardening during deformation. The zebra textures in the WCSB are textbook examples of these features, with local variations illustrated by examples from other sedimentary basins worldwide (Fig. 7.1B, C, D).

7.2. Methods

Carrara marble (CM; n = 4), Solnhofen limestone (SL; n = 10), and Portland limestone (PL; n = 4) were used as the experimental materials for this study. CM is a medium-grade metamorphic rock from the Tuscany region of Italy, comprising >99.9 wt% $CaCO_3$, with a mean grain size of 98.4 μm and 0.2% porosity. SL is a pelagic mudstone from the Bavaria region of Germany, comprising 99.1 wt% $CaCO_3$, with a mean grain size of 3.8 μm and 4.2% porosity. PL is a well-sorted ooid grainstone from the Isle of Portland, United Kingdom, comprising 95.6 wt% $CaCO_3$, with a mean grain size of 350 μm and 14.2% porosity. CM was cored in an arbitrary but constant direction (designated the *a*-direction in this block), whereas SL and PL was cored normal to bedding. Cylindrical samples were waisted to 13 mm in diameter over a central length of 16 mm, and then air-dried at a relative humidity of 60%.

Samples were held in a ¼ mm thick, annealed copper jacket that was heat-treated to ~600°C to remove crystal dislocations, quenched in water, and cleaned with nitric acid. Steel split-cones, with an included angle of 70°, were placed at each end of the jacket, and heat-shrink rubber tubing was placed around the loading piston assembly to prevent ingress of the confining fluid. A bayonet-style connector was placed on the bottom of the loading piston to engage with the top of the internal load cell, allowing for experiments to be conducted in axisymmetric extension. True tensile stresses were achieved because the sample diameter was less than that of the moving piston (19 mm) where it passes through the pressure seal. After the loading piston assembly is inserted into the pressure vessel, it is sealed, and dioctyl sebacate synthetic ester is pumped into the vessel. Experiments were conducted at 20°C and an axial displacement rate of 3.3×10^{-3} mm s^{-1}, which corresponds to a strain rate of 2.1×10^{-4} s^{-1}. Experiments were taken to at least –5% strain, after which the piston assembly was unloaded, and the vessel was depressurized to recover the sample.

Microstructural observations were made on polished sections that were prepared from samples deformed in the rock deformation experiments and those collected from the

Middle Cambrian strata in the WCSB. These samples were vacuum impregnated with blue-stained epoxy resin, prepared as 20 μm thick sections, and polished on their upper surfaces. Polished sections were examined in transmitted light and then analyzed using a CITL Mk5 cold cathodoluminescence system (operating conditions = 15 to 20 kV and 350 to 450 μA) that is mounted on a Nikon Eclipse LV100N POL petrographical microscope. Backscattered electron (accelerating voltage = 15.0 kV) imaging was conducted on these sections using a Thermo Fisher Scientific Quanta 650 FEG scanning electron microscope.

7.3. Experimental results

Four samples of CM were deformed in axisymmetric extension at confining pressures ($\sigma_1 = \sigma_2$) that range from 20 to 50 MPa. The average σ_3 at failure for these experiments, corrected for the strength of the copper jacket, is –4.6 ± 1.7 MPa (Table 7.1). Given that there is no angle on the failure surfaces ($\theta = 0$), the resolved shear stress (τ) is also equal to zero, and the resolved normal stress (σ_n) is equal to σ_3 (Table 7.1). Petrographically, the deformed samples include several discrete extension fractures, but the deformation is largely distributed throughout the sample with numerous examples of grain-scale cracks and widespread intracrystalline twinning (Fig. 7.2A, B). Each of the discrete extension fractures, and the distributed grain-scale cracks are oriented approximately normal to σ_3 and in the plane of $\sigma_1 = \sigma_2$ (Fig. 7.2A, B). There are also examples of incipient fractures that do not propagate throughout the entire sample, decreasing in aperture and terminating at their tip (Fig. 7.2A).

Ten samples of SL were deformed in axisymmetric extension at confining pressures that range from 20 to 90 MPa. The average σ_3 at failure for these experiments, corrected for the strength of the copper jacket, is –0.8 ± 1.6 MPa (Table 7.1). Petrographically, the deformed samples include numerous discrete extension fractures, with minimal deformation present in the regions between these fractures (Fig. 7.2C, D). In particular, distributed grain-scale cracks and intracrystalline twinning were not observed. Relative to

Lithology	Axial displacement	Sample ID	σ_1 (MPa)	σ_3 (MPa)	$\sigma_1 - \sigma_3$ (MPa)	Failure angle (°)	τ (MPa)	σ_n (MPa)
CM	Extension	CM_E01	20.0	-2.4	22.4	0	0	-2.4
CM	Extension	CM_E04	30.0	-3.4	33.4	0	0	-3.4
CM	Extension	CM_E02	40.0	-6.8	46.8	0	0	-6.8
CM	Extension	CM_E05	50.0	-5.7	55.7	0	0	-5.7
SL	Extension	SL_E30	20.0	-3.9	23.9	0	0	-3.9
SL	Extension	SL_E01	30.0	-0.5	30.5	0	0	-0.5
SL	Extension	SL_E02	30.0	-1.9	31.9	0	0	-1.9
SL	Extension	SL_E03	40.0	-0.8	40.8	0	0	-0.8
SL	Extension	SL_E04	40.0	-0.1	40.1	0	0	-0.1
SL	Extension	SL_E31	50.0	-2.2	52.2	0	0	-2.2
SL	Extension	SL_E29	60.0	-1.9	61.9	0	0	-1.9
SL	Extension	SL_E32	70.0	0.2	69.8	0	0	0.2
SL	Extension	SL_E07	80.0	2.1	77.9	0	0	2.1
SL	Extension	SL_E33	90.0	0.7	89.3	0	0	0.7
PL	Extension	PL_E01	20.0	-4.5	24.5	0	0	-4.5
PL	Extension	PL_E04	30.0	-4.5	34.5	0	0	-4.5
PL	Extension	PL_E02	40.0	-4.4	44.4	0	0	-4.4
PL	Extension	PL_E05	50.0	-5.9	55.9	0	0	-5.9

Table 7.1. Results from the rock deformation experiments conducted in axisymmetric extension on Carrara marble (CM), Solnhofen limestone (SL), and Portland limestone (PL). Values reported for the minimum principal stress (σ_3) at failure are corrected for the strength of the copper jacket following the method described in McCormick and Rutter (2022).

CM, the extension fractures in SL are more planar and intersect the sample precisely normal to σ_3 (Fig. 7.2C, D). The smaller, incipient fractures observed in CM are rare in SL as most of the extension fractures propagate through the entire sample, with strikingly consistent apertures (Fig. 7.2C).

Four samples of PL were deformed in axisymmetric extension at confining pressures that range from 20 to 50 MPa. The average σ_3 at failure for these experiments, corrected for the strength of the copper jacket, is –4.8 ± 0.6 MPa (Table 7.1). Petrographically, the deformed samples include several, poorly developed extension fractures, but the deformation is largely distributed throughout the sample (Fig. 7.2E, F). Overall, the extension fractures are weakly oriented normal to σ_3 and in the plane of $\sigma_1 = \sigma_2$ (Fig. 7.2E). Nevertheless, the matrix between the extension fractures includes highly fragmented and brecciated clasts, which are largely unoriented, with local evidence of grain comminution, rotation, and sliding (Fig. 7.2F).

The closely spaced, extension fractures that were produced in these experiments were only feasible due to the application of the annealed copper jacket. In experiments

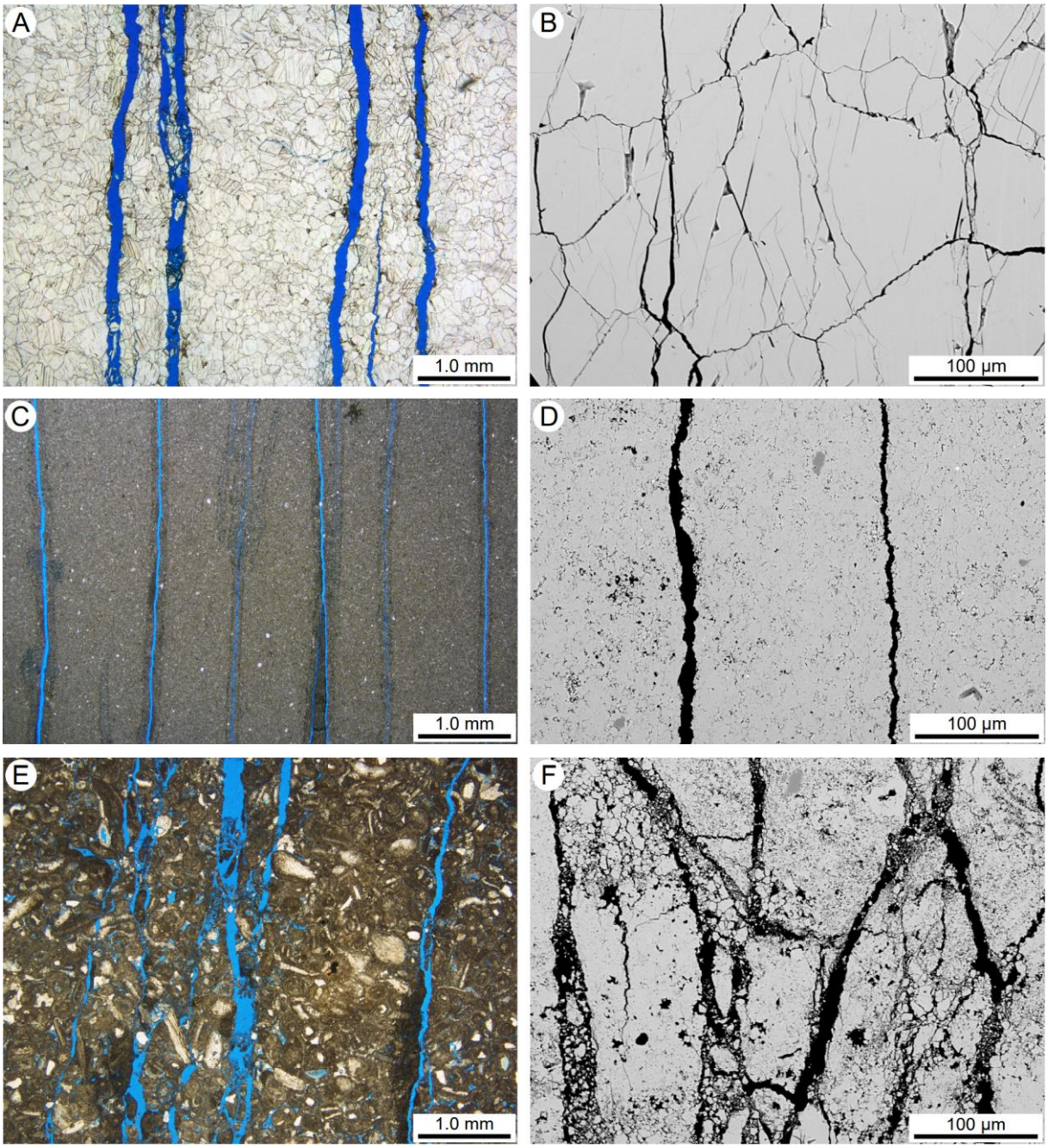

Figure 7.2. Transmitted light photomicrographs in plane-polarized light (left) and back-scattered electron photomicrographs (right) showing the results of the extensional rock deformation experiments, conducted at a confining pressure ($\sigma_1 = \sigma_2$) of 40 MPa, on **(A, B)** Carrara marble (CM), **(C, D)** Solnhofen limestone (SL), and **(E, F)** Portland limestone (PL). Note that the long axis of each image is oriented with σ_1 and the short axis is oriented with σ_1.

conducted without a copper jacket, the specimen fractures at its weakest point and separates into two pieces as no strain-hardening has occurred. In experiments conducted with a copper jacket, the jacket locally stretches and becomes strain-hardened as the first fracture propagates. It then requires less stress to initiate additional fractures in new

locations rather than to continue to open the first fracture where the strain-hardening has occurred. Evidently, there is not a copper jacket present in natural geological settings, used here as an analogue. Nevertheless, there are several other mechanisms that can contribute to strain-hardening during fault-controlled dolomitization, which are discussed below.

7.4. Strain-hardening mechanisms in fault-controlled dolomite bodies

Although carbonate sedimentary rocks can exhibit strain-softening behaviour during distributed cataclastic flow at the macro-scale (Micarelli et al. 2006; Nicolas et al. 2016), localized strain-hardening mechanisms such as dilatancy hardening, precipitation hardening, and the stress shadow effect may be operative at the meso- and the micro-scale (Brace and Martin, 1968; Kresse et al. 2013; Olson, 2004; Paterson and Wong, 2005; Noiriel et al. 2010).

7.4.1. Dilatancy hardening

Dilatancy hardening is a process by which, during brittle failure, an overall increase in the porosity of the rock reduces the pore-fluid pressure. This reduction in the pore-fluid pressure increases the effective stress, thus strengthening the rock (Brace and Martin, 1968; Scholz et al. 1973; Brantut, 2021). Given that the pore-fluid pressure in a fracture is in disequilibrium with the pore-fluid pressure in the matrix, dilatancy hardening is a function of permeability, with highly permeable rocks maintaining equilibrium at higher strain rates relative to low permeability rocks (Rutter, 1972; Paterson and Wong, 2005).

Zebra dolomite textures (Fig. 7.1) include numerous, closely spaced extension fractures, with local evidence of shear failure (Davies and Smith, 2006; Wallace and Hood, 2018; McCormick et al. Chapter VI). The mechanical properties of the host rock impact the formation of zebra textures because carbonate mudstones and wackestones are brittle, which promotes the stabilization of these fractures (Fig. 7.2C, D). In contrast, ductile lithologies promote failure through intracrystalline twinning and/or distributed cataclastic flow (Fig. 7.2A, B, E, F). During the development of zebra textures, the pore-fluid pressure

must rise to induce the first extension fracture. As the initial fracture forms, the pore fluid pressure drops and induces the precipitation of SD (cf. Walsh. 1981; Bruno and Nakagawa, 1991; Wang et al. 2013). Consequently, each subsequent fracture that forms the zebra texture requires numerous stress perturbations to develop, with low permeability carbonate mudstones and wackestones promoting the disequilibrium of the pore-fluid pressure.

7.4.2. Precipitation hardening

Microstructural observations of zebra dolomite textures, located in the Middle Cambrian strata in the WCSB (Fig. 7.1A), indicates that the light, coarsely crystalline, SD bands comprise a succession of syntaxial, crack-seal segments that nucleated on the RD host-rock (Fig. 7.3A, B, C, D, E). These SD crystals are elongate parallel to the opening direction of the fracture, whereas the crack-seal segments are oriented perpendicular to the opening direction. Such crack-seal textures arise due to the competition between the rate of cement precipitation and the rate of fracture opening (Ramsay, 1980; Bons, 2001; Holland and Urai, 2010). Thus, the occurrence of crack-seal textures in the SD crystals strongly suggest that the cementation of these zebra textures was syn-kinematic, with cementation occurring at the same time as fracturing (Fig. 7.3D, E). Cementation strengthens the host-rock through precipitation hardening (Bernabé et al. 1992; Yin and Dvorkin, 1994; Huang and Airey, 1998; Noiriel et al. 2010), thus promoting the formation of the closely spaced meso-fractures that comprise the zebra dolomite textures (Fig. 7.3A, B, C, D, E).

Based on these petrographical observations, coupled with insights from the rock deformation experiments, a conceptual model modified from Holland and Urai (2010) is applied to zebra dolomite textures (Fig. 7.3F). The model suggests that three mechanical components impact the development of closely spaced fractures, including the mechanical strength of the matrix, the cement, and the interface between them. In the first case, the matrix is the weakest part of the system, and thus, the initial stage of fracturing localizes within the matrix (Fig. 7.3F). Given that each successive fracture in the zebra texture is

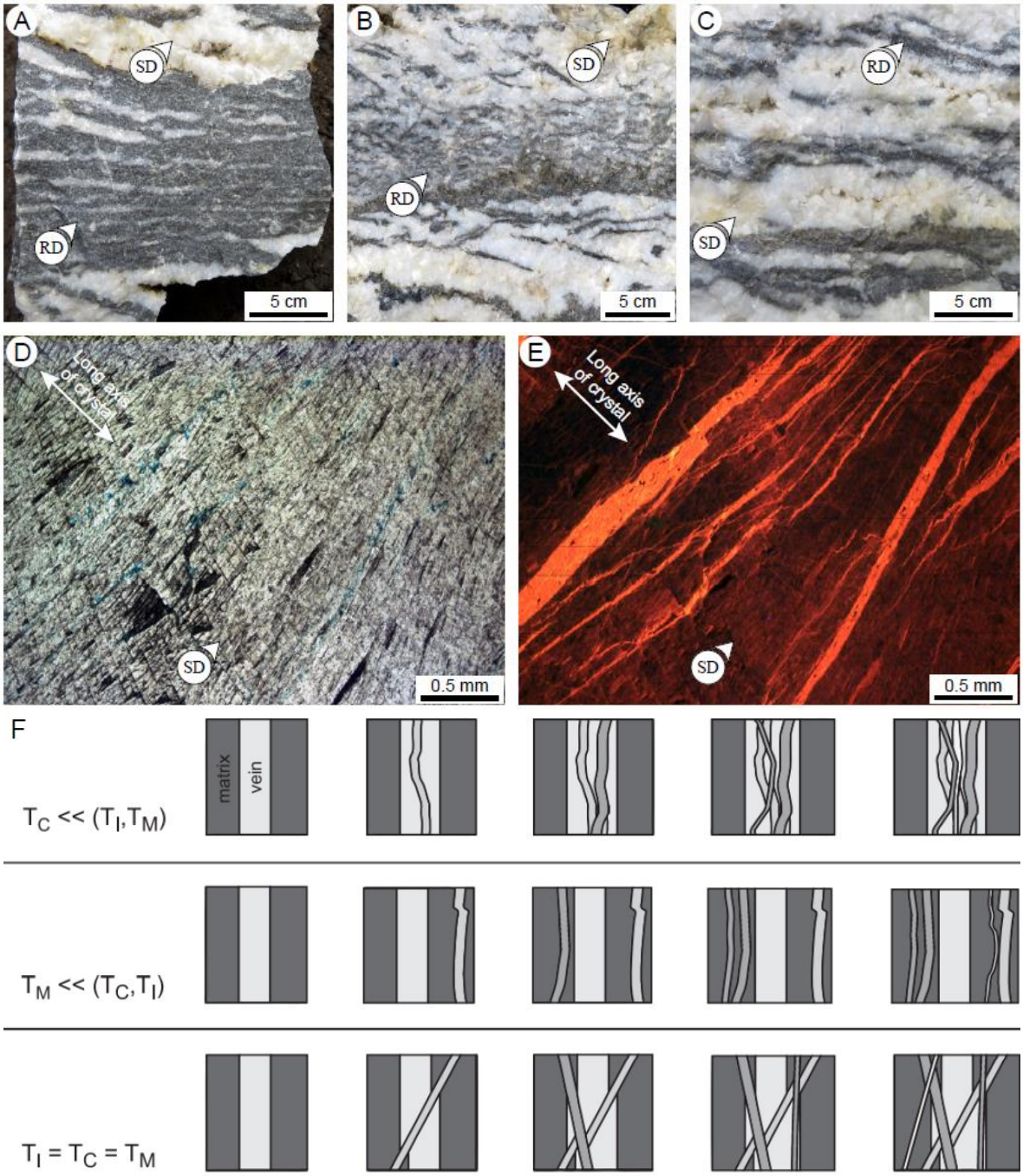

Figure 7.3. (A-C) Macro-scale crack seal textures showing the fragmented sheets of replacement dolomite (RD) that are commonly entrained within the saddle dolomite (SD) bands of the zebra textures (Eldon Formation, WCSB). **(D, E)** The SD bands comprise elongate crystals that were syntaxially built by a succession of crack-seal increments. **(F)** Conceptual model illustrating the impact that the mechanical strength of the matrix (T_M), the cement (T_C), and the interface between them (T_I) has on the formation of zebra dolomite textures (modified from Holland and Urai, 2010).

strain-hardened through the precipitation of SD, the fractures do not cross-cut one another. As fracturing and cementation progresses, the dolomite body strain-hardens and the mechanical strengths of the matrix and the cement become similar. The final paragenetic

stage, typically comprising oscillatory zoned ferroan dolomite (Nielsen et al. 1998; Gasparinni et al. 2006; Vandeginste et al. 2005 McCormick et al. 2021), strongly suggests that many of the zebra textures did not completely heal, with fracture porosity remaining open throughout their development. Chaotic zebra textures with irregular orientations probably develop during the later stages of dolomitization when the mechanical strengths of the matrix, the cement, and the interface between them are equal (Fig. 7.3F).

7.5. Synthesis and implications

Chapter IV of this Ph.D. thesis demonstrated that fault-controlled dolomite bodies, and their constituent rock textures, comprise several phases of replacement dolomite (RDa, RDb) and saddle dolomite (SDa, SDb, SDc) that were discerned using shortwave infrared hyperspectral imaging. The formation of zebra textures, cement supported breccias, and boxwork textures involves multi-phase dolomitization and cementation, which strongly suggests that their development spans a given period of time and cannot be grouped as a single step in the overall paragenetic sequence of the succession Such multi-phase dolomitization and cementation probably reflects the several stress perturbations and/or the local hardening mechanisms that are required to form the closely spaced meso-fractures that comprise zebra textures, cement supported breccias, and boxwork textures.

Chapter V of this thesis investigated the range of stress conditions that give rise to the brittle failure of two carbonate rocks, Carrara marble and Solnhofen limestone. These results provide an empirical framework to understand the stress states that control the transition from tensile failure to shear failure, thus establishing a foundation by which the stress states contributing to the formation of zebra textures in fault-controlled dolomite bodies can be interpreted. The experimental method of using an annealed copper jacket to simulate strain-hardening was developed throughout the course of this study. Coupled with textural observations of samples from the WCSB, the results from the rock deformation experiments demonstrate the requirement for a local hardening mechanism to propagate

multiple, closely spaced fractures. In fault-controlled dolomite bodies, the dilatancy that occurs during failure gives rise to the precipitation of SD, mechanisms that are interpreted contribute to strain-hardening and the formation of zebra textures.

Chapter VI of this thesis proposed a novel conceptual model that is based on the various sedimentological, tectonic, and metasomatic parameters that are interpreted to control the formation of rock textures in fault-controlled dolomite bodies. In the WCSB, there are different rock textures that are produced at different localities, and at different times, depending on their distance from the source of the dolomitizing fluid. The role of the original sedimentary textures and structural deformation are not as obvious at regions that are located closer to the fluid-source because repeated pulses of the dolomitizing fluid have resulted in the metasomatic overprinting of the preceding rock textures through recrystallization. This spatio-temporal framework also implies that the governing controls on strain-hardening in fault-controlled dolomite bodies will vary throughout the basin.

7.6. Conclusions and future directions

7.6.1. Conclusions

This Ph.D. project aimed to determine the genesis of the rock textures (e.g., zebra textures, cement supported breccias, boxwork textures) that are typically found in fault-controlled dolomite bodies, through the application of shortwave infrared hyperspectral imaging (Chapter IV) and rock deformation experiments (Chapter V), in conjunction with a range of petrographical and geochemical techniques (Chapter VI). The main conclusions of this Ph.D. project are presented as three original contributions, summarized as follows:

CHAPTER IV

- Shortwave infrared hyperspectral imaging is an invaluable method that can be used to determine compositional and textural heterogeneities in fault-controlled dolomite bodies.
- Based on their spectra, two phases of replacement dolomite and three phases of saddle dolomite were identified in the Middle Cambrian strata in the WCSB.

- The absorption-band position of each phase reveals changes in %Ca (molar Ca/(Ca+Mg)) and trace element substitution, whereas the spectral contrast correlates with texture.
- The mineral distribution maps that were constructed from the hyperspectral imagery provide meter-scale spatial information on the diagenetic history of the succession.
- The spatial distributions of each paragenetic stage strongly suggests that succession has undergone several phases of dolomitization, cementation, and recrystallization.

CHAPTER V

- To understand the geomechanical controls on the formation of zebra textures, a series of rock deformation experiments were conducted across a wide range of stress states.
- At low differential stress, when σ_3 is tensile, failure results in the formation of extension fractures. At high differential stress, when all principal stresses are compressive, failure involves the formation of numerous, grain-scale cracks that coalesce into a shear fault.
- The transition between these tensile failure and shear failure end-members involves the formation of several, transgranular cracks that coalesce into a low-angle shear fault.
- The failure surface angle increases as the differential stress increases, described by a continuously curving Mohr failure description in the τ versus σ_n coordinate frame.
- The stress states that give rise to the low-angle shear faults that are commonly found in zebra textures may be able to be predicted from the empirical failure criterion that is presented herein.

CHAPTER VI

- Each of the models for the formation of zebra textures fail to explain at least one of their characteristics, but the features of these models can be grouped into ternary diagrams.
- Based on petrographical and geochemical observations, a wide range of sedimentological, tectonic, and metasomatic processes contribute to the formation of zebra textures.

- Sedimentological and tectonic controls are prominent during the early stages of dolomitization and cementation. Conversely, metasomatism plays a critical role in the later stages of dolomitization, which is widely associated with recrystallization.
- This trend is also present at the basin-scale, with sedimentological and tectonic controls at the platform interior that are increasingly affected by metasomatism towards the platform margin.

7.6.2. Future directions

The results of this study highlight the importance rock mechanical characterization in the interpretation of zebra textures, cement supported breccias, and boxwork textures in fault-controlled dolomite bodies. Nevertheless, postulating burial depths and stress states in geological settings is challenging because the timing of dolomitization is typically poorly constrained, generally based on textural arguments. Thus, a clear future direction in the study of these rock textures is U-Pb geochronology. U-Pb geochronology has taken hold in its application to dating calcite, but dating dolomite is still in its infancy (Mangenot et al., 2018; Roberts et al. 2020). Dating the various dolomitization, cementation, and recrystallization events in fault-controlled dolomite bodies would provide invaluable information regarding how these rock textures evolve through time. Furthermore, studying rock textures in other sedimentary basins would provide spatio-temporal information on the processes that govern their formation. Lastly, the study of the rock textures in fault-controlled dolomite bodies could greatly benefit from geomechanical and/or reactive transport modelling (Yapparova et al. 2017; Consonni et al 2018; Benjakul et al. 2020; Brüch et al. 2021).

References

Bai, T., Pollard, D.D., 2000. Closely spaced fractures in layered rocks: initiation mechanism and propagation kinematics. Journal of structural geology, 22(10), 1409-1425.

Benjakul, R., Hollis, C., Robertson, H.A., Sonnenthal, E.L., Whitaker, F.F., 2020. Understanding controls on hydrothermal dolomitisation: insights from 3D reactive transport modelling of geothermal convection. Solid Earth, 11(6), 2439-2461.

Bernabé, Y., Fryer, D.T., Hayes, J.A., 1992. The effect of cement on the strength of granular rocks. Geophysical Research Letters, 19(14), 1511-1514.

Bons, P.D., 2001. Development of crystal morphology during unitaxial growth in a progressively widening vein: I. The numerical model. Journal of Structural Geology, 23(6-7), 865-872.

Brace, W.F., 1960. An extension of the Griffith theory of fracture to rocks. Journal of Geophysical Research, 65(10), 3477-3480.

Brace, W.F., Martin, R.J., 1968. A test of the law of effective stress for crystalline rocks of low porosity. International Journal of Rock Mechanics and Mining Sciences, 5(5) 415-426.

Brantut, N., 2021. Dilatancy toughening of shear cracks and implications for slow rupture propagation. Journal of Geophysical Research: Solid Earth, 126(11), e2021JB022239.

Brüch, A., Colombo, D., Frey, J., Berthelon, J., Cacas-Stentz, M.C., Cornu, T., Gout, C., 2021. Coupling 3D geomechanics to classical sedimentary basin modeling: From gravitational compaction to tectonics. Geomechanics for Energy and the Environment, 28, 100259.

Bruno, M.S., Nakagawa, F.M., 1991. Pore pressure influence on tensile fracture propagation in sedimentary rock. International journal of rock mechanics and mining sciences, 28(4), 261-273.

Consonni, A., Frixa, A., Maragliulo, C., 2018. Hydrothermal dolomitization: simulation by reaction transport modelling. Geological Society, London, Special Publications, 435(1), 235-244.

Davies, G.R., Smith Jr., L.B., 2006. Structurally controlled hydrothermal dolomite reservoir facies: an overview. American Association of Petroleum Geologists bulletin, 90, 1641-1690.

Fossen, H., Schultz, R.A., Shipton, Z.K., Mair, K., 2007. Deformation bands in sandstone: a review. Journal of the Geological Society, 164(4), 755-769.

Gasparrini, M., Bechstädt, T., Boni, M., 2006. Massive hydrothermal dolomites in the southwestern Cantabrian Zone (Spain) and their relation to the Late Variscan evolution. Marine and Petroleum Geology, 23(5), 543-568.

Green, A.H., Donnelly, T.H., Jahnke, F.M., Keays, R.R., 1982. Evolution of gold-bearing veins in dykes of the Woods Point dyke swarm, Victoria. Mineralium Deposita, 17(2), 175-192.

Hodgson, C.J., 1989. The structure of shear-related, vein-type gold deposits: a review. Ore Geology Reviews, 4(3), 231-273.

Holland, M., Urai, J.L., 2010. Evolution of anastomosing crack–seal vein networks in limestones: Insight from an exhumed high-pressure cell, Jabal Shams, Oman Mountains. Journal of Structural Geology, 32(9), 1279-1290.

Huang, J.T., Airey, D.W., 1998. Properties of artificially cemented carbonate sand. Journal of geotechnical and geoenvironmental engineering, 124(6), 492-499.

Kresse, O., Weng, X., Gu, H., Wu, R., 2013. Numerical modeling of hydraulic fractures interaction in complex naturally fractured formations. Rock mechanics and rock engineering, 46(3), 555-568.

Mangenot, X., Gasparrini, M., Gerdes, A., Bonifacie, M., Rouchon, V., 2018. An emerging thermochronometer for carbonate-bearing rocks: Δ_{47}/(U-Pb). Geology, 46(12), 1067-1070.

McCormick, C.A., Corlett, H., Clog, M., Boyce, A.J., Tartese, R., Steele-MacInnis, M., Hollis, C., Chapter VI: Basin-scale fluid-flow, dolomitization patterns, and diagnostic rock textures in fault-controlled dolomite bodies: Insights from the Western Canadian Sedimentary Basin. Unpublished Ph.D. thesis. The University of Manchester.

McCormick, C.A., Corlett, H., Stacey, J., Hollis, C., Feng, J., Rivard, B., Omma, J.E., 2021. Shortwave infrared hyperspectral imaging as a novel method to elucidate multi-phase dolomitization, recrystallization, and cementation in carbonate sedimentary rocks. Scientific reports, 11(1), 1-16.

McCormick, C.A., Rutter, E.H., 2022. An experimental study of the transition from tensile failure to shear failure in Carrara marble and Solnhofen limestone: Does “hybrid failure” exist?. Tectonophysics, 844, 229623.

Micarelli, L., Benedicto, A., Wibberley, C.A.J., 2006. Structural evolution and permeability of normal fault zones in highly porous carbonate rocks. Journal of Structural Geology, 28(7), 1214-1227.

Nicolas, A., Fortin, J., Regnet, J.B., Dimanov, A., Guéguen, Y., 2016. Brittle and semi-brittle behaviours of a carbonate rock: influence of water and temperature. Geophysical Journal International, 206(1), 438-456.

Nielsen, P., Swennen, R., Muchez, P.H., Keppens, E., 1998. Origin of Dinantian zebra dolomites south of the Brabant-Wales Massif, Belgium. Sedimentology, 45(4), 727-743.

Noiriel, C., Renard, F., Doan, M.L., Gratier, J.P., 2010. Intense fracturing and fracture sealing induced by mineral growth in porous rocks. Chemical Geology, 269(3-4), 197-209.

Olson, J.E., 2004. Predicting fracture swarms – The influence of subcritical crack growth and the crack-tip process zone on joint spacing in rock. Geological Society, London, Special Publications, 231(1), 73-88.

Paterson, M.S., Wong, T.F., 2005. *Experimental rock deformation – The brittle field* (2nd ed.). Springer-Verlag. 347 p.

Ramsay, J.G., 1980. The crack–seal mechanism of rock deformation. Nature, 284(5752), 135-139.

Ramsey, J.M., Chester, F.M., 2004. Hybrid fracture and the transition from extension fracture to shear fracture. Nature, 428(6978), 63-66.

Roberts, N.M., Drost, K., Horstwood, M.S., Condon, D.J., Chew, D., Drake, H., Milodowski, A.E., McLean, N.M., Smye, A.J., Walker, R.J., Haslam, R., Hodson, K., Imber, J., Beaudoin, N., Lee, J.K., 2020. Laser ablation inductively coupled plasma mass spectrometry (LA-ICP-MS) U–Pb carbonate geochronology: strategies, progress, and limitations. Geochronology, 2(1), 33-61.

Rutter, E.H., 1972. The effects of strain-rate changes on the strength and ductility of Solenhofen limestone at low temperatures and confining pressures. International Journal of Rock Mechanics and Mining Sciences, 9(2), 183-189.

Rutter, E.H., Glover, C.T., 2012. The deformation of porous sandstones; are Byerlee friction and the critical state line equivalent?. Journal of Structural Geology, 44, 129-140.

Scholz, C.H., Sykes, L.R., Aggarwal, Y.P., 1973. Earthquake prediction: a physical basis. Science, 181(4102), 803-810.

Turing, A.M., 1952. The chemical basis of morphogenesis. Bulletin of Mathematical Biology, 52(1), 153-197.

Vandeginste, V., Swennen, R., Gleeson, S.A., Ellam, R.M., Osadetz, K., Roure, F., 2005. Zebra dolomitization as a result of focused fluid flow in the Rocky Mountains Fold and Thrust Belt, Canada. Sedimentology, 52(5), 1067-1095.

Wallace, M.W., Hood, A.vS., 2018. Zebra textures in carbonate rocks: Fractures produced by the force of crystallization during mineral replacement. Sedimentary Geology, 368, 58-67.

Walsh, J.B., 1981. Effect of pore pressure and confining pressure on fracture permeability. International Journal of Rock Mechanics and Mining Sciences, 18(5), 429-435.

Wang, S.Y., Sloan, S.W., Fityus, S.G., Griffiths, D.V., Tang, C.A., 2013. Numerical modeling of pore pressure influence on fracture evolution in brittle heterogeneous rocks. Rock mechanics and rock engineering, 46(5), 1165-1182.

Yapparova, A., Gabellone, T., Whitaker, F., Kulik, D.A., Matthäi, S.K., 2017. Reactive transport modelling of hydrothermal dolomitisation using the CSMP++ GEM coupled code: Effects of temperature and geological heterogeneity. Chemical Geology, 466, 562-574.

Yin, H., Dvorkin, J., 1994. Strength of cemented grains. Geophysical Research Letters, 21(10), 903-906.

Blank page

Appendix 1. Sample information, locations, brief descriptions, and analyses that were conducted.

Location	Sample	Formation	Description	Sections	QEMSCAN	EPMA	LA-ICP-MS	$\delta^{13}C$ & $\delta^{18}O$	Δ_{47}	Fluid inclusions
	WP_01	Cathedral	South of roadcut, precursor texture, microbialite.							
	WP_02	Cathedral	South of roadcut, precursor texture, microbialite.							
	WP_03	Cathedral	South of roadcut, precursor texture, microbialite.							
	WP_04	Cathedral	Small aperture, bedding-parallel, zebra textures, includes ferroan dolomite.							
	WP_05	Cathedral	Small aperture, bedding-parallel, zebra textures, includes ferroan dolomite.							
	WP_06	Cathedral	Medium aperture, bedding-parallel, zebra textures, includes ferroan dolomite.	X	X	X	X	X	X	X
	WP_07	Cathedral	SD from main breccia zone.	X						
	WP_08	Cathedral	Large zebra texture in breccia zone. Altered breccia clast entrained in sample.	X						
	WP_09	Cathedral	Large bedding-parallel, planar zebra texture in breccia zone, ferroan dolomite.	X	X	X	X	X		X
	WP_10	Cathedral	Bedding-inclined zebra textures. Bioturbated mudstone facies. HW 65 m.							
	WP_11	Cathedral	Hangingwall, 85 from fault, dolomitic limestone near NE end of WP roadcut.					X	X	
	WP_12	Cathedral	Hangingwall, 95 from fault, limestone at the northeast end of WP roadcut.							
	WP_13	Cathedral	Hangingwall, 65 m from fault, zebra textures with ferroan dolomite.					X		
	WP_14	Cathedral	Hangingwall, 50 m from fault, precursor texture, bioturbated mudstone.							
	WP_15	Cathedral	Hangingwall, 50 m from fault, zebra textures with ferroan dolomite.							
	WP_16	Cathedral	Hangingwall, 40 m from fault, precursor texture, bioturbated mudstone.							
Whirlpool Point	WP_17	Cathedral	Hangingwall, 40 m from fault, cross-cutting fractures.							
52°00'07.5"N	WP_18	Cathedral	Hangingwall, 20 m from fault, fractures within breccia clast.							
116°28'13.5"W	WP_19	Cathedral	Hangingwall, 1.0 m from fault, zebra texture with cross-cutting fractures.							
	WP_20	Cathedral	Hangingwall, 20 m from fault, no zebras, subvertical fractures cross-cut bedding.							
	WP_21	Cathedral	Footwall, 1 m from fault, zebras with cross-cutting fractures and ferroan dolomite.							
	WP_22	Cathedral	Footwall, 20 m from fault, large zebra texture.							
	WP_23	Cathedral	Footwall, 45 m from fault, zebra texture with cross-cutting fractures.							
	WP_24	Cathedral	Footwall, 55 m from fault, large zebra texture.							
	WP_25	Cathedral	Footwall, 65 m from fault, large zebra texture with ferroan dolomite.							
	WP_26	Cathedral	Footwall, 65 m from fault, subvertical fractures perpendicular to WP_25.							
	WP_27	Cathedral	Footwall, 80 m from fault, zebra texture.							
	WP_28	Cathedral	Footwall, 95 m from fault, zebra texture.							
	WP_29	Cathedral	Footwall, 95 m from fault, subvertical fractures perpendicular to WP_28.							
	WP_30	Cathedral	Footwall, 105 m from fault, zebra texture.							
	WP_31	Cathedral	Footwall, 110 m from fault, zebra texture.							
	WP_32	Cathedral	Footwall, 120 m from fault, zebra texture.							
	WP_33	Mt. Whyte	Mt. Whyte subvertical fractures with ferroan dolomite.							
	WP_34	Cathedral	100 m north of WP (on top of roadcut). Zebra textures along strike from fault.							
	WP_35	Mt. Whyte	Mt. Whyte bedding parallel zebra textures, only in grainstone/packstone beds.	X				X		X
Whirlpool Point (N)	WPN_01	Cathedral	500 m north of WP roadcut, zebra textures.							
52°01'13.5"N	WPN_02	Cathedral	500 m north of WP roadcut, small veins.							
116°28'13.5"W	WPN_03	Cathedral	1000 m north of WP roadcut, zebra textures from pervasively dolomitized unit.							
	MC_01	Eldon	Bedding-inclined zebra textures, includes ferroan dolomite.		X			X		
	MC_02	Eldon	Bedding-inclined zebra textures, includes ferroan dolomite.		X			X	X	
	MC_03	Eldon	Bed 1 SD (20 m)	X				X		
	MC_04	Eldon	Bed 2 RD (20 m)	X				X		
	MC_05	Eldon	Bed 2 SD (20 m)	X				X		
Mistaya Canyon	MC_06	Eldon	Bed 1 SD (40 m)							
51°55'09.5"N	MC_07	Eldon	Bed 2 RD (40 m)							
116°43'23.5"W	MC_08	Eldon	Bed 2 SD (40 m)							
	MC_09	Eldon	Bed 1 SD (60 m)							
	MC_10	Eldon	Bed 2 RD (60 m)							
	MC_11	Eldon	Bed 1 SD (80 m)	X				X		
	MC_12	Eldon	Bed 2 RD (80 m)	X				X		

Location	Sample	Formation	Description	Sections	QEMSCAN	EPMA	LA-ICP-MS	$\delta^{13}C$ & $\delta^{18}O$	Δ_{47}	Fluid inclusions
	MC_13	Eldon	Bed 2 SD (80 m)	X				X		
	MC_14	Eldon	Bed 2 RD (100 m)							
	MC_15	Eldon	Bed 2 SD (100 m)							
	MC_16	Eldon	Bed 2 RD (120 m)							
	MC_17	Eldon	Bed 2 SD (120 m)							
	MC_18	Eldon	Bed 3 RD (120 m)							
	MC_19	Eldon	Bed 2 RD (140 m)	X				X	X	X
Mistaya Canyon	MC_20	Eldon	Bed 2 SD (140 m)	X		X	X	X		X
51°55'09.5"N	MC_21	Eldon	Bed 3 RD (140 m)	X				X		
116°43'23.5"W	MC_22	Eldon	Bed 2 SD (160 m)							
	MC_23	Eldon	Bed 3 RD (160 m)							
	MC_24	Eldon	Bed 3 RD (180 m)							
	MC_25	Eldon	Bed 3 RD (200 m)	X				X		
	MC_26	Eldon	West side of road, proximal to fault.							
	MC_27	Eldon	West side of road, medial to fault.							
	MC_28	Eldon	West side of road, distal to fault.							
	MC_29	Eldon	RD/SD boundary in zebras showing a series of smaller fractures in RD bands.	X				X		
	MC_30	Eldon	Zebra texture showing inclusion trails in SD bands.	X				X		
	NTJ_01	Eldon	RD at east end of outcrop (unit 2).	X				X	X	X
Num Ti Jah	NTJ_02	Eldon	RD at east end of outcrop, 20 m SW of NTJ_01 (unit 4; top).	X				X		
51°39'13.0"N	NTJ_03	Eldon	SD bed with zebras. East end of outcrop, 10 m SW of NTJ_01 (unit 1; bottom).	X				X		
116°29'59.0"W	NTJ_04	Eldon	SD bed with zebras. East end of outcrop, 30 m SW of NTJ_01 (unit 3).	X		X	X	X	X	
	NTJ_05	Eldon	SD bed near top of Eldon, numerous zebras, underlies Pika, left/east of waterfall.	X				X		X
	BC_01	Cathedral	North part of outcrop, 0 m from north end, zebras/vugs.							
Beauty Creek	BC_02	Cathedral	North part of outcrop, 10 m from north end, zebras/vugs.							
52°20'45.5"N	BC_03	Cathedral	North part of outcrop, 20 m from north end, zebras/vugs.							
117°20'21.0"W	BC_04	Cathedral	South part of outcrop, 0 m from south end, large zebra texture.							
	BC_05	Cathedral	South part of outcrop, 10 m from south end, zebra texture with basal stylolites.							
	BC_06	Cathedral	South part of outcrop, 20 m from south end, zebras with cross-cutting stylolites.							
	KHR_01	Cathedral	RD below zebra zone.					X	X	
Kicking Horse Rim (W)	KHR_02	Cathedral	Basal zebra bed, medium sized.							
51°26'8.5"N,	KHR_03	Cathedral	Middle zebra bed, medium to large sized.							
116°23'15.0"W	KHR_04	Cathedral	Upper zebra bed, very large sized with reaction rim along RD bands.	X		X	X	X	X	X
	KHR_05	Cathedral	RD above zebra zone.					X		
	KHR_06	Cathedral	Limestone, 10 m below basal limestone/dolomite contact.							
	KHR_07	Cathedral	Limestone, 0.5 m below basal limestone/dolomite contact.							
	KHR_08	Cathedral	Beige dolomite, 0.5 m above basal limestone/dolomite contact.							
	KHR_09	Cathedral	Beige dolomite with zebra texture, 10 m above basal limestone/dolomite contact.							
	KHR_10	Cathedral	Grey replacement dolomite, 11 m above basal limestone/dolomite contact.							
	KHR_11	Cathedral	Beige dolomite with zebra texture, 12 m above basal limestone/dolomite contact.							
	KHR_12	Cathedral	Beige dolomite with zebra texture, 21 m above basal limestone/dolomite contact.							
Kicking Horse Rim (E)	KHR_13	Cathedral	Beige zebra texture, 30.5 m above basal Lst. contact. 0.5 m below 2nd Lst. bed.							
51°26'11.5"N	KHR_14	Cathedral	2nd Limestone bed, 31 m above basal limestone/dolomite contact.							
116°22'48.5"W	KHR_15	Cathedral	Beige dolomite, 30.5 m above basal Ls/Dol contact. 0.5 m above 2nd Lst. bed.							
	KHR_16	Cathedral	Beige dolomite, 41 m above basal Lst. bed. 1.5 m below upper Ls/Dol contact.							
	KHR_17	Cathedral	Dolomite, 42 m above basal Lst. bed. 0.5 m below upper Ls/Dol contact.							
	KHR_18	Cathedral	Limestone, 43 m above basal Lst. bed. 0.5 m above upper Ls/Dol contact.							
	KHR_19	Cathedral	Zebra texture in grey dolomite above fault zone.							
	KHR_20	Cathedral	Zebra texture in grey dolomite with fracture associated overprint dolomite (beige).					X		
	KHR_21	Cathedral	Nascent zebra texture in grey dolomite, bioturbated mudstone, precursor texture.							
	KHR_22	Cathedral	Zebra texture in grey dolomite above fault zone.							

Appendix 2. Tabulated rare earth element (REE) data, including PAAS normalization based on Taylor and McLennan (1985) and Nance and Taylor (1976).

	La139 (ppm)	Ce140 (ppm)	Pr141 (ppm)	Nd146 (ppm)	Sm147 (ppm)	Eu153 (ppm)	Gd157 (ppm)	Tb159 (ppm)	Dy163 (ppm)	Y89 (ppm)	Ho165 (ppm)	Er166 (ppm)	Tm169 (ppm)	Yb172 (ppm)	Lu175 (ppm)
Taylor and McLennan (1985)	38.0	80.0	8.9	32.0	5.6	1.1	4.7	0.8	4.4	-	1.0	2.9	0.4	2.8	0.43
Nance and Taylor (1976)										28.0					
Whirlpool Point Lst.															
Minimum	0.62595	0.98814	0.12846	0.45260	0.08361	0.01761	0.06728	0.00944	0.05442	0.43833	0.01130	0.03547	0.00499	0.03258	0.00500
Average	0.66901	1.07506	0.14376	0.50038	0.08931	0.01933	0.07526	0.01027	0.05968	0.49455	0.01325	0.04296	0.00571	0.03822	0.00543
Average (PAAS normalized)	0.01761	0.01344	0.01615	0.01564	0.01595	0.01758	0.01601	0.01334	0.01356	0.01766	0.01325	0.01481	0.01427	0.01365	0.01264
Maximum	0.74803	1.23469	0.16774	0.57660	0.09772	0.02218	0.08582	0.01160	0.06891	0.59676	0.01598	0.05484	0.00653	0.04624	0.00619
Standard Deviation	0.05595	0.11302	0.01717	0.05447	0.00607	0.00203	0.00778	0.00095	0.00655	0.07240	0.00199	0.00849	0.00063	0.00582	0.00054
Whirlpool Point RDa															
Minimum	0.68086	0.92040	0.11718	0.39395	0.07106	0.01689	0.05432	0.00774	0.04881	0.26147	0.00913	0.02505	0.00449	0.01889	0.00280
Average	0.98552	1.89223	0.26319	1.01136	0.20903	0.04847	0.19262	0.02571	0.13201	0.78823	0.02531	0.06597	0.00891	0.05435	0.00838
Average (PAAS normalized)	0.02593	0.02365	0.02957	0.03161	0.03733	0.04406	0.04098	0.03339	0.03000	0.02815	0.02531	0.02275	0.02228	0.01941	0.01949
Maximum	1.36676	2.75014	0.54553	2.51682	0.60795	0.15075	0.63725	0.08214	0.37539	2.20749	0.06529	0.15805	0.01457	0.08604	0.01133
Standard Deviation	0.23565	0.57906	0.14032	0.70528	0.18253	0.04623	0.20034	0.02549	0.11029	0.65055	0.01831	0.04259	0.00309	0.01992	0.00274
Whirlpool Point RDb															
Minimum	0.49052	0.65619	0.08775	0.38269	0.07471	0.02191	0.07122	0.01090	0.04829	0.33302	0.00951	0.02383	0.00266	0.01771	0.00261
Average	0.62372	1.85429	0.32018	1.48700	0.31779	0.07848	0.29241	0.04221	0.21516	1.20853	0.03787	0.09234	0.01051	0.05551	0.00681
Average (PAAS normalized)	0.01641	0.02318	0.03598	0.04647	0.05675	0.07134	0.06222	0.05481	0.04890	0.04316	0.03787	0.03184	0.02628	0.01982	0.01583
Maximum	0.78711	3.72351	0.70936	3.34731	0.55059	0.13760	0.50822	0.07728	0.43463	2.64958	0.09193	0.20781	0.02423	0.12126	0.01640
Standard Deviation	0.10210	0.85082	0.18474	0.90047	0.16242	0.03503	0.14162	0.02229	0.12307	0.72045	0.02338	0.05766	0.00636	0.03275	0.00416
Whirlpool Point SDa															
Minimum	0.04766	0.36006	0.05845	0.28426	0.07442	0.01380	0.06826	0.01229	0.05296	0.29930	0.01056	0.02657	0.00316	0.01671	0.00236
Average	0.50225	1.31419	0.17195	0.69957	0.17362	0.04405	0.17415	0.02360	0.12474	0.64613	0.02336	0.06346	0.00856	0.05783	0.00816
Average (PAAS normalized)	0.01322	0.01643	0.01932	0.02186	0.03100	0.04005	0.03705	0.03065	0.02835	0.02308	0.02336	0.02188	0.02140	0.02065	0.01897
Maximum	1.95350	3.25274	0.55504	2.56883	1.17284	0.32771	1.67167	0.17875	0.77032	4.08739	0.13398	0.34513	0.04119	0.24450	0.02703
Standard Deviation	0.34163	0.67515	0.09063	0.39995	0.15821	0.04390	0.21505	0.02528	0.11917	0.59632	0.01901	0.04515	0.00517	0.03216	0.00394
Whirlpool Point SDb															
Minimum	0.01322	0.01643	0.01932	0.02186	0.03100	0.00928	0.03705	0.00603	0.02835	0.02308	0.00709	0.01736	0.00113	0.01307	0.00134
Average	0.38401	1.00767	0.13546	0.55887	0.14089	0.03553	0.14350	0.01931	0.10374	0.53509	0.01971	0.05283	0.00730	0.04882	0.00707
Average (PAAS normalized)	0.01011	0.01260	0.01522	0.01746	0.02516	0.03230	0.03053	0.02508	0.02358	0.01911	0.01971	0.01822	0.01825	0.01744	0.01644
Maximum	1.95350	3.25274	0.70033	3.31689	1.17284	0.32771	1.67167	0.17875	0.77032	4.08739	0.13398	0.34513	0.04119	0.24450	0.02703
Standard Deviation	0.31204	0.68408	0.10637	0.48473	0.16499	0.04496	0.21928	0.02540	0.11934	0.60766	0.01941	0.04667	0.00542	0.03208	0.00395
Whirlpool Point SDc															
Minimum	0.01913	0.16211	0.04763	0.28419	0.16853	0.08090	0.19551	0.02361	0.13169	0.61488	0.02345	0.05732	0.00474	0.02975	0.00448
Average	0.08696	0.55441	0.13037	0.80123	0.40627	0.13336	0.50399	0.06949	0.31134	1.57314	0.06322	0.14923	0.01740	0.10945	0.01508
Average (PAAS normalized)	0.00229	0.00693	0.01465	0.02504	0.07255	0.12124	0.10723	0.09025	0.07076	0.05618	0.06322	0.05146	0.04349	0.03909	0.03508
Maximum	0.29828	2.05211	0.44602	2.30162	0.92773	0.26418	1.02446	0.10276	0.58393	2.44034	0.12965	0.34025	0.03931	0.24166	0.03373
Standard Deviation	0.07147	0.46297	0.09949	0.51090	0.21092	0.05686	0.22700	0.02429	0.11965	0.57264	0.02766	0.07179	0.00930	0.05389	0.00742
Mistaya Canyon RDa															
Minimum	0.36164	0.93533	0.12139	0.48453	0.09915	0.01864	0.07250	0.00915	0.05501	0.36164	0.01111	0.02678	0.00276	0.01561	0.00282
Average	0.44778	1.07389	0.13793	0.52383	0.10801	0.02416	0.08645	0.01085	0.06398	0.38936	0.01256	0.02828	0.00376	0.02146	0.00310
Average (PAAS normalized)	0.01178	0.01342	0.01550	0.01637	0.01929	0.02197	0.01839	0.01409	0.01454	0.01391	0.01256	0.00975	0.00939	0.00766	0.00720
Maximum	0.53370	1.23876	0.15642	0.56327	0.11740	0.02877	0.11156	0.01406	0.07093	0.41481	0.01390	0.03058	0.00488	0.02726	0.00359
Standard Deviation	0.05736	0.09390	0.01207	0.02391	0.00671	0.00373	0.01521	0.00159	0.00557	0.02018	0.00101	0.00151	0.00083	0.00420	0.00033

	La139 (ppm)	Ce140 (ppm)	Pr141 (ppm)	Nd146 (ppm)	Sm147 (ppm)	Eu153 (ppm)	Gd157 (ppm)	Tb159 (ppm)	Dy163 (ppm)	Y89 (ppm)	Ho165 (ppm)	Er166 (ppm)	Tm169 (ppm)	Yb172 (ppm)	Lu175 (ppm)
Mistaya Canyon RDb															
Minimum	0.37157	1.03593	0.13638	0.54643	0.11364	0.01912	0.07904	0.01034	0.06231	0.41680	0.01290	0.03158	0.00276	0.01811	0.00306
Average	0.50077	1.24377	0.16120	0.60538	0.12692	0.02741	0.09996	0.01289	0.07576	0.45838	0.01507	0.03382	0.00425	0.02689	0.00346
Average (PAAS normalized)	0.01318	0.01555	0.01811	0.01892	0.02266	0.02491	0.02127	0.01673	0.01722	0.01637	0.01507	0.01166	0.01063	0.00960	0.00806
Maximum	0.62965	1.49107	0.18893	0.66453	0.14101	0.03431	0.13762	0.01771	0.08618	0.49654	0.01709	0.03728	0.00594	0.03559	0.00421
Standard Deviation	0.08604	0.14085	0.01810	0.03586	0.01007	0.00559	0.02281	0.00238	0.00835	0.03027	0.00151	0.00227	0.00125	0.00630	0.00049
Mistaya Canyon SDa															
Minimum	0.31633	0.61045	0.08060	0.31201	0.05626	0.01263	0.04785	0.00497	0.03277	0.21720	0.00653	0.01421	0.00198	0.00908	0.00236
Average	0.34179	0.73414	0.09139	0.36073	0.07019	0.01768	0.05944	0.00677	0.04043	0.25134	0.00753	0.01720	0.00277	0.01061	0.00236
Average (PAAS normalized)	0.00899	0.00918	0.01027	0.01127	0.01253	0.01607	0.01265	0.00879	0.00919	0.00898	0.00753	0.00593	0.00692	0.00379	0.00548
Maximum	0.37941	0.89641	0.11111	0.43388	0.09593	0.02653	0.08326	0.00791	0.05443	0.30418	0.00873	0.01901	0.00389	0.01214	0.00236
Standard Deviation	0.02531	0.09052	0.00994	0.04493	0.01454	0.00478	0.01185	0.00106	0.00667	0.02780	0.00080	0.00152	0.00077	0.00153	0.00000
Mistaya Canyon SDb															
Minimum	0.17925	0.34370	0.04267	0.18479	0.01839	0.00750	0.01756	0.00228	0.01552	0.11408	0.00154	0.00508	0.00085	0.00456	0.00148
Average	0.26373	0.56597	0.07004	0.27692	0.05421	0.01451	0.04745	0.00544	0.03075	0.18850	0.00581	0.01261	0.00267	0.00795	0.00234
Average (PAAS normalized)	0.00694	0.00707	0.00787	0.00865	0.00968	0.01319	0.01010	0.00706	0.00699	0.00673	0.00581	0.00435	0.00667	0.00284	0.00545
Maximum	0.27171	0.68863	0.07746	0.31105	0.07572	0.01528	0.05608	0.00541	0.04205	0.22610	0.00664	0.01110	0.00298	0.00865	0.00148
Standard Deviation	0.03327	0.11618	0.01217	0.05356	0.01872	0.00284	0.01329	0.00113	0.00962	0.03761	0.00169	0.00190	0.00076	0.00204	0.00000
Mistaya Canyon SDc															
Minimum	0.05146	0.46587	0.05948	0.30831	0.14035	0.05506	0.10498	0.01740	0.08979	0.50009	0.01096	0.03258	0.00375	0.02520	0.00377
Average	0.07903	0.77945	0.17242	1.12822	0.52884	0.15877	0.55384	0.05713	0.26196	1.44611	0.04117	0.09352	0.00933	0.04809	0.00631
Average (PAAS normalized)	0.00208	0.00974	0.01937	0.03526	0.09443	0.14434	0.11784	0.07420	0.05954	0.05165	0.04117	0.03225	0.02333	0.01717	0.01467
Maximum	0.11037	1.09009	0.26469	1.62426	1.06775	0.19365	1.21339	0.15194	0.66279	3.28836	0.10406	0.20100	0.01531	0.08919	0.00935
Standard Deviation	0.01957	0.21393	0.05990	0.40968	0.24839	0.03836	0.28406	0.03770	0.15490	0.74929	0.02509	0.04598	0.00367	0.01895	0.00154
Num Ti Jah RDa															
Minimum	0.14411	0.29054	0.03676	0.14217	0.03103	0.00533	0.02494	0.00303	0.02544	0.25671	0.00468	0.01508	0.00157	0.01178	0.00170
Average	0.17801	0.34917	0.04173	0.17362	0.04068	0.00941	0.03541	0.00472	0.03012	0.28587	0.00632	0.01887	0.00264	0.01683	0.00238
Average (PAAS normalized)	0.00468	0.00436	0.00469	0.00543	0.00726	0.00855	0.00753	0.00613	0.00685	0.01021	0.00632	0.00651	0.00660	0.00601	0.00553
Maximum	0.27571	0.45090	0.04514	0.19028	0.04919	0.01309	0.04192	0.00555	0.03839	0.31003	0.00754	0.02165	0.00373	0.02459	0.00374
Standard Deviation	0.03926	0.04363	0.00284	0.01606	0.00590	0.00255	0.00691	0.00077	0.00375	0.01828	0.00091	0.00219	0.00075	0.00385	0.00070
Num Ti Jah RDb															
Minimum	0.14690	0.29224	0.03754	0.12905	0.03301	0.00345	0.01961	0.00312	0.02465	0.24780	0.00430	0.01436	0.00159	0.00951	0.00163
Average	0.19533	0.37411	0.04394	0.18462	0.04308	0.01004	0.03495	0.00507	0.03155	0.29867	0.00671	0.01845	0.00304	0.01860	0.00238
Average (PAAS normalized)	0.00514	0.00468	0.00494	0.00577	0.00769	0.00912	0.00744	0.00658	0.00717	0.01067	0.00671	0.00636	0.00760	0.00664	0.00555
Maximum	0.35170	0.54652	0.04793	0.20900	0.05539	0.01481	0.04677	0.00608	0.03844	0.34305	0.00772	0.02127	0.00486	0.03119	0.00374
Standard Deviation	0.06160	0.07061	0.00302	0.02339	0.00670	0.00387	0.00937	0.00093	0.00488	0.02867	0.00103	0.00244	0.00124	0.00641	0.00067
Num Ti Jah SDa															
Minimum	0.14133	0.28884	0.03449	0.13900	0.02905	0.00581	0.02824	0.00293	0.02458	0.25211	0.00465	0.01574	0.00148	0.01189	0.00157
Average	0.16069	0.32424	0.03952	0.16262	0.03827	0.00878	0.03587	0.00437	0.02868	0.27306	0.00593	0.01928	0.00224	0.01506	0.00214
Average (PAAS normalized)	0.00423	0.00405	0.00444	0.00508	0.00683	0.00798	0.00763	0.00568	0.00652	0.00975	0.00593	0.00665	0.00559	0.00538	0.00498
Maximum	0.19972	0.35527	0.04576	0.19392	0.04954	0.01161	0.04710	0.00536	0.03923	0.30097	0.00757	0.02257	0.00273	0.01800	0.00305
Standard Deviation	0.01803	0.02053	0.00373	0.01806	0.00612	0.00209	0.00610	0.00074	0.00445	0.01520	0.00104	0.00223	0.00042	0.00182	0.00055

	La139 (ppm)	Ce140 (ppm)	Pr141 (ppm)	Nd146 (ppm)	Sm147 (ppm)	Eu153 (ppm)	Gd157 (ppm)	Tb159 (ppm)	Dy163 (ppm)	Y89 (ppm)	Ho165 (ppm)	Er166 (ppm)	Tm169 (ppm)	Yb172 (ppm)	Lu175 (ppm)
Num Ti Jah SDb															
Minimum	0.06757	0.18025	0.02210	0.08039	0.01324	0.00350	0.01548	0.00200	0.01420	0.13712	0.00338	0.00792	0.00135	0.00681	0.00128
Average	0.14580	0.31184	0.03747	0.14985	0.03629	0.00789	0.03432	0.00411	0.02621	0.25342	0.00576	0.01857	0.00236	0.01403	0.00216
Average (PAAS normalized)	0.00384	0.00390	0.00421	0.00468	0.00648	0.00718	0.00730	0.00533	0.00596	0.00905	0.00576	0.00640	0.00590	0.00501	0.00501
Maximum	0.18989	0.45904	0.04666	0.17155	0.06268	0.01292	0.05228	0.00706	0.04008	0.36716	0.00947	0.02352	0.00700	0.02492	0.00326
Standard Deviation	0.02677	0.06042	0.00662	0.02706	0.01371	0.00289	0.01041	0.00136	0.00756	0.05763	0.00171	0.00463	0.00165	0.00472	0.00072
Num Ti Jah SDc															
Minimum	0.03230	0.20604	0.04197	0.15698	0.09697	0.03032	0.04725	0.00293	0.02755	0.25006	0.00536	0.01493	0.00176	0.01333	0.00181
Average	0.07958	0.36075	0.07230	0.42152	0.16702	0.05108	0.16611	0.02145	0.13131	0.86413	0.02421	0.06187	0.00780	0.05189	0.00619
Average (PAAS normalized)	0.00209	0.00451	0.00812	0.01317	0.02982	0.04644	0.03534	0.02786	0.02984	0.03086	0.02421	0.02134	0.01949	0.01853	0.01439
Maximum	0.11088	0.50793	0.11133	0.73537	0.30029	0.08949	0.40770	0.04863	0.28721	1.77733	0.05483	0.14193	0.01714	0.09764	0.01245
Standard Deviation	0.02931	0.09660	0.02834	0.20479	0.06819	0.02138	0.11945	0.01486	0.08240	0.49545	0.01557	0.04069	0.00495	0.02739	0.00361
Kicking Horse Rim RDb															
Minimum	0.48537	1.10561	0.11019	0.42119	0.09042	0.01220	0.08211	0.00446	0.03749	0.25397	0.00537	0.01738	0.00322	0.01539	0.00128
Average	1.07224	2.33888	0.23684	0.88652	0.19563	0.04404	0.16684	0.02365	0.15879	0.89950	0.02797	0.08025	0.01160	0.06242	0.00917
Average (PAAS normalized)	0.02822	0.02924	0.02661	0.02770	0.03493	0.04003	0.03550	0.03072	0.03609	0.03213	0.02797	0.02767	0.02899	0.02229	0.02134
Maximum	1.74206	3.47512	0.38035	1.66423	0.37982	0.10128	0.32574	0.04186	0.26217	1.49562	0.04807	0.14327	0.02223	0.12321	0.01643
Standard Deviation	0.40934	0.80950	0.07799	0.32412	0.09649	0.02492	0.07768	0.01153	0.07143	0.41079	0.01376	0.03860	0.00535	0.03114	0.00475
Kicking Horse Rim SDa															
Minimum	0.36484	0.84199	0.08695	0.33014	0.05689	0.00856	0.05149	0.00619	0.03505	0.27701	0.00792	0.02351	0.00361	0.02364	0.00168
Average	0.56601	1.31386	0.14253	0.55627	0.12104	0.02633	0.10908	0.01496	0.09293	0.56915	0.01822	0.04993	0.00704	0.04065	0.00602
Average (PAAS normalized)	0.01489	0.01642	0.01601	0.01738	0.02161	0.02394	0.02321	0.01943	0.02112	0.02033	0.01822	0.01722	0.01761	0.01452	0.01401
Maximum	0.73741	1.64213	0.18221	0.76107	0.19109	0.04244	0.17765	0.02289	0.13415	0.83174	0.02614	0.07906	0.01113	0.06573	0.00838
Standard Deviation	0.10879	0.23102	0.02842	0.12799	0.04228	0.01061	0.03770	0.00517	0.02938	0.15864	0.00538	0.01662	0.00225	0.01269	0.00221
Kicking Horse Rim SDb															
Minimum	0.21115	0.46260	0.05543	0.20946	0.03594	0.00674	0.03617	0.00647	0.02894	0.28686	0.00839	0.01325	0.00192	0.01644	0.00187
Average	0.42324	1.00790	0.11341	0.45068	0.09923	0.02200	0.09168	0.01297	0.07368	0.46353	0.01567	0.04134	0.00625	0.03445	0.00548
Average (PAAS normalized)	0.01114	0.01260	0.01274	0.01408	0.01772	0.02000	0.01951	0.01685	0.01675	0.01655	0.01567	0.01425	0.01562	0.01230	0.01274
Maximum	0.53925	1.47948	0.19114	0.80049	0.22979	0.04820	0.20442	0.02786	0.15066	0.83138	0.03025	0.07354	0.00794	0.05168	0.00935
Standard Deviation	0.10188	0.29707	0.03965	0.15794	0.05387	0.01268	0.04684	0.00608	0.03321	0.15790	0.00609	0.01556	0.00176	0.00896	0.00200
Kicking Horse Rim SDc															
Minimum	0.11686	0.27056	0.04180	0.22101	0.05151	0.01251	0.05285	0.05443	0.02068	0.12067	0.00205	0.00994	0.00107	0.00510	0.00668
Average	0.46790	2.23702	0.45698	2.54648	0.95260	0.29395	0.95532	0.11766	0.49093	3.32649	0.10315	0.22778	0.02585	0.14278	0.02157
Average (PAAS normalized)	0.01231	0.02796	0.05135	0.07958	0.17011	0.26723	0.20326	0.15281	0.11157	0.11880	0.10315	0.07854	0.06463	0.05099	0.05017
Maximum	1.27896	4.63875	0.91007	6.50767	3.12113	0.96249	3.37133	0.31820	1.45614	11.70784	0.38073	0.82650	0.08343	0.48338	0.05966
Standard Deviation	0.33576	1.34004	0.27687	2.03172	1.06424	0.35669	1.13234	0.07615	0.44919	3.43103	0.11379	0.22788	0.02230	0.12884	0.01523

Blank page

scientific reports

Check for updates

OPEN

Shortwave infrared hyperspectral imaging as a novel method to elucidate multi-phase dolomitization, recrystallization, and cementation in carbonate sedimentary rocks

Cole A. McCormick[1]✉, Hilary Corlett[2], Jack Stacey[1], Cathy Hollis[1], Jilu Feng[3], Benoit Rivard[3] & Jenny E. Omma[4]

Carbonate rocks undergo low-temperature, post-depositional changes, including mineral precipitation, dissolution, or recrystallisation (diagenesis). Unravelling the sequence of these events is time-consuming, expensive, and relies on destructive analytical techniques, yet such characterization is essential to understand their post-depositional history for mineral and energy exploitation and carbon storage. Conversely, hyperspectral imaging offers a rapid, non-destructive method to determine mineralogy, while also providing compositional and textural information. It is commonly employed to differentiate lithology, but it has never been used to discern complex diagenetic phases in a largely monomineralic succession. Using spatial-spectral endmember extraction, we explore the efficacy and limitations of hyperspectral imaging to elucidate multi-phase dolomitization and cementation in the Cathedral Formation (Western Canadian Sedimentary Basin). Spectral endmembers include limestone, two replacement dolomite phases, and three saddle dolomite phases. Endmember distributions were mapped using Spectral Angle Mapper, then sampled and analyzed to investigate the controls on their spectral signatures. The absorption-band position of each phase reveals changes in %Ca (molar Ca/(Ca + Mg)) and trace element substitution, whereas the spectral contrast correlates with texture. The ensuing mineral distribution maps provide meter-scale spatial information on the diagenetic history of the succession that can be used independently and to design a rigorous sampling protocol.

Hyperspectral imaging involves the collection and analysis of reflectance data in the form of many, narrow and contiguous, spectral bands[1,2]. Laboratory-, field-, and satellite-based spectroscopy are well-established methods with numerous geological applications, including lithological mapping[3,4], mineral prospectivity[5–7], and environmental monitoring[8,9]. The application of such methods to carbonate rocks, however, is limited, with previous research largely focusing on the measurement of the laboratory-based spectral characteristics of minerals[10–13] and their abundance in rocks[14–16]. The few studies that have applied hyperspectral imaging to carbonate rocks in the field have focused on up-scaling and accelerating the identification of lithological heterogeneities[17,18].

Previous studies on the reflectance of carbonate minerals have recognized up to seven absorption-bands, from 1600 to 2550 nm, caused by the vibration of the carbonate ion[10–13]. The positions, depths, and asymmetries of these bands reflect the mineral structure and properties of the substituted cations[15,19]. Calcite (Ca^{+2} mass = 40.078 amu; radius = 100 pm) has an absorption-band at ~ 2335 nm, whereas the same band for magnesite (Mg^{+2} mass = 24.305 amu; radius = 72 pm) is at ~ 2300 nm[11,12]. This absorption-band for dolomite, centered

[1]Department of Earth and Environmental Sciences, The University of Manchester, Manchester M13 9PL, UK. [2]Department of Physical Sciences, MacEwan University, Edmonton, AB T5J 4S2, Canada. [3]Department of Earth and Atmospheric Sciences, University of Alberta, Edmonton, AB T6G 2E3, Canada. [4]Rocktype Ltd., Magdalen Centre, Robert Robinson Avenue, Oxford OX4 4GA, UK. ✉email: cole.mccormick@manchester.ac.uk

at ~ 2315 nm, is not equidistant between the calcite and magnesite band positions because the Mg–O bond is shorter than the Ca–O bond in dolomite[11]. Several studies have effectively used absorption-band positions to differentiate carbonate minerals[15,18,20,21], but this method has not been used to discern multiple diagenetic phases in a largely monomineralic carbonate system. Furthermore, textural properties of minerals (e.g., crystal size, shape, orientation) affect the surface and volume scattering of light[11–14,22] and can, thus, be used to further discern individual phases in carbonate rocks.

This study is based on the shortwave infrared (SWIR) hyperspectral imaging of an exposure of variably dolomitized limestone that belongs to the Cathedral Formation (Middle Cambrian; 509–497 Ma) in the Western Canadian Sedimentary Basin (WCSB). Non-stratabound dolomite bodies originate from normal-to-transtensional faults and include several diagenetic mineral phases that have distinct compositions and textures. Given that the timing and mechanism of dolomitization are well-constrained[23–26], this succession is ideal to test whether hyperspectral imaging can be used to identify and map multiple, visibly indistinguishable, phases of dolomite in outcrop. In particular, this methodological study investigates the extent to which dolomite stoichiometry and texture can be determined by hyperspectral imaging. Consequently, the mineral distribution map products facilitate the validation and/or revision of existing fault-controlled dolomitization models[23–26].

Geological setting

The WCSB is a southwest-thickening wedge of sedimentary rocks, up to ~ 18 km thick in the southern Rocky Mountains, that extends from the southwest corner of the Northwest Territories to the north-central United States and includes four unconformity-bounded packages of strata[27,28]. The (1) Purcell Supergroup (Mesoproterozoic) records deposition and volcanic activity in an intracratonic basin, whereas the (2) Windermere Supergroup (Neoproterozoic) records the rifting of northwest Laurentia that waned in the Cryogenian to Ediacaran[27–29]. (3) Lower Cambrian (541–509 Ma) to Triassic strata were deposited on a passive margin. Episodic basement reactivation and renewed rifting in the Cambrian gave rise to regional thermal subsidence with evidence that heat flow and tectonic activity remained high[26,30,31]. (4) Jurassic to Paleocene strata were deposited in a foreland basin that developed during the Columbian (Jurassic to Early Cretaceous) and Laramide (Late Cretaceous to Paleocene) orogenies. The Cathedral Formation outcrops at Whirlpool Point (52°00′07.5″N, 116°28′13.5″W), the focus of this study, in the Bourgeau Thrust (Fig. 1a,b).

Middle Cambrian strata in the southern Rocky Mountains record a series of northeast-transgressing carbonate-mudrock cycles that comprise regional facies belts (Fig. 1c). The Cathedral Formation was deposited on a carbonate platform that developed with its margin proximal to the Kicking Horse Rim; an elevated paleotopographic feature that formed due to the syn-depositional reactivation of deep-rooted basement faults[32,33]. The formation is up to ~ 365 m thick and comprises a central shoal complex that grades laterally to proximal slope facies to the southwest and intrashelf basin facies to the northeast (Fig. 1d)[34,35]. At Whirlpool Point, the Cathedral Formation overlies the Mount Whyte Formation and is unconformably overlain by the Stephen Formation; host to the Burgess Shale lagerstätte[31,33].

Overview of the diagenetic features in the Cathedral Formation

In the southern Rocky Mountains, the Cathedral Formation consists of light-grey limestone, medium-grey to tan finely-crystalline replacement dolomite (RD), and white coarsely-crystalline saddle dolomite (SD). Dolomitization is most pervasive proximal to the Cambrian platform margin and dolomite grades laterally to limestone towards the northeast (Fig. 1d)[26]. Such dolomite bodies are typically non-stratabound (inclined-to-bedding) at their cores with stratabound (bedding-parallel) margins[24–26]. Cement-supported breccias and zebra textures are widespread in the Kicking Horse Rim area, with local occurrences of talc, magnesite, and Mississippi Valley-type (MVT) minerals[30,31,36]. These minerals are absent to the northeast, but zebra textures and cement-supported breccias are locally common[26,37].

This study focuses on an outcrop, 240 m in width and 40 m in height, at Whirlpool Point that includes a fault-controlled dolomite body in the Cathedral Formation. The outcrop contains a fault that is oriented at 028/52, has a normal offset of 30 cm, and intersects the formation 100 m from the east end (Fig. 1e). At the core of the dolomite body, coarsely-crystalline breccias extend 25 m into the hanging-wall, 5 m into the footwall, and are limited to the fault damage zone. Proximal to the fault, the hanging-wall (146/32) comprises cement-supported breccias and bedding-inclined zebra textures. The medial part of the hanging-wall includes fabric-retentive dolomitized microbial bindstone with bedding-parallel and rare bedding-inclined zebra textures. At the margin of the dolomite body, the hanging-wall includes fabric-retentive, finely-crystalline dolomitized peloidal wackestone with rare bedding-parallel zebra textures. The lower part of the Cathedral Formation includes a sharp, bedding-parallel contact with a 2 m thick bed of limestone. In the footwall (179/25), the upper part of the formation is similar to the hanging-wall, but cement-supported breccias and bedding-inclined zebra textures are rare. The medial part of the footwall includes fabric-retentive dolomitized microbial bindstone with bedding-parallel zebra textures that grade laterally to fabric-retentive, finely-crystalline dolomite at the margin (Fig. 1e).

Methods

Collection and processing of the infrared reflectance data. A set of four SWIR (930–2508 nm) spectral images were acquired on June 12, 2018 between 11 am and 2 pm using a Specim SisuROCK hyperspectral scanner (a linescan imager) that is mounted on a rotary stage for wall rock imaging. Integration time varied from 5 to 10 ms depending on the time of acquisition and it required 30 s for the stage to rotate 90°. The scanner contains a 256 spectral by 320 spatial pixels mercury-cadmium-telluride detector array that acquires data at a 6.3 nm sampling interval and a 10 nm spectral bandwidth. Two Spectralon panels of 2% and 99% reflectance were positioned in each scene. Data were acquired under clear sky conditions and the sun directly illuminated

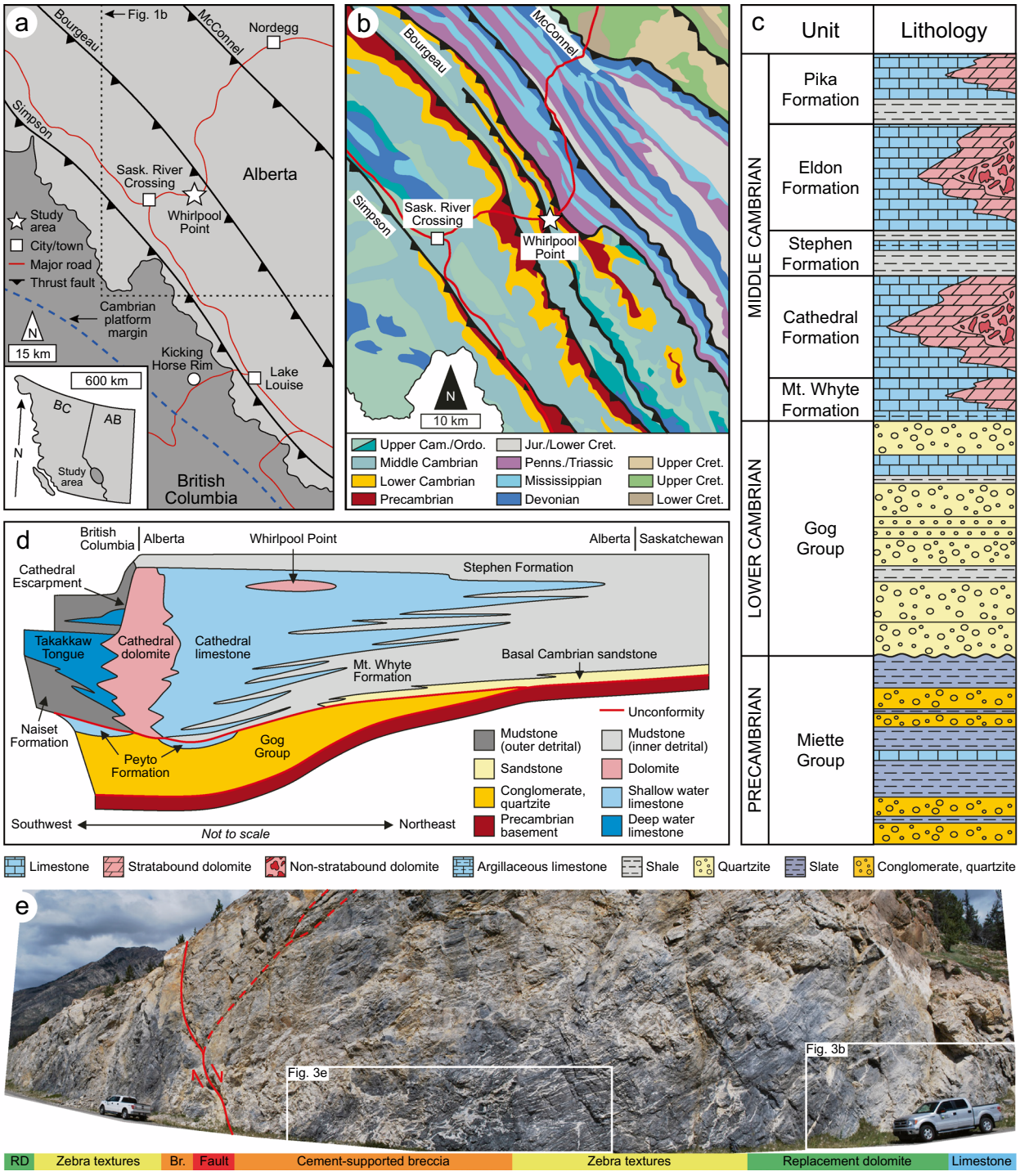

Figure 1. (**a**) Location of the study area in Alberta, Canada showing the major thrust faults and the Cambrian platform margin (modified from Stacey et al.[26]; based on Vandeginste et al.[37]). (**b**) Geological map of the study area (modified from Stacey et al.[26]; based on the Alberta Geological Survey Interactive Minerals Map: https://ags.aer.ca/publication/iam-001). (**c**) Stratigraphy of the southern Rocky Mountains (drafted by Dr. J. Stacey, based on Aitken[32,34]). (**d**) Schematic cross-section of the Cathedral carbonate platform in the southern Rocky Mountains (modified from Stacey et al.[26]; based on Aitken[32,34]). (**e**) Photomosaic of the Cathedral Formation at Whirlpool Point showing the diagenetic facies in relation to a normal-to-transtensional fault. Photographs provided by Dr. C. Hollis. Note that the scale changes throughout the photomosaic. Vehicle = 5 m in length.

the outcrop. For each scene, radiance data was obtained by applying appropriate gain and offset and conversion to reflectance, then an empirical line correction was applied based on the known reflectance of the Spectralon panels relative to their measured radiance spectrum. The latter were obtained as the mean radiance spectrum for a 20 × 20 pixel area over the panel (nominal pixel size of the acquired imagery = 5 cm). The empirical line method has the advantage of correcting for the influence of the atmosphere on the target radiance[38–40]. In contemporaneous studies with the same camera[7,41], the wavelength position of SWIR absorptions of a National Institute of Standards and Technology referenced Mylar standard were accurate within 1 nm.

Following calibration of the spectral data to reflectance, bands with the poorest signal to noise (e.g., 930–991, 1295–1435, 1735–1998, and 2461–2508 nm) were removed from the ensuing analysis. The four images were then spatially co-registered using tie points, resulting in a single image for further analysis. Next, an iterative spatial spectral filter was used to compare the spectral similarity of spatially adjacent pixels within a 3 × 3 pixel window[42–44]. When the spectral signatures were within a predefined similarity threshold, an average spectrum was substituted for the original data, thereby reducing the intra-class spectral variability. Lastly, areas in shadow and the calibration panels were masked.

Mineralogical and lithological information in the imagery was obtained by the extraction of endmember spectra and their distributions were mapped. To derive an image endmember set, spatial-spectral endmember extraction (SSEE) was used to divide the image into equal spatial subsets (each subset = 7 × 7 pixels)[42–44]. This method is designed to discern spectrally similar endmembers that occupy different portions of the scene. The endmember set derived from SSEE was clustered and labelled to derive final endmember sets for mapping. For clustering, we used a tree cluster that recursively merges a pair of clusters based on a similarity measurement. To start, each endmember was treated as an individual cluster and endmembers that are most similar were successively merged. In this study, the Spectral Angle (SA) between two endmembers was used as the measure of similarity. A minimum SA threshold was defined to stop the merging process that took place when all pairwise clusters had a similarity greater than the threshold. To address the spectral variability of the extracted endmembers, the tree cluster tool was applied twice on the given data. The first time, using all endmembers, a SA threshold of 0.2 radians produced clusters that capture the broad material classes, namely non-geological (e.g., panels, vegetation, weathering) and geological. The next level of clustering focused on the geological class to capture subclasses and define multiple geological endmember clusters. In this case, a smaller SA threshold (0.05 radians) was used because these endmembers are more spectrally similar. Clustered endmembers were then averaged to obtain an individual endmember that represents the given class, contributing to an endmember set of thirteen geological endmembers. This clustering process was data-driven.

After accounting for the spectral similarity between classes, these thirteen endmembers were condensed into four groups (Fig. 2a,b): limestone (Lst), two groups of replacement dolomite (RDa, RDb), and saddle dolomite (SD). Groups were labelled based on spectral interpretations that were supported by field and petrographical observations. Group Lst was defined by all pixels with a carbonate absorption-band position > 2330 nm and was validated in the field using dilute hydrochloric acid. Group RDa includes the spectral endmembers that correspond to light- and medium- grey replacement dolomite. Endmembers that corresponded to clasts, bedding, and bedding-parallel fractures within the RDa intervals were also included. Group RDb includes the endmembers that correspond to light-brown replacement dolomite and the alteration rims along the margins of the saddle dolomite intervals. Group SD includes three subgroups (SDa, SDb, SDc), labelled based on their paragenesis, that correspond to white, coarsely crystalline, saddle dolomite. Their paragenesis was determined by the relative positions of each endmember in macro-pores that were validated by petrographical analyses.

Distribution maps of the spectral endmembers. Mapping of the endmember spectra resulted in two image products. The first examined the distributions of limestone (Lst), replacement dolomite (RDa, RDb), and saddle dolomite (SD) and is suited for a synoptic view of the outcrop. The second, more detailed image product, examined the distribution of the saddle dolomite subgroups (SDa, SDb, SDc). In both instances, mapping the distribution of each endmember was conducted using a spectral angle mapper (SAM) algorithm that treats spectra as multidimensional vectors and computes the angle between spectral pairs[45]. For this purpose, the spectrum from each pixel of the image after processing was compared to that of each endmember. Spectra with the smallest SAM angles indicate the greatest similarity. In the first image product, the SAM results for RDa, RDb, and SD are presented as a red–green–blue composite where a higher color hue corresponds to a higher spectral similarity to the given endmember. If two or more of the endmembers predominate within a given pixel, then a color other than RGB is seen. In the second image product, the SAM results for SDa, SDb and SDc are classified in such a way that the endmember of highest similarity to that of the given pixel is assigned to that pixel. Consequently, only the colors that were assigned to the endmembers are seen in the second image product and when the SAM angle exceeds 5 degrees the pixel is not classified.

Sampling, petrography, and geochemical analyses. Fieldwork and sampling were conducted over two field seasons. Prior to obtaining the hyperspectral reflectance data, Stacey et al.[26] collected 72 samples from the Cathedral Formation in the Whirlpool Point area; 35 of these samples were systematically taken from the roadcut at ~ 2 m intervals along a 62 m logged section. After processing the hyperspectral data, an additional 33 samples were taken from the roadcut to support the analysis of the reflectance data and to evaluate specific features and trends within the mineral distribution maps. Samples were impregnated with blue epoxy and prepared as polished sections that were partially stained with alizarin red-S and potassium ferricyanide[46]. Polished sections were examined under plane- and cross-polarized light and then analysed using a CITL Mk5 cold cathodoluminescence (CL) system (operating conditions 15–20 kV and 350–450 µA) mounted on a Nikon Eclipse LV100N POL microscope. Dolomite crystal textures are described according to Sibley and Gregg[47].

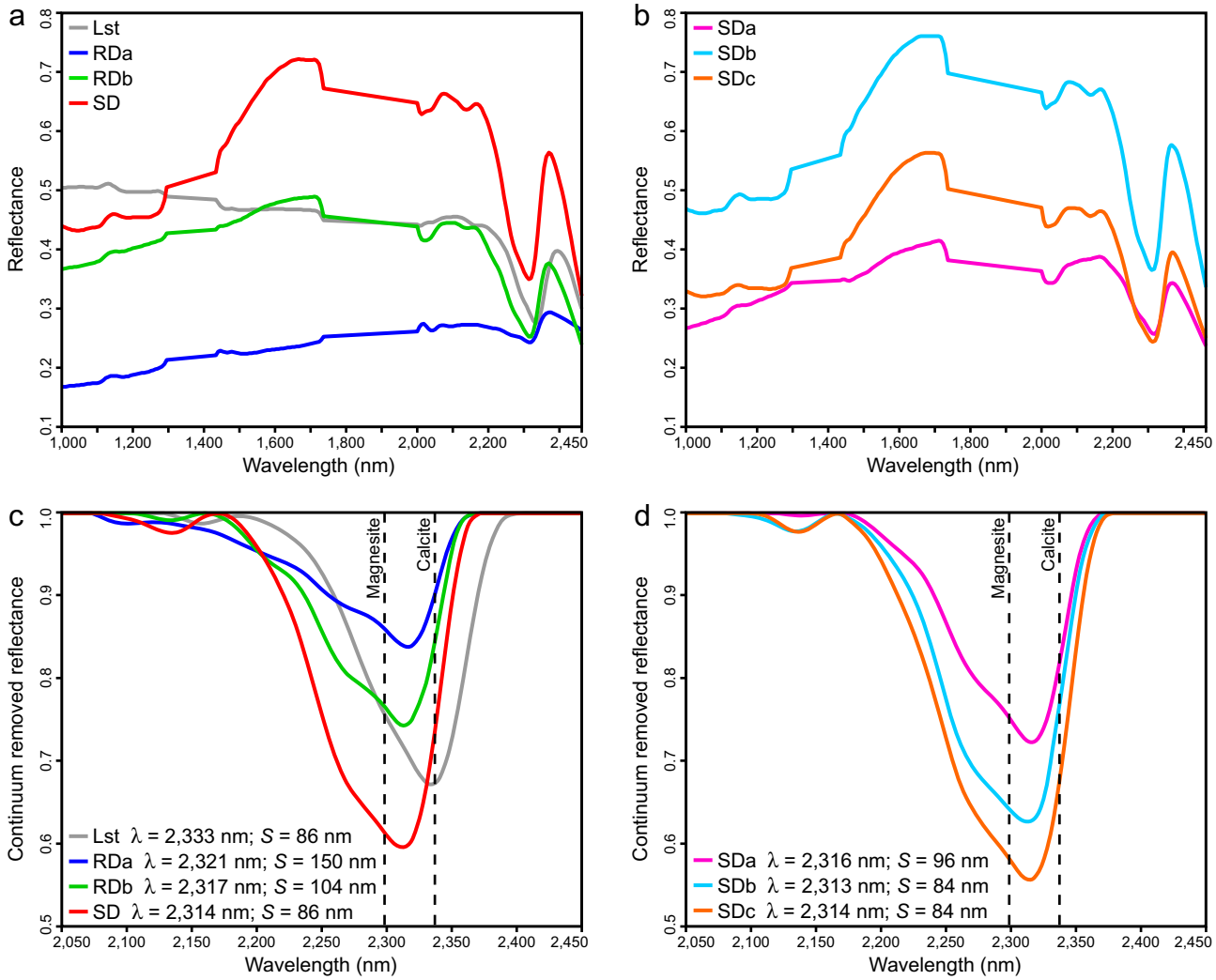

Figure 2. Reflectance spectra for (**a**) limestone (Lst), replacement dolomite a (RDa), replacement dolomite b (RDb), and saddle dolomite (SD). (**b**) Endmember SD consists of saddle dolomite a (SDa), saddle dolomite b (SDb), and saddle dolomite c (SDc). (**c**) Continuum removed reflectance for the ~ 2315 nm absorption-band showing Lst, RDa, RDb, and SD. (**d**) Continuum removed reflectance for the ~ 2315 nm absorption-band showing SDa, SDb, and SDc. Absorption-band positions (λ) were calculated using the linear interpolation method of van der Meer (his Fig. 2)[19]. Absorption-band asymmetry (*S*) is calculated as A–B, where A is the width from the short-wavelength shoulder to the absorption-band position and B is the width from absorption-band position to the long-wavelength shoulder[19].

Thirty-eight representative samples from endmembers RDa, RDb, and SD were analysed for mineralogical composition by powder X-ray diffraction (XRD) using a Bruker D8 Advance diffractometer. Quartz was added as a standard and samples were scanned at 40 kV and 30 mA from 5° to 70° 2θ in 0.02° increments. %Ca is calculated based on Lumsden[48] and degree of ordering is based on Goldsmith and Graf[49]. Two polished mounts that included each of the SD subgroups (SDa, SDb, SDc) were analysed by quantitative evaluation of minerals by scanning electron microscopy (QEMSCAN) and energy-dispersive X-ray (EDX) spectroscopy using an FEI Aspex eXstreme equipped with Bruker 5030 EDX detectors and an iExplorer software suite. An initial 10 × 10 mm mineral map was created for each sample at a stepping interval of 50 µm and 4 × 4 mm areas of interest were mapped at a stepping interval of 4 µm. An X-ray spectrum was generated for each point, matched against a standard library, and the map was constructed by assigning the library mineral to each point.

Twenty-four representative samples from endmembers RDa, RDb, and SD were analysed for trace elements by inductively coupled plasma mass spectrometry (ICP-MS) using an Agilent 7700× at the Advanced Isotope Geochemistry and Cosmochemistry Suite, The University of Manchester. Two polished sections that included each of the SD subgroups (SDa, SDb, SDc) were analysed by electron probe micro-analysis (EPMA) using a Cameca SX100. An initial 2 × 10 mm map was created at a stepping interval of 10 µm and 1.536 × 1.536 mm areas of interest were mapped at a stepping interval of 3 µm. Ca (Kα; PET) and Mg (Kα; TAP) were analysed at 15 kV, 10 nA, and a dwell time of 100 ms using calcite and magnesite as standards. Fe (Kα; LLIF) and Mn (Kα; LLIF) were analysed at 15 kV, 200 nA, and a dwell time of 200 ms using fayalite and tephroite as standards.

Results

SWIR hyperspectral imaging. Each of the endmembers can be discerned based on their absorption-band positions and spectral contrast (the difference between the peaks and the valleys in the spectrum). Phase Lst presents an absorption-band position of 2333 nm, akin to calcite and unique among all endmembers. RDa, RDb, and SD have absorption-band positions of 2321, 2317, and 2314 nm, respectively, and display increasing spectral contrast (Fig. 2c). Phase SD includes SDa, SDb, and SDc that have absorption-band positions of 2316, 2313, and 2314 nm, respectively, and display increasing spectral contrast (Fig. 2d). The absorption-band asymmetry for Lst, RDa, RDb, and SD are 86, 150, 104, and 86 nm, respectively (Fig. 2c) and the asymmetry for SDa, SDb, and SDc are 96, 84, and 84 nm, respectively (Fig. 2d).

At the margin of the fault-controlled dolomite body, a sharp, bedding-parallel contact occurs between Lst, RDa, and RDb (Fig. 3a, b). Scattered RDa pixels are located below the limestone-dolomite contact but RDb and SD are absent. Phase Lst is absent above this contact and throughout the remainder of the hanging-wall and the footwall. The distal parts of the hanging-wall comprise a mixture of RDa and RDb, the contacts between which follow the bedding (Fig. 3b, c). Phase SD is rare in the distal parts of the hanging-wall and is typically restricted to isolated beds of bioturbated wackestone. The spatial distribution of RDb pixels correlate with the occurrence of SD pixels, whereas RDa pixels are typically not in contact with SD pixels (Fig. 3b, c). This isolated SD bed illustrates the paragenetic sequence of each of the constituent SD phases. SDa lines the margins of the SD intervals and is post-dated by SDb. SDc is rare, but this phase is located at the centers of the SD intervals (Fig. 3b, d).

At the core of the dolomite body, the hanging-wall largely comprises cement-supported breccias and zebra textures (Fig. 3e). Consequently, phase SD is more abundant at the core of the dolomite body relative to at the margins. Isolated clasts of RDa and RDb are suspended and fully surrounded by SD (Fig. 3e, f). Typically, RDb pixels are located adjacent to SD pixels, but contacts between RDa and SD are locally common (Fig. 3e, f). The spatial distributions of the constituent phases of SD correlate with fault proximity. SDa and SDb are located throughout the hanging-wall but increase in abundance towards the core of the dolomite body (Fig. 3e, g). SDc post-dates these phases and is located at the centers of macro-pores such as breccias, fractures, zebra textures, and bedding planes. SDc increases in abundance towards the fault (Fig. 3e, g).

Petrography. Petrographical analysis of samples from the Cathedral Formation identified several diagenetic phases based on their crystal size, texture, fluid inclusions, CL properties, and mineral associations (Table 1). In addition to the host limestone, two phases of RD and three phases of SD were identified. RDa includes finely-crystalline (20–150 µm), planar-e to planar-s dolomite with dull-purple luminescent cores and bright-orange to dull-red luminescent rims (Fig. 4a, b). RDb includes medium-crystalline (100–400 µm), planar-s to non-planar-a dolomite with dull-red luminescent cores and dull- to moderate-red luminescent rims (Fig. 4a, b). The crystal size distribution in RDa has a normal distribution with a mode of 84 µm, a mean of 86 µm, and a standard deviation (±) of 24 µm (Fig. 4c). The crystal size distribution in RDb is broader than RDa and has a slight negative skew (−0.3). The modal crystal size of RDb is 284 µm with a mean of 267 µm (±59 µm; Fig. 4c). RDa includes trace clay minerals, detrital quartz, organic matter, and pyrite that are rare in RDb. Phase SD consists of three separate phases of non-planar (saddle) dolomite that have different petrographical characteristics (Table 1).

SDa includes medium-crystalline (250–550 µm), non-planar dolomite that typically grew syntaxially on RDb (Fig. 4d). SDb includes coarsely-crystalline (up to 4500 µm), non-planar dolomite crystals that are abundant in cement-supported breccias, zebra textures, and fractures (Fig. 4d, e). SDb crystals are elongate, oriented normal to the cavity wall, and are polymodal in size depending on the size of the cavity in which they were precipitated. SDa and SDb are unzoned with a dull- to medium-red luminescence. SDc includes coarsely-crystalline, non-planar dolomite that are largely indistinguishable from SDb based on their textural properties. SDc crystals, however, have a characteristic dull- to bright-red and dull- to bright-orange oscillatory zonation (Fig. 4e). SDc typically form rims (250 to 1250 µm thick) that are nucleated on SDb crystals in zebra textures and fractures. Individual SDc crystals (up to 4500 µm) are common in the central parts of cement-supported breccias.

Geochemistry. QEMSCAN indicates that the RD phases comprise 97.87% dolomite, 1.67% clay minerals (trace illite) and muscovite, 0.41% quartz, 0.02% calcite, 0.01% pyrite, and 0.02% other minerals (Fig. 5a, b). In contrast, phase SD comprises 99.91% dolomite, 0.06% clay minerals and muscovite, 0.02% pyrite, and 0.01% calcite (Fig. 5a, c). Although RDb and SDa are clearly discernible in outcrop and hand-sample due to their color and crystallinity, EDX spectroscopy indicates that there is minimal contrast in the abundances of Ca, Mg, and Fe between these phases (Fig. 5d–f). In contrast, SDb and SDc cannot be confidently distinguished in outcrop and hand-sample, but they are clearly distinguished by their composition (Fig. 5g–i).

Each of the RD phases are stoichiometric with %Ca = 50.21 (±0.471) and 49.79 (±0.404) for RDa and RDb, respectively (Table 2). Phase SD has %Ca = 49.65 (±0.540), however, the range (48.8–50.6%Ca) and standard deviation are markedly higher relative to each of the RD phases. Dolomite ordering increases from RDa (0.920 ± 0.088) to RDb (1.00 ± 0.232). The [Sr] decreases from RDa (171 ± 168 ppm) to RDb (18.1 ± 6.70 ppm). The [Fe] increases from RDa (2410 ± 2100 ppm), to RDb (4910 ± 3650 ppm), to SD (7570 ± 4270 ppm) and the [Mn] correlates with the [Fe] in each of these phases of dolomite (Table 2).

Each of the constituent phases of SD were further analysed by EPMA (Table 2). SDa has %Ca = 49.92, SDb has %Ca = 49.67, and SDc has %Ca = 50.53. SDa has similar concentrations of Fe (2170 ± 1420 ppm) and Mn (290 ± 140 ppm) relative to SDb ([Fe] = 3310 ± 1590 ppm; [Mn] 380 ± 180 ppm). SDc is markedly enriched in Fe (12,100 ± 2030 ppm) and Mn (1190 ± 660 ppm) relative to each of the RD and the other SD phases (Table 2).

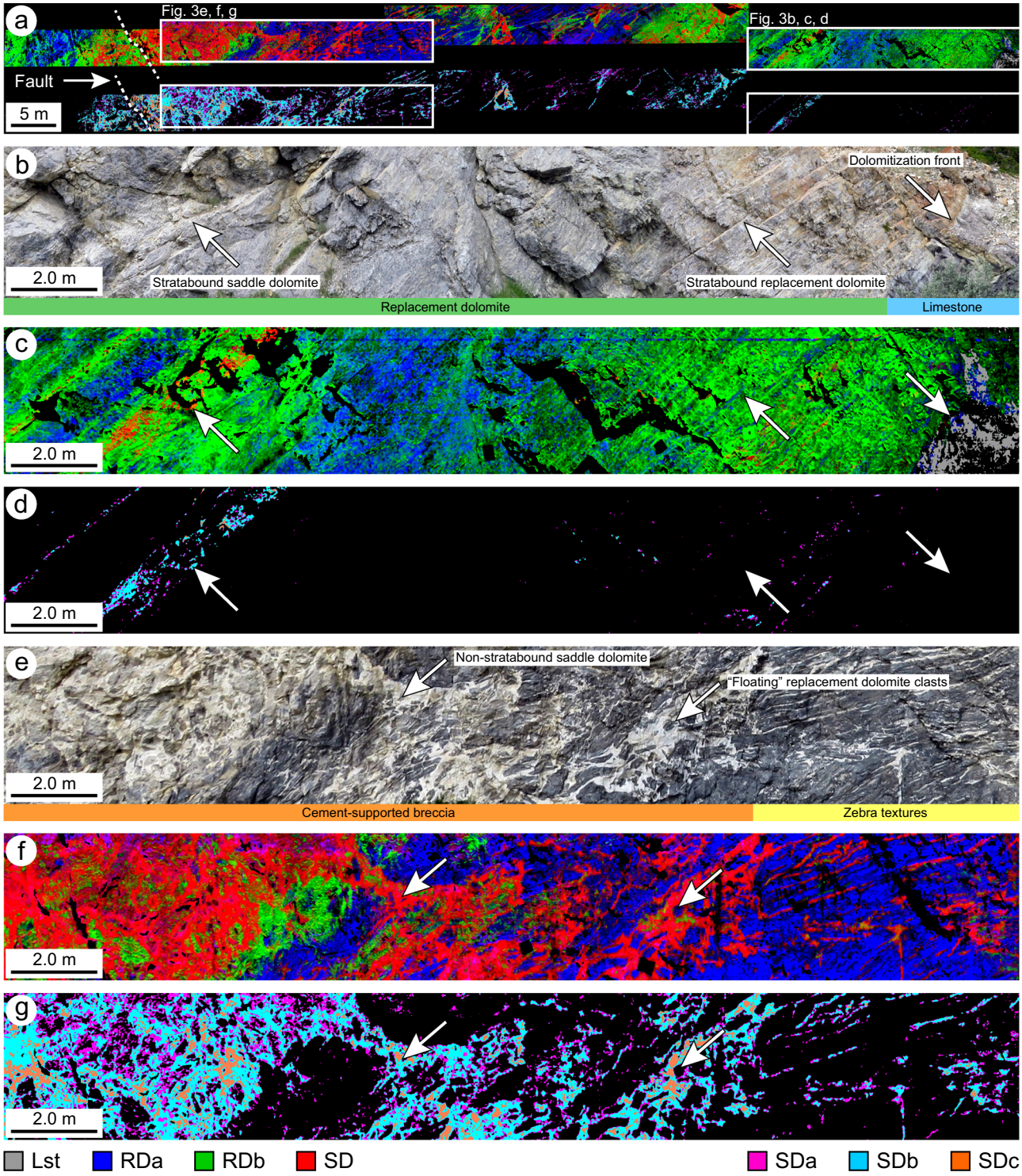

Figure 3. Endmember mineral distribution maps of the Cathedral Formation at Whirlpool Point showing (**a**) an overview of the acquired imagery illustrating the spatial distributions of each diagenetic phase (upper panels show Lst, RDa, RDb, and SD; lower panels show SDa, SDb, and SDc). Lst was mapped by retaining all pixels with a carbonate absorption-band position > 2330 nm. (**b**) The distal part of the fault-controlled dolomite body (white box in **a**) showing the abundant stratabound dolomite at the dolomitization front (limestone-dolomite contact) accompanied by (**c**) the corresponding Lst, RDa, RDb, and SD mineral distribution map, as well as (**d**) the SDa, SDb, and SDc mineral distribution map. (**e**) The proximal part of the fault-controlled dolomite body (white box in **a**) showing the abundant non-stratabound dolomite, cement-supported breccias, and zebra textures accompanied by (**f**) the corresponding Lst, RDa, RDb, and SD mineral map, as well as (**g**) the SDa, SDb, and SDc mineral map. Original, full-resolution, images are available in supplementary material.

Diagenetic phase		Crystal size (μm)	Texture	Inclusions	CL	Other features
Matrix calcite (host limestone)	Lst	~25	Blocky	Turbid	Unzoned, mottled dark-purple to dull-orange	Detrital quartz, clay minerals, organic matter, and pyrite common
Replacement dolomite (RD)	RDa	20–150, mean = 86	Planar-e to planar-s	Turbid	Concentric zoning, dull-purple cores, bright-orange to dull-red rims	Fabric-retentive. Detrital quartz, clay minerals, organic matter, and pyrite locally common
	RDb	100–400, mean = 267	Planar-s to nonplanar-a	Limpid, rare inclusions	Weak blotchy zoning, dull-red cores, dull-red to moderate-red rims	Fabric-destructive. Locally associated with stylolites. Detrital quartz, clay minerals, and organic matter rare
Saddle dolomite (SD)	SDa	250–550, mean = 400	Nonplanar (saddle)	Limpid, rare inclusions	Unzoned, dull-red to medium-red	Fabric-destructive. Form syntaxial layers on RDb. Detrital quartz and clay minerals rare
	SDb	250–2500 wide, up to 4500 long, mean = 2000	Nonplanar (saddle)	Limpid	Unzoned, dull-red to medium-red	Breccia and fracture fill. Elongate crystals normal to cavity walls, crystal size increases to center
	SDc	250–1250 thick rims, crystals up to 4500, mean = 2000	Nonplanar (saddle)	Limpid	Oscillatory zoning, dull-red to bright-red, dull-orange to bright-orange	Breccia and fracture fill. Commonly form rims nucleated on SDb. Associated with Pb–Zn-Fe–Mn-Cu sulphides/oxides

Table 1. Summary table of the microscopic features of the diagenetic phases in the Cathedral Formation at Whirlpool Point, southern Rocky Mountains based on transmitted light, cathodoluminescence (CL), and scanning electron microscopy.

Interpretations

Paragenesis of the Cathedral Formation at Whirlpool Point. Petrographical observations, compositional changes, and hyperspectral imaging were used to establish the paragenesis of the Cathedral Formation. Stacey et al.[26] documented micritized grains, post-dated by a blocky calcite cement that is consistent with cementation at or below the seafloor. Cross-cutting relationships between RDa and RDb are absent, but RDb is interpreted to have formed by the recrystallization of RDa due to (1) increasing crystal size, (2) decreasing %Ca, (3) decreasing [Sr], and (4) increasing [Fe + Mn] (Tables 1, 2). Recrystallization is associated with a change from planar-e to planar-s dolomite in RDa to planar-s to non-planar-a dolomite in RDb (Fig. 4a, b). Given that RDa and RDb are cross-cut by low-amplitude, bedding-parallel stylolites, replacement dolomitization is interpreted to have occurred during shallow burial[26,50].

Saddle dolomite (SD) grows within pores in RDa and RDb and, therefore, post-dates them. SDa is consistently located at the margins of these pores and is overgrown and postdated by SDb (Fig. 4d). In thin-section, SDa forms a syntaxial rim that is in optical continuity with RDb; a common feature of cavity-filling cements with the same mineralogy as the cavity-wall[37]. SDa and SDb have similar compositions, gradational contacts, and were likely derived from a similar fluid-flow event. SDb crystals are an order of magnitude larger than SDa (Table 1) due to competitive crystallization; a process by which favourably-oriented crystals obstruct the growth of poorly-oriented crystals[51]. Although SDc is not present throughout the outcrop, it consistently nucleates on and, thus, postdates SDb. SDc is restricted to the central parts of vugs, fractures, zebra textures, and cement-supported breccias (Fig. 3).

Spatial distribution of each diagenetic phase. Dolomitization fronts in the Cathedral Formation and the underlying Mount Whyte Formation at Whirlpool Point are interpreted to have "retreated" over time due to the occlusion of porosity from repeated fluid-pulses[23–26]. In this model, the core of the dolomite body is younger than the margins; with each successive fluid-pulse contributing to the recrystallization of earlier phases during the cementation of the dolomite body[23–26]. This retreating dolomitization front is associated with increased dolomite stoichiometry and ordering towards the core of the dolomite body[24]. The cement-supported breccias and associated zebra textures imaged in this study are largely restricted to the core of the dolomite body and are interpreted to have formed as a final event when the occlusion of porosity gave rise to high pore-fluid pressures and the rupturing of the formation during seismic valving[26].

The mineral distribution maps, derived from the hyperspectral data, reveal outcrop-scale heterogeneities that provide evidence of how fault-controlled dolomitization in the Cathedral Formation progressed and terminated. Each paragenetic stage increases in abundance from the margin of the dolomite body to the core and their spectral signatures indicate that the %Ca decreases between each phase (Fig. 6). At the margin, the dolomitization front (contact between Lst and RDa) is sharp and bed-parallel (Fig. 3b, c). RDa grades laterally to RDb and the phases have a patchy distribution throughout the outcrop. Bedding planes can be identified by the distribution of RDa and RDb (Fig. 3b, c), which suggests that that they acted as permeability pathways that circulated the initial dolomitizing fluids during replacement dolomitization[52]. RDb has a spatial relationship to SD, which suggests that recrystallization occurred during the later fluid-pulses that also precipitated SD (Fig. 3). Consequently, there are textural changes from the nonstoichiometric RDa (concentrically zoned, poorly-ordered, planar-e to planar-s

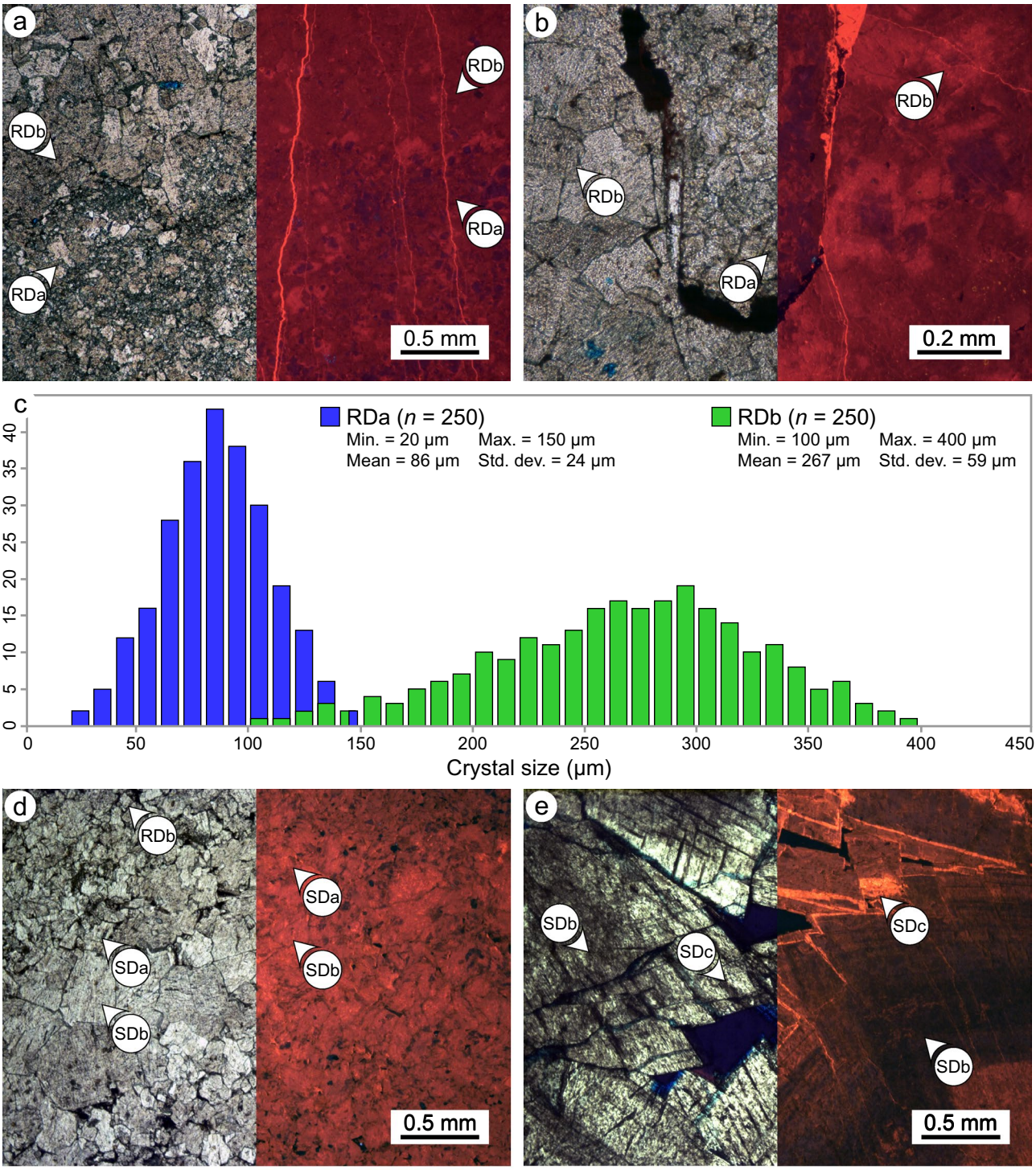

Figure 4. Plane polarized light (PPL; left) and cathodoluminescence (CL; right) photomicrographs of the replacement dolomite (RD) and saddle dolomite (SD) phases in the Cathedral Formation. (**a**) The contact between RDa and RDb showing their respective microscopic features. (**b**) RDa and RDb located above and below a bedding-parallel stylolite, respectively. (**c**) Crystal size histogram for RDa and RDb showing their mean crystal size, range, and standard deviation. Note that the histogram for RDb has a negative skew (−0.3). (**d**) Bedding-parallel zebra texture showing the gradational increase in crystal size between SDa and SDb and their respective microscopic features. Note that SDa and SDb have similar CL signatures. (**e**) SDc, which commonly form rims nucleated on SDb, comprises alternating zones of dull-red to bright-red luminescent dolomite.

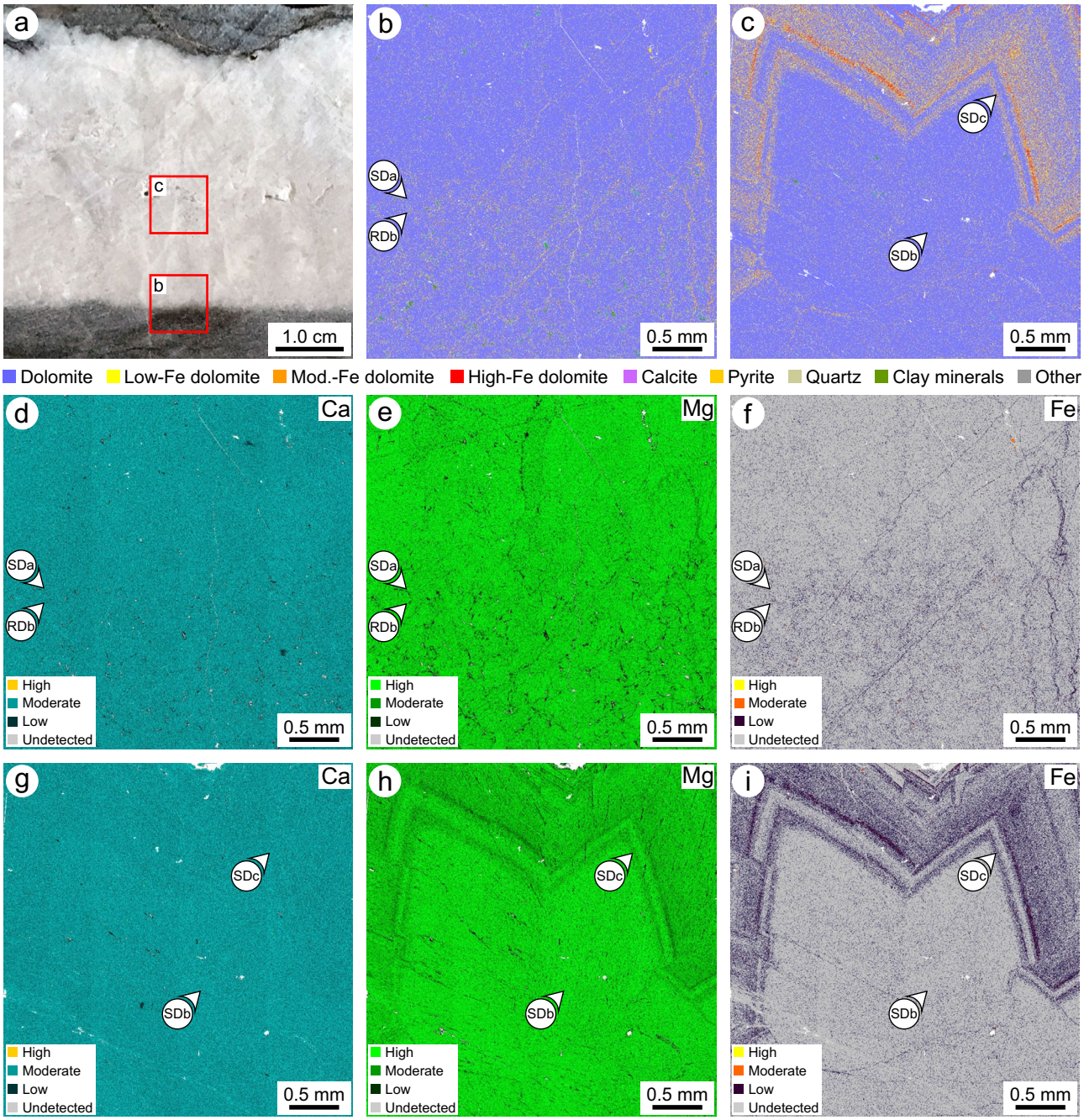

Figure 5. (**a**) Photograph of a sample from the Cathedral Formation showing the locations of quantitative evaluation of minerals by scanning electron microscopy (QEMSCAN) and energy-dispersive X-ray (EDX) spectroscopy images. Photographs taken by C.A. McCormick. (**b**) QEMSCAN image showing the contact between RDb and SDa. (**c**) QEMSCAN image showing the contact between SDb and SDc. (**d**, **e**, **f**) EDX spectroscopy images showing the relative abundances of Ca, Mg, and Fe across the contact between RDb and SDa. (**g**, **h**, **i**) EDX spectroscopy images showing the relative abundances of Ca, Mg, and Fe across the contact between SDb and SDc. Stepping interval of QEMSCAN and EDX spectroscopy = 4 μm.

dolomite) at the margins of the dolomite body to the more stoichiometric RDb (weakly zoned, well-ordered, planar-s to nonplanar-a dolomite) at the core.

SD is present throughout the dolomite body, but it is more abundant at the core relative to at the margins and in the hanging-wall of the fault relative to in the footwall (Fig. 3a). Each of the constituent phases of SD, which are indistinguishable in visible light, also increase in abundance from the margin of the dolomite body to the core (Fig. 3a). SDa occurs as isolated pixels in RDa and RDb, and lines the margins of vugs, zebra textures, and cement-supported breccias (Fig. 3d, g). SDb has a gradational contact with SDa and is restricted to the central parts of these rock textures. Finally, SDc precipitated in macro-pores that were proximal to the fault (Fig. 3g), but occasionally occurs along fractures, stylolites, and bedding planes that were likely the few remaining permeability

Phase	X-ray diffraction (XRD)	Inductively coupled plasma mass spectrometry (ICP-MS)		
	%Ca	Sr (ppm)	Fe (ppm)	Mn (ppm)
Replacement dolomite a (RDa)	*XRD (n = 9)*			*ICP-MS (n = 5)*
Min	49.27	24.7	958.0	38.6
Mean	50.21	171.3	2,407.1	182.7
Max	50.72	377.7	6,057.1	546.5
SD	0.471	167.8	2,097.6	212.7
Replacement dolomite b (RDb)	*XRD (n = 12)*			*ICP-MS (n = 13)*
Min	49.12	11.3	1444.5	101.4
Mean	49.79	18.1	4907.1	340.4
Max	50.30	37.5	11,006.0	813.3
SD	0.404	6.7	3649.7	218.3
Saddle dolomite (SD)	*XRD (n = 17)*			*ICP-MS (n = 6)*
Min	48.79	11.5	2026.1	183.6
Mean	49.65	20.2	7571.8	552.9
Max	50.57	26.8	12,290.0	813.6
SD	0.540	5.8	4272.9	278.4
	Electron probe microanalysis (EPMA)			
Phase	**Ca (wt%)**	**Mg (wt%)**	**Fe (ppm)**	**Mn (ppm)**
Saddle dolomite a (SDa)	*Mean %Ca = 49.92*			
Min	15.92	8.42	0	0
Mean	21.07	12.82	2170	290
Max	26.22	16.46	4910	630
SD	2.209	1.751	1420	140
Saddle dolomite b (SDb)	*Mean %Ca = 49.67*			
Min	16.13	8.85	0	0
Mean	21.06	12.94	3310	380
Max	25.99	17.03	5040	710
SD	2.202	1.744	1590	180
Saddle dolomite c (SDc)	*Mean %Ca = 50.53*			
Min	14.77	7.53	0	0
Mean	20.45	12.14	12,130	1190
Max	26.13	16.75	36,740	2030
SD	2.261	1.822	2030	660

Table 2. Major and trace element concentrations of the diagenetic phases in the Cathedral Formation at Whirlpool Point, southern Rocky Mountains. %Ca = molar Ca/(Ca + Mg).

pathways after brecciation and cementation[50]. Consequently, the back-stepping and paragenesis of the SD subgroups could only be resolved using hyperspectral imaging because the endmembers are indistinguishable at the outcrop-scale and thin-sections are at too small a scale to capture their spatial distributions.

Compositional characteristics derived from the reflectance spectra. The position of the 2315–2335 nm absorption-band is commonly used to differentiate dolomite from calcite in the laboratory[10,11] and in remotely-sensed imagery[18,21,53]. Van der Meer[13] suggested that this absorption-band has a linear relationship with the degree of dolomitization and Zaini et al.[14,15] applied this approach to track the band positions of synthetic mixtures of calcite and dolomite. This methodology, however, has not been used to infer the %Ca of multiple phases of dolomite with varying compositions. RDa is the most calcium-rich phase of dolomite identified in the Cathedral Formation (%Ca = 50.21; Table 2) and has an absorption-band positioned at the longest wavelength (λ = 2321 nm; Fig. 2c). In contrast, SDb is the most magnesium-rich phase (%Ca = 49.67; Table 2), with an absorption-band positioned at the shortest wavelength (λ = 2313 nm; Fig. 2d). When SDc is excluded, the phases with intermediate compositions plot along a linear trendline with a slope of 0.07%Ca/nm and a correlation coefficient (r) of 0.94, $p < 0.05$, n = 5 (Fig. 6a).

SDc deviates from this trend because it includes substantial trace element substitution for Mg ([Fe + Mn] = 13,320 ppm; Fig. 6b, c). Increased [Fe + Mn], each with a mass greater than Ca and a radius between Mg and Ca, shift the carbonate absorption-bands to longer wavelengths[11,16]. The [Fe + Mn], however, has a poor correlation (r = 0.50, $p > 0.05$, n = 6) with the position of the ~ 2315 nm absorption-band of each of the dolomite phases in the Cathedral Formation (Fig. 6d). In the laboratory, Gaffey[11] documented a broad Fe^{+2} absorption-band at 1200 nm and Mn^{2+} bands from 300 to 800 nm, but these features are difficult to identify in the field due to spectral range limitations of the equipment[17]. Strontium, which substitutes for Ca in dolomite[54], reveals the

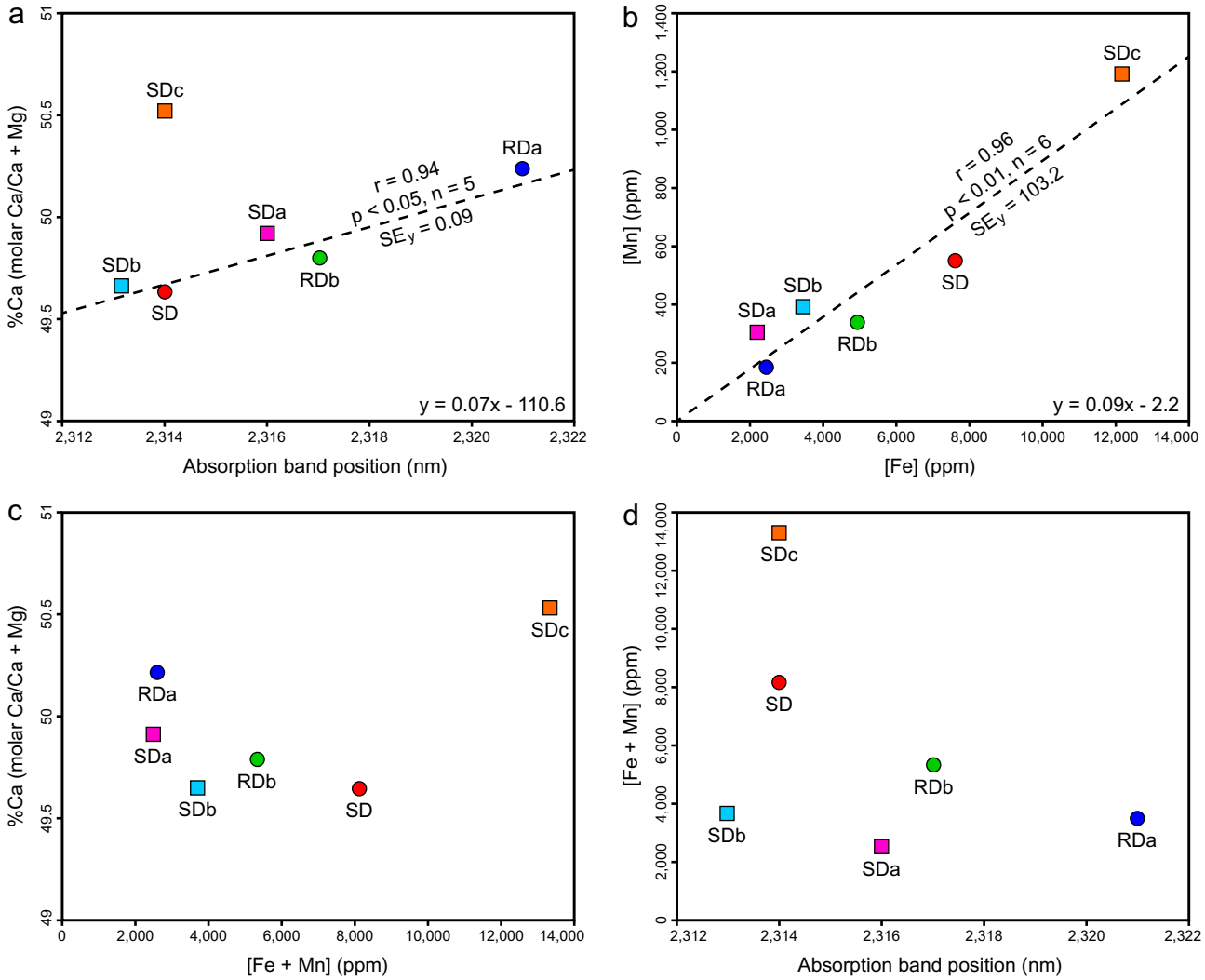

Figure 6. Scatterplots showing the relationships between: (**a**) %Ca versus the position of the ~ 2315 nm absorption-band, (**b**) the [Mn] versus the [Fe], (**c**) %Ca versus the [Mn + Fe], and (**d**) the [Mn + Fe] versus the position of the ~ 2315 nm absorption-band. r = correlation coefficient. SEy = standard error of the y-estimate. Note that the r and SEy for (**a**) omit SDc.

recrystallization pathway from RDa (%Ca = 50.21; [Sr] = 171.3 ppm) to RDb (%Ca = 49.79; [Sr] = 18.1 ppm). The effect of [Sr] on the position of the ~ 2315 nm absorption-band, however, has not been systematically investigated in dolomite and is equivocal[12].

Although each of the RD and SD phases are > 97% dolomite, the asymmetry of the ~ 2315 nm absorption-band generally relates to the volume of non-carbonate grains identified in thin-section. RDa (S = 150 nm) and RDb (S = 104 nm) include trace clay minerals and detrital quartz that are absent in each SD phase (S = 84–96 nm). QEMSCAN indicates that RD includes 1.67% clay minerals and muscovite, whereas they are negligible in SD (Fig. 5b, c). Clay minerals in RD reflect the composition of the precursor limestone, whereas their absence in SD is consistent with it being precipitated as a void-filling cement. A muscovite absorption feature at ~ 2200 nm could not be distinguished, and it is unclear if non-carbonate minerals affect the absorption-band asymmetry of each phase.

Influence of textural characteristics on the reflectance spectra. Several laboratory-based studies have demonstrated that the textural properties of minerals and rocks impact the surface scattering and volume scattering of light[11,13,14,22]. Gaffey[11] and Zaini et al.[14], for example, studied the reflectance of powdered carbonate minerals that were sieved to various sizes, typically < 500 µm, and showed that finer powders have a higher overall reflectance with shallower absorption features, whereas coarser powders have a lower overall reflectance with deeper absorption features. The degree of compaction in rocks relative to powders, as well as the occlusion of porosity, can minimize these differences and it is not always possible to infer the grain or crystal size of rocks from their spectra.

In the Cathedral Formation, the endmembers present three broad groups based on their spectral contrast (Fig. 2). RDa, with a mean crystal size of 86 µm, has the lowest overall reflectance and absorption-band depths

(Fig. 2a, c). Organic matter (OM), which reduces the reflectance of a sample and attenuates its absorption-bands[13], is locally common in RDa and rare in RDb (Fig. 3a, b). Consequently, the presence of OM in RDa may contribute to its low overall reflectance. RDb and SDa (mean crystal size = 267 µm and 400 µm, respectively) have similar overall reflectance and absorption-band depths (Fig. 2). These phases are more coarsely crystalline than RDa and their spectral contrasts are intermediate between RDa and the remaining SD phases. SDb and SDc have the largest crystals (mean size = 2000 µm), roughly five times larger than SDa, and they display the highest overall reflectance and absorption-band depths (Fig. 2b, d). In this case, it is likely that the specular reflectance from crystal facets dominates over volume scattering, thus, explaining their high reflectance[55].

Discussion

The results of this work demonstrate that hyperspectral imaging is an invaluable tool that reveals mineralogy, composition, and texture in carbonate rocks at a macro-scale. Nevertheless, care must be taken to consider the scale of observation, or spatial resolution, because each imaged pixel comprises several phases that contribute to the reflectance[56,57]. Diagenetic phases in the Cathedral Formation, for example, comprise crystals that are below the image resolution (5 cm). Although each of the phases of dolomite are monomineralic, they are represented by an endmember because they are compositionally and texturally distinct. RDa and RDb co-exist in samples at the thin-section scale and their spectral signatures are, therefore, a linear average of their relative surface abundances. For this reason, applying the laboratory-based spectra of a single dolomite endmember to our field-based imagery would not have captured the compositional and textural diversity that is present at the outcrop-scale without petrographical and geochemical calibration. Similarly, Beckert et al.[18] cautioned against the over-reliance on published spectral libraries, based on pure, end-member, minerals (i.e., stoichiometric well-ordered dolomite), to discriminate carbonate rocks in the field. Given that most sedimentary dolomite is nonstoichiometric with 48.0–62.5%Ca[48,58], consists of different crystal shapes and boundaries[47], and includes different volumes of substituted trace elements, the application of a single dolomite endmember to field- or satellite-based imagery without calibration should be treated with caution.

Initial observations of the Cathedral Formation suggests that the succession comprises only limestone, a single phase of RD, and a single phase of SD. Detailed petrographical and geochemical analyses[26], however, revealed that the succession includes several diagenetic phases. Accordingly, this study examined the extent to which hyperspectral imaging can be used to map multiple phases of dolomite at the outcrop-scale and to determine their cross-cutting relationships; features that have traditionally only been revealed petrographically. The method presented here yields a map that illustrates the spatial distribution of each diagenetic phase in an outcrop; a feat that could not be achieved with photogrammetry or Lidar, even if supported by a dense sampling campaign[17,18]. As a result, hyperspectral imaging provides a geological toolkit that facilitates systematic sampling and improves confidence that all of the phases in the paragenetic history have been sampled, thereby allowing for macro-scale fluid flow pathways to be determined. This has economic implications because structurally-controlled deposits of magnesite and MVT-minerals (e.g., Mount Brussilof, Kicking Horse, Monarch) are associated with "hydrothermal sparry dolomite" in the Cathedral Formation[30,59,60]. Their effective exploitation, therefore, requires a robust understanding of the spatial distributions of each of the SD subgroups and their relationship to mineralization.

The methodological study presented here, with a wavelength accuracy greater than 1 nm[7,41], tested whether hyperspectral imaging can be used to discriminate a narrow range of dolomite stoichiometries and textures in a Middle Cambrian succession. We distinguished five phases of dolomite, ranging from 49.67 to 50.21%Ca, that are approaching a stoichiometric, well-ordered endmember following 100's of millions of years of diagenesis and several kilometers of burial[23–26]. The progressive recrystallization of dolomite over geological time is driven by mineralogical stabilization during burial that increases dolomite stoichiometry and cation ordering[61]. Consequently, this methodology has profound transferability to other, younger, successions that have not been subject to such burial, recrystallization, and mineralogical stabilization. This includes the Cenozoic "island-type" dolomite bodies that have a wider range of dolomite stoichiometries[62–64]. With careful calibration, hyperspectral imaging can provide an upscaled view of the distribution of each of these diagenetic phases in an outcrop, akin to a geocellular model, that cannot be replicated by conventional geological methods.

Conclusions

Exposures of Middle Cambrian strata in the WCSB offer an unparalleled natural laboratory to unravel the extent and timing of dolomitization, recrystallization, and cementation in carbonate rocks. Hyperspectral imaging, in conjunction with the detailed analysis of samples from a fault-controlled dolomite body, has led to the following important conclusions:

(1) The position of the ~ 2315 nm absorption-band is an effective analogue for the %Ca of dolomite and this can be used to map outcrop-scale variations in dolomite stoichiometry.
(2) The relationship between %Ca and absorption-band positions is convoluted in dolomite with high trace element substitution (SDc; %Ca = 50.53; [Fe + Mn] = 13,320 ppm), therefore, non-stoichiometric dolomite can be distinguished using hyperspectral imaging.
(3) The spectral contrast of the reflectance profile, which accounts for overall reflectance and absorption-band depths, correlates with the textural properties (e.g., crystal size, boundary-shape) of each dolomite phase, thus, enabling their discrimination and mapping.
(4) The paragenesis and spatial distributions of the RD and SD phases in the Cathedral Formation support the prior interpretation that the dolomitization front "retreated" towards the fluid source during the ensuing recrystallization and cementation of the dolomite body.

The results of this study demonstrate that SWIR hyperspectral imaging is capable of discerning subtle diagenetic heterogeneities in carbonate rocks, beyond the routine identification of calcite and dolomite. Consequently, robust multi-scale studies can be conducted through the targeted sampling of individual diagenetic phases for further petrographical and geochemical analyses.

Received: 8 July 2021; Accepted: 18 October 2021
Published online: 05 November 2021

References

1. Cloutis, E. A. Hyperspectral geological remote sensing: Evaluation of analytical techniques. *Int. J. Remote Sens.* **17**, 2215–2242 (1996).
2. van der Meer, F. D. *et al.* Multi-and hyperspectral geologic remote sensing: A review. *Int. J. Appl. Earth Obs. Geoinf.* **14**, 112–128 (2012).
3. Rivard, B., Zhang, J., Feng, J. & Sanchez-Azofeifa, G. A. Remote predictive lithologic mapping in the Abitibi Greenstone Belt, Canada, using airborne hyperspectral imagery. *Can. J. Remote. Sens.* **35**, S95–S105 (2009).
4. Feng, J., Rogge, D. & Rivard, B. Comparison of lithological mapping results from airborne hyperspectral VNIR-SWIR, LWIR and combined data. *Int. J. Appl. Earth Obs. Geoinf.* **64**, 340–353 (2018).
5. Turner, W. A., Laamrani, A. & Rivard, B. Laboratory reflectance spectra of hydrothermally altered carbonate facies, Pine Point mining camp, NWT, Canada. *Geochem. Explor. Environ. Anal.* **3**, 369–379 (2003).
6. Krupnik, D. & Khan, S. Close-range, ground-based hyperspectral imaging for mining applications at various scales: Review and case studies. *Earth Sci. Rev.* **198**, 102952 (2019).
7. Lypaczewski, P. *et al.* Using hyperspectral imaging to vector towards mineralization at the Canadian Malartic gold deposit, Québec, Canada. *Ore Geol. Rev.* **111**, 102945 (2019).
8. Bellante, G. J., Powell, S. L., Lawrence, R. L., Repasky, K. S. & Dougher, T. A. O. Aerial detection of a simulated CO_2 leak from a geologic sequestration site using hyperspectral imagery. *Int. J. Greenh. Gas Control* **13**, 124–137 (2013).
9. Zabcic, N., Rivard, B., Ong, C. & Müller, A. Using airborne hyperspectral data to characterize the surface pH and mineralogy of pyrite mine tailings. *Int. J. Appl. Earth Obs. Geoinf.* **32**, 152–162 (2014).
10. Hunt, G. R. & Salisbury, J. W. Visible and near-infrared spectra of minerals and rocks: II. Carbonates. *Mod. Geol.* **2**, 23–30 (1971).
11. Gaffey, S. J. Spectral reflectance of carbonate minerals in the visible and near infrared (0.35–2.55 microns): calcite, aragonite, and dolomite. *Am. Mineral.* **71**, 151–162 (1986).
12. Gaffey, S. J. Spectral reflectance of carbonate minerals in the visible and near infrared (0.35–2.55 μm): Anhydrous carbonate minerals. *J. Geophys. Res. Solid Earth* **92**, 1429–1440 (1987).
13. van der Meer, F. Spectral reflectance of carbonate mineral mixtures and bidirectional reflectance theory: Quantitative analysis techniques for application in remote sensing. *Remote Sens. Rev.* **13**, 67–94 (1995).
14. Zaini, N., van der Meer, F. & van der Werff, H. Effect of grain size and mineral mixing on carbonate absorption features in the SWIR and TIR wavelength regions. *Remote Sens.* **4**, 987–1003 (2012).
15. Zaini, N., van der Meer, F. & van der Werff, H. Determination of carbonate rock chemistry using laboratory-based hyperspectral imagery. *Remote Sens.* **6**, 4149–4172 (2014).
16. Green, D. & Schodlok, M. Characterisation of carbonate minerals from hyperspectral TIR scanning using features at 14,000 and 11,300 nm. *Aust. J. Earth Sci.* **63**, 951–957 (2016).
17. Kurz, T. H. *et al.* Hyperspectral image analysis of different carbonate lithologies (limestone, karst and hydrothermal dolomites): the Pozalagua Quarry case study (Cantabria, North-west Spain). *Sedimentology* **59**, 623–645 (2012).
18. Beckert, J., Vandeginste, V., McKean, T. J., Alroichdi, A. & John, C. M. Ground-based hyperspectral imaging as a tool to identify different carbonate phases in natural cliffs. *Int. J. Remote Sens.* **39**, 4088–4114 (2018).
19. van der Meer, F. Analysis of spectral absorption features in hyperspectral imagery. *Int. J. Appl. Earth Obs. Geoinf.* **5**, 55–68 (2004).
20. Windeler, D. S. & Lyon, R. J. P. Discriminating dolomitization of marble in the Ludwig Skarn near Yerington, Nevada using high-resolution airborne infrared imagery. *Photogramm. Eng. Remote Sens.* **57**, 1171–1177 (1991).
21. van der Meer, F. Classification of remotely-sensed imagery using an indicator kriging approach: Application to the problem of calcite-dolomite mineral mapping. *Int. J. Remote Sens.* **17**, 1233–1249 (1996).
22. Crowley, J. K. Visible and near-infrared spectra of carbonate rocks: Reflectance variations related to petrographic texture and impurities. *J. Geophys. Res. Solid Earth* **91**, 5001–5012 (1986).
23. Koeshidayatullah, A. *et al.* Evaluating new fault-controlled hydrothermal dolomitisation models: Insights from the Cambrian Dolomite Western Canadian Sedimentary Basin. *Sedimentology* **67**, 2945–2973 (2020).
24. Koeshidayatullah, A. *et al.* Origin and evolution of fault-controlled hydrothermal dolomitization fronts: A new insight. *Earth Planet. Sci. Lett.* **541**, 116291 (2020).
25. Koeshidayatullah, A., Corlett, H., & Hollis, C. An overview of structurally-controlled dolostone-limestone transitions in the stratigraphic record. *Earth Sci. Rev.* 103751 (2021).
26. Stacey, J. *et al.* Regional fault-controlled shallow dolomitization of the Middle Cambrian Cathedral Formation by hydrothermal fluids fluxed through a basal clastic aquifer. *Geol. Soc. Am. Bull.* https://doi.org/10.1130/B35927.1 (2021).
27. Bond, G. C. & Kominz, M. A. Construction of tectonic subsidence curves for the early Paleozoic miogeocline, southern Canadian Rocky Mountains: Implications for subsidence mechanisms, age of breakup, and crustal thinning. *Geol. Soc. Am. Bull.* **95**, 155–173 (1984).
28. Desjardins, P. R., Buatois, L. A., Pratt, B. R. & Mángano, M. G. Stratigraphy and sedimentary environments of the Lower Cambrian Gog Group in the southern Rocky Mountains of Western Canada: Transgressive sandstones on a broad continental margin. *Bull. Can. Pet. Geol.* **58**, 403–439 (2010).
29. Li, Z. X. *et al.* Assembly, configuration, and break-up history of Rodinia: A synthesis. *Precambr. Res.* **160**, 179–210 (2008).
30. Powell, W. G., Johnston, P. A., Collom, C. J. & Johnston, K. J. Middle Cambrian brine seeps on the Kicking Horse Rim and their relationship to talc and magnesite mineralization and associated dolomitization, British Columbia, Canada. *Econ. Geol.* **101**, 431–451 (2006).
31. Johnston, P. A., Johnston, K. J., Collom, C. J., Powell, W. G. & Pollock, R. J. Palaeontology and depositional environments of ancient brine seeps in the Middle Cambrian Burgess Shale at The Monarch, British Columbia, Canada. *Palaeogeogr. Palaeoclimatol. Palaeoecol.* **277**, 86–105 (2009).
32. Aitken, J. D. Control of lower Paleozoic sedimentary facies by the Kicking Horse Rim, southern Rocky Mountains, Canada. *Bull. Can. Pet. Geol.* **19**, 557–569 (1971).
33. Collom, C. J., Johnston, P. A. & Powell, W. G. Reinterpretation of 'Middle' Cambrian stratigraphy of the rifted western Laurentian margin: Burgess Shale Formation and contiguous units (Sauk II megasequence), Rocky Mountains, Canada. *Palaeogeogr. Palaeoclimatol. Palaeoecol.* **277**, 63–85 (2009).

34. Aitken, J. D. Stratigraphy of the Middle Cambrian platformal succession, southern Rocky Mountains. *Geol. Surv. Can. Bull.* **398**, 1–322 (1997).
35. Pratt, B. R. Teepees in peritidal carbonates: Origin via earthquake-induced deformation, with example from the Middle Cambrian of western Canada. *Sed. Geol.* **153**, 57–64 (2002).
36. Vandeginste, V. *et al.* Geochemical constraints on the origin of the Kicking Horse and Monarch Mississippi Valley-type lead-zinc ore deposits, southeast British Columbia, Canada. *Miner. Depos.* **42**, 913–935 (2007).
37. Vandeginste, V. *et al.* Zebra dolomitization as a result of focused fluid flow in the Rocky Mountains Fold and Thrust Belt, Canada. *Sedimentology* **52**, 1067–1095 (2005).
38. Kurz, T. H., Buckley, S. J., Howell, J. A. & Schneider, D. Integration of panoramic hyperspectral imaging with terrestrial lidar data. *Photogram. Rec.* **26**, 212–228 (2011).
39. Kurz, T. H., Buckley, S. J. & Howell, J. A. Close-range hyperspectral imaging for geological field studies: Workflow and methods. *Int. J. Remote Sens.* **34**, 1798–1822 (2013).
40. Murphy, R. J., Taylor, Z., Schneider, S. & Nieto, J. Mapping clay minerals in an open-pit mine using hyperspectral and LiDAR data. *Eur. J. Remote Sens.* **48**, 511–526 (2015).
41. Lypaczewski, P. & Rivard, B. Estimating the Mg# and Al^{VI} content of biotite and chlorite from shortwave infrared reflectance spectroscopy: Predictive equations and recommendations for their use. *Int. J. Appl. Earth Obs. Geoinf.* **68**, 116–126 (2018).
42. Rogge, D. M. *et al.* Integration of spatial–spectral information for the improved extraction of endmembers. *Remote Sens. Environ.* **110**, 287–303 (2007).
43. Rogge, D.M. & Rivard, B. Iterative spatial filtering for reducing intra-class spectral variability and noise. In *IEEE GRSS workshop on hyperspectral image and signal processing: Evolution in remote sensing*, Reykjavik, Iceland, June 14–16, 1–4 (2010).
44. Rogge, D. *et al.* Spatial sub-sampling using local endmembers for adapting OSP and SSEE for large-scale hyperspectral surveys. *IEEE J. Sel. Top. Appl. Earth Observ. Remote Sens.* **5**, 183–195 (2012).
45. Kruse, F. A. *et al.* The spectral image processing system (SIPS)–interactive visualization and analysis of imaging spectrometer data. *Remote Sens. Environ.* **44**, 145–163 (1993).
46. Dickson, J. A. D. A modified staining technique for carbonates in thin section. *Nature* **205**, 587 (1965).
47. Sibley, D. F. & Gregg, J. M. Classification of dolomite rock textures. *J. Sediment. Res.* **57**, 967–975 (1987).
48. Lumsden, D. N. Discrepancy between thin-section and X-ray estimates of dolomite in limestone. *J. Sediment. Res.* **49**, 429–435 (1979).
49. Goldsmith, J. R. & Graf, D. L. Structural and compositional variations in some natural dolomites. *J. Geol.* **66**, 678–693 (1958).
50. Martín-Martín, J. D. *et al.* Activation of stylolites as conduits for overpressured fluid flow in dolomitized platform carbonates. *Geol. Soc. Lond. Spec. Publ.* **459**, 157–176 (2018).
51. Wallace, M. W. & Hood, Av. S. Zebra textures in carbonate rocks: fractures produced by the force of crystallization during mineral replacement. *Sediment. Geol.* **368**, 58–67 (2018).
52. Budd, D. A. & Park, A. J. Formation of bed-scale spatial patterns in dolomite abundance during early dolomitization: Part I. Mechanisms and feedbacks revealed by reaction transport modelling. *Sedimentology* **65**, 209–234 (2018).
53. Beirami, M. R. & Tangestani, M. H. A new band ratio approach for discriminating calcite and dolomite by ASTER imagery in arid and semiarid regions. *Nat. Resour. Res.* **29**, 2949–2965 (2020).
54. Vahrenkamp, V. C. & Swart, P. K. New distribution coefficient for the incorporation of strontium into dolomite and its implications for the formation of ancient dolomites. *Geology* **18**, 387–391 (1990).
55. van Ginneken, B., Stavridi, M. & Koenderink, J. J. Diffuse and specular reflectance from rough surfaces. *Appl. Opt.* **37**, 130–139 (1998).
56. Woodcock, C. E. & Strahler, A. H. The factor of scale in remote sensing. *Remote Sens. Environ.* **21**, 311–332 (1987).
57. van der Meer, F. Remote-sensing image analysis and geostatistics. *Int. J. Remote Sens.* **33**, 5644–5676 (2012).
58. Jones, B., Luth, R. W. & MacNeil, A. J. Powder X-ray diffraction analysis of homogeneous and heterogeneous sedimentary dolostones. *J. Sediment. Res.* **71**, 790–799 (2001).
59. Paradis, S. & Simandl, G. J. Is there a genetic link between the SEDEX and MVT deposits of the Canadian Cordillera? In Rogers, N. (Ed.). *Targeted Geoscience Initiative: 2016 Report of Activities*, Geological Survey of Canada, Open File 8199, 107–113 (2017). https://doi.org/10.4095/299573.
60. Paradis, S. & Simandl, G. J. Are there genetic links between carbonate-hosted barite-zinc-lead sulphide deposits and magnesite mineralization in southeast British Columbia? In: Rogers, N. (Ed.). *Targeted Geoscience Initiative: 2017 Report of Activities*, Geological Survey of Canada, Open File 8358, 217–227 (2017). https://doi.org/10.4095/306391.
61. Manche, C. J. & Kaczmarek, S. E. A global study of dolomite stoichiometry and cation ordering through the Phanerozoic. *J. Sediment. Res.* **91**, 520–546 (2021).
62. Budd, D. A. Cenozoic dolomites of carbonate islands: Their attributes and origin. *Earth Sci. Rev.* **42**, 1–47 (1997).
63. Ren, M. & Jones, B. Genesis of island dolostones. *Sedimentology* **65**, 2003–2033 (2018).
64. Wang, R. *et al.* Dolomitization micro-conditions constraint on dolomite stoichiometry: A case study from the Miocene Huangliu Formation, Xisha Islands. *South China Sea. Mar. Pet. Geol.* **133**, 105286 (2021).

Acknowledgements

This research was made possible by an infrastructure grant from the Canadian Foundation for Innovation under the John R. Evans Leaders Fund—Funding for research infrastructure (Project 22222) and by the National Science and Engineering Research Council of Canada (Discovery grant to B. Rivard). The authors acknowledge the Natural Environment Research Council funded Nanoscale Imaging and Analysis Facility for Environmental Materials in the Williamson Research Centre for Molecular Environmental Science, The University of Manchester (NERC CC042). Additional support to C.A. McCormick came from the Society for Sedimentary Geology Foundation (Student Research Grant), the International Association of Sedimentologists (Postgraduate Research Grant), the British Sedimentological Research Group (Trevor Elliot Memorial Grant), and the American Association of Petroleum Geologists Foundation (Classen Family Named Grant). We are grateful to Alberta Tourism, Parks, and Recreation for the Research and Collection Permit to sample in the Kootenay Plains Ecological Reserve. We are indebted to Tyler Hauck and Jesse Peterson (Alberta Geological Survey), who provided logistical assistance in the field; John Waters (The University of Manchester) who conducted the XRD; Paul Lythgoe (The University of Manchester) who ran the ICP-MS; Jonathan Fellows (The University of Manchester) who conducted the EPMA; and Christine Gopon and Aukje Benedictus (Rocktype Ltd.), who ran the QEMSCAN and EDX spectroscopy. We are grateful for the careful reviews on an earlier version of this manuscript that were provided by two anonymous reviewers and for the comments from the Editor, Dr. Hong Hanlie.

Author contributions

C.A.M. conducted formal analysis, wrote the manuscript, and prepared figures. Drs. H.C., C.H. and B.R. conceptualized and supervised the project and edited the manuscript. Drs. J.S., J.F. and J.E.O. were involved in formal analysis, methods, and software. Resources were obtained by C.A.M., and Drs. C.H., B.R., and J.E.O.

Competing interests

The authors declare no competing interests.

Additional information

Supplementary Information The online version contains supplementary material available at https://doi.org/10.1038/s41598-021-01118-4.

Correspondence and requests for materials should be addressed to C.A.M.

Reprints and permissions information is available at www.nature.com/reprints.

Publisher's note Springer Nature remains neutral with regard to jurisdictional claims in published maps and institutional affiliations.

Blank page

Tectonophysics 844 (2022) 229623

Contents lists available at ScienceDirect

Tectonophysics

journal homepage: www.elsevier.com/locate/tecto

An experimental study of the transition from tensile failure to shear failure in Carrara marble and Solnhofen limestone: Does "hybrid failure" exist?

Cole A. McCormick *, Ernest H. Rutter

Department of Earth and Environmental Sciences, The University of Manchester, Manchester M13 9PL, United Kingdom

ARTICLE INFO

Keywords:
Hybrid failure
Tensile crack
Shear fault
Mohr-Coulomb
Rock failure criteria
Geomechanics

ABSTRACT

Failure of brittle rocks under axisymmetric extensional loading, when the minimum principal stress is tensile, results in the formation of one or more opening-mode cracks that are oriented normal to the extension axis. When all the principal stresses are compressive, failure occurs through the formation of numerous grain-scale tensile cracks, which coalesce into a shear-mode fault that is inclined at >20° to the maximum principal stress. There have been few attempts to study the transition between these failure modes, particularly those that incorporate microstructural analyses. A transitional mode of failure, termed "hybrid failure", is often proposed to describe the orientation of faults between these end-member loading conditions, but this concept has traditionally been based on a parabolic, "Griffith-type" failure envelope that describes the growth of the single most critically-oriented crack. By integrating axisymmetric rock deformation experiments with microstructural analyses, it can be shown that failure under these transitional conditions involves the formation of several transgranular tensile cracks, which coalesce into a shear-mode fault that is inclined at <10° to the maximum principal stress. The stress intensity at the tip of each crack interacts with adjacent cracks to produce a stair-step geometry along the failure surface. These are what may be appropriately considered "hybrid faults", the angle of which systematically increase as the maximum principal stress, and thus the differential stress increases. There is, however, no evidence of a distinct "hybrid failure" mode, which involves the in-plane propagation of a single crack that is subject to a combined shear stress and tensile normal stress. The results of this experimental study provide novel insights into the mechanical behaviour of carbonate rocks and into the interpretation of meso-scale natural examples of failure under mixed stress-states.

1. Introduction

Experimental rock mechanics, which forms the foundation for interpreting natural examples of brittle failure in modern and ancient geological settings (Ferrill et al., 2012; Busetti et al., 2014; Peacock et al., 2021), comprises a great number of rock mechanical studies of brittle failure that have been carried out over a wide range of confining pressures. Most experimental studies have been conducted under axisymmetric shortening, where the principal stresses $\sigma_1 > \sigma_2 = \sigma_3$, and $\sigma_2 = \sigma_3$ is the hydraulic confining pressure. Fewer studies have been reported under polyaxial compressive stress states ($\sigma_1 > \sigma_2 > \sigma_3$) (e.g., Handin et al., 1967; Mogi, 1967, 1971; Haimson and Chang, 2000; Colmenares and Zoback, 2002; Haimson and Rudnicki, 2010; Chang and Haimson, 2012; Feng et al., 2016), but the variation in σ_2 typically does not cover the whole range of stress conditions from axisymmetric shortening to extension. Similarly, few investigations have been reported on brittle rocks under confined, axisymmetric extensional loading ($\sigma_1 = \sigma_2 > \sigma_3$) (e.g., Heard, 1960; Brace, 1964; Ramsey and Chester, 2004; Hackston and Rutter, 2016; Lan et al., 2019), but only Bobich (2005) and Huang et al. (2022) reported experiments spanning the transition from true tensile failure to shear failure in both axisymmetric extension and shortening.

It is generally considered that tensile failure and shear failure represent the end-members of a continuous spectrum of brittle failure (Fig. 1A) (Brace, 1964; Hancock, 1985; Engelder, 1999; Ramsey and Chester, 2004). Tensile failure occurs when the minimum principal stress (σ_3) is negative and results in the formation of one or more opening-mode cracks that are oriented normal to σ_3 and in the plane of $\sigma_1 = \sigma_2$ (Brace, 1960; Coviello et al., 2005; Lan et al., 2019). Conversely, shear failure occurs when all of the principal stresses are positive and it involves the precursory formation of numerous, grain-scale, tensile cracks that are oriented parallel to σ_1 and that coalesce into a shear-

* Corresponding author.
E-mail address: cole.mccormick@manchester.ac.uk (C.A. McCormick).

https://doi.org/10.1016/j.tecto.2022.229623
Received 16 May 2022; Received in revised form 17 October 2022; Accepted 20 October 2022
Available online 30 October 2022

mode fault, inclined at >20° to σ_1 (Heard, 1960; Reches and Lockner, 1994; Wibberley et al., 2000). Due to a wide array of experimental challenges, there have been relatively few attempts to study the transition between these two end-member failure modes, particularly those that incorporate microstructural analyses. A transitional mode of dilatant shear failure, termed "hybrid failure" (Fig. 1A), is often proposed to describe a progressive transition in the orientation of the macroscopic failure surfaces from tensile failure to shear failure (Ramsey and Chester, 2004; Bobich, 2005; Ferrill et al., 2012; Huang and Zhu, 2018; Huang et al., 2022). Nevertheless, a Griffith (1921)-type failure envelope is commonly invoked to describe this transition, despite the approach being applicable only to the growth of the single-most critically-oriented flaw in the material.

In this study, we investigate failure through this transitional region in two markedly different carbonate rocks, Carrara marble (CM) and Solnhofen limestone (SL), both of which have been widely used in previous experimental studies. Using a single rock deformation apparatus, we examine (i) the stress conditions at failure over a wide range of stress states, alongside (ii) the microstructural evolution from true tensile failure to shear failure in both axisymmetric extension and shortening. A series of experiments were initially conducted on SL, but additional tests on CM were incorporated as an independent comparison and validation of works by Ramsey (2003), Ramsey and Chester (2004), and Rodriguez (2005).

2. Outline of the Mohr-Coulomb criterion for failure

The Mohr-Coulomb criterion, which is a description of shear failure under axisymmetric shortening, is the most widely applied criterion to the brittle failure of geological materials. This description represents the starting point for this study, and its main features are outlined below. Although it does not have to be assumed to be linear, a simple linear relationship is typically applied to relate the principal stresses at failure (Hoek and Martin, 2014):

$$\sigma_1 = m\sigma_3 + C_0 \quad (1)$$

where the slope (m) and the unconfined compressive strength (C_0) are material parameters. Furthermore, it is commonly assumed that failure

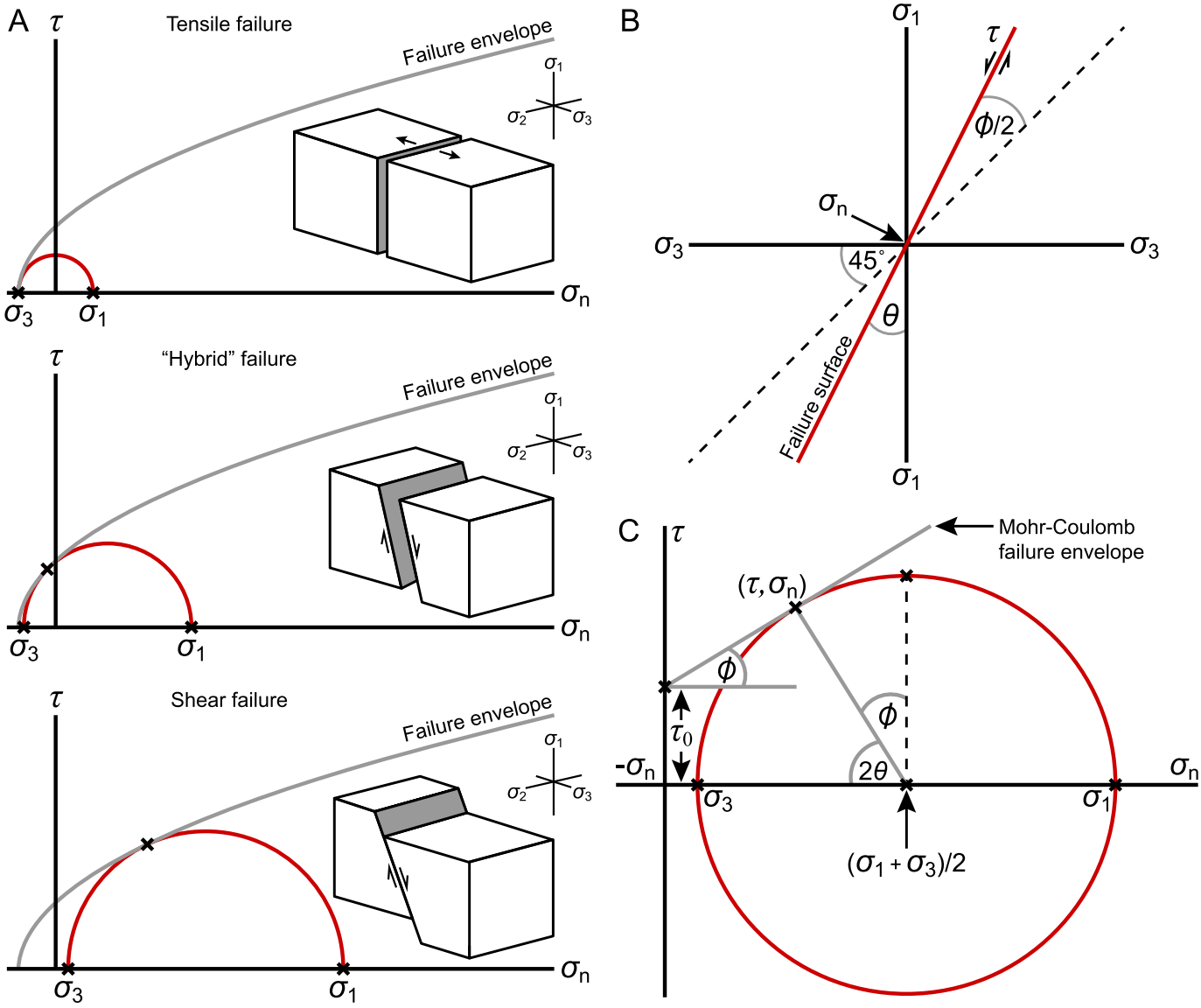

Fig. 1. (A) Conceptual model for the transition from tensile failure to shear failure (modified from Ferrill et al., 2012, their Fig. 1) using a parabolic failure envelope based on Hoek and Brown (1988). (B) Diagram illustrating the material parameters in the σ_1 versus σ_3 coordinate frame and their linear transformations to (C) a Mohr diagram in the τ versus σ_n coordinate frame.

produces a shear fault that is inclined at the angle θ to the maximum principal stress (σ_1), so that the maximum resolved normal stress (σ_n) and shear stress (τ) on the failure surface satisfy the relationships (Fig. 1B, C):

$$\tau = \pm\frac{\sigma_1 - \sigma_3}{2} sin2\theta \quad (2)$$

$$\sigma_n = \frac{\sigma_1 + \sigma_3}{2} \pm \left(\frac{\sigma_1 - \sigma_3}{2} cos2\theta\right) \quad (3)$$

The Mohr-Coulomb failure criterion can be transformed into the τ versus σ_n coordinate frame:

$$\tau = \sigma_n tan\phi + \tau_0 \quad (4)$$

where $\phi = (90 - 2\theta)$, $C_0 = 2\tau_0\sqrt{m}$, and $m = (1 + \sin\phi)/(1 - \sin\phi)$. The result is a linear envelope to the family of Mohr circles that represent a succession of stress states at failure, each having the diameter (σ_1 - σ_3). When failure occurs, the limited combination of σ_n and τ within the material are given by the tangent points on each of the Mohr circles where they intersect the failure envelope, represented by the co-ordinates (σ_n, τ) (Fig. 1B, C). The Mohr-Coulomb description of failure in the compressive domain is commonly linked and extended into the tensile domain such that the cohesive strength (0, τ_o) is connected to the tensile strength (T, 0) by a segment of the failure envelope that is assumed to be parabolic in form:

$$\sigma_n = T\left(\frac{\tau}{\tau_0}\right)^2 - 1 \quad (5)$$

where T is the uniaxial tensile strength of the rock. This parabolic form is empirical, but it is often compared to the form of the Griffith (1921) criterion that assumes failure arises from the propagation of the single most unfavourably oriented crack in the material. Sometimes the above criteria are a good description of experimental data, but in many cases the relationships between the observed orientation of the failure surface and the orientation implied by the stress states along the Mohr envelope do not conform well to these empirical descriptions.

The Mohr-Coulomb criterion is two dimensional, which assumes that the intermediate principal stress has no influence on failure, and that it always lies in the plane of the resulting failure surface. Many experimental studies have demonstrated that the intermediate principal stress affects failure, producing significant departures from the Mohr-Coulomb criterion, especially when σ_2 is midway between σ_1 and σ_3. Consequently, the conventional, two-dimensional Mohr-Coulomb failure criterion is not adequate for polyaxial loading conditions and other empirically derived failure criteria, typically based on functions of stress invariants, have had to be devised (e.g., Colmenares and Zoback, 2002; Chang and Haimson, 2012).

3. Methods

3.1. Starting material

Carrara marble (CM) and Solnhofen limestone (SL) were used as the experimental materials for this study (Table 1; Fig. 2A). Cylindrical specimens, 45 mm in length and 15 mm in diameter, of each lithology were prepared for axisymmetric shortening experiments. Samples of CM were cored in an arbitrary but constant direction (designated the *a*-direction in this block), whereas samples of SL were cored normal to bedding. Axisymmetric extension experiments were conducted on "dog-bone" shaped samples that were waisted to 13 mm in diameter over a central length of 16 mm. Samples of CM were oven-dried at 60 °C, whereas samples of SL were air-dried at a relative humidity of 60%, in each case resulting in a constant sample mass. The strength of CM is unaffected by ambient water vapour pressure, whereas the unconfined compressive strength (C_0) of SL in the oven-dried (100 °C) state is reduced by ~30% through water saturation at room temperature or when exposed to the atmosphere at laboratory relative humidity (60%) (Rutter, 1972). French et al. (2022) reported that the ultimate strength of "nominally dry" Solnhofen limestone was unaffected by wetting, which would be expected if "nominally" dry means air-dry.

Carrara marble, with a mean grain size of 98.4 μm (± 72.7 μm; standard deviation of the grain size distribution) and 0.2% porosity, is a medium-grade metamorphic rock from the Tuscany region of Italy (Table 1; Fig. 2B, C). CM comprises >99.9 wt% $CaCO_3$ and includes rare muscovite, quartz, dolomite, and graphite grains (Rutter, 1995; Pieri et al., 2001; Kandula et al., 2019; Rybacki et al., 2021; Rutter et al., 2022). Grain boundaries range from straight to gently curving with slightly sutured edges. The calcite crystals are equant, lack optical strain features and observable intragranular crack damage, are free from any significant crystallographic preferred orientation, and possess only low densities of lamellar twinning (Rutter, 1995; de Raadt et al., 2014). At ambient pressure, the variation of acoustic *P*-wave velocities for CM vary by ~3% in the plane normal to the cylinder axis relative to the velocity parallel to the cylinder axis (Fig. 2A). The CM used for this study was derived from a block of "Lorano Bianco" statuary marble that was collected as a laboratory standard by D. Olgaard and M. Pieri (ETH Zürich, Switzerland), and M. Coli (University of Florence, Italy).

Solnhofen limestone, with a mean grain size of 3.8 μm (± 0.3 μm; standard deviation on measurements of the mean) and 4.2% porosity, is a pelagic mudstone from the Bavaria region of Germany (Table 1; Fig. 2D, E). SL comprises 99.1 wt% $CaCO_3$ and includes minor detrital quartz grains with a mean grain size of 20 μm as a secondary phase. Minor impurities (e.g., organic matter, oxide particles, clay minerals) also occur along the grain boundaries (Schmid et al., 1977; Rutter et al., 1994). Llana-Fúnez and Rutter (2005), their Fig. 2) demonstrated that the calcite in SL has a weak crystallographic preferred orientation of c-axes that lie parallel to bedding, but there is no preferred orientation within that plane. Thus, the fabric is transversely isotropic. The anisotropy of *P*-wave velocities in SL (4.92% faster normal to bedding; Fig. 2A) is therefore analogous to that of an individual calcite crystal (e.g., Khazanehdari et al., 1998). The mean velocity of CM is ~18% less than that of SL, which suggests that there are grain boundary cracks present at ambient pressure. However, these would be likely to close rapidly through the application of even a small confining pressure.

3.2. Experimental design

Samples of CM and SL were held in a ¼ mm thick, annealed copper jacket and deformed using an axisymmetric rock deformation apparatus. Following deformation, the copper jacket holds the specimen together to facilitate subsequent thin-sectioning and microstructural analyses, particularly in the case of tensile failure. Each copper jacket was heat-treated to ~600 °C to remove crystal dislocations, quenched in water, and cleaned with nitric acid. Cylindrical steel split-cones, with an

Table 1
Summary table showing the mineralogy (from X-ray diffraction), grain size, porosity, and *P*-wave velocities of the experimental material used in this study.

Experimental material	Composition (from XRD)	Grain size (μm)	Porosity (%)	*P*-wave velocity (m/s)		Anisotropy
				(Axial)	(Radial)	$2(V_A - V_R) / (V_A + V_R)$
Carrara marble (CM)	Calcite (100%)	98.4 ± 72.7	0.2 ± 0.11	4574.3 ± 8.6	4705.4 ± 34.7	−2.82
Solnhofen limestone (SL)	Calcite (99.1%) Quartz (0.9%)	3.8 ± 0.3	4.2 ± 0.37	5815.4 ± 28.1	5536.4 ± 48.9	4.92

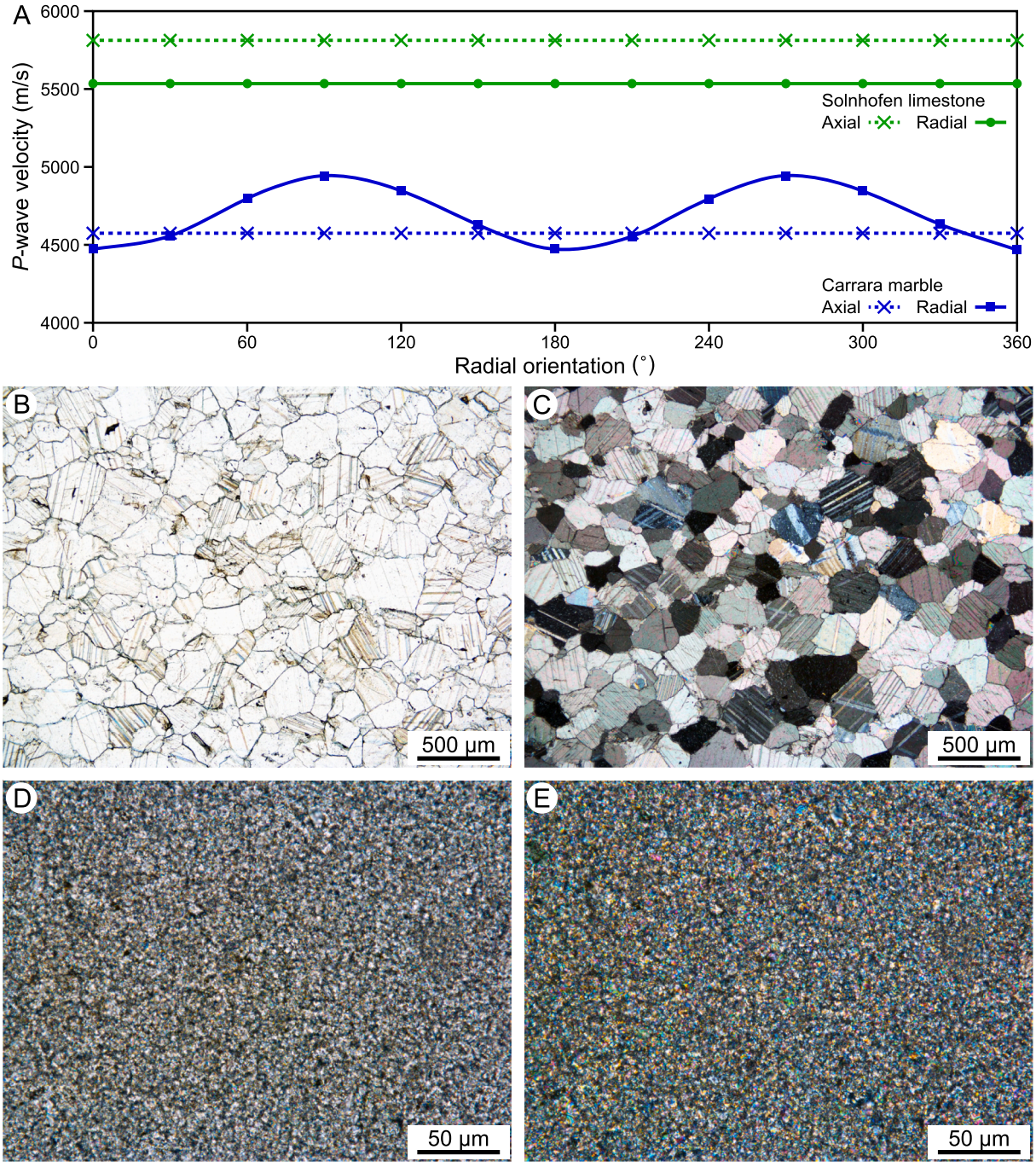

Fig. 2. (A) Axial and radial *P*-wave velocities of Carrara marble and Solnhofen limestone showing the velocity anisotropy of each lithology. (B, C) Transmitted light photomicrographs of Carrara marble showing its representative petrography in plane-polarized light (left) and between crossed-polars (right). (D, E) Transmitted light photomicrographs of Solnhofen limestone showing its representative petrography in plane-polarized light (left) and between crossed-polars (right).

included angle of 70°, were placed at each end of the jacket to grip the specimen (Fig. 3). Heat-shrink synthetic rubber tubing was then placed around the specimen and the loading piston assembly to prevent ingress of the confining fluid.

The deformation apparatus used for this study allows experiments in both axisymmetric extension and shortening to be carried out, the former owing to a bayonet-style connector on the bottom loading piston that engages with the top of the internal load cell assembly (Fig. 3). Once the loading piston assembly is inserted into the pressure vessel, it is sealed, and confining fluid is pumped into the vessel to apply radial pressure to the exterior of the specimen (up to ~300 MPa). The confining fluid is dioctyl sebacate synthetic ester, which has a low rate of change of viscosity with pressure (Rutter and Mecklenburgh, 2018). Confining pressure measurements were made using a 700 MPa Heise Bourdon tube pressure gauge, with an accuracy of 0.1 MPa, that was also used to calibrate all the other electronic pressure transducers. Experiments were conducted at room temperature (20 °C) and an axial displacement rate of 3.3×10^{-3} mm s^{-1}. This corresponds to a strain rate of 2.1×10^{-4} s^{-1} over the waisted portion of the specimen in extension tests and 7.4×10^{-5} s^{-1} over the full length of the specimen in shortening tests. Forty-seven axisymmetric extension experiments (CM = 12, SL = 35) and 16 axisymmetric shortening experiments (CM = 8, SL = 8) were conducted, typically at 10 MPa intervals of confining pressure across the range of stress conditions. In extension, true tensile

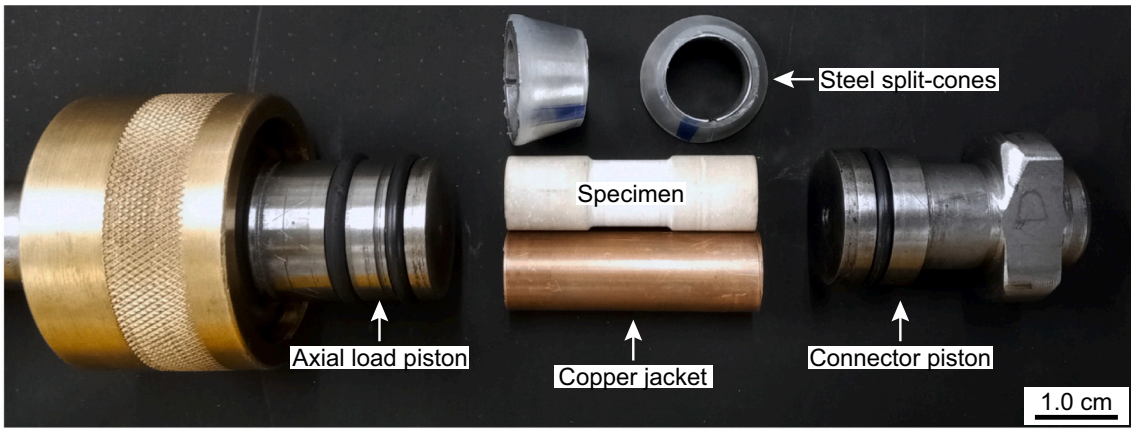

Fig. 3. Loading piston assembly showing the specimen (in this case, Solnhofen limestone), the annealed copper jacket, and the steel split-cones that grip the ends of the specimen in axisymmetric extension. Note that in extension, the bayonet-style connector piston rotates 90° to engage with the top of the internal load cell assembly.

stresses could be achieved because the specimen diameter was smaller than that of the moving piston (19.0 mm) where it passes through the pressure seal. The maximum tensile force that can be applied to the specimen is given by the difference between its cross-sectional area and that of the moving piston, multiplied by the confining pressure.

Although most tests were conducted without pore pressure, the apparatus allows pore pressure tests to be carried out. Two tests were run with an elevated pore pressure of argon gas that was generated by a servo-controlled pressure generator. Confining pressure was controlled by a similar but larger servo-controlled pressure generator. As the axial loading piston is displaced into or withdrawn from the pressure vessel, the volume change within the vessel causes an increase or decrease in confining pressure, respectively. Accordingly, the servo-controller compensates for this to maintain a constant confining pressure during a test.

Experiments were terminated at different values of bulk strain, depending on the failure mode that was identified by the stress/strain behaviour during the experiment. The piston assembly was then unloaded, and the vessel was depressurized to recover the specimen.

3.3. Calibrations, data processing, and jacket strength correction

In this type of rock deformation apparatus, the total displacement of the axial column was measured using a linear displacement transducer that was mounted outside the pressure vessel. The total displacement includes both the deformation of the specimen and the axial distortion of the apparatus. The latter was determined by calibration tests, using a steel specimen, over a range of confining pressures. Strain measurements in the specimen were determined to be accurate to ±0.1%. The axial load on the specimen was measured using a Heard (1963)-type semi-internal load cell that was mounted inside the pressure medium directly below the specimen assembly. This was calibrated against a 25,000 kg load cell over a range of confining pressures, both in axisymmetric extension and shortening. Stress measurements in the specimen were determined to be accurate to ±1.0 MPa. Given that the axial column is long, induced flexural forces can contribute to the stress state in the sample at the point of rock failure (Mackwell and Paterson, 2002) and this can influence the apparent differential stress at failure. However, the largest source of uncertainty in the measurements of stress and strain arises from the natural variability between different rock specimens.

Data processing involved the correction of the measured axial load for (1) the effects of confining pressure on the load cell calibration and (2) the subtraction of machine axial distortion from the total measured displacement to determine the total axial strain in the specimen. The axial force on the sample was calculated using the load cell calibration. Next, the axial differential stress was calculated, taking into account the change in the cross-sectional area of the specimen arising from axial strain, assuming homogeneous deformation at constant volume. The axial force that was supported by the annealed copper jacket was also removed.

In low temperature experiments, the copper jacket can support a significant fraction of the total axial load, particularly at low mean pressures when the rock is very weak or fails in tension. The analysis of results particularly requires the load supported by the copper jacket at the point of tensile failure or shear failure (ultimate strength) to be determined and subtracted from the total load at failure. To this end, the stress/strain behaviour of an annealed specimen that was fabricated from a solid copper bar was measured. The yield stress of copper is 31.0 MPa, after which rapid strain hardening begins. The strain in the jacket and the rock are the same, but the smaller cross-sectional area of the jacket reduces the load it supports by ~90%. From the measured strain at failure and the known stress/strain behaviour of the jacket, the load supported by the jacket at the onset of failure was determined for each test. This was inferred to correspond to the formation of the first tensile crack.

Using only a synthetic rubber jacket, measured to be of negligible strength, the formation of the first tensile crack splits the specimen into two pieces that are no longer able to support an axial differential load. In contrast, localized strain hardening of the copper jacket stabilizes the first crack, allowing a succession of several cracks to form in locations where strain hardening has not yet occurred. Each of these cracks are stabilized by the local strain of the copper jacket at the periphery of the crack. This avoids jacket rupture in extension and the flooding of the specimen with hydraulic fluid, which would complicate subsequent petrographical study.

3.4. Microstructural analyses

Microstructural observations were made on optical thin-sections cut parallel to the specimen cylinder axis and oriented to capture the maximum failure surface angle. For shortening tests, these angles are specified by the angle between the failure surface and the specimen axis (σ_1), and between the failure surface and the plane normal to the specimen axis (σ_1) for extension tests. Samples were vacuum impregnated with blue-stained epoxy resin and prepared as 20 μm thick sections. The jacketing material was removed, and the section was polished on its upper surface. Polished sections were examined under plane-polarized light and between crossed-polars using a Nikon Eclipse LV100N POL microscope. Six representative samples of SL that cover the

full range of failure modes were analysed by scanning electron microscopy using a Thermo Fisher Scientific Quanta 650 FEG instrument and backscattered electron imaging was conducted at an accelerating voltage of 15.0 kV.

4. Mechanical behaviour of Carrara marble and Solnhofen limestone

4.1. Stress-strain behaviour

Differential stress (σ_1 - σ_3) and axial strain were measured during each rock deformation experiment by the internal force gauge and the axial displacement transducer, respectively. The confining pressure is $\sigma_1 = \sigma_2$ in extension tests, and it is $\sigma_2 = \sigma_3$ in shortening tests. Compressive stress components are shown as positive and tensile stresses as negative.

In axisymmetric extension, for both CM and SL, the differential stress at failure increases as the confining pressure ($\sigma_1 = \sigma_2$) is increased, whereas the bulk strain at failure decreases (becomes more negative) (Fig. 4A, B). At the lowest of confining pressures, and when the value of σ_3 is very small or negative, the support of the copper jacket (strain-hardening) causes the stress-strain curve to have a flat post-yield stage, as a succession of tension cracks form along the length of the specimen. Consequently, the specimen can be deformed to an apparent bulk extensional strain of $\sim -8\%$ before the jacket will rupture. At the highest of confining pressures, the post-yield differential stress increases, and the copper jacket will eventually tear at a lower bulk strain due to sliding on the shear failure surface. In CM, this transition from extensional cracking to shear failure occurs at a confining pressure of 60 MPa (Fig. 4A), whereas the transition occurs at a confining pressure of 100 MPa in SL (Fig. 4B).

In axisymmetric shortening, for both CM and SL, the differential stress at failure increases with increasing confining pressure (σ_3), as does the bulk strain at failure (Fig. 4C, D). The post-faulting frictional sliding stress also increases with increasing confining pressure. CM shows clear evidence of ductile (distributed) deformation above a confining pressure of 20 MPa (Fig. 4C), whereas SL shows more subtle evidence of ductility above 40 MPa (Fig. 4D). Consequently, CM can accommodate a larger magnitude of strain before fault localization relative to SL, both in axisymmetric extension and shortening (Fig. 4A, B, C, D).

4.2. Maximum principal stress versus minimum principal stress at failure

Results from the rock deformation experiments on CM and SL are summarized in Table 2. For CM in axisymmetric extension, the average σ_3 at failure for samples deformed at the lowest confining pressures ($\sigma_1 < 40$ MPa) is -2.9 ± 0.5 MPa ($n = 2$; Table 2). Up to a confining pressure of 50 MPa, σ_3 at failure displays a slight negative deflection (Fig. 5A). The point where this negative deflection changes orientation towards the positive domain coincides with the point at which inclination of the failure surface away from normal to the specimen axis was first observed

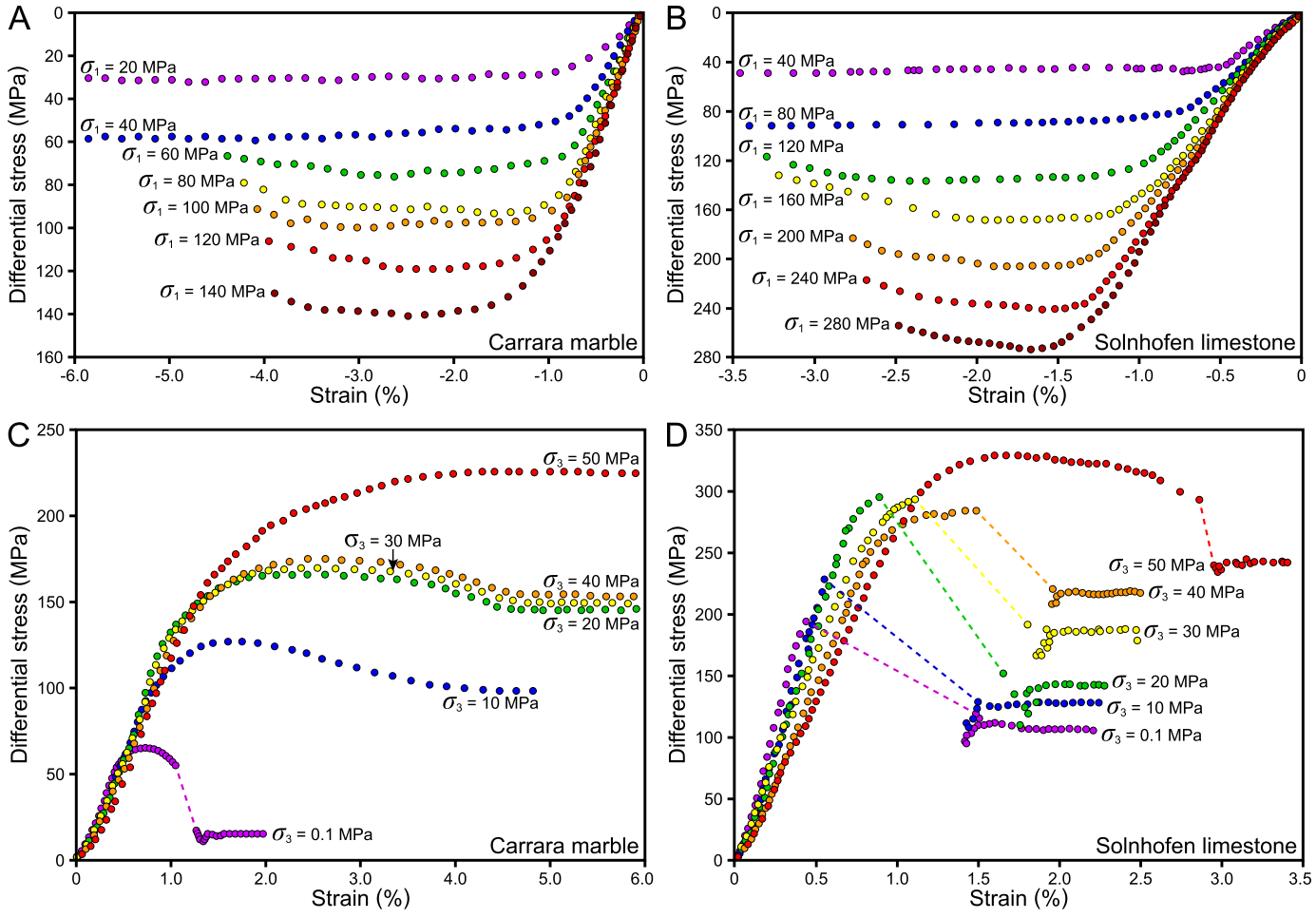

Fig. 4. Differential stress versus axial strain curves showing the results from the (A) axisymmetric extension experiments on Carrara marble, (B) extension experiments on Solnhofen limestone, (C) shortening experiments on Carrara marble, and (D) shortening experiments on Solnhofen limestone. Note that to emphasise the distinction between the two types of test, differential stresses in the extensional tests are plotted downwards and shortening tests are plotted upwards. Axial strains are shown as negative in extensional tests and as positive in shortening tests.

Table 2
Results from the rock deformation experiments conducted in axisymmetric extension and shortening on Carrara marble (CM) and Solnhofen limestone (SL). Experiments designated with an asterisk (*) were conducted with 10 MPa of pore pressure and Terzaghi (1923) effective stresses are shown in the table.

Lithology	Axial displacement	Sample ID	σ_1 (MPa)	σ_3 (MPa)	σ_1 - σ_3 (MPa)	Failure angle (°)	τ (MPa)	σ_n (MPa)
CM	Extension	CM_E01	20.0	−2.4	22.4	0	0	−2.4
CM	Extension	CM_E04	30.0	−3.4	33.4	0	0	−3.4
CM	Extension	CM_E02	40.0	−6.8	46.8	0	0	−6.8
CM	Extension	CM_E05	50.0	−5.7	55.7	0	0	−5.7
CM	Extension	CM_E03	60.0	–	–	–	–	Faulty test
CM	Extension	CM_E12	60.0	−4.2	64.2	2.0	2.2	−4.1
CM	Extension	CM_E10	70.0	−2.5	72.5	5.0	6.3	−2.0
CM	Extension	CM_E06	80.0	−0.2	80.2	6.0	8.3	0.7
CM	Extension	CM_E11	90.0	5.2	84.8	14.0	19.9	10.1
CM	Extension	CM_E07	100.0	10.9	89.1	16.0	23.6	17.6
CM	Extension	CM_E08	120.0	14.7	105.3	22.0	36.6	29.5
CM	Extension	CM_E09	140.0	16.7	123.3	26.0	48.6	40.4
CM	Shortening	CM_S07	59.5	0.1	59.4	22.0	20.6	8.4
CM	Shortening	CM_S06	93.5	5.0	88.5	26.0	34.9	22.0
CM	Shortening	CM_S01	130.2	10.0	120.2	32.0	54.0	43.7
CM	Shortening	CM_S05	146.7	15.0	131.7	33.0	60.1	54.1
CM	Shortening	CM_S02	178.1	20.0	158.1	34.0	73.3	69.4
CM	Shortening	CM_S03	189.8	30.0	159.8	38.0	77.5	90.6
CM	Shortening	CM_S04	206.9	40.0	166.9	36.0	79.4	97.7
CM	Shortening	CM_S08	256.2	50.0	206.2	37.0	99.1	124.7
SL	Extension	SL_E30	20.0	−3.9	23.9	0	0	−3.9
SL	Extension*	SL_E01	30.0	−0.5	30.5	0	0	−0.5
SL	Extension*	SL_E02	30.0	−1.9	31.9	0	0	−1.9
SL	Extension	SL_E03	40.0	−0.8	40.8	0	0	−0.8
SL	Extension	SL_E04	40.0	−0.1	40.1	0	0	−0.1
SL	Extension	SL_E31	50.0	−2.2	52.2	0	0	−2.2
SL	Extension	SL_E29	60.0	−1.9	61.9	0	0	−1.9
SL	Extension	SL_E32	70.0	0.2	69.8	0	0	0.2
SL	Extension	SL_E07	80.0	2.1	77.9	0	0	2.1
SL	Extension	SL_E33	90.0	0.7	89.3	0	0	0.7
SL	Extension	SL_E05	100.0	3.7	96.3	4.0	6.7	4.2
SL	Extension	SL_E34	110.0	−0.3	110.3	3.0	5.8	0
SL	Extension	SL_E18	120.0	−2.3	122.3	2.0	4.3	−2.1
SL	Extension	SL_E35	130.0	1.5	128.5	3.5	7.8	2.0
SL	Extension	SL_E10	140.0	0.9	139.1	3.0	7.3	1.3
SL	Extension	SL_E06	150.0	–	–	–	–	Faulty test
SL	Extension	SL_E12	150.0	−0.6	150.6	3.5	9.2	−0.1
SL	Extension	SL_E11	160.0	2.2	157.8	4.3	11.7	3.0
SL	Extension	SL_E09	170.0	6.1	163.9	4.3	12.1	7.0
SL	Extension	SL_E15	180.0	−0.3	180.3	5.3	16.4	1.2
SL	Extension	SL_E16	190.0	−3.5	193.5	5.5	18.5	−1.7
SL	Extension	SL_E08	200.0	0.8	199.2	6.0	20.7	3.0
SL	Extension	SL_E25	210.0	−3.1	213.1	6.5	24.0	−0.4
SL	Extension	SL_E24	220.0	2.9	217.1	6.5	24.4	5.7
SL	Extension	SL_E21	230.0	–	–	–	–	Faulty test
SL	Extension	SL_E27	230.0	−0.5	230.5	3.5	14.0	0.4
SL	Extension	SL_E26	240.0	6.8	233.2	8.0	32.1	11.3
SL	Extension	SL_E13	250.0	4.1	245.9	10.3	43.1	11.9
SL	Extension	SL_E28	260.0	10.0	250.0	10.0	42.8	17.5
SL	Extension	SL_E14	270.0	11.6	258.4	11.0	48.4	21.0
SL	Extension	SL_E17	280.0	15.3	264.7	11.0	49.6	24.9
SL	Extension	SL_E19	300.0	20.4	279.6	13.0	61.3	34.5
SL	Extension	SL_E20	300.0	–	–	–	–	Faulty test
SL	Extension	SL_E22	300.0	–	–	–	–	Faulty test
SL	Extension	SL_E23	300.0	–	–	–	–	Faulty test
SL	Shortening	SL_S01	211.4	5.0	206.4	14.5	50.0	17.9
SL	Shortening	SL_S07	246.6	10.0	236.6	16.0	62.7	28.0
SL	Shortening	SL_S05	298.0	20.0	278.0	15.0	69.5	38.6
SL	Shortening	SL_S08	312.9	25.0	287.9	16.5	78.4	48.2
SL	Shortening	SL_S06	297.1	30.0	267.1	17.5	76.6	54.1
SL	Shortening	SL_S02	400.8	40.0	360.8	16.0	95.6	67.4
SL	Shortening	SL_S04	360.1	50.0	310.1	20.0	99.7	86.3
SL	Shortening	SL_S03	376.8	60.0	316.8	19.5	99.7	95.3

(Table 2; Fig. 5A). From a confining pressure of 60 to 140 MPa, σ_3 at failure has a near-linear relationship to σ_1 (Fig. 5A). Data points from the extension tests with a compressive σ_3 at failure are coincident (within experimental error) with the results of the shortening tests (Fig. 5A). In axisymmetric shortening, σ_1 at failure has a near-linear relationship to σ_3, up to a confining pressure of 20 MPa. Extrapolating the values below $\sigma_3 = 20$ MPa ($n = 12$; Table 2), the CM used in this study has an unconfined compressive strength (C_0) of 72.8 MPa and a slope ($d\sigma_1/d\sigma_3$) of 4.34 (Fig. 5A).

For SL in axisymmetric extension, the average σ_3 at failure for samples deformed at the lowest confining pressures ($\sigma_1 < 100$ MPa) is −0.8 ± 1.6 MPa ($n = 10$; Table 2). Inclination of the failure surface was first observed at a confining pressure of 100 MPa, which coincides with the point at which σ_3 at failure is distinctly compressive (Table 2; Fig. 5B). The negative deflection in the data trend that was observed for CM in the tensile region is not present for SL, which has a near vertical trend of the

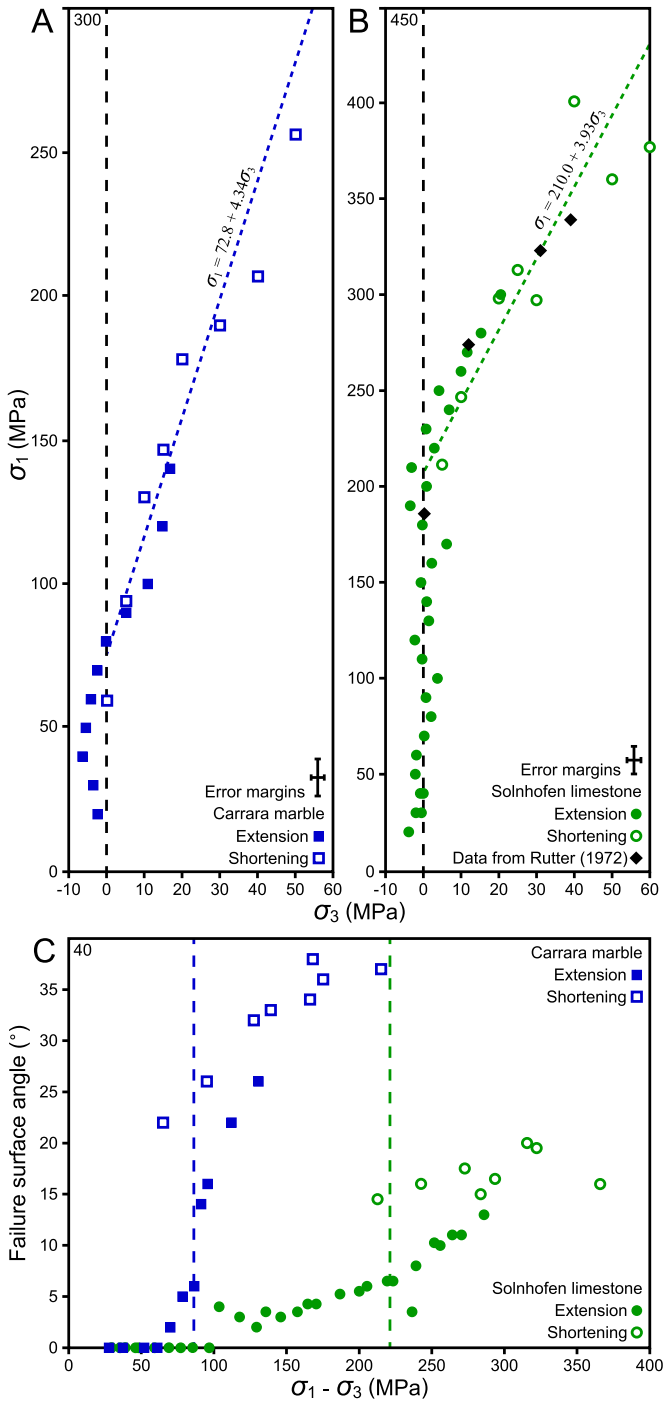

Fig. 5. (A) Maximum principal stress (σ_1) versus minimum principal stress (σ_3) plots showing the experimental results on Carrara marble and (B) Solnhofen limestone. For illustrative purposes, the linear Mohr-Coulomb failure criterion is shown in the compressive domain (dotted lines). Whilst differential stresses are measured to an accuracy of ± -1.0 MPa, the error bars shown take into account the variability in the response of each individual specimen. (C) Failure surface angle versus differential stress (σ_1 - σ_3) plot for Carrara marble and Solnhofen limestone. Note the rapid increase in the failure surface angle where σ_3 has a marked shift into the compressive domain, which occurs at a slightly higher differential stress than the unconfined compressive strength (dotted lines).

σ_1 versus σ_3 data up to a confining pressure of 210 MPa (Table 2; Fig. 5A, B). From a confining pressure of 210 to 300 MPa, σ_3 at failure has a near-linear relationship to σ_1 (Fig. 5B). As with CM, data points from the extension tests on SL with a compressive σ_3 at failure are coincident with the results of the shortening tests (Fig. 5B). In axisymmetric shortening, σ_1 at failure has a near-linear relationship to σ_3, up to a confining pressure of 40 MPa. Extrapolating the values below $\sigma_3 = 40$ MPa ($n = 21$; Table 2), the SL used in this study has an C_0 of 210.0 MPa and a slope ($d\sigma_1/d\sigma_3$) of 3.93 (Fig. 5B).

4.3. Failure surface angle

The two carbonate lithologies that were investigated in this study show clear differences in terms of the failure surface angles (θ) that were produced, which is the maximum angle measured between the σ_1 direction and the failure plane (Table 2; Fig. 5C). Both CM and SL show a trend of increasing θ with increasing differential stress, and they both display a degree of discontinuity between the failure surface angles that were produced in axisymmetric extension and in shortening (Fig. 5C). This apparent discontinuity, however, could be argued in each case to lie within experimental uncertainty. In axisymmetric extension, θ in CM ranges from 0 to 26.0°, whereas θ ranges from 0 to 13.0° in SL (Table 2; Fig. 5C). In axisymmetric shortening, θ in CM ranges from 22.0 to 37.0°, whereas θ ranges from 14.5 to 20.0° in SL (Table 2; Fig. 5C). In the transitional region between tensile failure and shear failure, there is a distinct change in the rate at which θ increases with increasing differential stress (Fig. 5C). This change occurs at a slightly higher differential stress than the C_0 for each lithology (σ_1 - σ_3 = σ_1 = C_0), which is also where the σ_3 at failure has a marked excursion into the compressive (positive) domain, and thus a more rapid rate of increase in the values of θ (Fig. 5A, B, C).

5. Petrographical characterization of failure

5.1. Macrostructural characterization of failure

From a macroscopic perspective, the results of this study are analogous to the failure characteristics that have been documented in previous works (cf. Brace, 1964; Hancock, 1985; Reches and Lockner, 1994; Wibberley et al., 2000; Ramsey and Chester, 2004). Tensile failure results in a one or more discrete cracks, which are oriented parallel to σ_1, with displacement normal to the crack surface (Fig. 6A). Although these cracks have a measured angle of 0°, their surfaces are commonly undulating at the grain-scale with areas of reflective intragranular cleavages and plumose markings. In contrast, shear failure on an inclined surface results in a fault with displacement parallel to the fault surface (Fig. 6B, C, D). The failure surface is typically covered by a fine powder of comminuted grains (fault gouge) and the surface has small mechanical wear grooves that are oriented parallel to the line of slip (slickenlines). As the confining pressure increases, the failure surface angle (θ) progressively increases with respect to σ_1, and this occurs both in axisymmetric extension and shortening.

In the transitional region between tensile failure and shear failure, the shear faults that are formed have intermediate characteristics between these two endmembers. In both CM and SL, these petrographical characteristics include isolated patches of reflective, intragranular cleavages between areas of comminuted grains with slip lineations (slickenlines). At lower confining pressures (σ_1), the failure surfaces have a higher proportion of cleaved grains relative to comminuted grains. In contrast, the failure surfaces at higher confining pressures have a higher proportion of comminuted grains relative to the proportion of cleaved grains.

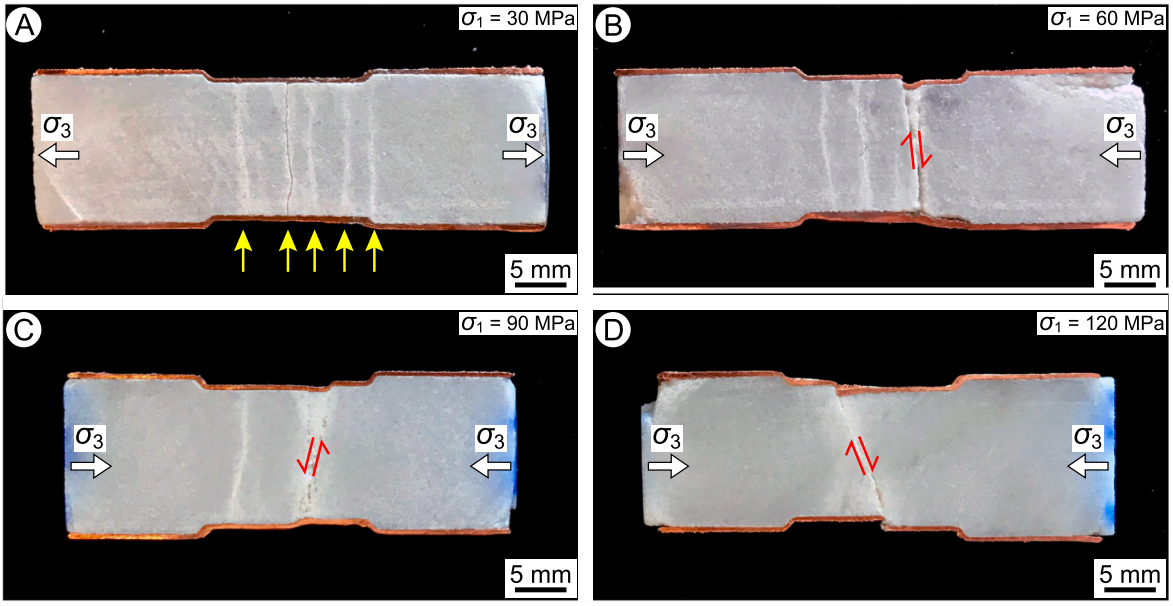

Fig. 6. Photographs of longitudinally-cut samples of Carrara marble tested in axisymmetric extension, illustrating the transition with increasing confining pressure $\sigma_1 = \sigma_2$) from tensile failure to shear failure, showing the deformed samples (A) CM_E04 (failure angle = 0°), (B) CM_E12 (failure angle = 2°), (C) CM_E11 (failure angle = 14°), and (D) CM_E08 (failure angle = 22°). Note that σ_3 is tensile in Fig. 6A, whereas it is compressive in Fig. 6B, C, D, which display shear failure (shear sense indicated). The local strain-hardening of the copper jacket allows multiple cracks to develop during tensile failure. Yellow arrows = extensional cracks. (For interpretation of the references to colour in this figure legend, the reader is referred to the web version of this article.)

Ramsey (2003), Ramsey and Chester (2004), and Rodriguez (2005) presented detailed petrographical studies of the transition from tensile failure to shear failure in CM. Thus, the following microstructural analyses focus on the behaviour of SL.

5.2. *Microstructural characterization of tensile failure in Solnhofen limestone*

In sections cut parallel to the specimen axis, tensile failure in SL involves a series of discrete cracks with negligible strain present in the regions between cracks (Fig. 7A). These long, transgranular cracks are consistently oriented parallel to σ_1 and normal to σ_3. The cracks typically cleave and propagate through numerous calcite grains, but rarely propagate through quartz grains (Fig. 7B). Under plane-polarized light, a thin, discoloured region is typically present in the region that is adjacent to the macroscopic crack surface (Fig. 7A). Given that there are no grain-scale cracks adjacent to the macroscopic crack (Fig. 7B), this discoloration is due to the epoxy resin that was able to enter the matrix intergranular porosity by permeation from the crack.

5.3. *Microstructural characterization of shear failure in Solnhofen limestone*

Under extensional loading conditions, shear failure in SL involves the coalescence of multiple tensile cracks into a shear-mode fault (Fig. 7C, D). These tensile cracks are typically short, but transgranular, and have numerous grain-scale tensile cracks and comminuted grains that are located in-between them (Fig. 7D). The abundances of the grain-scale tensile cracks and the comminuted grains are heterogeneously distributed throughout the rock matrix (Fig. 7D). The failure surface has a pronounced stair-step pattern that links these short transgranular cracks (Fig. 7C).

When loaded in axisymmetric shortening, shear failure in SL involves the coalescence of numerous, grain-scale tensile cracks into a shear-mode fault (Fig. 7E, F). The longer, transgranular tensile cracks that were present in axisymmetric extension are strikingly absent in shortening. Adjacent to the macroscopic failure surface, comminuted grains are notably more abundant in axisymmetric shortening relative to in extension (Fig. 7E). In contrast, the grain-scale tensile cracks are largely homogenously distributed throughout the rock matrix (Fig. 7E, F). At higher confining pressures ($\sigma_3 \geq 40$ MPa), ductile deformation (e.g., intracrystalline twinning, dislocation glide, distributed cataclastic flow) is the dominant way that strain is accommodated within the specimen. In particular, differential stresses above 350 MPa are required to induce deformation twinning in SL at room temperature, as compared to 90 MPa in CM (Rowe and Rutter, 1990; Rutter et al., 2022).

5.4. *The transition from tensile failure to shear failure in Solnhofen limestone*

In the region of transition between tensile failure and shear failure in SL, failure initially involves the coalescence of relatively few, long tensile cracks into a shear-mode fault (Fig. 8A, B, C, D). With increasing confining pressure (σ_1), these tensile cracks systematically become shorter and more tightly spaced as the failure surface angle (θ) increases (Fig. 8B, D). At lower confining pressures, the tensile cracks are widely spaced, and they are linked by a low angle failure surface that has a faint stair-step pattern (Fig. 8B). In contrast, the tensile cracks are more tightly spaced at higher confining pressures, and they are linked by a moderate angle failure surface that has a more pronounced stair-step pattern (Fig. 8D). The discolouration adjacent to the macroscopic failure surface (Fig. 8A, C) is due to the infiltration of the epoxy resin into the dilated region that includes these grain-scale and transgranular cracks.

It is challenging to investigate the role of stepped tensile cracks and their contribution to brittle failure within the throughgoing macroscopic fault because there has been a loss of fragmented and incohesive material from the fault region during shearing prior to fabrication of the section. In the matrix of the sample, however, there are numerous examples of these stepped cracks where the rock has accommodated less bulk strain (Fig. 8E, F). These long tensile cracks are consistently oriented parallel to σ_1, normal to σ_3, and terminate laterally within the sample where no faulting has developed. Their apertures are greatest at the mid-point of the crack, and they decrease laterally until the crack

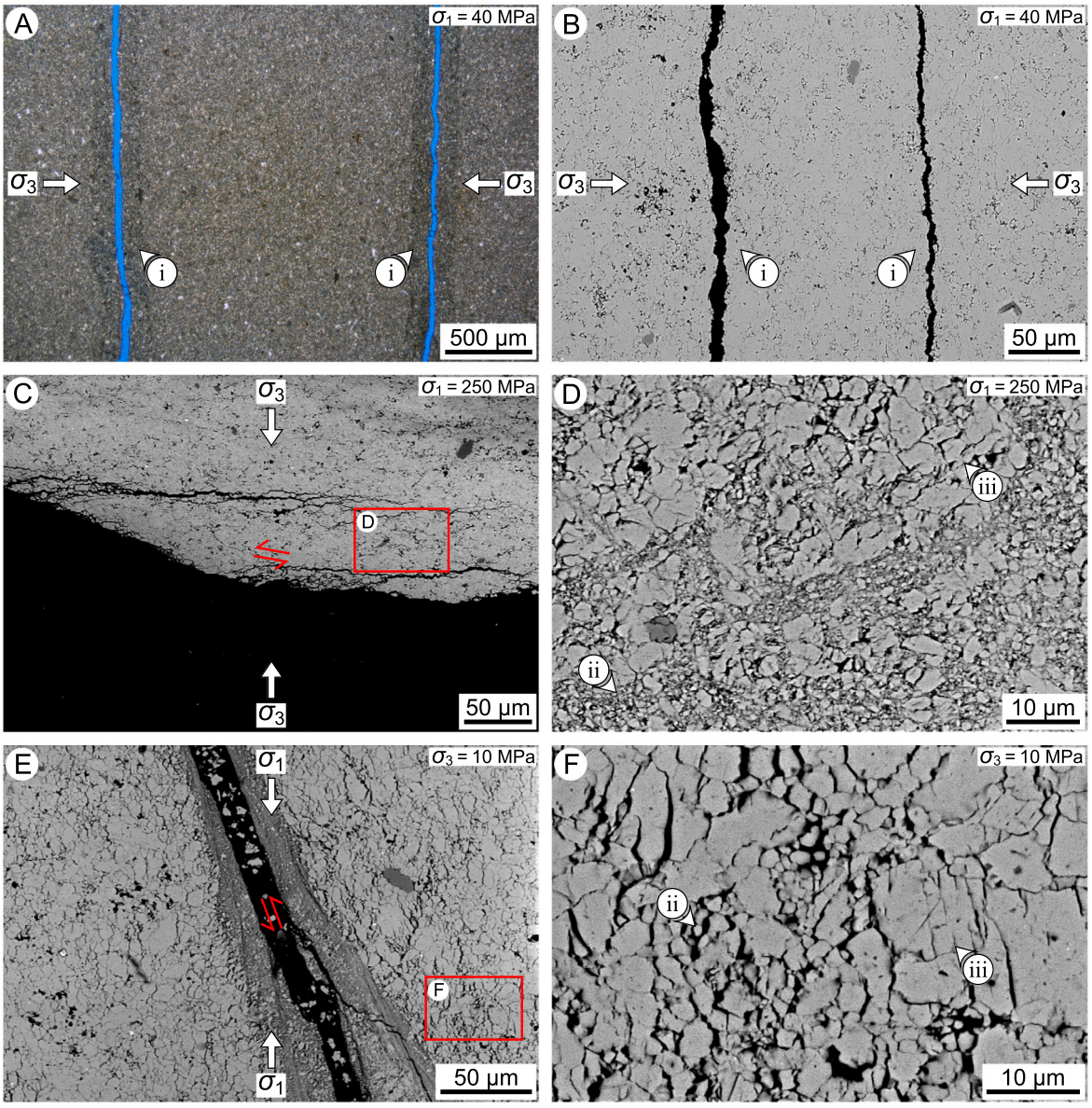

Fig. 7. (A) Transmitted light photomicrograph in plane-polarized light and (B) back-scattered electron photomicrograph showing the grain boundaries and long tensile failure cracks in Solnhofen limestone (sample ID = SL_E04). Note that (i) there are no grain-scale cracks that are adjacent to the macroscopic crack. (C, D) Back-scattered electron photomicrographs showing shear failure in axisymmetric extension in Solnhofen limestone (sample ID = SL_E13). (E, F) Back-scattered electron photomicrographs showing shear failure in axisymmetric shortening in Solnhofen limestone (sample ID = SL_S07). Note the (ii) grain-scale tensile cracks and (iii) comminuted grains.

tips (Fig. 8F). Smaller, nascent cracks (i.e., wing cracks) have formed at the margins of these larger tensile cracks and are typically inclined at a similar angle as the risers of the stepped macroscopic failure surface (Fig. 8F).

Based on their petrographical characteristics, it is unfeasible to distinguish samples that were deformed in the upper part of the tensile failure regime from those that were deformed in the lower part of a theoretical "hybrid failure" regime. Similarly, it is unfeasible to differentiate samples that were deformed in the upper part of this "hybrid failure" regime from those that were deformed in the lower part of the shear failure regime.

6. Interpretation of the experimental data

6.1. Compatibility of tests in axisymmetric extension versus axisymmetric shortening

Fig. 5 shows the results of experiments performed under axisymmetric extension and shortening. These are the end-members of polyaxial deformation, with $\sigma_1 = \sigma_2 > \sigma_3$ in extension and $\sigma_1 > \sigma_2 = \sigma_3$ in shortening. It is widely considered that σ_1 and σ_3 are the main controls on brittle failure, but σ_2 also affects the mean ($(\sigma_1 + \sigma_2 + \sigma_3)/3$) and differential stress at failure, as well as the failure surface angle (Handin

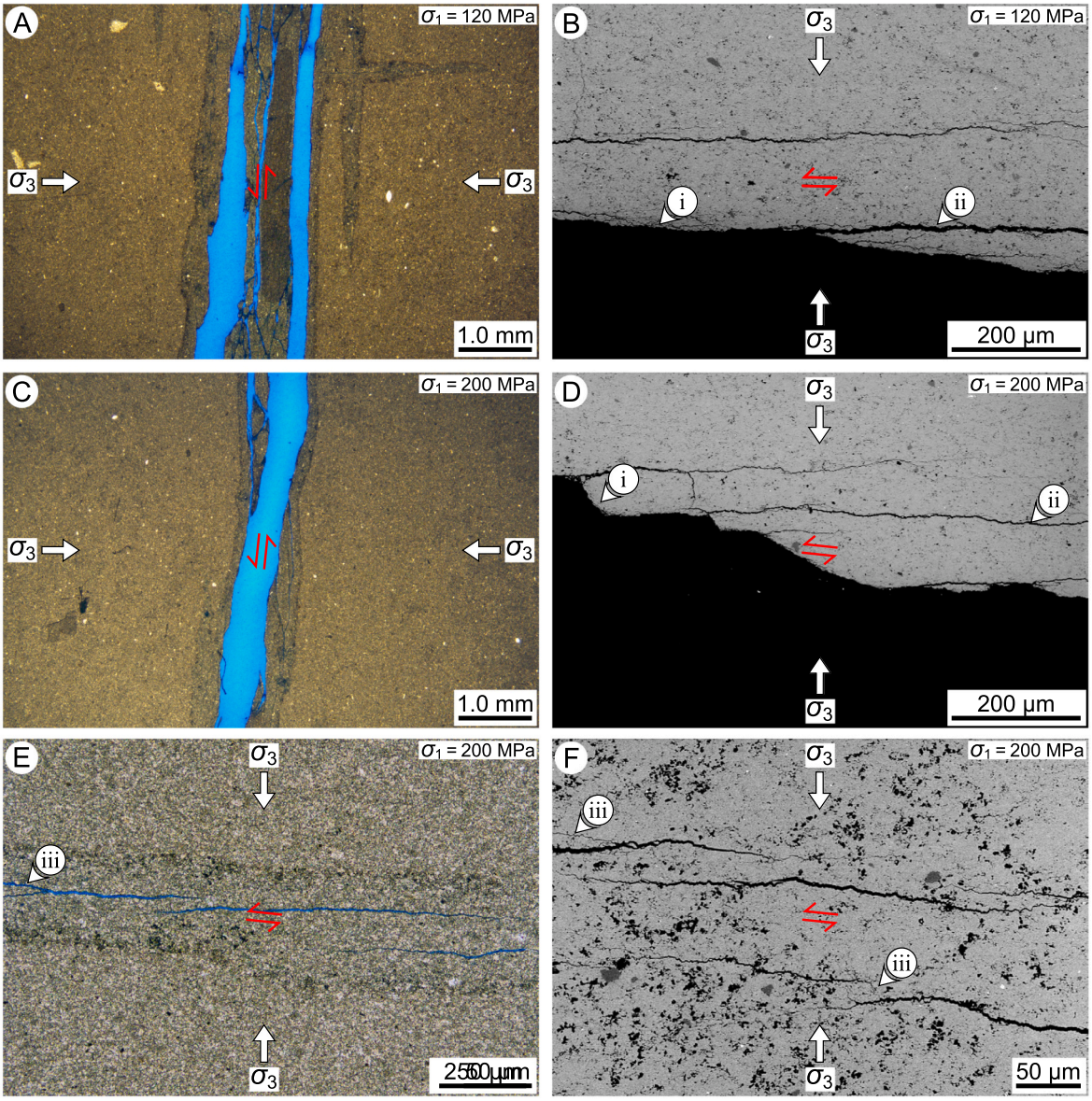

Fig. 8. (A, C) Transmitted light photomicrographs in plane-polarized light and (B, D) back-scattered electron photomicrographs showing the transitional region between tensile failure and shear failure in Solnhofen limestone (sample IDs = SL_E18 and SL_E08). Note the orientation of the (i) inclined failure surface between the (ii) transgranular tensile cracks. (E) Transmitted light photomicrograph in plane-polarized light and (F) back-scattered electron photomicrograph showing the nucleation of stepped cracks in Solnhofen limestone (sample ID = SL_E08). Note the (iii) nascent, inclined cracks at the margins of the transgranular tensile cracks (i.e., wing cracks) that probably imply incipient sliding along the extensional cracks.

et al., 1967; Colmenares and Zoback, 2002; Haimson and Rudnicki, 2010). Volume expansion, due to the creation and opening of microcracks, requires mechanical work to be done against the mean stress on the rock. It is therefore to be anticipated that higher values of σ_2, as well as of σ_3, will result in higher values of mean, and thus of differential stress at failure. For both CM and SL, the data at the axisymmetric extension and shortening end-members are, considering the limits of experimental error, contiguous (Fig. 5A, B). Consequently, no corrections to the data are necessary in this respect. Bobich (2005) found that the same was true for Berea sandstone.

Colmenares and Zoback (2002) examined data from Mogi (1967, 1971), Takahashi and Koide (1989), and Chang and Haimson (2000) for failure of several lithologies, across a range of true triaxial conditions, using seven different failure criteria (typically based on functions of stress invariants). For all lithologies, the main strengthening effect of σ_2 occurs when it lies approximately halfway between σ_1 and σ_3. For SL, however, only the Mogi (1971) criterion and the modified Lade criterion (Lade, 1977; Ewy, 1999) describe the mechanical behaviour fairly well across the range of stress conditions. The Mogi (1971) criterion also predicts no difference between the strengths at the axisymmetric extension and shortening end-members, such as is observed in our data (Fig. 5A, B). To demonstrate the expected strengthening for intermediate values of σ_2, Fig. 9 shows the application of the Mogi (1971) criterion to our experiments on SL and CM. Critically, the application of the Mogi (1971) criterion facilitates the prediction of polyaxial behaviour, while also satisfying the empirical constraint that the differential stress is the same at both the axisymmetric shortening and axisymmetric extension ends of the curves for constant values of σ_3 (Fig. 9C, D).

Mogi (1971) proposed that the octahedral shear stress (τ_{oct}) at failure is a function of the mean of the maximum and minimum principal stresses ($\sigma_{m,2} = (\sigma_1 + \sigma_3)/2$). The function can be linear, a power function, or a polynomial. The justification for using $\sigma_{m,2}$ rather than $\sigma_{m,3}$ ($(\sigma_1 + \sigma_2 + \sigma_3)/3$) is that the failure plane is expected to contain the σ_2 axis, hence the mean stress should be independent of σ_2. Thus, the

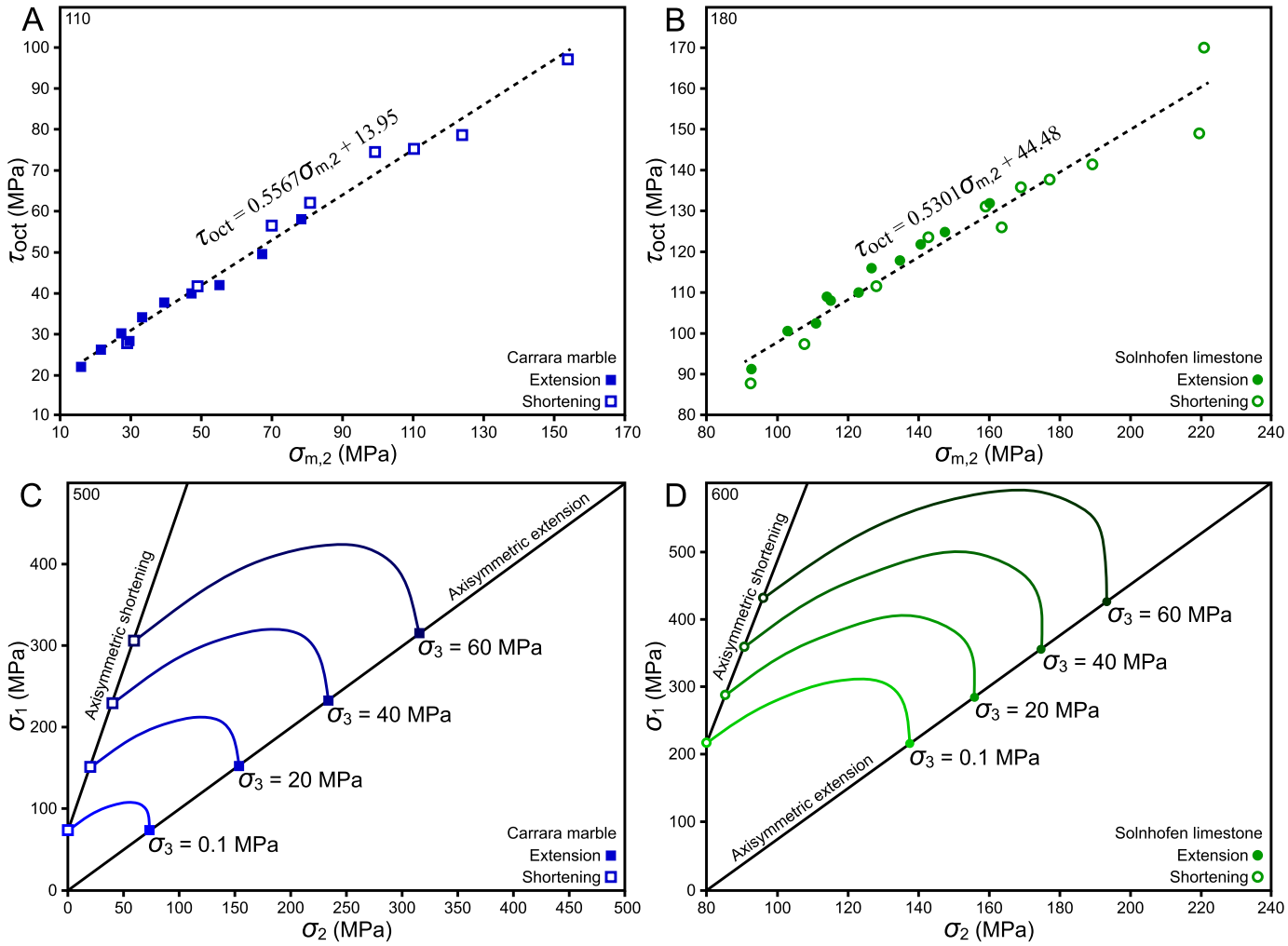

Fig. 9. Application of the Mogi (1971) criterion to our data on (A) Carrara marble ($n = 18$) and (B) Solnhofen limestone ($n = 22$). (C, D) Such a criterion allows polyaxial behaviour to be predicted by using axisymmetric extension and shortening data to plot σ_1 versus σ_2 for a series of constant values of σ_3. Note that the fits do not include data from the low-pressure parabolic part of the failure envelope, and they do not include data from the highest confining pressures, where intracrystalline plasticity and deformation twinning are significant.

Mogi (1971) polyaxial criterion is given by:

$$\tau_{oct} = \frac{1}{3}\sqrt{(\sigma_1 - \sigma_2)^2 + (\sigma_2 - \sigma_3)^2 + (\sigma_3 - \sigma_1)^2} = f(\sigma_{m,2}) \quad (6)$$

The octahedral shear stress is related to the second stress invariant (J_2) by:

$$\tau_{oct} = \sqrt{\frac{2J_2}{3}} \quad (7)$$

Assuming a linear form for $f(\sigma_{m,2})$, the criterion becomes:

$$\tau_{oct} = m\frac{(\sigma_1 + \sigma_3)}{2} + b \quad (8)$$

where m and b are empirical coefficients obtained by plotting experimental data (Fig. 9A, B).

6.2. Fitting a function to shear stress versus normal stress on the failure surface

The maximum values of resolved normal stress (σ_n) and shear stress (τ) on the observed failure surfaces from each experiment, calculated using Eqs. (2) and (3), are summarized in Table 2. For each lithology, a parabola provides an ideal fit to the data (Fig. 10A, B). For CM and SL, the least-squares best fit parabolic functions plotted in Fig. 10A and B are:

$$\sigma_n = 0.0144\tau^2 - 2.9 \quad (9)$$

for Carrara marble, and:

$$\sigma_n = 0.0085\tau^2 - 0.8 \quad (10)$$

for Solnhofen limestone. For CM, the standard errors in σ_n and τ are 6.8 and 6.2 MPa, whereas they are 3.1 and 5.5 MPa for SL (Fig. 10A, B). The tensile strengths (T) are not well constrained by the curve fitting because the uncertainties of the measured values of T are commensurate with the values themselves. The values of T depend on the difference between two similarly sized numbers, the applied confining pressure and the measured differential stress. Thus, the values of T used to constrain the curve fitting were taken to be −2.9 MPa ($n = 2$; Table 2) and − 0.8 MPa ($n = 10$; Table 2) for CM and SL, respectively. These are the averages of the measured values for the samples that were deformed at the lowest of confining pressures, and that underwent tensile failure. According to the above measurements, the apparent T of CM is greater than that of SL. This is to be expected because the greater brittleness of the latter implies a lower fracture toughness (K_{1c}). Xu et al. (2018), following Zhang (2002), compared tensile strength with fracture toughness for a wide

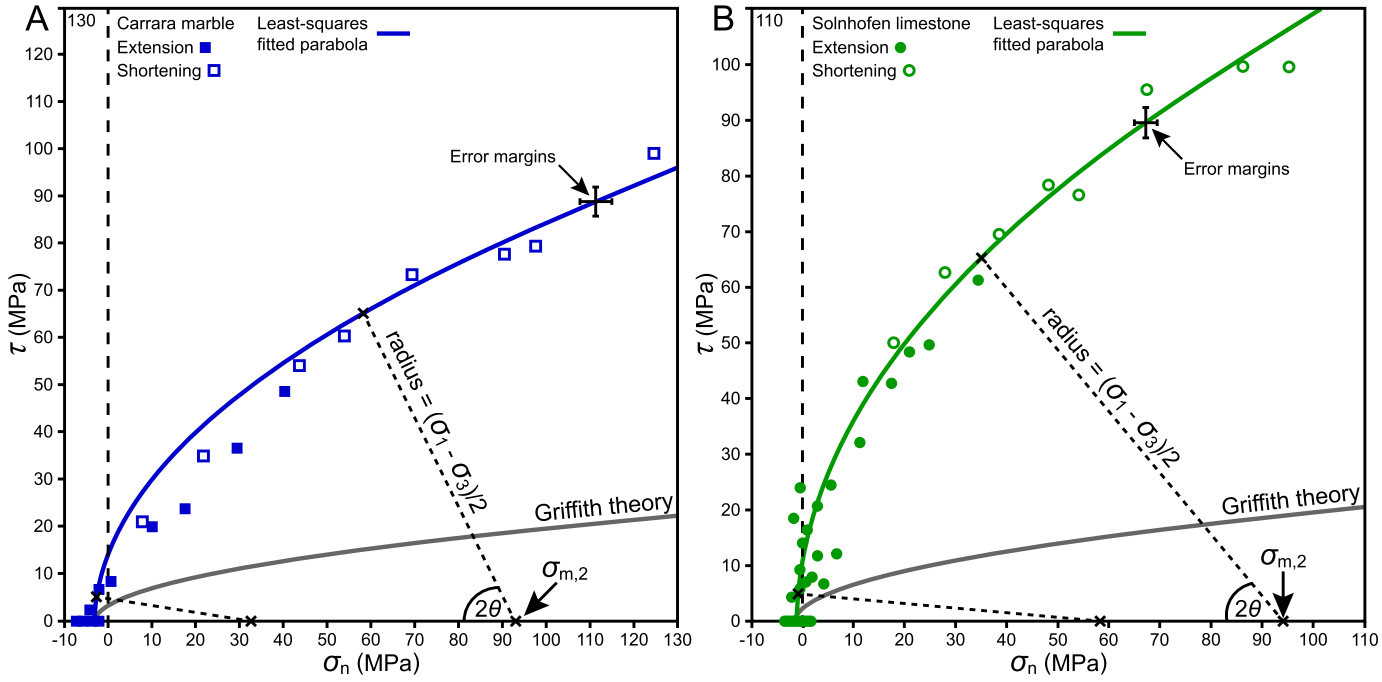

Fig. 10. Least-squares fitted parabolas for the experimental results on (A) Carrara marble (Eq. (9)) and (B) Solnhofen limestone (Eq. (10)) plotted in the τ versus σ_n coordinate frame (Mohr diagrams). Note that the mechanical strengths of both lithologies are considerably higher than predicted by the Griffith (1921) failure criterion for the observed tensile strengths. The radii of Mohr circles (dashed lines) are to illustrate how the circles that are tangents to the parabolic fitted curves correspond to failure surface angles θ, according to the "classical" Mohr-Coulomb theory outlined in Section 2, and hence how θ is observed to increase with increasing σ_n.

range of rock types and concluded that tensile strength increases linearly with fracture toughness, albeit with a wide scatter. Spagnoli et al. (2015) report K_{1c} for CM to be 1.3 MPa$\sqrt{m}$ and Atkinson (1984) reports K_{1c} for SL to be 0.8 MPa$\sqrt{m}$. However, Yang et al. (2021) found that K_{ic} is indistinguishable between CM and SL (at 0.8 MPa$\sqrt{m}$), within experimental error.

The classical application of the Mohr analysis can involve two different approaches to obtain a Mohr failure criterion from a suite of experimental data. The first method involves fitting a function to the values of σ_n and τ on the observed failure surfaces, calculated from the measured values of σ_1, σ_3, and θ; as has been done above. At any given value of σ_n and τ, the expected failure surface angle (θ), and values of the mean stress ($\sigma_{m,2}$), σ_1, and σ_3 can be calculated from a line that is normal to the best-fit parabola (radius of the Mohr circle at that point; Fig. 10A, B). The radii of these circles intersect the parabola at tangent points that are given by Eqs. (11) and (12) for CM and SL, respectively:

$$\frac{d\sigma_n}{d\tau} = 0.0288\tau = tan2\alpha \tag{11}$$

$$\frac{d\sigma_n}{d\tau} = 0.0170\tau = tan2\alpha \tag{12}$$

where α is the orientation of the failure surface relative to the observed (σ_n, τ), assuming that the Mohr circle is precisely tangent to the parabola. In this case $\alpha = \theta$. For CM and SL, the measured values of θ are compared to the back-calculated angle α in Fig. 11. For CM, $\alpha = 0.93\theta$, but for SL $\alpha = 1.60\theta$ (Fig. 11A, B, C). The difference between α and θ is probably insignificant for CM, within the limits of experimental error, but it is substantial in the case of SL. Thus, the Mohr circles that are based on the observed differential stresses for SL lie beyond the Mohr failure criterion that was calculated from the observed failure angles, and the Mohr envelope to these circles will lie above the above parabola from Eq. (10) (Fig. 11C).

6.3. Fitting an envelope to a series of Mohr circles

The second approach to the Mohr analysis and the description of failure involves fitting an enveloping curve, in this case a different parabola, to the tangents to a series of Mohr circles drawn using the measured values of σ_1 and σ_3 (e.g., Lisle and Strom, 1982; Bland, 1983). The enveloping curve is expected to have the same tensile strength intercept ($-T$) on the σ_n axis, but the previous parabola (Eqs. (9)–(10)) will intersect any Mohr circle (defined by the measured values σ_1 and σ_3) in two points (Fig. 11B, C). Writing these equations in general terms, $\sigma_n = a\tau^2 + b$, where parameter b equals the tensile strength intercept. Decreasing the parameter a by a multiplier n to become $a' = an$, which expands the parabola vertically, will cause the two intercepts of the circle on the parabola to move together. The two intercepts become one at the point (σ_n, τ), when the circle is tangent to the parabola, and the condition for one intercept is given by:

$$\left(2a'\sigma_{m,2} - 1\right)^2 = 4a'^2r^2 + 4a'b \tag{13}$$

where r is the radius of the Mohr circle. The two roots of this equation (a') are equal and of opposite sign, and they correspond to the two arms of the parabola, reflected across $\tau = 0$.

A single parabolic Mohr envelope will not lie precisely as tangent to all of the Mohr circles, which are defined by the values of σ_1 and σ_3 from the experimental data. A best fit parabola must be found. This can be done by calculating the tangent point coordinates to a parabola for each Mohr circle, then carrying out a least-squares analysis to obtain the best fit enveloping parabola to the entire set of Mohr circles, in the same way as was done in Section 6.2. The coordinates of the points (σ_n, τ) to be fitted to this parabolic envelope are given by:

$$\sigma_n = \sqrt{\frac{(\sigma_1 + \sigma_3)}{2} - \left(\frac{1}{2}a'\right)} \tag{14}$$

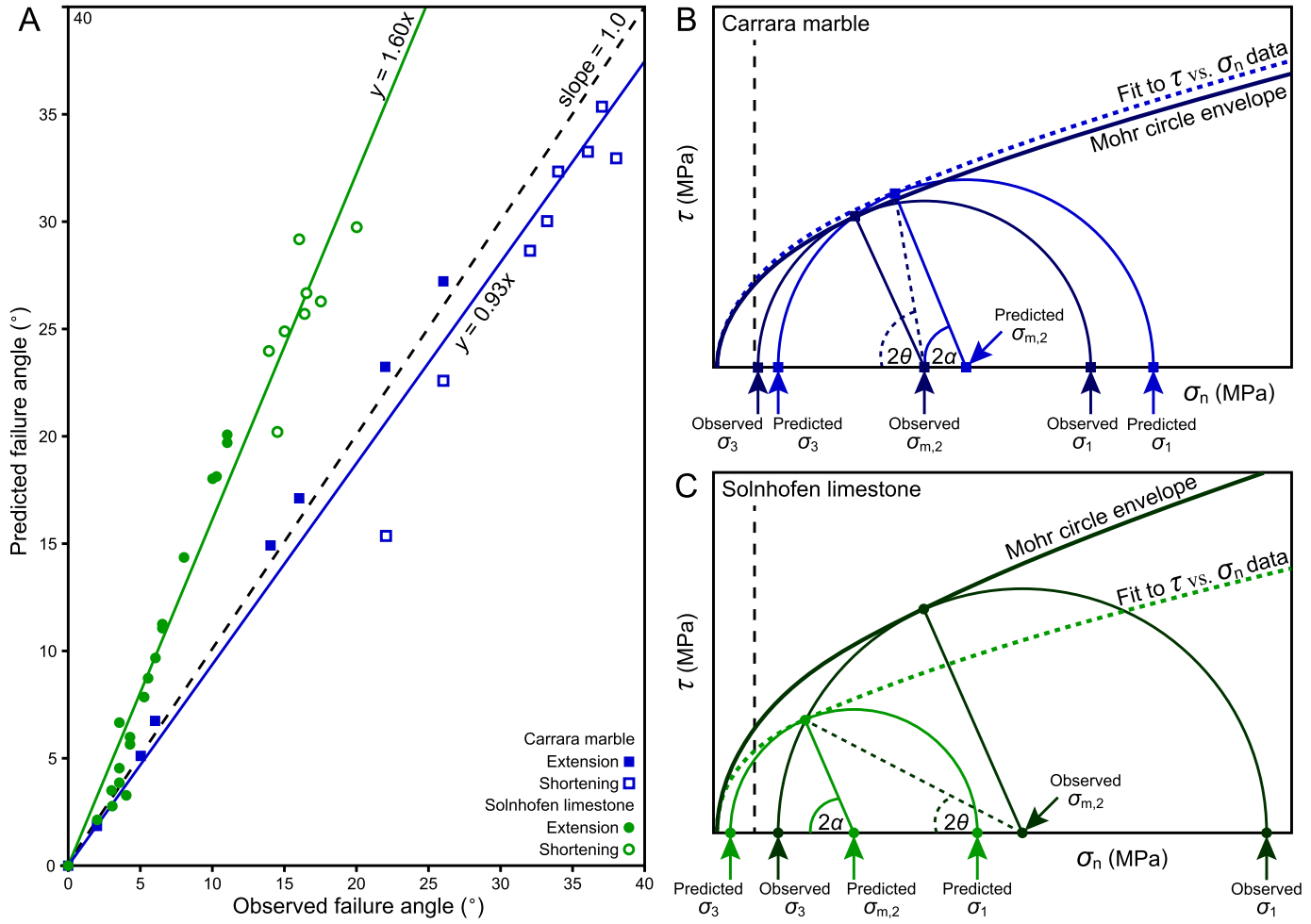

Fig. 11. (A) Relationship between the failure surface angles that are predicted from an envelope to a series of Mohr circles relative to the observed failure surface angles. (B, C) Conceptual diagrams showing the two different methods to obtain Mohr envelopes from the suite of experimental data on Carrara marble and Solnhofen limestone, respectively.

$$\tau = \sqrt{(\sigma_1 - \sigma_3)^2 - \left(\frac{1}{2}a'\right)^2} \tag{15}$$

Thus, the parabolas that best describe the envelopes to the Mohr circles are given by:

$$\sigma_n = 0.0145\tau^2 - 2.9 \tag{16}$$

$$\sigma_n = 0.0064\tau^2 - 0.8 \tag{17}$$

for CM and SL, respectively. For CM, there is no significant difference between the parabola that describes failure in terms of the resolved σ_n and τ on the observed failure surfaces and the parabola that is an envelope to a series of Mohr circles (Fig. 11B). There is also no significant difference between the two parabolas after transformation to the σ_1 versus σ_3 coordinate frame (Fig. 12B). For SL however, the difference between the two parabolas is pronounced in the τ versus σ_n coordinate frame (Fig. 12A) and when they are transformed into σ_1 versus σ_3 and compared with the experimental data (Fig. 12C). For CM, the standard errors in σ_3 and σ_1 are 3.5 and 12.9 MPa, whereas they are 3.7 and 14.4 MPa for SL (Fig. 12B, C).

6.4. Evolution of the failure surface angle with increasing differential stress

Following the Mohr-Coulomb model outlined in Section 2, the slope of the failure envelope in the positive stress quadrant is commonly assumed to be linear. The coefficient of internal friction (μ_c) is in this instance a constant value, and it implies that the deviatoric stress state (i.e., the relative value of the intermediate principal stress) is irrelevant. Therefore, the orientation of the localized shear failure surface (θ) is expected to be constant and given by:

$$\theta = \frac{\pi}{4} - \frac{1}{2}tan^{-1}\mu_c \tag{18}$$

In a plot of τ versus σ_n, the angle 2θ is subtended by a line that is normal to the failure envelope $f(\sigma_n, \tau)$ that intersects the abscissa at ($\sigma_{m,2}$, 0). Our experimental results for CM and SL show that the Mohr-Coulomb model is an inadequate descriptor because μ_c is not constant. For CM, however, the failure surface angle does appear to be related to the local orientation of the normal to the parabolic failure envelope (Fig. 10A, 11A, B).

Following the Rudnicki and Rice (1975) analysis of the failure of dilatant materials using bifurcation theory, Rudnicki and Olsson (1998) investigated the controls on the localization of deformation into shear bands. For the orientation of failure surfaces with respect to the direction of maximum principal stress, Rudnicki and Olsson (1998) suggested that:

$$\theta = \frac{\pi}{4} - \frac{1}{2}sin^{-1}\alpha \tag{19}$$

where

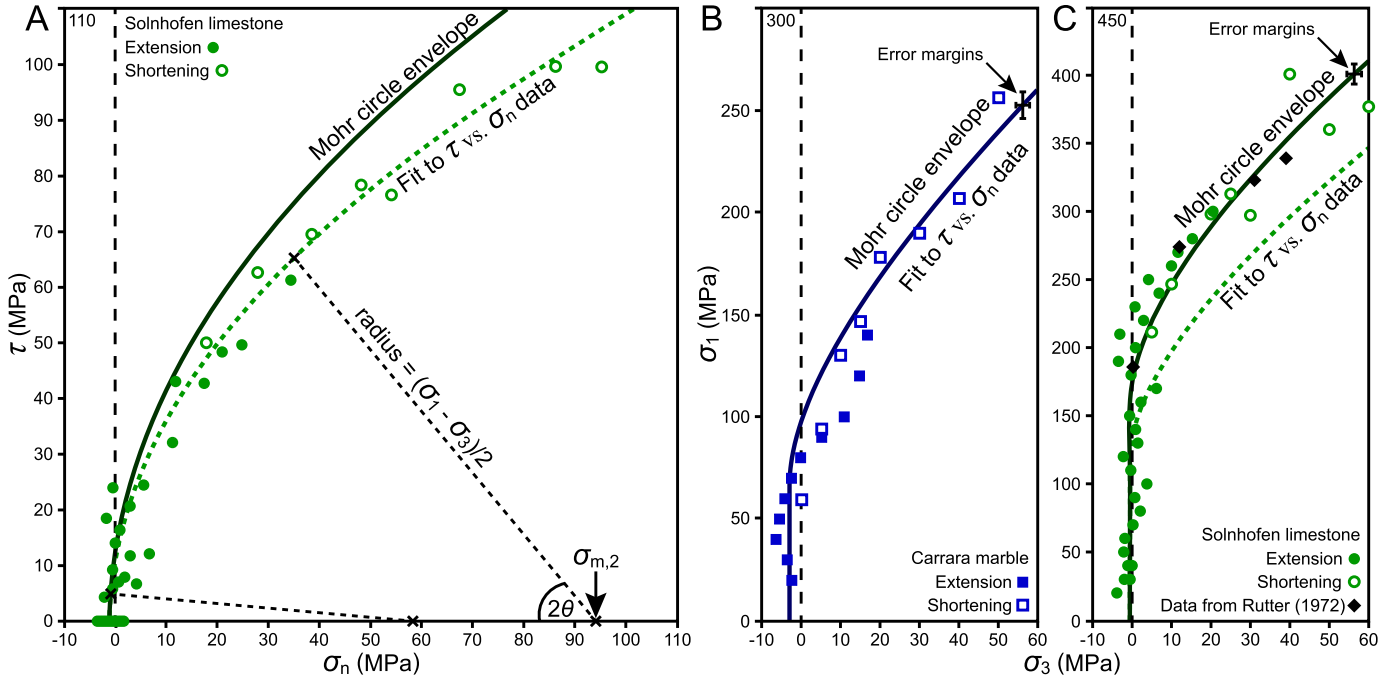

Fig. 12. (A) Relationship between the two types of Mohr envelopes for Solnhofen limestone (for Carrara marble there is negligible difference between the two parabolas). (B, C) Relationships between the plots of the observed σ_1 versus σ_3 data and the corresponding curves arising from the two types of parabolic Mohr envelopes for Carrara marble and Solnhofen limestone, respectively.

$$\alpha = \frac{\frac{2}{3}(1+\nu)(\beta+\mu) - N(1-2\nu)}{\sqrt{4-3N^2}} \tag{20}$$

in which ν is Poisson's ratio and β is the dilatancy angle. The dilatancy angle is given by the rate of change of volumetric strain with respect to the shear strain at the point of failure. In brittle rocks at low confining pressures, the volumetric strain is dilatant. The term μ is the local slope of the yield curve in a plot of von-Mises equivalent stress (σ_{vm}) against the mean stress ($\sigma_{m,3} = (\sigma_1 + \sigma_2 + \sigma_3)/3$), and the von-Mises equivalent stress (σ_{vm}) is given by:

$$\sigma_{vm} = \frac{1}{\sqrt{3}}\sqrt{\frac{(\sigma_1-\sigma_2)^2 + (\sigma_1-\sigma_3)^2 + (\sigma_2-\sigma_3)^2}{2}} \tag{21}$$

N describes the deviatoric stress state and is the ratio of the intermediate principal deviatoric stress to σ_{vm} ($N = (\sigma_2 - \sigma_{m,3})/\sigma_{vm}$). N ranges from $-1/\sqrt{3}$ in axisymmetric extension to $1/\sqrt{3}$ in shortening, and it is implied that failure surface angles are smaller in extension than in shortening. N is zero for deviatoric pure shear. Anisotropy, including preferentially-oriented microcracks, impacts the values of the above parameters at failure (Rudnicki, 1977). Planar crack arrays develop in axisymmetric extension, but in shortening they are oriented radially and intersect in the maximum compressive stress orientation. These differences between axisymmetric extension and shortening are not considered here, but constraints on the values of all the above listed parameters are discussed by Rudnicki and Olsson (1998).

The values of these parameters are rarely available from experimental studies, but see Haimson and Rudnicki (2010), Ingraham et al. (2013), and Ma et al. (2017) for siliciclastic rocks. Rybacki et al. (2021) and Edmond and Paterson (1972) provide volumetric strain data for CM and SL, respectively, but not to sufficient resolution for the purposes required. We can, however, examine semi-quantitatively how reasonable values predict the failure surface angles compared to those that were measured in this study. Von-Mises equivalent stresses were plotted against values of mean stress for both CM and SL (Fig. 13A, B). From their slopes, which decrease as the mean stress increases, a function $\mu = f$ (σ_n) is obtained. Next, the observed failure surface angles were plotted against the respective angles that were calculated using Eq. (19) (Fig. 13C, D). Estimated values for Poisson's ratio (ν) and dilatancy angle (β) were used to obtain a reasonable match to the observed fault angles. The dilatancy angle was first assumed be equal to the friction angle (ϕ), and then iteratively modified by a multiplier of 1.25×. Linking β to ϕ means that the former decreases with increasing mean stress, as is expected given that dilatancy is progressively suppressed by elevation of the mean pressure (Edmond and Paterson, 1972; Rybacki et al., 2021). Eq. (19) explains the observed trend that the failure surface angle increases with increasing mean pressure, and that the trend is continuous from axisymmetric extension to shortening (Fig. 13C, D). Accordingly, there appears to be no reason to believe that the orientation of the failure surface should be predictable simply from the local orientation of the normal to the Mohr failure envelope, as it also depends on other factors.

7. Discussion

7.1. Evolution of the failure surface angle with increasing differential stress

For both CM and SL, a progressive increase of the failure surface angle with increasing differential stress was observed to occur. For CM the observed variation was in accordance with the normal to the envelope of Mohr circles, but this was not the case for SL, for which observed failure angles were consistently smaller than predicted. Studies by other authors, mainly on siliciclastic rocks, have demonstrated variations in failure surface angles with differential stress also occur. Back-analysis of the data of Ma et al. (2017) for Coconino sandstone shows that the behaviour is very similar to that of our results for CM. Our SL data also show that the failure surface angles evolve markedly with the differential stress at failure, but the resolved σ_n and τ on the failure surfaces for SL are systematically much less than at the tangent point of each Mohr circle with the envelope of those circles (Fig. 11A, C). The same applies to the SL (1.5% porosity) data that was reported by Heard (1960)

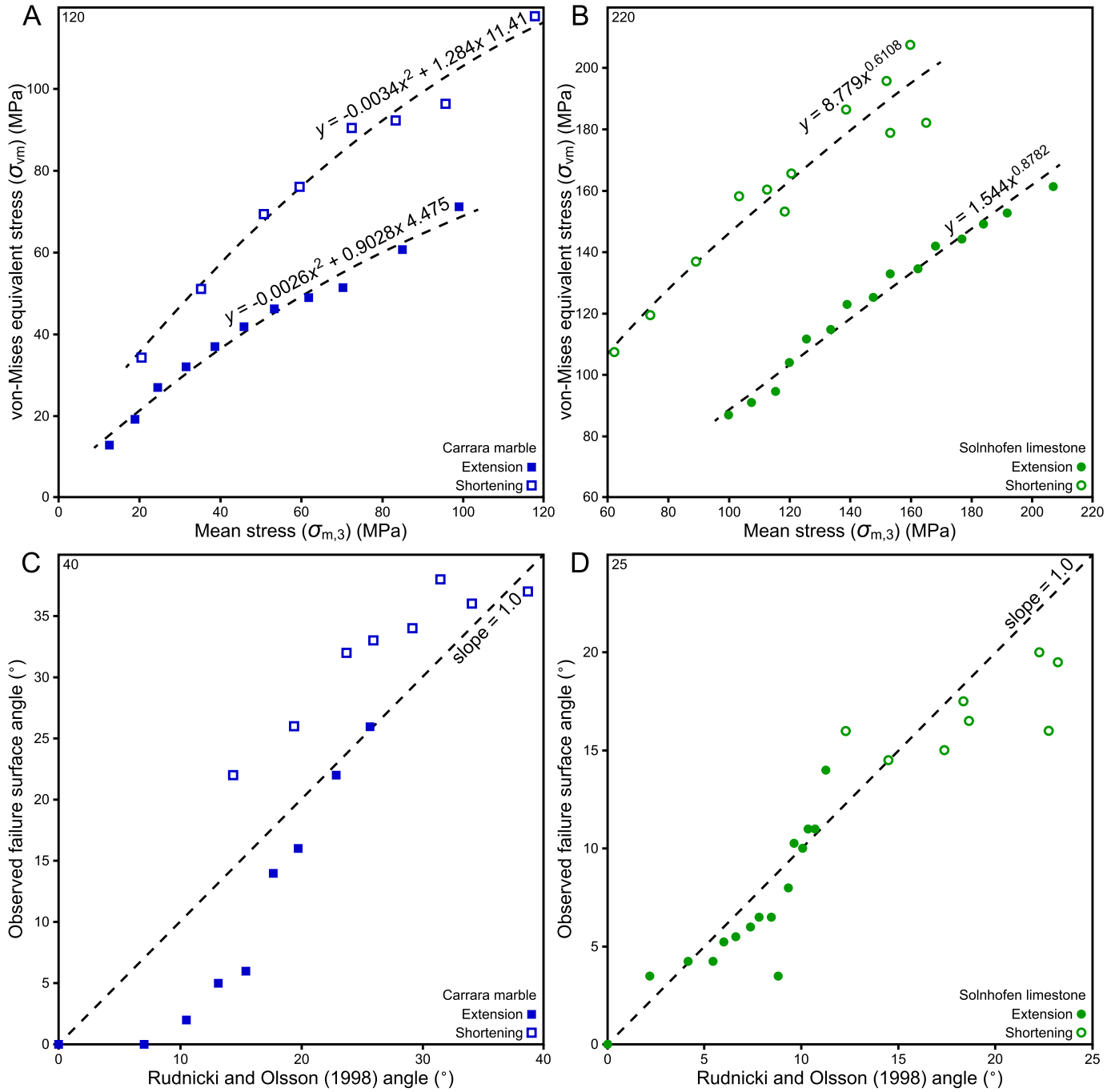

Fig. 13. (A) von-Mises equivalent stress (σ_{vm}) versus mean stress ($\sigma_{m,3}$) for Carrara marble and (B) Solnhofen limestone. From their slopes, the predicted failure surface angles calculated from Eq. (19) (Rudnicki and Olsson, 1998) were plotted against the observed failure surface angles for (C) Carrara marble and (D) Solnhofen limestone.

and to two siltstone samples from the Taiwan Chelungpu Fault Drilling Project (Haimson and Rudnicki, 2010). Similarly, Dansereau et al. (2019) carried out numerical simulations of damage accumulation in a theoretical elasto-damageable material that predicted faults can occur along orientations that are different from the Mohr-Coulomb maximum stress prediction. Their results are congruent with previous works by Girard et al. (2010), Kaus (2010), and Finzi et al. (2013). Thus, while the Mohr envelope is a widely used criterion for failure and the prediction of failure surface orientation, it does not always accurately predict the latter.

Upon failure, lithologies that had high initial porosities commonly exhibit a range of banded failure localizations, including dilation, shear, and compaction bands, whose geometry is controlled by the dilatancy angle and the coefficient of internal friction (Issen and Rudnicki, 2000; Du Bernard et al., 2002). Although dilation bands typically form in planes that are normal to σ_3 (Du Bernard et al., 2002), these structural features are not analogous to the opening-mode brittle fractures reported in CM and SL, which have much lower porosities.

7.2. Evolution of the failure mechanism with increasing differential stress

Although the empirical Mohr-Coulomb criterion provides a first-order approximation of the stress conditions that give rise to failure and the general failure mode, the mechanistic sequence by which tensile

microcracking transitions into mesoscopic shear faulting is equivocal. Thus, a "hybrid failure" mode has long been hypothesized as a transitional regime between the end-members failure modes and their respective criteria (Brace, 1964; Hancock, 1985; Engelder, 1999; Ramsey and Chester, 2004). According to Hancock (1985), this transitional failure mode occurs from 4 $T < \sigma_1 - \sigma_3 < 8\ T$; a range commonly repeated in more recent works (Ferrill et al., 2012, 2017). Our experiments on CM and SL demonstrate that the transition from tensile failure to shear failure occurs at a much higher differential stress than previously suggested. Based on the fitted parabola for CM ($T = -2.9$ MPa), the differential stress at failure when $\sigma_n = 0$ is 75.0 MPa, thus $\sigma_1 - \sigma_3 = 25.9\ T$ (Fig. 10A). Based on the parabola for SL ($T = -0.8$ MPa), the differential stress at failure when $\sigma_n = 0$ is 119.1 MPa, thus $\sigma_1 - \sigma_3 = 148.9\ T$ (Fig. 10B). Attributing a definitive range of stress conditions to a "hybrid failure" mode, however, is imprecise because our mechanical and petrographical data suggests that the transitions between failure modes are part of a continuous spectrum. There is neither a single experiment that defines the boundary between tensile failure and a theoretical "hybrid failure" mode, nor is there an experiment that defines the boundary between "hybrid failure" and shear failure. There are also clear lithological controls on characteristics of the failure surface that are not captured by variations in T.

The first experiments investigating the transition from tensile failure to shear failure are those of Brace (1964), but poor experimental reproducibility led Ramsey and Chester (2004) to improve the Brace (1964) sample and jacketing arrangement. Next, Rodriguez (2005) examined the microstructure of the CM samples from Ramsey and Chester (2004), and Bobich (2005) investigated this region of the failure envelope in Berea sandstone. Such works attempted to extrapolate a Griffith-type failure envelope into the tensile field but found that the observed failure surface angles were systematically less than predicted and the mechanical strengths of CM and Berea sandstone were not consistent with a description based on Griffith theory (Ramsey and Chester, 2004; Bobich, 2005). Although Ramsey and Chester (2004) did not propose a revised criterion, they noted that a continuous, parabolic failure envelope was not an ideal fit to their σ_1 versus σ_3 data. In the τ versus σ_n coordinate frame, however, back-analysis of the Ramsey and Chester (2004) data for CM shows that the behaviour is largely analogous to our results. More recent experimental results (Cen and Huang, 2017; Lan et al., 2019; Huang et al., 2022) and numerical modelling studies (Zhu, 2017; Huang and Zhu, 2018; Boyce et al., 2020) expanded on the work by Ramsey and Chester (2004) in attempt to propose a new failure criterion. Each of these studies noted that there is smooth and continuous transition between tensile failure and shear failure, but a "hybrid failure" mode was arbitrarily, and somewhat inconsistently placed between these end-members. A failure criterion based on a single parabolic function, as is applied here, (i) justifies a smooth transition between failure modes and (ii) can be scaled based on material properties of different lithologies.

Stepped (en-echelon) opening-mode crack arrays have been widely noted to play a role in the transition from tensile failure to shear failure (Engelder, 1999; Ramsey and Chester, 2004; Cen and Huang, 2017), but the failure criteria that are applied and described are typically not rooted in such microstructural observations. Our observations note that tensile failure involves the formation of one or more, discrete, sample-traversing tensile cracks, whereas shear failure involves the formation of numerous, grain-scale tensile cracks that coalesce into a shear-mode fault. A smooth and continuous transition between these end-member failure modes is facilitated by a gradual change in the lengths, spacing, and apertures of the precursory tensile cracks, illustrated schematically in Fig. 14. Failure in this transitional region involves the formation of several transgranular, tensile cracks that coalesce into a shear-mode fault. As the confining pressure and differential stress at failure increases, the lengths and spacing of these transgranular cracks gradually become shorter as the failure surface angle increases (Fig. 14). The most pronounced differences between the two lithologies that were

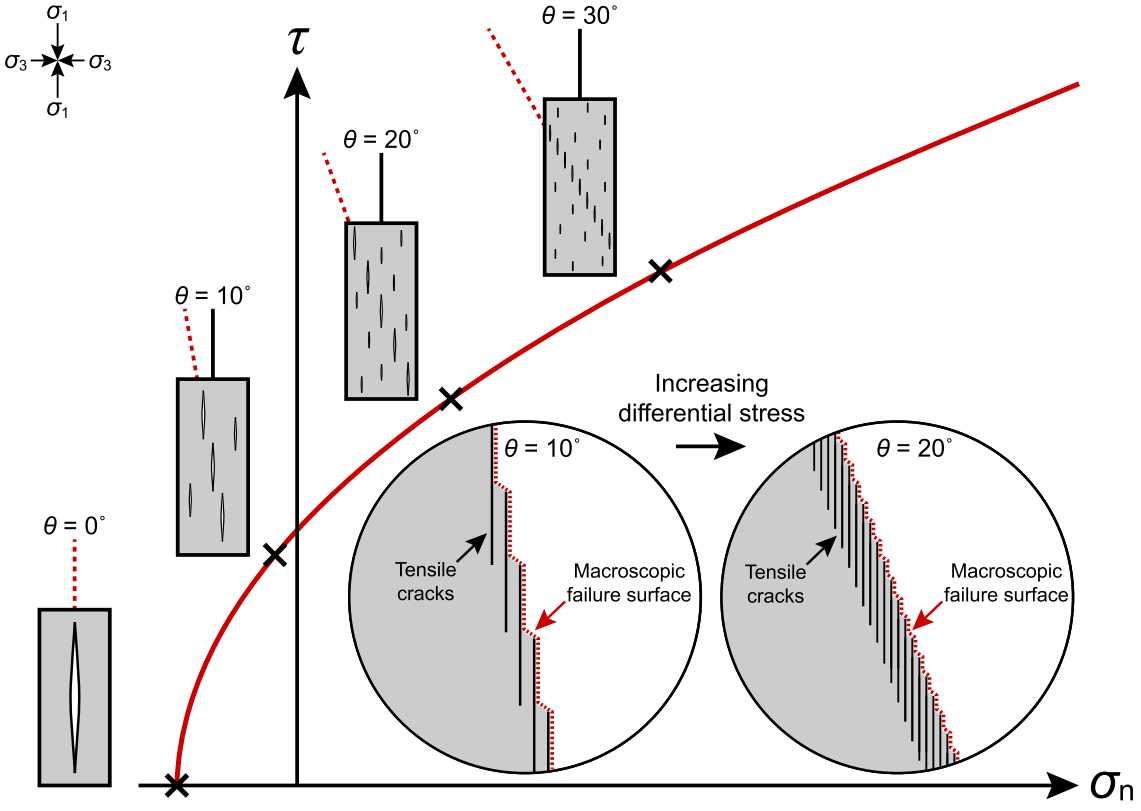

Fig. 14. Conceptual diagram showing the relative frequency of transgranular and grain-scale tensile cracks spanning the transitional region from true tensile failure to shear failure. Note the observed trend that the lengths, spacing, and apertures of the precursory tensile cracks decrease with increasing differential stress.

investigated in this study is that CM is slightly stronger than SL in tensile failure, but SL is stronger than CM in shear failure. Even at the lowest confining pressures, such differences between their mechanical strengths are largely attributed to the pronounced grain size differences and the fact that CM is much more ductile than SL (Schmid et al., 1977; Rutter et al., 1994, 2022; Rybacki et al., 2021). In tensile failure, it requires a larger magnitude of σ_3 (more negative) to nucleate and propagate cracks in CM relative to the more brittle SL. With increasing confining pressure, ductile deformation mechanisms (e.g., intracrystalline twinning, dislocation glide, distributed cataclastic flow) contribute to failure in CM at lower confining pressures relative to SL.

7.3. Irregularities in the form of the failure envelope when σ_3 is tensile

Huang et al. (2022) investigated the mechanical behaviour of a granite (from Hubei, China) and recognized a phase of negative deflection where the σ_3 decreases with increasing confining pressure in the tensile failure regime, reaches a maximum negative value, then increases as the confining pressure increases in shear failure. Such a distinct negative deflection was noted for CM (Ramsey and Chester, 2004) and our data for CM also show the same effect in the σ_1 versus σ_3 coordinate frame (Fig. 5A, 12B). Such a phenomenon, however, is not present in our data for SL (Fig. 5B, 12C). The effect seems to be relatively minor for more brittle lithologies, including Berea sandstone (Bobich, 2005), Longmaxi shale (Lan et al., 2019), and Hubei granite (Huang et al., 2022). Huang et al. (2022) attributed this phenomenon to variation in the frictional force between grains and in the shear stress between the grains as the failure surface angle increases. These factors are impacted by grain size and shape, porosity, and the ductility of the rock. Clearly, increasing the differential stress also increases the mean stress, which in turn increases the frictional forces and inhibits loss of cohesion between the grains. Such a phenomenon would likely be manifested as an increased resistance to the formation of the precursory tensile cracks with increasing differential stress and mean stress.

It should be noted that the negative deflection observed in the σ_1 versus σ_3 coordinate frame is less apparent when the data are transformed into the τ versus σ_n coordinate frame. This occurs due to the corresponding increase in the failure surface angle (θ), which implies that there is an increase in the inter-granular frictional forces. In a similar way to our results on CM and SL, back-analysis of the experiments on CM (Ramsey and Chester, 2004), Berea sandstone (Bobich, 2005), Longmaxi shale (Lan et al., 2019), and Hubei granite (Huang et al., 2022) suggests that a parabolic failure envelope in the τ versus σ_n coordinate frame describes their mechanical behaviour fairly well across the range of stress conditions investigated.

7.4. Influence of boundary conditions on failure

Experimental studies of rock failure are most frequently carried out under conditions of lateral confinement by a hydraulic fluid (stress boundary conditions), thus there is no constraint on lateral displacements. Brittle failure under such loading conditions typically involves the formation of a single tensile crack or shear fault. In nature however, a rock at depth is constrained by an elastic solid in all directions. Together with the effects of polyaxial loading, this can lead to a greater variety of failure geometries, including polymodal faulting, to satisfy the displacement boundary conditions (Reches and Dieterich, 1983; Healy et al., 2015; Reches and Wetzler, 2022). As a result, natural examples of "hybrid failure" are rare and evidence for this mode of failure in the field can be somewhat ambiguous (Engelder, 1999; Blenkinsop et al., 2020). Ferrill and Morris (2003), for example, documented shear-mode faults in mechanically layered strata where the failure surface angles of the faults in less competent units (10 to 39°) were significantly larger than in more competent units (1 to 9°). Other potential candidates include pinnate joints and en-echelon fractures that are associated with shear-mode faults, as well as veins with oblique crystal growth orientations (Engelder, 1999; Belayneh and Cosgrove, 2010; Bons et al., 2012). Similarly, bedding-inclined zebra textures in fault-controlled dolomite bodies are potential natural examples of low-angle, "hybrid", shear-mode faulting (Vandeginste et al., 2005; McCormick et al., 2021). It is unclear however, whether these rock textures were initiated as such or if the mineralized fractures simply record their post-failure displacement. Such examples of mineralized fractures with oblique crystal growth orientations may involve slow, time-dependent processes and are not definitive evidence of a brittle failure mechanism (Price, 1966; Price and Cosgrove, 1990; Belayneh and Cosgrove, 2010; Bons et al., 2012).

Price (1966) paid particular attention to the occurrence of "semi-brittle" shear zones that, when occurring in conjugate pairs of opposite shear sense inferred to be bisected by the maximum principal stress direction, often subtend a low dihedral angle between them (10 to 20°). Such shear zones are often characterized by an array of dilatant, extensional mineral veins inferred to lie normal to σ_3. These occurrences can be interpreted to imply shear failure under conditions of low differential stress, potentially with a negative effective σ_3. At depths of a few kilometers to mid-crustal depths, the failure of brittle rock under such low differential stress conditions is likely only to occur if pore-fluid pressures are exceptionally high, close to the least principal stress (σ_3). Such elevated pore-fluid pressures may be produced by a combination of pore compaction, the influx of pressurized fluids expelled from greater depths (e.g., seismic pumping), or diagenetic to low-grade metamorphic dewatering.

8. Conclusions

Rock deformation experiments were carried out at room temperature (20 °C) on samples of Carrara marble (CM) and Solnhofen limestone (SL) using a rock deformation apparatus that is capable of loading under axisymmetric extension and shortening. This study aimed to investigate the transition from failure under true tensile loading conditions to compressive loading under high effective confining pressures (up to 300 MPa), while also observing the evolution of the peak strength, the orientation of the failure surfaces, and their microstructural characteristics. The results of 63 experiments, which were conducted at an axial strain rate of 2.1×10^{-4} s^{-1} in axisymmetric extension and 7.4×10^{-5} s^{-1} in axisymmetric shortening, are reported. The key conclusions of this study are as follows:

(1) At low differential stresses, and when σ_3 is tensile, failure results in the formation of one or more opening-mode cracks that are oriented normal to σ_3 and parallel to σ_1.
(2) At moderate differential stresses, as σ_3 shifts towards the compressive domain, failure involves the formation of several, transgranular tensile cracks that coalesce into a shear-mode fault; typically oriented at $<10°$ to σ_1.
(3) At high differential stresses, and when all the principal stresses are fully compressive, failure involves the formation of numerous, grain-scale tensile cracks that coalesce into a shear-mode fault, typically oriented in the range of 10 to 30° to σ_1 and with θ increasing as the differential stress increases.
(4) A continuous parabolic failure envelope, defined by the resolved shear stress and normal stress on the failure surfaces, fits the mechanical behaviours of both lithologies and such a function is rooted in the observation that the lengths, spacing, and apertures of the precursory tensile cracks decrease with increasing differential stress and mean stress.
(5) Furthermore, the failure surface angle with respect to σ_1 increases for both lithologies as the differential stress increases. Hence, the region often described as "hybrid" failure appears to be nothing other than part of the progressive evolution of the failure angles associated with a continuously curving Mohr failure description in the τ versus σ_n coordinate frame.

(6) The failure criterion can also be expressed in terms of an envelope of the Mohr circles at failure. For CM, this envelope coincides with the parabola defined by fitting a function to σ_n and τ. In the case of SL, the Mohr envelope parabola is much larger, and the failure surface angles are consistently smaller than those predicted by the "classical" Mohr envelope approach. This discrepancy accords with the application of bifurcation theory by Rudnicki and Olsson (1998) to the prediction of shear fault angles in brittle rocks.

Critically, the mechanical behaviours of CM and SL demonstrate that the transition from tensile failure to shear failure follows a smooth, parabolic failure envelope. This transition occurs when σ_3 at failure displays a marked shift towards, or into, the compressive domain, which is accompanied by the onset of inclination of the failure surface away from being parallel to σ_1 and the development of shear offset. A smooth, parabolic failure envelope is supported by microstructural observations of the number, lengths, and spacing of the precursory tensile cracks that contribute to failure. Whilst there is no evidence of a distinct "hybrid failure" mode, the low-angle shear-mode faults that are produced in this transitional region of the failure envelope may still be considered "hybrid faults" for descriptive purposes.

CRediT authorship contribution statement

Cole A. McCormick: Conceptualization, Methodology, Formal analysis, Investigation, Validation, Writing – original draft. **Ernest H. Rutter:** Conceptualization, Methodology, Software, Formal analysis, Investigation, Supervision, Writing – review & editing.

Declaration of Competing Interest

The authors declare that they have no known competing financial interests or personal relationships that could have appeared to influence the work reported in this paper.

Data availability

All of the data used for this research is described in the article.

Acknowledgements

This work was conducted as part of C.A. McCormick's doctoral research that was funded by the President's Doctoral Scholar Award (The University of Manchester). The authors acknowledge the Natural Environment Research Council funded Nanoscale Imaging and Analysis Facility for Environmental Materials in the Williamson Research Centre for Molecular Environmental Science, The University of Manchester (NERC CC042). We are indebted to Dr. John Waters (The University of Manchester) who conducted the XRD, and to Experimental Officer Lee Paul for equipment maintenance, the development of techniques, and general laboratory assistance. We are also grateful for the helpful discussions provided by Dr. Julian Mecklenburgh and Dr. Cathy Hollis on an earlier version of this manuscript. We are grateful for the careful reviews on an earlier version of this manuscript that were provided by Dr. Neelima Kandula and two anonymous reviewers, as well as for the comments from the Editor, Dr. Samuel Angiboust.

References

Atkinson, B.K., 1984. Subcritical crack growth in geological materials. J. Geophys. Res. Solid Earth 89 (B6), 4077–4114.
Belayneh, M., Cosgrove, J.W., 2010. Hybrid veins from the southern margin of the Bristol Channel Basin, UK. J. Struct. Geol. 32 (2), 192–201.
Bland, J.A., 1983. Fitting failure envelopes by the method of least squares. Q. J. Eng. Geol. 16 (2), 143–147.
Blenkinsop, T.G., Rowland, J.V., Baker, T., 2020. Mechanical regimes of hydrothermal gold mineralization. In: Rowland, J.V., Rhys, D.A. (Eds.), Applied Structural Geology of Ore-Forming Hydrothermal Systems, Reviews in Economic Geology, Society of Economic Geologists, pp. 205–214.
Bobich, J.K., 2005. Experimental Analysis of the Extension to Shear Fracture Transition in Berea Sandstone. Unpublished M.Sc. thesis. Texas A&M University, College Station, p. 52.
Bons, P.D., Elburg, M.A., Gomez-Rivas, E., 2012. A review of the formation of tectonic veins and their microstructures. J. Struct. Geol. 43, 33–62.
Boyce, S., Lei, Z., Euser, B., Knight, E.E., Rougier, E., Stormont, J.C., Reda Taha, M.M., 2020. Simulation of mixed-mode fracture using the combined finite-discrete element method. Comp. Part. Mech. 7 (5), 1047–1055.
Brace, W.F., 1960. An extension of the Griffith theory of fracture to rocks. J. Geophys. Res. 65 (10), 3477–3480.
Brace, W.F., 1964. Brittle fracture of rocks. In: Judd, W.R. (Ed.), State of Stress in Earth's Crust. Elsevier, New York, pp. 111–180.
Busetti, S., Jiao, W., Reches, Z.E., 2014. Geomechanics of hydraulic fracturing microseismicity: Part 1. Shear, hybrid, and tensile events. Am. Assoc. Pet. Geol. Bull. 98 (11), 2439–2457.
Cen, D., Huang, D., 2017. Direct shear tests of sandstone under constant normal tensile stress condition using a simple auxiliary device. Rock Mech. Rock. Eng. 50 (6), 1425–1438.
Chang, C., Haimson, B., 2000. True triaxial strength and deformability of the German Continental Deep Drilling Program (KTB) deep hole amphibolite. J. Geophys. Res. Solid Earth 105 (B8), 18999–19013.
Chang, C., Haimson, B., 2012. A failure criterion for rocks based on true triaxial testing. Rock Mech. Rock. Eng. 45 (6), 1007–1010.
Colmenares, L.B., Zoback, M.D., 2002. A statistical evaluation of intact rock failure criteria constrained by polyaxial test data for five different rocks. Int. J. Rock Mech. Min. Sci. 39 (6), 695–729.
Coviello, A., Lagioia, R., Nova, R., 2005. On the measurement of the tensile strength of soft rocks. Rock Mech. Rock. Eng. 38 (4), 251–273.
Dansereau, V., Démery, V., Berthier, E., Weiss, J., Ponson, L., 2019. Collective damage growth controls fault orientation in quasibrittle compressive failure. Phys. Rev. Lett. 122 (8), 085501.
de Raadt, W.S., Burlini, L., Kunze, K., Spiers, C.J., 2014. Effect of pre-existing crystallographic preferred orientation on the rheology of Carrara marble. J. Struct. Geol. 68, 44–57.
Du Bernard, X., Eichhubl, P., Aydin, A., 2002. Dilation bands: a new form of localized failure in granular media. Geophys. Res. Lett. 29 (24), 1–29.
Edmond, J.M., Paterson, M.S., 1972. Volume changes during the deformation of rocks at high pressures. Int. J. Rock Mech. Min. Sci. Geomech. Abstr. 9 (2), 161–182.
Engelder, T., 1999. Transitional-tensile fracture propagation: a status report. J. Struct. Geol. 21 (8–9), 1049–1055.
Ewy, R.T., 1999. Wellbore-stability predictions by use of a modified Lade criterion. SPE Drill. Complet. 14 (02), 85–91.
Feng, X.T., Zhang, X., Kong, R., Wang, G., 2016. A novel Mogi type true triaxial testing apparatus and its use to obtain complete stress-strain curves of hard rocks. Rock Mech. Rock. Eng. 49 (5), 1649–1662.
Ferrill, D.A., Morris, A.P., 2003. Dilational normal faults. J. Struct. Geol. 25 (2), 183–196.
Ferrill, D.A., McGinnis, R.N., Morris, A.P., Smart, K.J., 2012. Hybrid failure: field evidence and influence on fault refraction. J. Struct. Geol. 42, 140–150.
Ferrill, D.A., Morris, A.P., McGinnis, R.N., Smart, K.J., Wigginton, S.S., Hill, N.J., 2017. Mechanical stratigraphy and normal faulting. J. Struct. Geol. 94, 275–302.
Finzi, Y., Muhlhaus, H., Gross, L., Amirbekyan, A., 2013. Shear band formation in numerical simulations applying a continuum damage rheology model. Pure Appl. Geophys. 170 (1), 13–25.
French, M.E., Zhu, W., Xiao, X., Evans, B., Prior, D.J., 2022. Thermally enhanced water weakening of the Solnhofen Limestone. J. Geophys. Res. Solid Earth 127 (3), e2021JB022742.
Girard, L., Amitrano, D., Weiss, J., 2010. Failure as a critical phenomenon in a progressive damage model. J. Stat. Mech. Theory Exp. 2010 (01), P01013.
Griffith, A.A., 1921. The phenomena of rupture and flow in solids. Philosophical transactions of the royal society of London (Series A) 163–198.
Hackston, A., Rutter, E., 2016. The Mohr-Coulomb criterion for intact rock strength and friction-a re-evaluation and consideration of failure under polyaxial stresses. Solid Earth 7 (2), 493–508.
Haimson, B., Chang, C., 2000. A new true triaxial cell for testing mechanical properties of rock, and its use to determine rock strength and deformability of Westerly granite. Int. J. Rock Mech. Min. Sci. 37 (1–2), 285–296.
Haimson, B., Rudnicki, J.W., 2010. The effect of the intermediate principal stress on fault formation and fault angle in siltstone. J. Struct. Geol. 32 (11), 1701–1711.
Hancock, P.L., 1985. Brittle microtectonics: principles and practice. J. Struct. Geol. 7 (3–4), 437–457.
Handin, J., Heard, H.A., Magouirk, J.N., 1967. Effects of the intermediate principal stress on the failure of limestone, dolomite, and glass at different temperatures and strain rates. J. Geophys. Res. 72 (2), 611–640.
Healy, D., Blenkinsop, T.G., Timms, N.E., Meredith, P.G., Mitchell, T.M., Cooke, M.L., 2015. Polymodal faulting: time for a new angle on shear failure. J. Struct. Geol. 80, 57–71.
Heard, H.C., 1960. Chapter 7: transition from brittle fracture to ductile flow in Solenhofen limestone as a function of temperature, confining pressure, and interstitial fluid pressure. In: Griggs, D.T., Handin, J. (Eds.), Rock Deformation, Geological Society of America Memoirs, 79, pp. 193–226.

Heard, H.C., 1963. Effect of large changes in strain rate in the experimental deformation of Yule marble. J. Geol. 71 (2), 162–195.
Hoek, E., Brown, E.T., 1988. The Hoek-Brown failure criterion - a 1988 update. In: Curran, J. (Ed.), Proceedings of the 15th Canadian Rock Mechanics Symposium. University of Toronto, Toronto, Canada, pp. 31–38.
Hoek, E., Martin, C.D., 2014. Fracture initiation and propagation in intact rock - a review. J. Rock Mech. Geotech. Eng. 6 (4), 287–300.
Huang, D., Zhu, T.T., 2018. Experimental and numerical study on the strength and hybrid fracture of sandstone under tension-shear stress. Eng. Fract. Mech. 200, 387–400.
Huang, D., Liu, Y., Cen, D., Zeng, B., Wu, Z., Yang, Y., 2022. Effect of confining pressure on deformation and strength of granite in confined direct tension tests. Bull. Eng. Geol. Environ. 81 (3), 1–20.
Ingraham, M.D., Issen, K.A., Holcomb, D.J., 2013. Response of Castlegate sandstone to true triaxial states of stress. J. Geophys. Res. Solid Earth 118 (2), 536–552.
Issen, K.A., Rudnicki, J.W., 2000. Conditions for compaction bands in porous rock. J. Geophys. Res. Solid Earth 105 (B9), 21529–21536.
Kandula, N., Cordonnier, B., Boller, E., Weiss, J., Dysthe, D.K., Renard, F., 2019. Dynamics of microscale precursors during brittle compressive failure in Carrara marble. J. Geophys. Res. Solid Earth 124 (6), 6121–6139.
Kaus, B.J., 2010. Factors that control the angle of shear bands in geodynamic numerical models of brittle deformation. Tectonophysics 484 (1–4), 36–47.
Khazanehdari, J., Rutter, E.H., Casey, M., Burlini, L., 1998. The role of crystallographic fabric in the generation of seismic anisotropy and reflectivity of high strain zones in calcite rocks. J. Struct. Geol. 20 (2–3), 293–299.
Lade, P.V., 1977. Elasto-plastic stress-strain theory for cohesionless soil with curved yield surfaces. Int. J. Solids Struct. 13 (11), 1019–1035.
Lan, H., Chen, J., Macciotta, R., 2019. Universal confined tensile strength of intact rock. Sci. Rep. 9 (1), 1–9.
Lisle, R.J., Strom, C.S., 1982. Least-squares fitting of the linear Mohr envelope. Q. J. Eng. Geol. Hydrogeol. 15 (1), 55–56.
Llana-Fúnez, S., Rutter, E.H., 2005. Distribution of non-plane strain in experimental compression of short cylinders of Solnhofen limestone. J. Struct. Geol. 27 (7), 1205–1216.
Ma, X., Rudnicki, J.W., Haimson, B.C., 2017. Failure characteristics of two porous sandstones subjected to true triaxial stresses: applied through a novel loading path. J. Geophys. Res. Solid Earth 122 (4), 2525–2540.
Mackwell, S.J., Paterson, M.S., 2002. New developments in deformation studies: high-strain deformation. In: Karato, S.I., Wenk, H.R., (Eds.) Plastic deformation of minerals and rocks. Rev. Mineral. Geochem. 51 (1), 1–19.
McCormick, C.A., Corlett, H., Stacey, J., Hollis, C., Feng, J., Rivard, B., Omma, J.E., 2021. Shortwave infrared hyperspectral imaging as a novel method to elucidate multi-phase dolomitization, recrystallization, and cementation in carbonate sedimentary rocks. Sci. Rep. 11 (1), 1–16.
Mogi, K., 1967. Effect of the intermediate principal stress on rock failure. J. Geophys. Res. 72 (20), 5117–5131.
Mogi, K., 1971. Effect of the triaxial stress system on the failure of dolomite and limestone. Tectonophysics 11 (2), 111–127.
Peacock, D.C.P., Sanderson, D.J., Leiss, B., 2021. Use of Mohr diagrams to predict fracturing in a potential geothermal reservoir. Geosciences 11 (12), 501.
Pieri, M., Burlini, L., Kunze, K., Stretton, I., Olgaard, D.L., 2001. Rheological and microstructural evolution of Carrara marble with high shear strain: results from high temperature torsion experiments. J. Struct. Geol. 23 (9), 1393–1413.
Price, N.J., 1966. Fault and Joint Development in Brittle and Semi-Brittle Rock. Pergamon Press, Oxford, p. 176.
Price, N.J., Cosgrove, J.W., 1990. Analysis of Geological Structures. Cambridge University Press, Cambridge.
Ramsey, J.M., 2003. Experimental Study of the Transition from Brittle Shear Fractures to Joints. Unpublished M.Sc. thesis. Texas A&M University, College Station, p. 291.
Ramsey, J.M., Chester, F.M., 2004. Hybrid fracture and the transition from extension fracture to shear fracture. Nature 428 (6978), 63–66.
Reches, Z.E., Dieterich, J.H., 1983. Faulting of rocks in three-dimensional strain fields I. Failure of rocks in polyaxial, servo-control experiments. Tectonophysics 95 (1–2), 111–132.
Reches, Z.E., Lockner, D.A., 1994. Nucleation and growth of faults in brittle rocks. J. Geophys. Res. Solid Earth 99 (B9), 18159–18173.
Reches, Z.E., Wetzler, N., 2022. An energy-based theory of rock faulting. Earth Planet. Sci. Lett. 597, 117818.
Rodriguez, E., 2005. A Microstructural Study of the Extension-to-Shear Fracture Transition in Carrara Marble. Unpublished M.Sc. thesis. Texas A&M University, College Station, p. 62.
Rowe, K.J., Rutter, E.H., 1990. Palaeostress estimation using calcite twinning: experimental calibration and application to nature. J. Struct. Geol. 12 (1), 1–17.
Rudnicki, J.W., 1977. The effect of stress-induced anisotropy on a model of brittle rock failure as localization of deformation. In: The 18th U.S. Symposium on Rock Mechanics (USRMS), Energy Resources and Excavation Technology, pp. 1–8.
Rudnicki, J.W., Olsson, W.A., 1998. Reexamination of fault angles predicted by shear localization theory. In: Proceedings of Third North American Rock Mechanics Symposium (NARMS'98), Rock Mechanics in Mining, Petroleum and Civil Works, 3-5 June, 1998, Cancun, Mexico. Extend. Abstr. Intern. J. Rock Mech. Min. Sci. 35 (415), 512–513.
Rudnicki, J.W., Rice, J.R., 1975. Conditions for the localization of deformation in pressure sensitive dilatant materials. J. Mech. Phys. Solids 23 (6), 371–394.
Rutter, E.H., 1972. The influence of interstitial water on the rheological behaviour of calcite rocks. Tectonophysics 14, 13–33.
Rutter, E.H., 1995. Experimental study of the influence of stress, temperature, and strain on the dynamic recrystallization of Carrara marble. J. Geophys. Res. Solid Earth 100 (B12), 24651–24663.
Rutter, E.H., Mecklenburgh, J., 2018. Influence of normal and shear stress on the hydraulic transmissivity of thin cracks in a tight quartz sandstone, a granite, and a shale. J. Geophys. Res. Solid Earth 123 (2), 1262–1285.
Rutter, E.H., Casey, M., Burlini, L., 1994. Preferred crystallographic orientation development during the plastic and superplastic flow of calcite rocks. J. Struct. Geol. 16 (10), 1431–1446.
Rutter, E., Wallis, D., Kosiorek, K., 2022. Application of electron backscatter diffraction to calcite-twinning paleopiezometry. Geosciences 12 (6), 222.
Rybacki, E., Niu, L., Evans, B., 2021. Semi-brittle deformation of Carrara marble: Hardening and twinning induced plasticity. J. Geophys. Res. Solid Earth 126, e2021JB022573.
Schmid, S.M., Boland, J.N., Paterson, M.S., 1977. Superplastic flow in finegrained limestone. Tectonophysics 43 (3–4), 257–291.
Spagnoli, A., Carpinteri, A., Vantadori, S., 2015. Interpreting experimental fracture toughness results of quasi-brittle natural materials through multi-parameter approaches. Frattura ed Integrità Strutturale 9 (33), 80–88.
Takahashi, M., Koide, H., 1989. Effect of the intermediate principal stress on strength and deformation behavior of sedimentary rocks at the depth shallower than 2000 m. In: Maury, V., Fourmaintraux, D. (Eds.), Rock at Great Depth, vol. 1. Balkema, Rotterdam, pp. 19–26.
Terzaghi, K., 1923. Die Berechnung der Durchlässigkeitsziffer des Tones aus dem Verlauf der hydrodynamischen Spannungserscheinungen (in German). Sitzungsber. Akad. Wissen. Wien Math-Naturwiss. Kl. Abt. IIa. 132, 105–124.
Vandeginste, V., Swennen, R., Gleeson, S.A., Ellam, R.M., Osadetz, K., Roure, F., 2005. Zebra dolomitization as a result of focused fluid flow in the Rocky Mountains Fold and Thrust Belt, Canada. Sedimentology 52 (5), 1067–1095.
Wibberley, C.A., Petit, J.P., Rives, T., 2000. Micromechanics of shear rupture and the control of normal stress. J. Struct. Geol. 22 (4), 411–427.
Xu, X., Wu, S., Jin, A., Gao, Y., 2018. Review of the relationships between crack initiation stress, mode I fracture toughness and tensile strength of geo-materials. Intern. J. Geomech. 18 (10), 04018136.
Yang, H., Krause, M., Renner, J., 2021. Determination of fracture toughness of mode I fractures from three-point bending tests at elevated confining pressures. Rock Mech. Rock. Eng. 54 (10), 5295–5317.
Zhang, Z.X., 2002. An empirical relation between mode I fracture toughness and the tensile strength of rock. Int. J. Rock Mech. Min. Sci. 39 (3), 401–406.
Zhu, Q.Z., 2017. A new rock strength criterion from microcracking mechanisms which provides theoretical evidence of hybrid failure. Rock Mech. Rock. Eng. 50 (2), 341–352.

Blank page